11-9-2017 10:00 AM

Gamma-Radiation Induced Corrosion of Alloy 800

Mojtaba Momeni, *The University of Western Ontario*

Supervisor: Dr. Jungsook Clara Wren, *The University of Western Ontario*
A thesis submitted in partial fulfillment of the requirements for the Doctor of Philosophy degree in Chemistry
© Mojtaba Momeni 2017

Abstract

This thesis presents a newly developed mechanism and predictive model for the corrosion of Alloy 800. The Fe-Cr-Ni Alloy (Incoloy 800) is mainly used for steam generator (SG) tubing in CANDU and PWR reactors and is a candidate material for the proposed Canadian Supercritical Water Reactor (SCWR) in which it will be exposed to extreme conditions of high radiation flux and large temperature gradients. The influence of gamma radiation and water chemistry conditions on the corrosion behaviour of Alloy 800 are studied in this work. Ionizing radiation creates reducing ($\bullet e_{aq}^-$, $\bullet H$, $\bullet O_2^-$) and oxidizing radiolysis ($\bullet OH$, H_2O_2, O_2) products that affect the redox chemistry, controlling corrosion. Water chemistry conditions including pH, temperature and redox agents can significantly influence the corrosion kinetics. A systematic study of Alloy 800 corrosion was carried out to investigate the effect of these solution conditions. This analysis was used to develop a mechanistic model that takes into account both metal dissolution and oxide formation during the corrosion of Alloy 800. This model is designed to predict the effect of different variables on the corrosion behaviour of Alloy 800 in extreme environments where direct corrosion measurement is nearly impossible.

A series of electrochemical experiments and corrosion tests along with post-test surface analyses were performed in order to gather information on the composition and thickness of the oxide formed during corrosion and the metal cations dissolved in the solution. This combination of electrochemical measurements and surface analyses provided a highly-detailed understanding of Alloy 800 corrosion, allowing a mechanism to be proposed. The proposed mechanism can explain the corrosion behaviour of Alloy 800 in a variety of environments and temperatures, including aqueous and steam corrosion.

The principles behind the proposed mechanism were used to develop a model to account for both oxide formation and metal cation dissolution. The model was used successfully to model oxide thickness on pure iron, the Co-Cr alloy Stellite-6 and Alloy 800 in neutral and moderately alkaline aqueous solutions. The modeled results correlate well with

experimental data. Using the model, it was possible to predict the time-dependent corrosion potential in environments where direct measurements are not possible.

Dedication

To my wonderful and lovely family and wife

Co-Authorship Statement

This thesis includes published data in chapters 7 and 8.

For all the chapters, I was the main author and Prof. J.C. Wren was co-author and Dr. J. Joseph and G. Whitaker helped with writing and editing.

Chapter 4: The electrochemical data in the absence of radiation was done by T.V. Do and J. Joseph helped with the experiments.

Chapter 5: The electrochemical experiments were done by T.V. Do and J. Joseph helped with the experiments.

Chapter 6: The samples in the argon environment were prepared and analyzed by V. Subramaniam and S. Hariharan. J. Joseph helped with all the experimental setup and analysis.

Chapter 8: The experimental works were done by M. Behazin and I modeled them.

Acknowledgments

This works was not possible to complete without the help of my colleagues and friends.

I would like to thank my supervisor, Dr. Clara Wren. She gave me the opportunity to work on my dream project and helped me a lot to widen my horizons and think critically. She was not only my research supervisor, but was a great help in every aspect of my life and helped me whenever I asked for it. This work would not have been possible without her mentorship.

I also would like to thank Dr. Jiju Joseph for being a great source of support over the past four years and Dr. Jamie Noël for all of our scientific discussions. I also would like to thank Dr. Dave Wren and G. Whitaker who helped me with the writing and gave me valuable professional advice.

I would like to thank my wonderful friends and also all of my student peers, both past and present, in the Wren lab and Shoesmith and Noël lab.

Most importantly, I would like to thank my family and my wife, Nasrin, from the bottom of my heart for their unconditional support throughout my academic career.

Symbols

°C	Degree celcius
DR	Dose rate
$\alpha_{\rho\delta\xi\#}$	Transfer coefficient or symmetry factor, normally equal to 0.5
A_{sol}	Surface area exposed to solution (cm^2)
$\Delta\varphi_{oxide}(t)$	Potential drop across the oxide layer at time t (V)
$E_{(i=0)}$	Potential at which net current is zero
E_{APP}	Applied potential during polarization (V)
E_{CORR}	Corrosion potential (V)
E_{final}	Final potential
$E_{initial}$	Initial potential
F	Faraday's constant (96485 $C\times mol^{-1}$)
$f_{k-MO\#}$	Relative ratio of the oxide formation and dissolution constants
f_l	Relative monolayer length of Cr_2O_3 to chromite
φ_m^{eq}	Fermi level at the metal oxide interface (V)
φ_{sol}^{eq}	Fermi level at the oxide solution interface (V)
L_{Cr2O3}	Thickness of air-formed chromium oxide (cm)
L_{MCr2O4}	Thickness of growing chromite (cm)
$\lambda_{MO\#}$	Constant related to the potential drop in the oxide (cm^{-1})
$L_{MO\#}(t)$	Thickness of the MO# oxide layer (cm)
m|ox	Metal/oxide interface
$m_{diss\#}$	Dissolved amount of metal cations (mol)
N	Number of electrons involving in the reaction.
ox|sol	Oxide/solution interface
R	Universal gas constant (8.314 $J\times mol^{-1}\times K^{-1}$)
T	Absolute temperature (K)
$\upsilon_{MO\#}$	Molar volume of oxide ($cm^3\times mol^{-1}$)
V	Driving force for corrosion (V)
V_{SCE}	Potential vs. SCE
$E_{red\#}^{eq}$	Equilibrium potential of a redox pair # involved in corrosion (V)
$E_{rdx\#}(t)$	Electrochemical potential of the reacting system at time t (V)
$E_{ox\#}^{eq}$	Equilibrium potential for oxidation half-reaction (V)
$E_{red\#}^{eq}$	Equilibrium reduction half reaction potential (V)
E_{eq}	Equilibrium half reaction potential (V)
$E_{elec}(t)$	Electrode potential at time t. It is E_{CORR} in an open circuit and E_{app} in potentiostatic polarization (V)

$\eta_{rdx\#}(t)$	Overpotential at the reaction interface (V)
$\eta_{ox\#}(t)$	Anodic overpotential (V)
$\eta_{red\#}(t)$	Cathodic overpotential (V)
$i_{rdx\#}^{eq}$	Exchange current density (A·cm^{-2})
$i_{rdx\#}(t)$	Current density at time t (A·cm^{-2})
$J_{M\#^{n+}}(t)|_{m|ox}$	Metal oxidation flux at the metal/oxide interface (mol×s^{-1}×cm^{-2})
$J_{red\#}(t)|_{ox|sol}$	Solution reduction flux (mol×s^{-1}×cm^{-2})
$\langle J_{M^{n+}}(z,t)\rangle_{oxide}$	Average flux of metal cations across the oxide layer (mol×s^{-1}×cm^{-2})
$J_{M\#^{n+}}(t)|_{ox|sol}$	Total flux of metal cations arriving at the ox|sol interface (mol×s^{-1}×cm^{-2})
$J_{MO\#}(t)|_{oxide}$	Oxide growth flux (mol×s^{-1}×cm^{-2})
$J_{diss\#}(t)|_{sol}$	Dissolution flux (mol×s^{-1}×cm^{-2})
$-\Delta_r G(t)$	Free energy of reaction (J×mol^{-1})
φ_m^{eq}	Fermi level of metal at equilibrium
φ_{sol}^{eq}	Fermi level of solution at equilibrium
$\varphi_{E(Ox)}$	Density of unoccupied electron energy states of oxidants
$\varphi_{E(red)}$	Density of occupied electron energy states of reduction reaction products
$\varphi_{E(M^{n+})}$	Density of unoccupied electron energy states of metal cation
$\varphi_{E(M)}$	Density of occupied electron energy states of metal atom
φ_{CB}	Lowest energy of conduction band
φ_{VB}	Highest energy of valence band
$\varepsilon_{MO\#}$	Specific potential gradient of oxide (V×cm^{-1})
$\Delta Ea_{MO\#}(t)$	Activation energy barrier for oxide growth at time t (J×mol^{-1})
$\Delta Ea_{MO\#}(0)$	Activation energy barrier for oxide growth at time $t = 0$ (no oxide on the surface) (J×mol^{-1})
$\Delta Ea_{oxide}(t)$	Activation energy barrier for oxide growth across the oxide present on the surface at time t (J×mol^{-1})
$c_{MO\#}$	Specific activation energy gradient of oxide (J×mol^{-1}×cm^{-1})
$\Delta V_{oxide}(t)$	Potential drop across an oxide layer at time t (V)
$\Delta V_{oxide}(0)$	Potential drop across an oxide layer at time zero (V)
$\Delta V_{MO\#}(t)$	Potential drop across the layer of MO# at time t (V)
$J_{MO}{''}$	Constant component of metal cation flux

Acronyms

AES	Auger electron spectroscopy
Ag/Ag/Cl	Silver/silver chloride reference electrode
BE	Binding energy
BSE	Backscattered electron
CANDU	Canada deuterium uranium
DH	Dissolved hydrogen
DO	Dissolved oxygen
FCC	Face-center cubic
HCP	Hexagonal close packed
ICP-MS	Inductively coupled plasma - mass spectroscopy
ICP-OES	Inductively coupled plasma- optical emission spectroscopy
KE	Kinetic energy
LET	Linear energy transfer
PDM	Point defect model
PHWR	Pressurized heavy water reactor
PHTS	Primary heat transport system
PLWR	Pressurized light water reactor
PTFE	Polytetrafluoroethylene
PWR	Pressurized water reactor
SCE	Saturated calomel electrode
SCW	Supercritical water
SCWR	Supercritical water reactor
SEM	Scanning electron microscopy
SHE	Standard hydrogen electrode
SG	Steam generator
EDX	Energy dispersive X-Ray spectroscopy
XPS	X-Ray photoelectron spectroscopy

Table of Contents

List of Tables

List of Figures

Chapter 1

Introduction

1.1 Motivation

Nuclear energy is a clean, affordable and low greenhouse gas emitting energy source with the power-generating capacity to meet industrial needs. Nuclear power contributes 10% of worldwide energy production, 15% of Canada's power generation and more than 60% of Ontario's energy supply.

The processes of electricity generation in a nuclear power plant are similar to those in fossil fuel power plants, but the way heat is generated is different. A nuclear reactor uses fissile material as fuel, typically in the form of uranium dioxide. When a neutron collides with a fissile atom such as ^{235}U the nucleus splits into two lighter nuclei and 2-3 neutrons, a process known as fission. During fission, a large amount of heat is produced which is used to generate steam which drives the turbines to produce electricity.

There are several types of nuclear reactor in operation around the world. The most common design is the pressurized light water reactor (PLWR), which uses 3-4%, enriched uranium (i.e., 3-4% ^{235}U in mostly ^{238}U) as fuel, and light water for both coolant and moderator. All the nuclear reactors in Canada are the Canadian designed CANDU® (Canada deuterium uranium) reactors which are pressurized heavy water reactors (PHWR) that use natural uranium (containing only 0.7% ^{235}U) as the fuel and heavy water as both coolant and moderator. A schematic of a CANDU® reactor is shown in Figure 1-1.

The UO$_2$ fuel is encased in Zr-alloy cladding to avoid contact of fuel with the coolant. The structure that houses the circulating coolant is referred to as the heat transport system (HTS). The materials and configuration of the HTS also depend on the reactor type. For CANDU® the HTS system consists of Zr-pressure tubes inside the reactor core, connected to carbon steel feeder pipes that feed the coolant to a header (a tank), which is then connected to heat exchangers inside a steam generator. Heat exchanger tubes are usually constructed

from iron-chromium-nickel alloys such as Alloy 800. Nickel alloys are chosen because of their good mechanical properties and resistance to corrosion.
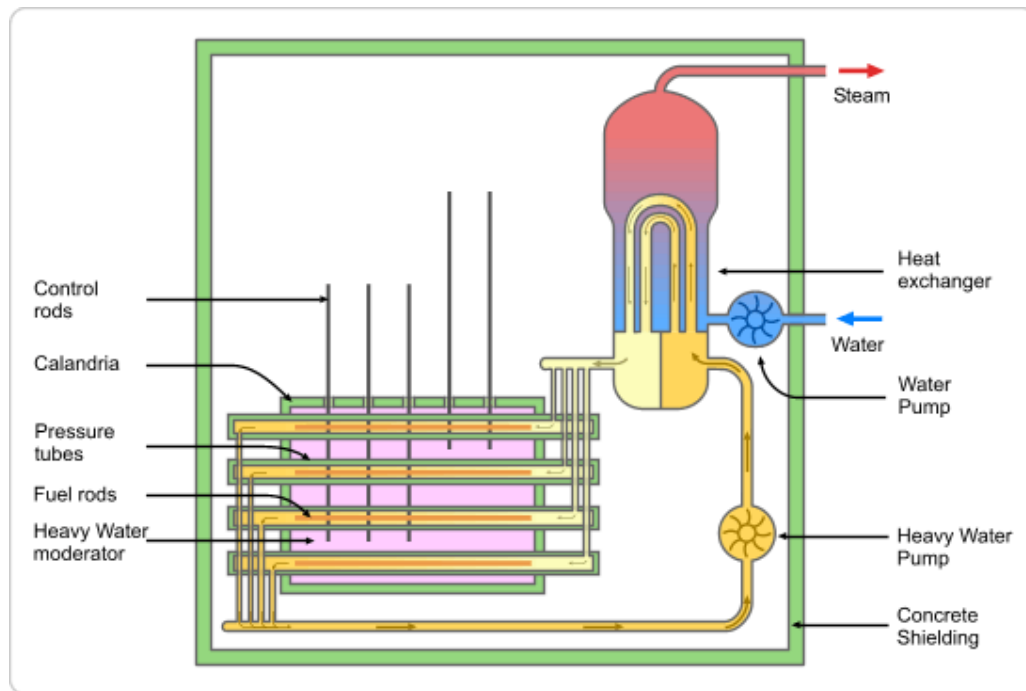
Figure 1-1:   A simplified schematic of a CANDU reactor

One of the major issues for nuclear power plants is the performance of materials in irradiated environments. Under the highly ionizing radiation conditions in the reactor core, the coolant water decomposes to form a range of chemically reactive species which include highly oxidizing ($\cdot OH$, H_2O_2, O_2) and reducing ($\cdot e_{aq}^-$, $\cdot H$, $\cdot O_2^-$) species as shown in reaction 1-1 [1].

$$H_2O \xrightarrow{\hspace{1cm}} \cdot OH, \cdot e_{aq}^-, \cdot H, HO_2\cdot, H_2, H_2O_2, H^+ \hspace{2cm} (1\text{-}1)$$
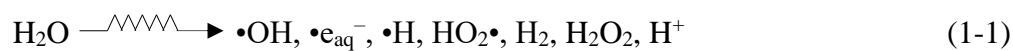
In environments where there is a constant flux of radiation such as those in nuclear reactors, the radiolysis products stabilize to steady state concentrations. These concentrations will determine the redox properties of the water which will affect the corrosion kinetics.

Corrosion is a complex process involving oxidation of metal, reduction of solution species and interfacial transfer of electrons and ions. The transfer of metal cations to the solution phase can induce changes in the physical and (electro-) chemical nature of the

interfacial region. Changes in the surface layer, in turn, can strongly affect the metal oxidation rate and alter the corrosion pathway.

Corrosion of heat exchangers, while slow, poses two major concerns. Changing defective tubes inside a steam generator is very costly, so ideally, they should last for the lifetime of the reactor, or be repaired only at the time of planned reactor refurbishment. Another concern involves transport of radioactive corrosion products inside the coolant circuit. Corrosion of heat exchangers releases dissolved or dispersed metal cations into the coolant. As the coolant circulates in and out of the reactor core, the metal cations are exposed to neutron radiation and can become neutron-activated, producing radioactive products. For example, neutron activation of Ni produces radioactive ^{58}Co, which is a β and γ emitter with a half life of 70 d:

$$^{58}\text{Ni} + \text{neutron} \rightarrow \text{proton} + {}^{58}\text{Co} \tag{1-2}$$

If the neutron-activated product later deposits on the wall of the heat transport tubing outside the reactor core, it can create radioactive hot spots outside the core (Figure 1-2). This can pose a safety concern for reactor maintenance workers and make any maintenance activities during planned reactor shutdown or decommissioning very expensive.
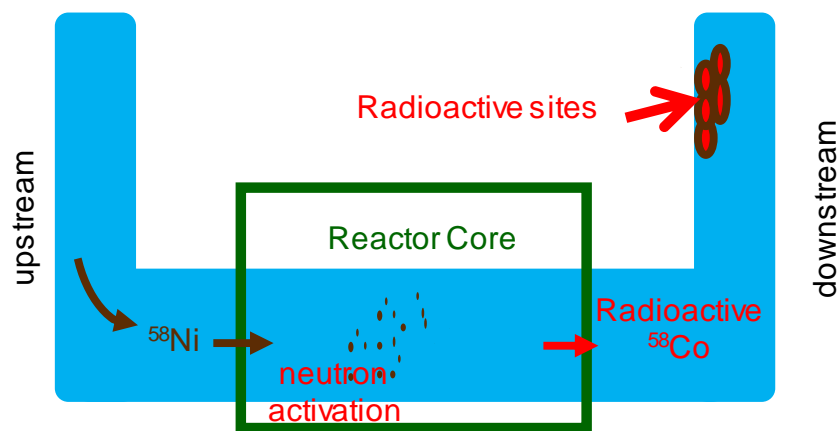
Figure 1-2: **Schematics of corrosion product transport**

Although oxide film formation and corrosion of Fe-Cr-Ni alloys, including Alloy 800, have been investigated extensively [2-25], there is a complete lack of understanding of corrosion behaviour of Alloy 800 under radiation. The effect of changing pH or temperature has not been systematically investigated and the individual contributions of these parameters to oxide film formation have not yet been established. Moreover, no comprehensive studies of the effect of solution parameters on corrosion behaviour on Alloy 800 in the presence of ionizing radiation have been carried out. This work is part of an extensive project on the influence of environmental parameters on the corrosion of Alloy 800 under gamma radiation.

1.2   Research Objective and Approaches

The main aim of this research project is to develop a mechanistic understanding of radiation induced corrosion of Alloy 800 and to develop a corrosion kinetic model that can predict the corrosion rate of heat exchangers in the reactor coolant environments and the probability of stress corrosion cracking over the reactor's lifetime. To achieve these objectives the corrosion kinetics of Alloy 800 are being studied using electrochemical techniques and coupon-exposure tests. The electrochemical techniques include corrosion potential (E_{CORR}), linear polarization resistance, and potentiodynamic polarization measurements. The corrosion tests are performed using Alloy 800 coupons immersed in solutions in sealed quartz vials under different exposure conditions. These measurements are supplemented by post-test surface analyses including scanning electron microscopy (SEM), X-ray photoelectron spectroscopy (XPS) and Auger electron spectroscopy (AES), Raman spectroscopy and dissolved metal analysis by inductively coupled plasma mass spectrometry or optical emission spectroscopy (ICP-MS and ICP-OES). The solution parameters studied are pH, presence of γ-radiation, oxygen content of the environment, temperature, and corrosion environment in aqueous and steam conditions.

1.3   Thesis Outline

Chapter 1: Thesis motivation, objectives, approaches, and thesis outline.

Chapter 2: Materials background, literature reviews, and theoretical background for the experimental results in chapters 4-7.

Chapter 3: Descriptions of the techniques used to obtain the data reported in Chapters 4-6.

Chapter 4: Comparative study of oxide formation on Alloy 800 to probe the roles of pH and gamma-radiation. The oxides that formed were studied both electrochemically and by using surface analytical methods.

Chapter 5: Results of experiments on the combined effects of pH and gamma-irradiation on the kinetics of corrosion of Alloy 800. The electrochemical data and the coupon study was only carried out at 150 °C.

Chapter 6: Results of experiments on the effect of γ-radiation and oxygen content on the early stages of steam corrosion of Alloy 800H at 285 °C.

Chapter 7: Principles of the mass and charge balance model.

Chapter 8: Modeling and simulation results for the corrosion of Co-Cr-Stellite-6.

Chapter 9: Modeling and simulation results for the corrosion of Alloy 800.

Chapter 10: Thesis summary. Brief discussion of the scope for future work.

1.4   References

[1] J. Wren, Steady-state radiolysis: effects of dissolved additives, in: Nuclear Energy and the Environment, ACS Publications, 2010, pp. 271-295.

[2] N.S. McIntyre, R.D. Davidson, T.L. Walzak, A.M. Brennenstuhl, F. Gonzalez, S. Corazza, The corrosion of steam generator surfaces under typical secondary coolant

conditions: Effects of pH excursions on the alloy surface composition, Corrosion Science, 37 (1995) 1059-1083.

[3] M. Sennour, L. Marchetti, F. Martin, S. Perrin, R. Molins, M. Pijolat, A detailed TEM and SEM study of Ni-base alloys oxide scales formed in primary conditions of pressurized water reactor, Journal of Nuclear Materials, 402 (2010) 147-156.

[4] L. Marchetti, S. Perrin, Y. Wouters, F. Martin, M. Pijolat, Photoelectrochemical study of nickel base alloys oxide films formed at high temperature and high pressure water, Electrochimica Acta, 55 (2010) 5384-5392.

[5] M. Dumerval, S. Perrin, L. Marchetti, M. Sennour, F. Jomard, S. Vaubaillon, Y. Wouters, Effect of implantation defects on the corrosion of 316L stainless steels in primary medium of pressurized water reactors, Corrosion Science, 107 (2016) 1-8.

[6] L. Marchetti, S. Perrin, F. Jambon, M. Pijolat, Corrosion of nickel-base alloys in primary medium of pressurized water reactors: New insights on the oxide growth mechanisms and kinetic modelling, Corrosion Science, 102 (2016) 24-35.

[7] S. Guillou, C. Cabet, C. Desgranges, L. Marchetti, Y. Wouters, Influence of Hydrogen and Water Vapour on the Kinetics of Chromium Oxide Growth at High Temperature, Oxidation of Metals, 76 (2011) 193-214.

[8] T. Dieudonné, L. Marchetti, M. Wery, F. Miserque, M. Tabarant, J. Chêne, C. Allely, P. Cugy, C.P. Scott, Role of copper and aluminum on the corrosion behavior of austenitic Fe–Mn–C TWIP steels in aqueous solutions and the related hydrogen absorption, Corrosion Science, 83 (2014) 234-244.

[9] H. Lefaix-Jeuland, L. Marchetti, S. Perrin, M. Pijolat, M. Sennour, R. Molins, Oxidation kinetics and mechanisms of Ni-base alloys in pressurised water reactor primary conditions: Influence of subsurface defects, Corrosion Science, 53 (2011) 3914-3922.

[10] L. Marchetti, S. Perrin, O. Raquet, M. Pijolat, Corrosion mechanisms of Ni-base alloys in pressurized water reactor primary conditions, in: Materials Science Forum, Trans Tech Publ, (2008) 529-537.

[11] M. Sennour, L. Marchetti, S. Perrin, R. Molins, M. Pijolat, O. Raquet, Characterization of the oxide films formed at the surface of Ni-base alloys in pressurized water reactors primary coolant by transmission electron microscopy, in: Materials Science Forum, Trans Tech Publ, (2008) 539-547.

[12] X. Li, J. Wang, E.-H. Han, W. Ke, Corrosion behavior for Alloy 690 and Alloy 800 tubes in simulated primary water, Corrosion Science, 67 (2013) 169-178.

[13] J. Crum, Stress corrosion cracking testing of Inconel alloys 600 and 690 under high-temperature caustic conditions, CORROSION, 42 (1986) 368-372.

[14] J.Z. Wang, J.Q. Wang, E.H. Han, Influence of temperature on electrochemical behavior and oxide film property of Alloy 800 in hydrogenated high temperature water, Materials and Corrosion, 67 (2016) 796-803.

[15] P. Marcus, J. Grimal, The anodic dissolution and passivation of NiCrFe alloys studied by ESCA, Corrosion Science, 33 (1992) 805-814.

[16] S. Leistikow, I. Wolf, H. Grabke, Effects of cold work on the oxidation behavior and carburization resistance of Alloy 800, Materials and Corrosion, 38 (1987) 556-562.

[17] M. Faichuk, "Characterization of the Corrosion and Oxide Film Properties of Alloy 600 and Alloy 800" (2013). Electronic Thesis and Dissertation Repository. 1777.

[18] T. Nickchi, A. Alfantazi, Electrochemical corrosion behaviour of Incoloy 800 in sulphate solutions containing hydrogen peroxide, Corrosion Science, 52 (2010) 4035-4045.

[19] T. Nickchi, A. Alfantazi, Effect of Buffer Capacity on Electrochemical Corrosion Behavior of Alloy 800 in Sulfate Solutions, Corrosion, The Journal of Science and Engineering, 68 (2012) 015003-015001-015003-015011.

[20] D.-H. Xia, Y. Behnamian, H.-N. Feng, H.-Q. Fan, L.-X. Yang, C. Shen, J.-L. Luo, Y.-C. Lu, S. Klimas, Semiconductivity conversion of Alloy 800 in sulphate, thiosulphate, and chloride solutions, Corrosion Science, 87 (2014) 265-277.

[21] J. Hickling, N. Wieling, Electrochemical investigations of the resistance of Inconel 600, Incoloy 800, and Type 347 stainless steel to pitting corrosion in faulted PWR secondary water at 150 to 250 °C, CORROSION, 37 (1981) 147-152.

[22] J. Huang, X. Wu, E.-H. Han, Influence of pH on electrochemical properties of passive films formed on Alloy 690 in high temperature aqueous environments, Corrosion Science, 51 (2009) 2976-2982.

[23] S. Persaud, A. Korinek, J. Huang, G. Botton, R. Newman, Internal oxidation of Alloy 600 exposed to hydrogenated steam and the beneficial effects of thermal treatment, Corrosion Science, 86 (2014) 108-122.

[24] S. Persaud, J. Smith, A. Korinek, G. Botton, R. Newman, High resolution analysis of oxidation in Ni-Fe-Cr alloys after exposure to 315° C deaerated water with added hydrogen, Corrosion Science, 106 (2016) 236-248.

[25] B. Langelier, S. Persaud, R. Newman, G. Botton, An atom probe tomography study of internal oxidation processes in Alloy 600, Acta Materialia, 109 (2016) 55-68.

Chapter 2
Technical Background and Literature Review

2.1 Fe-Cr-Ni alloys in Nuclear Reactors

Iron-chromium-nickel (Fe-Cr-Ni) alloys, nickel-based alloys (Incoloy® Alloys) and stainless steels are important materials used in nuclear power plants. Ni alloys are mainly used for steam generator (SG) tubes (alloys 600, 800 and 690). Alloy 800 (also known as Incoloy® 800) is considered a Ni-based alloy but is not technically a Ni-based alloy, as it contains only 33 Wt.% Ni with 22 Wt.% Cr with 45 Wt.% Fe. These alloys are selected for their good uniform and stress corrosion cracking resistance, and good mechanical properties [1]. Stainless steels are used for components holding radioactive water or gas. The stainless steels most commonly used in nuclear reactors are the 300 ASTM series (like 304 and 316), which contain approximately 10 wt.% Ni and 20 wt.% Cr.

Fe-Cr-Ni alloys and in particular Alloy 800 are exposed to different solution environments. These types of alloys are also candidate materials for fuel cladding in the generation IV (Gen IV) supercritical water-cooled reactors (SCWR). In conventional nuclear reactors, and in particular pressurized water reactors (PWR) and Canadian deuterium uranium (CANDU®) reactors, they are used as thin-walled heat exchanger tubes in the steam generators that are exposed to both primary and secondary coolant water systems. Firstly, the principles of corrosion will be outlined, and then the solution environments in a range of reactor environments will be summarized.

2.2   Principles of Corrosion

Corrosion is an electrochemical process typically involving the oxidation of a metal (anodic reaction) coupled with the reduction of solution species (cathodic reaction). For example, in the Ni case:

Anodic Reaction (oxidation): $Ni^0(m) \rightarrow Ni^{2+}(aq) + 2e^-$ (2-1a)

Cathodic Reaction (reduction): $H_2O(aq) + e^- \rightarrow OH^- + \frac{1}{2} H_2$ (2-1b)

Overall Corrosion Reaction: $Ni^0(m) + 2\ H_2O(aq) \rightarrow Ni^{2+}(aq) + 2OH^- + H_2$

(2-1c)
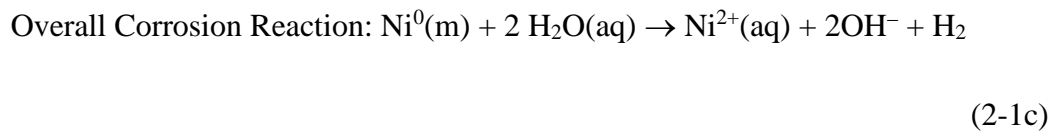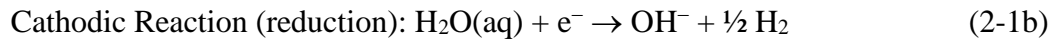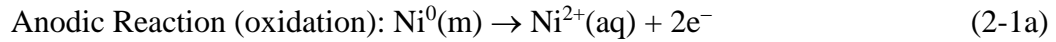
The oxidized metals (or metal cations) are then hydrated and diffuse to the solution phase and/or precipitate with hydroxide or oxygen anions to form solid metal oxides.

When a metal with a specific chemical potential comes into contact with water which has a different chemical potential, corrosion occurs because the metal-solution system is trying to reach (electro-) chemical equilibrium by exchanging metal cations and electrons between the two reacting phases. The thermodynamic driving force for each half-reaction is:

$$-\Delta_{ox}G = nF\left(E_{CORR} - E_{eq}^{ox}\right)$$ (2-2a)

$$-\Delta_{red}G = -nF\left(E_{CORR} - E_{eq}^{red}\right)$$ (2-2b)

where E_{eq}^{ox} and E_{eq}^{red} are the equilibrium potentials for the metal oxidation half-reaction and the solution reduction half-reaction, and E_{CORR} is the electrochemical potential of the corroding system at the time of reaction. By convention the reference potential is the standard reduction potential for hydrogen. The equilibrium potential of each half reaction is quantified by the Nernst equations:

$$E_{eq}^{ox} = E_{(Ni^{2+}/Ni)}^o + \frac{RT}{nF}\ln\left(\frac{a_{eq}^{Ni^{2+}}}{a_{eq}^{Ni^0}}\right)$$ (2-2c)

$$E_{eq}^{red} = E_{(H_2/H_2O)}^o + \frac{RT}{nF} \ln \left(\frac{a_{eq}^{H2O}}{a_{eq}^{OH^-} \cdot a_{eq}^{H2^{1/2}}} \right) \tag{2-2d}$$

where R is the gas constant (8.314 J/mol), T is the temperature (in Kelvin), n is the number of electrons transferred, F is Faraday's constant (96485 C/mol), $E_{(Ni^{2+}/Ni)}^o$ and $E_{(H_2/H_2O)}^o$ are the standard reduction potentials for the corresponding half-reactions, and $a_{eq}^{Ni^{2+}}$, $a_{eq}^{Ni^0}$, a_{eq}^{H2O}, a_{eq}^{H2} and $a_{eq}^{OH^-}$ represent the chemical activities of the corresponding species when the corroding system reaches equilibrium. By definition, the activity of a solid metal species and solvents is 1.0.

As a practically measurable quantity, the corrosion potential is the voltage difference between a corrosion cell (a metal immersed in a solution) and a designated standard reference electrode. The corrosion-cell potential is often referred to as the electrode potential.

As described above, at the corrosion potential, E_{CORR}, the rates of the anodic reaction and the cathodic reaction are equal. If the rate of each half reaction is controlled by the interfacial transfer rate of electrons, the rate can be determined as a function of electrode potential according to the Butler-Volmer equation.

$$i(E) = i_0 \left(\exp\left(\frac{\alpha nF}{RT} \left(E - E_{eq} \right) \right) - \exp\left(\frac{-(1-\alpha)nF}{RT} \left(E - E_{eq} \right) \right) \right) \tag{2-3}$$

Where $i(E)$ is the current or the rate of charge transfer at electrode potential E, F is Faraday's constant, E_{eq} is the equilibrium potential, T is the absolute temperature, n is the number of electrons, α is the charge transfer coefficient and i_0 is the exchange current at equilibrium.

For a system to corrode, E_{CORR} must lie sufficiently above the E_{eq} of the metal oxidation half reaction (E_{eq}^{ox}) and sufficiently below the E_{eq} of the solution reduction half reaction (E_{eq}^{red}). That is, if interfacial electron transfer is rate determining, the rates of metal oxidation ($i_{ox}^{E_{CORR}}$) and solution reduction ($i_{red}^{E_{CORR}}$) can be approximated as:

$$i_{ox}^{E_{CORR}} \approx i_{ox}^{E_{eq}^{ox}} \cdot \exp\left(\alpha_{ox} \cdot \left(\frac{nF}{RT} \right) \cdot \left(E_{CORR} - E_{eq}^{ox} \right) \right) \tag{2-4}$$

$$i_{red}^{E_{CORR}} \approx -i_{red}^{E_{eq}^{ox}} \cdot \exp\left(-(1 - \alpha_{red}) \cdot \left(\frac{nF}{RT}\right) \cdot \left(E_{CORR} - E_{eq}^{red}\right)\right) \qquad \text{(2-5)}$$

The Butler-Volmer relationships for anodic and cathodic half reactions and the corrosion potential are schematically presented in Figure 2-1. At E_{CORR} the total oxidation rate is the same as the total reduction rate, and the net current is zero:

$$i_{ox}^{E_{CORR}} = -i_{red}^{E_{CORR}} = i_{CORR} \qquad \text{(2-6a)}$$

$$i_{net}(at\ E_{CORR}) = i_{ox}^{E_{CORR}} + \left(-i_{red}^{E_{CORR}}\right) = 0 \qquad \text{(2-6b)}$$

The corrosion current, i_{CORR}, corresponds to the rate of metal oxidation, whereas $i_{net}(E_{CORR})$ is the current that we actually measure. The measured current on a naturally corroding system is thus zero, and the corrosion rate, or corrosion current, cannot be obtained by measuring the current of the corroding system directly.
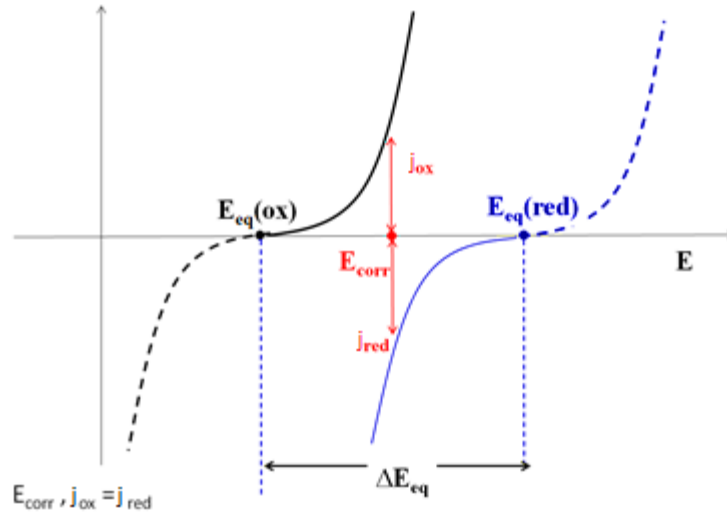
Figure 2-1: **Schematic illustrating the Butler-Volmer relationships for metal oxidation and solution reduction reactions.**

One way to determine the corrosion rate is to polarize the electrode away from E_{CORR}, and to measure the current as a function of polarization or applied potential (E_{APP}). The measured relationship between current and E_{APP} can then be used to extract the corrosion

11

current at E_{CORR} because from equations outlined above, we can derive the following current-E_{APP} relationship:

$$i_{ox}^{E_{APP}} \approx i_{ox}^{E_{eq}^{ox}} \cdot \exp\left(\left(\frac{\alpha_{ox}nF}{RT}\right) \cdot \left(E_{APP} - E_{CORR} + E_{CORR} - E_{eq}^{ox}\right)\right) \qquad \text{(2-7a)}$$

$$i_{ox}^{E_{APP}} \approx i_{ox}^{E_{eq}^{ox}} \cdot \exp\left(\left(\frac{\alpha_{ox}nF}{RT}\right) \cdot \left(E_{CORR} - E_{eq}^{ox}\right)\right) \cdot \exp\left(\left(\frac{\alpha_{ox}nF}{RT}\right) \cdot \left(E_{APP} - E_{CORR}\right)\right)$$

$$\text{(2-7b)}$$

$$i_{ox}^{E_{APP}} \approx i_{CORR} \cdot \exp\left(\left(\frac{\alpha_{ox}nF}{RT}\right) \cdot \left(E_{APP} - E_{CORR}\right)\right) \qquad \text{(2-7c)}$$

And similarly,

$$i_{red}^{E_{APP}} \approx -i_{CORR} \cdot \exp\left(-\left(\frac{(1-\alpha_{red})nF}{RT}\right) \cdot \left(E_{APP} - E_{CORR}\right)\right) \qquad \text{(2-7d)}$$

And the net current as a function of E_{APP} is:

$$i_{net} = i_{ox}^{E_{APP}} + i_{red}^{E_{APP}} \qquad \text{(2-8a)}$$

$$i_{net} \approx i_{CORR} \cdot \left(\exp\left(\left(\frac{\alpha_{ox}nF}{RT}\right) \cdot \left(E_{APP} - E_{CORR}\right)\right) - \exp\left(-\left(\frac{(1-\alpha_{red})nF}{RT}\right) \cdot \left(E_{APP} - E_{CORR}\right)\right)\right) \qquad \text{(2-8b)}$$

This current-potential relationship is known as the Wagner-Trude equation. If E_{APP} is sufficiently greater than E_{CORR} that the cathodic current has a negligible contribution to the net current, it can be approximated to:

$$i_{net}(at\ E_{APP}) \approx i_{ox}^{E_{APP}} \approx i_{CORR} \cdot \exp\left(\left(\frac{\alpha_{ox}nF}{RT}\right) \cdot \left(E_{APP} - E_{CORR}\right)\right) \qquad \text{(2-9a)}$$

$$\log i_{net} \approx \log i_{CORR} + \left(\frac{\alpha_{ox}nF}{2.303RT}\right) \cdot \left(E_{APP} - E_{CORR}\right) \qquad \text{(2-9b)}$$

Similarly, for $E_{APP} \ll E_{CORR}$, the net current is approximated to:

$$i_{net}(at\ E_{APP}) \approx i_{red}^{E_{APP}} \approx -i_{CORR} \cdot \exp\left(-\alpha_{red} \cdot \left(\frac{nF}{RT}\right) \cdot (E_{APP} - E_{CORR})\right) \quad \text{(2-9c)}$$

$$\log(-i_{net}) \approx \log(i_{CORR}) - \left(\frac{(1-\alpha_{red})nF}{2.303RT}\right) \cdot (E_{APP} - E_{CORR}) \quad \text{(2-9d)}$$

Equations 2-9b and 2-9d are known as Tafel equations and the slope of E_{APP} versus log ($|i_{net}|$) is known as a Tafel slope.

The above equations show that the corrosion current can be theoretically obtained by performing potentiodynamic polarization experiments, which measure the current as a function of E_{APP} while scanning E_{APP} at a specific rate, and then by extrapolating to the polarization curve to E_{CORR}. However, the above current-potential relationships assume that the overall metal oxidation rate is determined by the rate of interfacial electron transfer between metal and solution phases, that only one type of metal oxidation reaction occurs and that the interfacial electron transfer rate does not change over the potential range over which the current-potential relationships are obtained.

2.3 Environment of Corrosion

2.3.1 The Primary Coolant Water

The role of primary coolant water is to transport the heat generated from the fission reaction in the reactor core to the SG to produce steam. Due to the complexity of this system, there are many types of materials used in this primary heat transport system (PHTS). The design of PHTS varies in the different types of nuclear reactor that are currently in service or under development. One of the primary objectives of water chemistry control in the PHTS is to minimize the corrosion of alloys in the heat transport system. This goal causes different coolant chemistry in the different type of reactors. The other objectives of chemistry control in the PHTS are minimizing deposition of corrosion products on the fuel and controlling the concentration of activated corrosion products and fission products in the system. These objectives are accomplished through constant control of the pH, oxygen content and ion concentrations in the coolant. As CANDU and PWR reactors comprise the vast majority of

in-service reactors worldwide, the main focus of this review will be on the published data for these two types of reactors.

Normally, the water chemistry is different for each individual plant with each maintaining its own chemistry practices and operational guidelines but general guidelines for water chemistry in PHTS of CANDU are shown in Table 2-1. The water chemistry in the PWRs is different from that of CANDU. It is reported as B: 1200 ppm (weight percentages) as H_3BO_3, Li: 2.0 ppm as LiOH, and pressure $\sim$ 12.2 MPa at 310 °C. The pH of the solution at 310 °C is 6.99. The normal PWR primary water chemistry or hydrogenated water chemistry has a dissolved oxygen (DO) level <5 ppb and a dissolved hydrogen (DH) level of 2.65 ppm [2].

Table 2-1: CANDU Primary Coolant Chemistry [3]

Parameter	Typical Specification Range
pH	10.2 – 10.4
$[Li^+]$	0.35 – 0.55 mg/kg (ppm)
$[D_2]$	3 – 10 mL/kg
conductivity	0.86 – 1.4 mS/m (dependent upon LiOH concentration)
Dissolved O_2	< 0.01 mg/kg
$[Cl^-]$, $[SO_4^{2-}]$, etc	< 0.05 mg/kg
Isotopic	> 98.65 % D_2O
Fission products	< 106 Bq/kg D_2O; monitoring I-131 indicative of fuel failure
Temperature	260 – 325 °C

2.3.2 Secondary System

The Secondary Heat Transport System (also known as secondary system) is responsible for producing steam to drive the turbines and generate electricity. Generally, the secondary system environments are similar for both PWR and CANDU. However, the secondary systems at each plant differ in terms of steam generator (SG) configuration and the materials used for the various components. Normally, there are two classifications: all-ferrous and copper-containing. These different configurations and materials produce

different solution chemistries in the SG. For iron-based systems the pH can be up to 10 because corrosion of iron is minimized at moderately alkaline pH. For copper-based systems, the corrosion rate is at a minimum at pH close to 9, so the environmental pH is maintained at 9.2-9.4. In addition, the use of ammonia is limited or totally avoided because of its detrimental effect on copper corrosion. Hydrazine is added to produce a reducing environment and help to reduce the risk of cracking in the tubing. Chemistry parameters that are targets for the secondary system chemistry control (mainly in CANDU reactors) and are shown in Table 2-2.

Table 2-2: Secondary System Water chemistry [3]

Parameter	Typical Specification Range
pH	9.5 - 10 (for all-ferrous systems)
Hydrazine	0.020 – 0.030 mg/kg (ppm)
Na^+	< 0.05 mg/kg
Dissolved O_2	< 0.01 mg/kg
$[Cl^-]$, $[SO_4^{2-}]$, etc	< 0.05 mg/kg
Temperature	220 – 288 °C

2.4   Corrosion of Alloy 800

Before examining the corrosion of Alloy 800, it is useful to review the oxides that are known to form as it corrodes. While there are a few minor alloying elements in this alloy, we will only examine the oxides of the major components of Alloy 800, Fe, Ni and Cr. The oxides of these elements control the corrosion of Alloy 800. The oxy-hydroxides of these elements are also considered as they are known to form as the hydrolyzed outermost layer of the oxide that is in contact with water.

2.4.1   Iron, Nickel and Chromium Oxides

2.4.1.1   Magnetite (Fe_3O_4)

Magnetite is an oxide with a spinel structure (Figure 2-2). The formula Fe_3O_4 for magnetite is sometimes written as $FeO \cdot Fe_2O_3$, which is one part wüstite (FeO) and one part hematite (Fe_2O_3). This indicates the two different oxidation states of iron in this compound. Figure 2-2 is a schematic of the atomic locations in a spinel structure. The whole spinel unit cell can be thought as cubic close-packed arrays of oxide ions with cations in the octahedral and tetrahedral interstices. The distance between two adjacent O^{2-} is 0.298 nm [4]. The cubic unit cell dimensions are a = b = c = 0.8396 nm [4]. The unit cell contains 32 oxide anions, providing 16 octahedral sites and 8 tetrahedral sites for Fe cations. The tetrahedral sites are located at the corners, face centres and quadrant centres in half of the quadrants. The octahedral sites are in the other half of the quadrants, immediately above or below the oxide anions. In magnetite (Fe_3O_4), the 8 tetrahedral sites and 8 of the octahedral sites are occupied by Fe^{III} ions, while the remaining 8 octahedral sites are occupied by Fe^{II} ions resulting a formula $Fe_8^{II}Fe_{16}^{III}O_{32}$, or Fe_3O_4 [5]. Magnetite, with its small band gap of 0.07 eV [6] and a dielectric permittivity of 16.9 is considered to be an almost conductive material [7]. Under most of the experimental conditions of this study magnetite is reported to be insoluble [8].
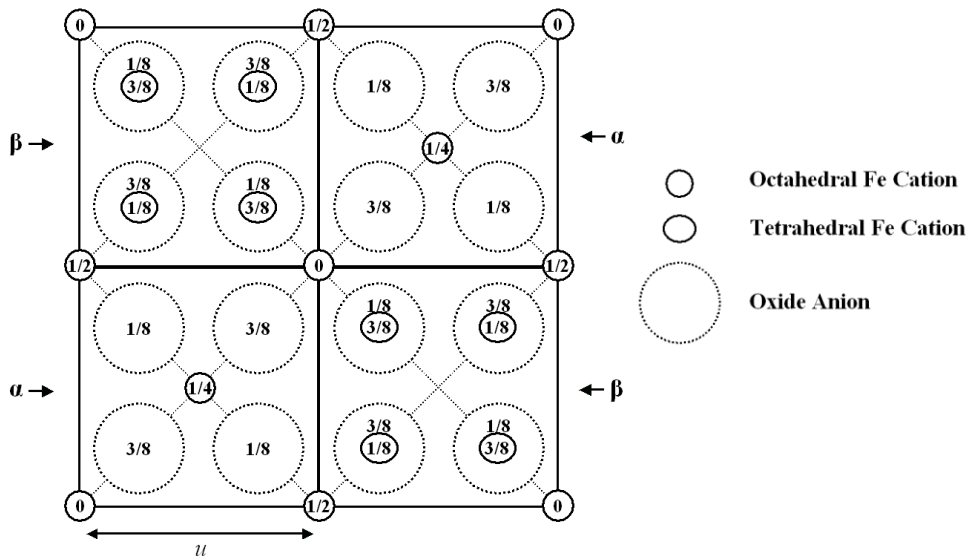
Figure 2-2: Diagram of atomic locations in a normal spinel (or inverse spinel). Only the bottom half of a single unit cell, i.e., four quadrants of the total eight is shown. Oxide ions are represented by large dashed circles and each quadrant contains four. The height of the oxide ions in the z-axis out of the plane of the page is shown in units of the lattice parameter. Tetrahedral sites are represented by oval circles, with their heights shown in units of lattice parameter. Octahedral sites are represented by the smallest open circles, with their height above the base plane in units of lattice parameter. Two of the four quadrants contain a tetrahedral site in their center, and these are categorized as α-type quadrants in this figure. The remaining two quadrants contain the octahedral sites and are categorized as β-type quadrants [5].

2.4.1.2 **Maghemite (γ-Fe₂O₃)**

Maghemite is another spinel ferrite, which has the same structure as magnetite. The distance between two adjacent O^{2-} is 0.295 nm [4]. The cubic unit cell dimensions for maghemite are a = b = c = 0.8347 nm; however, the structure of maghemite is less well definedas the 8 tetrahedral cation sites are fully occupied but the 16 octahedral cation sites are fractionally occupied with, on average, 13.33 Fe^{III} per unit cell. Specifically, 25% of the octahedral sites have a 33% vacancy with a formula $(Fe_8^{III})_{tetra}(Fe_{40/3}^{III}M_{8/3})_{oct}O_{32}$ where M represents a vacancy, which gives the stoichiometry of Fe₂O₃ [5]. Maghemite can be

17

considered as an Fe^{II} deficient magnetite, or alternatively magnetite can be considered as maghemite doped with Fe^{II} [9]. Maghemite is an insulator with a dielectric permittivity of 4.5 [4]. Under the mildly basic conditions used in this study, maghemite is insoluble [8]

2.4.1.3   Lepidocrocite (γ-FeOOH)

γ-FeOOH can be thought of as as FeO(OH). As with the above two iron oxides, lepidocrocite has a cubic close-packed (ccp) oxygen (O^{2-}/OH) lattice structure with the distance between two adjacent O^{2-} being 0.28 nm [10]. However, the cell unit is orthorhombic rather than cubic. There are four FeO(OH) moieties in the orthorhombic unit cell which has dimensions a = 1.252 nm, b = 0.3871 nm and c = 0.3071 nm [4]. There are 8 oxide anions forming 8 octahedral sites in each unit cell, which consists of arrays of ccp anions (O^{2-}/OH^-) stacked with Fe^{III} ions occupying the octahedral interstices, i.e., 4 of the 8 octahedral sites are occupied by Fe^{III} cations as illustrated in Figure 2-3. The cations form an octahedral arrangement in corrugated layers and they are bonded by hydrogen bonding via hydroxide layers. Thus, the conversion of either magnetite or maghemite to γ-FeOOH within the oxide matrix will result in a change to the O-O bond distance, and producing stress that can cause film breakdown. γ-FeOOH is an insulator [7, 11] with a dielectric permittivity of 9.6 [7].
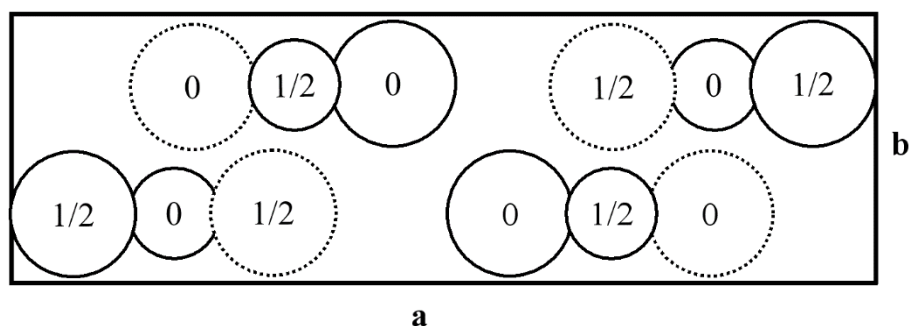
Figure 2-3:   **A projection along c of the orthorhombic unit cell of lepidocrocite. The small circles represent Fe^{III} cations, the larger circles are the hydroxyl anions and the dashed larger circles are oxide anions. Four of the 8 octahedral sites formed by O^{2-}/OH^- anions are occupied by Fe^{III} cations [11].**

2.4.1.4   **Nickel oxide (NiO)**

NiO has the same crystal structure as NaCl, with octahedral Ni^{II} and O^{2-} sites (Figure 2-4). This theoretically simple structure is commonly known as the rock salt structure. However, as is common for many of binary metal oxides, NiO is often non-stoichiometric which means the Ni:O ratio deviates from 1:1. This non-stoichiometry in the NiO causes a colour change. If the ratio is 1:1, NiO appears green and the non-stoichiometric NiO is black. The reported optical band-gap of NiO is in the range of 3.4 eV [12] to 4.3 eV [13].
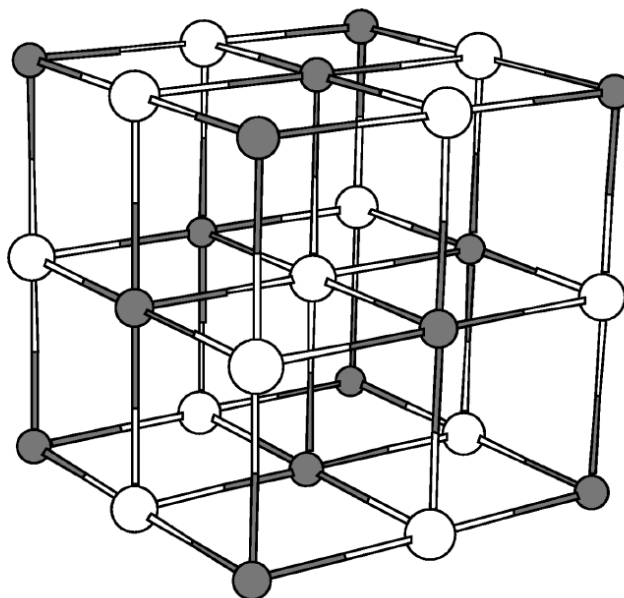
Figure 2-4:   Crystal structure of nickel oxide. Oxygen sites are shown in white; nickel sites are shown in grey [14].

2.4.1.5   **Nickel hydroxide (Ni(OH)₂)**

Nickel hydroxide has two well-characterized polymorphs. The α structure (Figure 2-5) consists of Ni(OH)$_2$ layers with intercalated anions or water [15, 16]. The β form (Figure 2-6) adopts a hexagonal close-packed structure of Ni^{II} and OH^- ions [15, 16]. In the presence of water, the α polymorph typically recrystallizes to the β form [16, 17]. In addition to the α

and β polymorphs, several γ nickel hydroxides have been described, distinguished by crystal structures with much larger inter-sheet distances [16].

(*a*) (*b*)

3 Ni^{2+}: $(0,0,0)$, $(1/3,2/3,0)$, $(2/3,1/3,0)$

6 OH^-: $(1/3,0,z)$, $(0,1/3,z)$, $(2/3,2/3,z)$

$(2/3,0,\bar{z})$, $(0,2/3,\bar{z})$, $(1/3,1/3,\bar{z})$

2 H_2O $(1/3,2/3,1/2)$, $(2/3,1/3,1/2)$
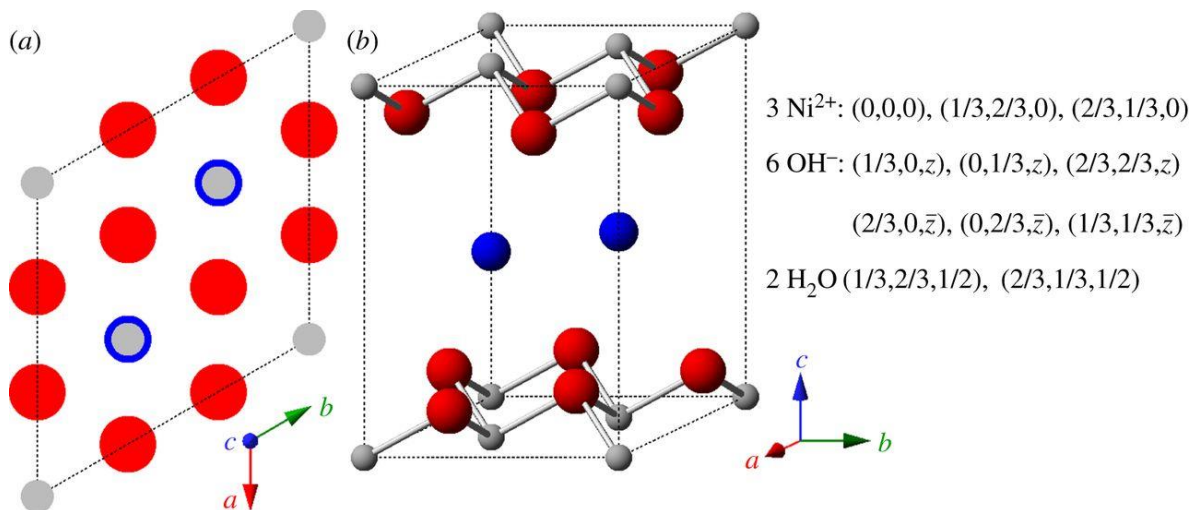
Figure 2-5: **The idealized crystal structure of α-Ni(OH)₂·xH₂O represented by (a) unit cell projection and (b) ball-and-stick unit cell for x = 0.67 (actual value varies, 0.41 ≤ x ≤ 0.7). Small (grey) spheres, Ni^{2+}; large (red) spheres, OH^-; medium size (blue) spheres, H_2O [18, 19]**
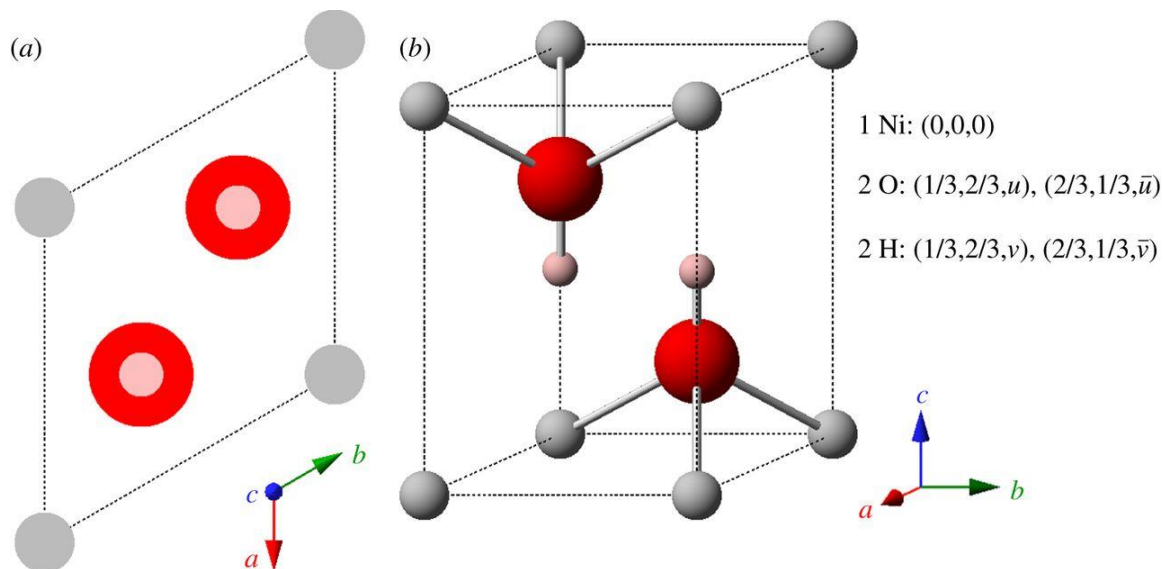
Figure 2-6: **The crystal structure of *β*-Ni(OH)$_2$ represented by (*a*) unit cell projection and (*b*) ball-and-stick unit cell . Medium size (grey) spheres, Ni^{2+}; large (red) spheres, O^{2-}; small (pink) spheres, H$^+$ [18, 19]**

2.4.1.6   **Cr$_2$O$_3$ and FeCr$_2$O$_4$**

Alloy 800 contains approximately 25% Cr. Even brief contact of chromium with moist air is sufficient to create a thin oxide layer, Cr$_2$O$_3$, on the alloy surface, which protects the alloy from further rapid oxidation [20]. This oxide has a corundum structure which consists of a hexagonal close packed array of oxide anions with 2/3 of the octahedral sites occupied by chromium atoms (Figure 2-7) [21]. Like corundum, Cr$_2$O$_3$ is a hard, brittle material. The band gap of Cr$_2$O$_3$ is 3.3 eV [22]. Chromium oxide is a stable oxide but in highly oxidizing conditions Cr^{III} oxidizes to Cr$^{VI.}$ This leads to the dissolution of Cr as a chromate, CrO$_4^{2-}$ [20].
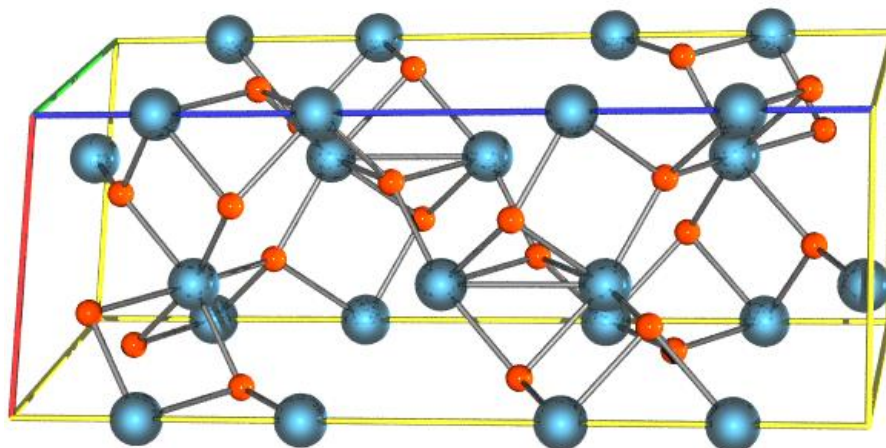
Figure 2-7: **Crystal structure of Cr$_2$O$_3$ [33].**

Chromium is known to form mixed oxides with many transition metal ions in a spinel structure. In Alloy 800, Cr can combine with Fe to form FeCr$_2$O$_4$ [23]. This oxide is very important in the corrosion of Alloy 800 under the conditions that we have studied. Like Fe$_3$O$_4$, FeCr$_2$O$_4$ is spinel oxide in which Fe^{II} occupies the tetrahedral sites and Cr^{III} lies at the octahedral sites. It has been reported that the formation of FeCr$_2$O$_4$ is promoted at high temperatures [23].

2.4.2 Review of Corrosion of Fe-Ni-Cr Alloys

2.4.2.1 The Behaviour of the Ni-H$_2$O System at 25-300 °C

Predicting the corrosion behaviour of Ni Alloys requires a good understanding of the behaviour of pure Ni metal in aqueous media, and in particular the solubility and stability of applicable Ni species in water at 25-300 °C.

In aqueous solutions Ni^{II} ions are stable and the Ni^{2+} ion can exist in acidic and neutral conditions. The known nickel hydroxyl monomers in solution are: NiOH$^+$, Ni(OH)$_{2\ (aq)}$, Ni(OH)$_3{}^-$, and Ni(OH)$_4{}^{2-}$. The Ni^{III} and Ni^{IV} ions are unstable and they are reported to be highly oxidizing [24].

The solubility of each species can be determined by a thermodynamic relationship,

$$Ni^{2+} + H_2O \rightleftarrows NiOH^+ + H^+ \tag{2-10a}$$
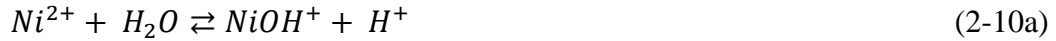
$$\text{logK} = \frac{-\Delta G^0_{reaction}}{2.303 \text{ RT}} = \log(\frac{[Ni(OH)^+][H^+]}{[Ni^{2+}]}) = -pH_T + \log[Ni(OH)^+] - \log[Ni^{2+}]$$

$$\tag{2-10b}$$

where ΔG^0 is the free energy of the reaction (kJ·mol^{-1}), R is the ideal gas constant (8.314 J·mol^{-1}·K^{-1}), and T is the temperature at which the reaction takes place (K). The pH$_T$ is the pH of the solution at the temperature T of the reaction. The total solubility for a given set of conditions is equal to the sum of the concentrations from the individual reactions which contribute to the dissolution of the solid.

To obtain the solubility of Ni^{II} at T > 25 °C, the free energy of each reaction must be calculated to enable us to determine their equilibrium constants. According to chemical thermodynamics the free energy of formation of a substance at temperature T$_2$, can be determined from the free energy of formation of that substance at T$_1$, by evaluating equation 2-11,

$$\Delta G_{T_2} = \Delta G_{T_1} + \int_{T_1}^{T_2} dG \tag{2-11}$$

where ΔG_{T_1} and ΔG_{T_2} are the free energy of formation of the substance at temperature T$_1$ and T$_2$, and $\int_{T_1}^{T_2} dG$ is the change in the free energy between T$_1$ and T$_2$.

Equation 2-11 can be transformed to,

$$\Delta G_{T_2} = \Delta G_{T_1} + \int_{T_1}^{T_2}(-SdT + VdP) \tag{2-12}$$

where S is the entropy of the substance and V is the standard molar volume and P is vapour pressure.

The contribution of VdP to the free energy of solid and dissolved substances due to the change in vapour pressure of water between 25 °C and 300 °C is small, and may be neglected [22]. Thus equation 2-12 reduces to

$$\Delta G_{T_2} = \Delta G_{T_1} - \int_{T_1}^{T_2}(SdT) \tag{2-13}$$

which expands to,

$$\Delta G_{T_2} = \Delta G_{T_1} - \int_{T_1}^{T_2} d(S \cdot T) + \int_{T_1}^{T_2} TdS \tag{2-14}$$

and subsequently,

$$\Delta G_{T_2} = \Delta G_{T_1} - \left[T_2 \cdot S_{T_2} - T_1 \cdot S_{T_1}\right] + \int_{T_1}^{T_2} T\left(\frac{\partial S}{\partial T}\right) dT \tag{2-15}$$

The change in entropy with temperature can be expressed as,

$$S_{T_2} = S_{T_1} + \int_{T_1}^{T_2}\left(\frac{C_p^0}{T}\right) dT \tag{2-16}$$

where C_p^0 is the heat capacity of the substance of interest. Since,

$$\left(\frac{\partial S}{\partial T}\right)_p = \frac{C_p^0}{T} \tag{2-17}$$

then substitution of equations (2-16) and (2-17) into equation (2-15) gives:

$$\Delta G_{T_2} = \Delta G_{T_1} - \left[S_{T_1}[T_2 - T_1] + T_2 \int_{T_1}^{T_2}\left(\frac{C_p^0}{T}\right) dT\right] + \int_{T_1}^{T_2} C_p^0 dT \tag{2-18}$$

This is the basic equation for determining the free energies of substances at elevated temperatures from known free energies at 25 °C and heat capacities. Figure 2-8 shows the comparison between the theoretical and experimental solubility of NiO at 150 °C, 200 °C and 300 °C.
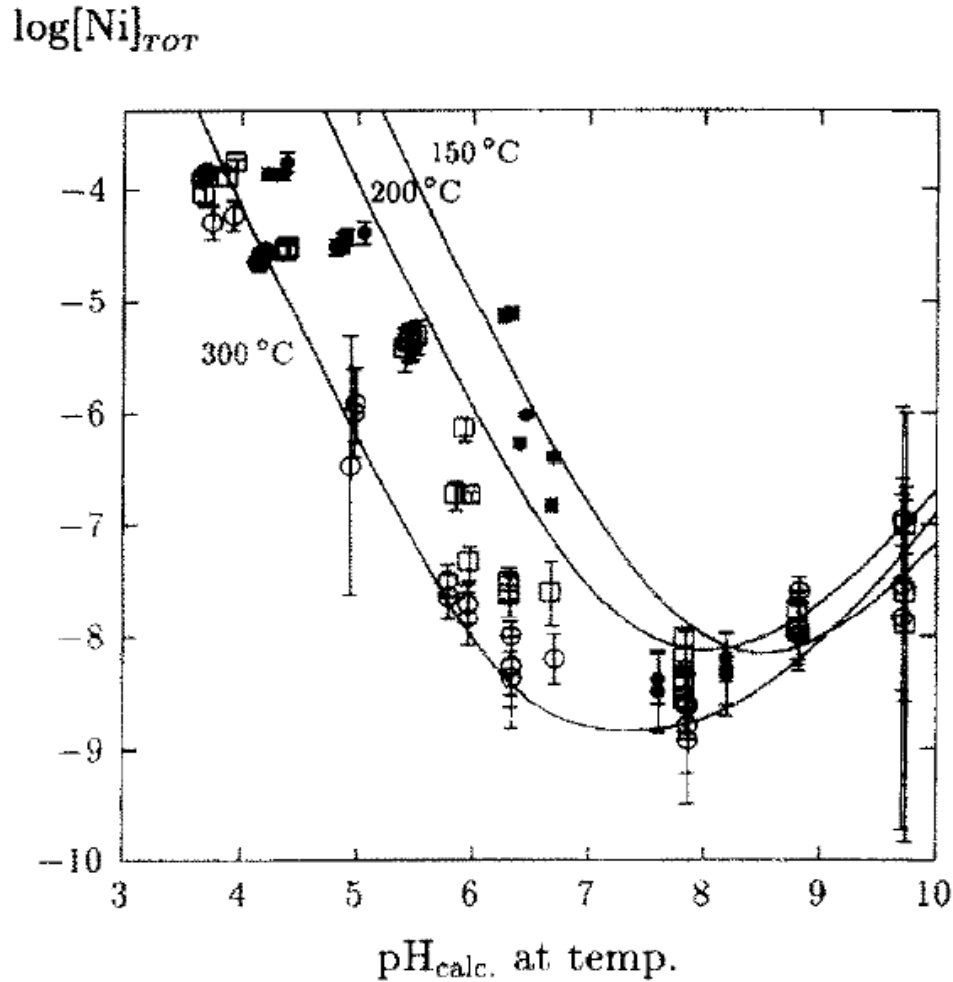
Figure 2-8: **Comparison between calculated and experimental solubility of NiO [24].**

One of the most common ways to represent the thermodynamic stabilities of the different metal species is with a Pourbaix, or E-pH diagram [25]. These diagrams show the regions of potential and pH within which a particular species is the most thermodynamically stable (stability region). Because Pourbaix diagrams do not include kinetic information, they only provide an indication of the driving direction for a system [26]. The diagram can be generated from the Nernst equations of the metal oxy-hydroxides [27]. The E-pH diagram for the Ni-H_2O system at 25 °C – 300 °C is presented in Figure 2-9. The areas between two dashed lines represent the stability domain of water. The dashed vertical line indicates the

neutral pH at the particular pH and the solid lines demarcate the stability domains of solid phases in the Ni-H$_2$O system.

The E-pH diagrams at 25-300 °C indicate that the thermodynamically stable solid compounds of nickel in equilibrium with aqueous solutions are NiH$_{0.5}$ and β-Ni(OH)$_2$/NiO. They also indicate that nickel hydroxide is more stable than the nickel monoxide at temperatures approximately below 200°C. As temperature increases, the region of stability of the Ni^{II} oxide/hydroxide increases [24].
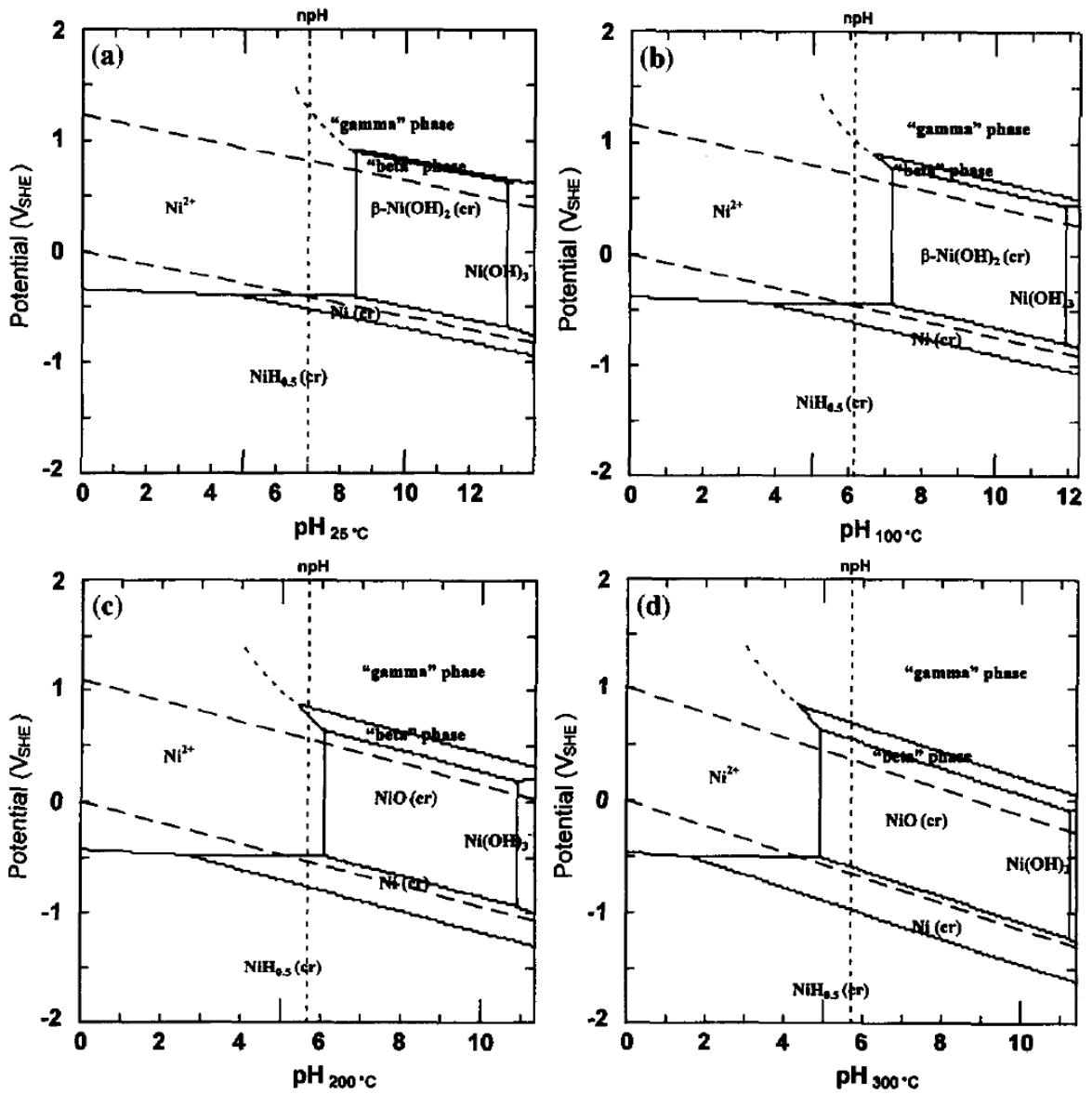
Figure 2-9:   Ni Pourbaix diagram at different temperature from 25 °C to 300 °C [24]

2.4.2.2   The Behaviour of the Cr-H$_2$O System at 25-300 °C

Figure 2-10 shows the solubility of chromic oxide Cr$_2$O$_3$ as Cr^{3+}, CrO$_2^-$ and CrO$_3^{3-}$ ions as a function of pH. The minimum solubility of Cr$_2$O$_{3(s)}$ is at pH 7.0.
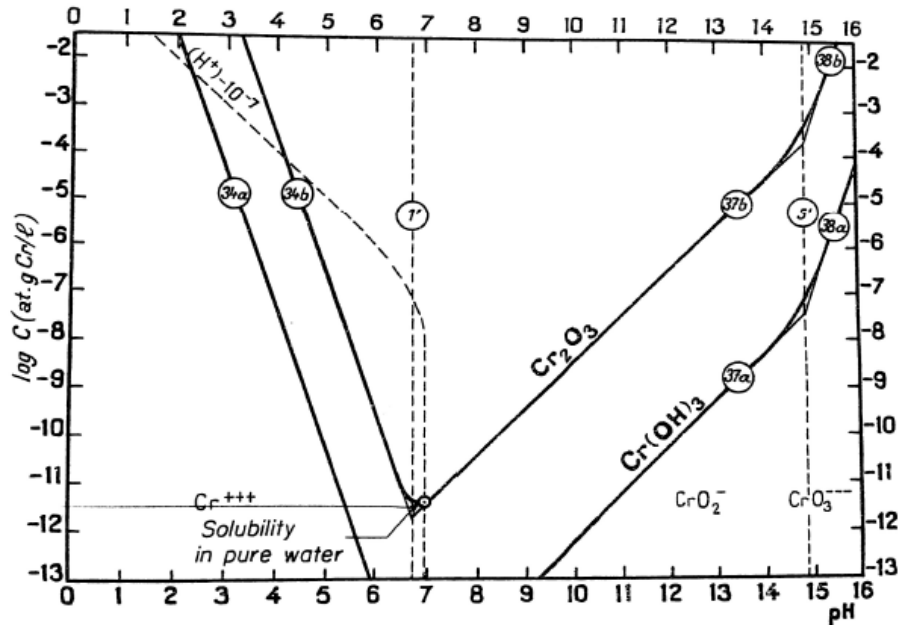
Figure 2-10: Influence of pH on the solubility of Cr$_2$O$_3$ and Cr(OH)$_3$, at 25 °C [25].

The E-pH diagram for the Cr-H$_2$O system at 25 °C is shown in Figure 2-11. It can be seen that in alkaline solutions Cr$_2$O$_3$ is stable and can dissolve as CrO$_4^{2-}$ only at high potentials (E > 0.25 V$_{SHE}$). For Cr-containing alloys such as Alloy 800, very brief contact with moist air is sufficient to form Cr$_2$O$_3$ on the alloy surface. This naturally-formed air oxide acts as a protective layer and suppresses further oxidation. The Cr/Cr^{2+} equilibrium is unchanged in the temperature range of 25-150 °C, but the stability region for the Cr^{2+} and Cr^{3+} decreases, and the stability region for CrO$_4^{2-}$ increases. The stability region of Cr(OH)$_3$/Cr$_2$O$_3$ increases at low pHs but decreases at high pHs.[28].

28
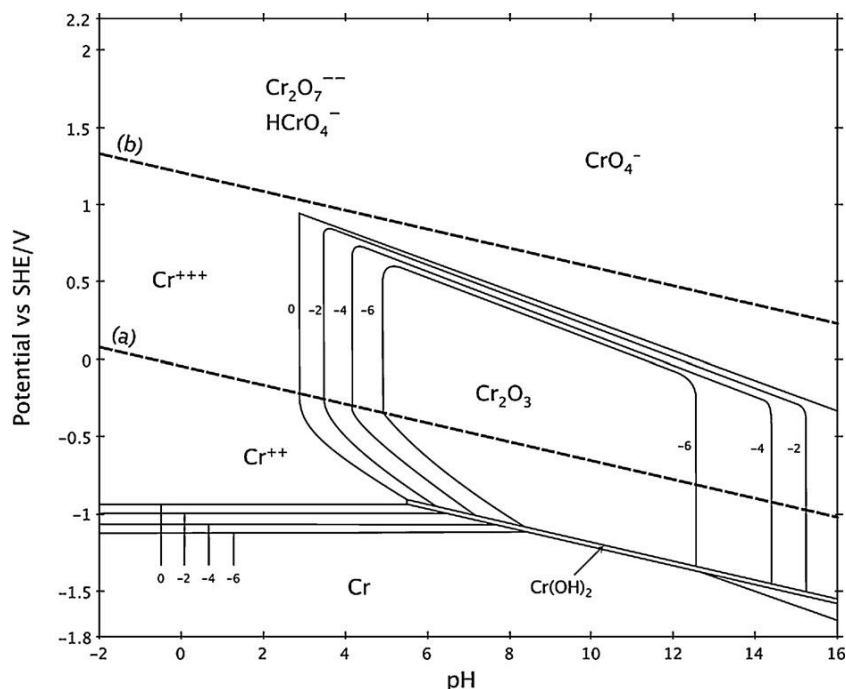
Figure 2-11: Pourbaix diagram of the Cr-H₂O system at 25 °C with all ions at an activity of 10⁻⁵ M. The potential scale is relative to the standard hydrogen electrode (SHE) [25]. The lines labelled 0, –2, –4 and –6 correspond to order of concentrations of Cr³⁺ [25]

2.4.2.3   The Behaviour of the Fe-H₂O System at 25-300 °C

Iron has the electron configuration $[Ar]3d^6 4s^2$. The relatively low energy in the s- and d levels makes it possible for iron to have the oxidation states 0-VI. For iron in water solutions, the most common oxidation numbers are II and III. Fe (IV) and Fe (VI) might be found in strongly alkaline solutions. The oxidation numbers −II, −I, 0 and I are usually not stable in aqueous solutions [29]. In acidic solutions the Fe^{2+} ion is the predominant form of iron(II), which hydrolyses to $FeOH^+$ and $Fe(OH)_2(aq)$ in neutral solutions and may precipitate as $Fe(OH)_2(s)$. In alkaline solutions, anionic species, such as $Fe(OH)_3^-$ and $Fe(OH)_4^{2-}$, are formed. For iron(III) the aqueous species Fe^{3+} is formed in very acidic solutions, and it hydrolyses as pH increases to $FeOH^{2+}$, $Fe(OH)_2^+$, $Fe(OH)_3(aq)$ and several polynuclear complexes like $Fe_2(OH)_2^{4+}$ $Fe_3(OH)_4^{5+}$. Iron (III) hydroxide $(Fe(OH)_3(s))$ precipitates in neutral solutions, but the solubility increases again in very alkaline solutions via formation of $Fe(OH)_4^-$.

29

The aqueous stable Fe species are listed in Table 2-3. Figure 2-12 shows the solubility plot for Fe(II) and Fe(III) species.
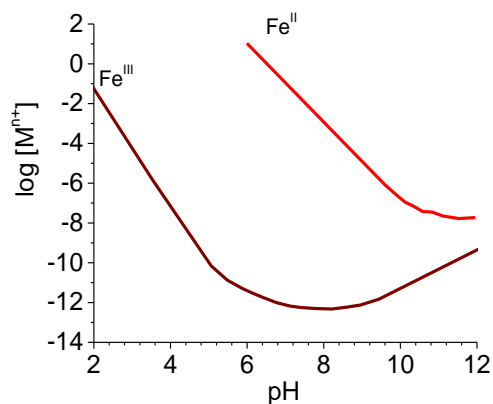
Figure 2-12: Solubility of Fe(II) and Fe(III) in aqueous environment at 25 °C [30].

Table 2-3: Thermodynamic data for iron species [29]

Species	$\Delta_f G°$ (kJmol^{-1})	$S°$ (J K^{-1} mol^{-1})	$C_p° T/(j\ K^{-1}\ mol^{-1}) = a+bT+cT^{-2}$		
			a	B	c
Fe(cr)	0	27.28	28.18	−7.32	−0.290
Fe$_3$O$_4$(cr)	−1012.57	146.14	2659.108	−2521.53	20.7344
α-Fe$_2$O$_3$(cr)	−744.3	87.40	−838.61	−2343.4	
Fe(OH)$_2$(cr)	−491.98	88	116.064	8.648	−2.874
α-FeOOH(cr)	−485.3	60.4	49.37	83.68	
Fe(OH)$_3$(cr)	−705.29	106.7	127.612	41.639	−4.217
Fe^{2+}	−91.88	−105.6	−2		
FeOH$^+$	−270.80	−120	450		
Fe(OH)$_2$(aq)	−447.43	−80	435		
Fe(OH)$_3^-$	−612.65	−70	560		
Fe(OH)$_4^{2-}$	−775.87	−170	600		
Fe^{3+}	−17.59	−276.94	−143		
FeOH^{2+}	−242.23	−118	50		
Fe(OH)$_2^+$	−459.50	8	230		
Fe(OH)$_3$(aq)	−660.51	30	365		
Fe(OH)$_4^-$	−842.85	45	300		
Fe(OH)$_5^{2-}$	−322	37.7	−212		

The Pourbaix diagrams for iron species at 25 °C – 300 °C are presented in Figure 2-13.
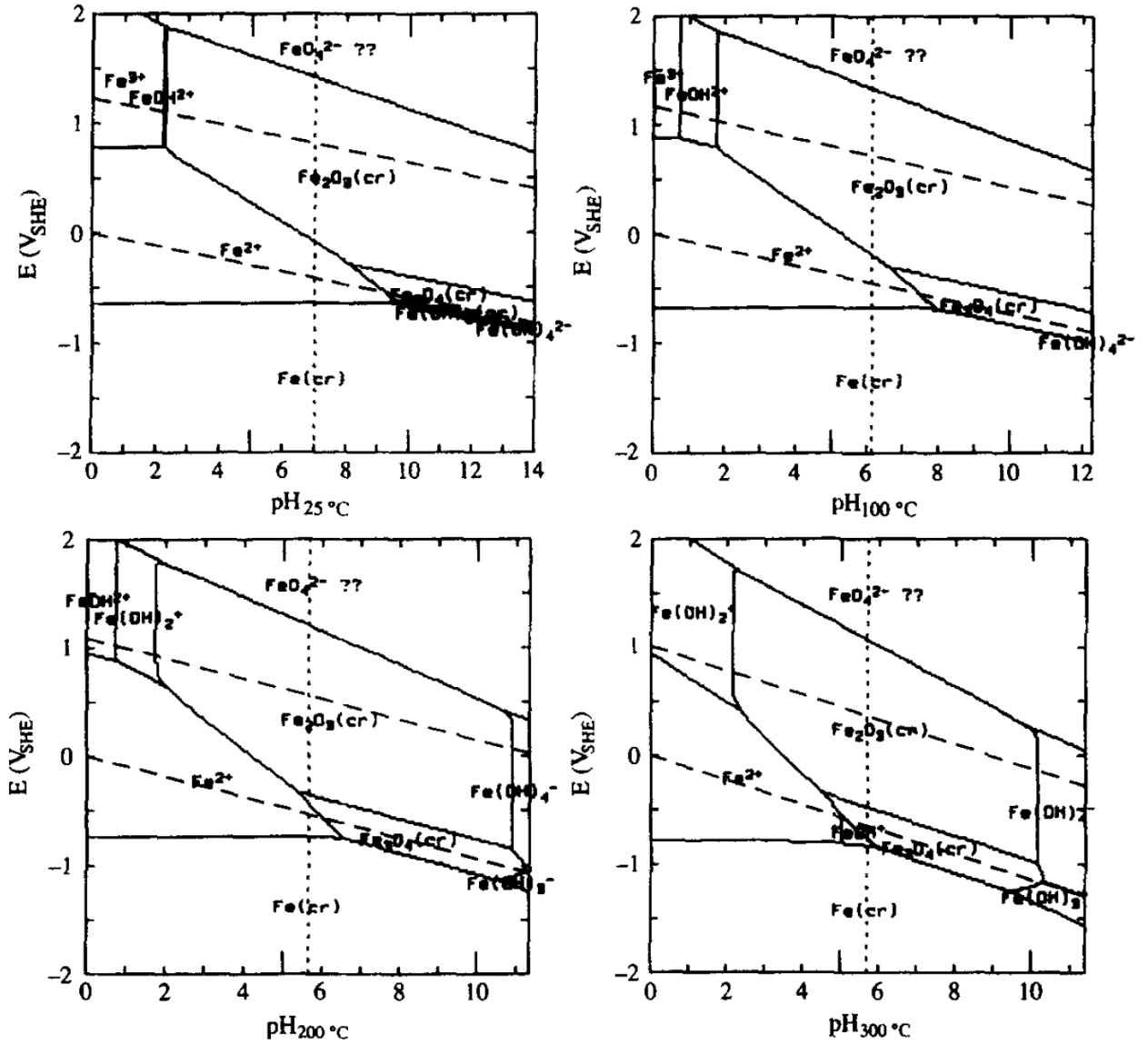
Figure 2-13: E-pH diagram for pure iron at temperature 25 °C to 300 °C [29].

The results show that the Fe(OH)$_2$(cr) is stable at T < 85 °C, and therefore the Schikorr reaction [29] is not thermodynamically possible above this temperature. In addition, Fe(OH)$_3$(cr) and goethite (α-FeOOH) are not thermodynamically stable at any temperature

31

and the stable form of Fe(III) is hematite. In addition, the Fe^{3+} cation is only stable at temperatures below 100 °C in acidic environments.

2.4.2.4 **Pourbaix Diagram for the Ternary Fe-Cr-Ni System**

Beverskog and Puigdomenech [31] calculated Pourbaix diagrams for the ternary system of Fe-Cr-Ni at 25 °C to 300 °C. These calculations are needed because with this alloying system and at elevated temperatures, mixed-cation spinel formation is possible. Their results show that, depending on the metallic composition of the alloy, the passive film may be built up by different oxides. One group of oxides, formed hydrothermally, has the spinel structure. Spinels are very corrosion resistant and have very low solubilities. The system Fe-Cr-Ni-O-H contains four spinel oxides: magnetite (Fe_3O_4), trevorite ($NiFe_2O_4$), chromite ($FeCr_2O_4$), and nichromite ($NiCr_2O_4$). Figure 2-14, Figure 2-15 and Figure 2-16 show the Pourbaix diagram for Fe, Cr and Ni in the ternary system. The high stability of the bimetallic spinel oxides (trevorite [$NiFe_2O_4$], chromite [$FeCr_2O_4$], and nichromite [$NiCr_2O_4$]) is indicated by their large stability regions at the top of their single metal Pourbaix diagrams. $NiFe_2O_4$ has the largest stability area of the spinels, covering the entire potential range for the stability of water at intermediate pH. $FeCr_2O_4$ has a stability area located around the hydrogen line. $NiCr_2O_4$ has the smallest stability area and is the least stable of the bimetallic spinels.
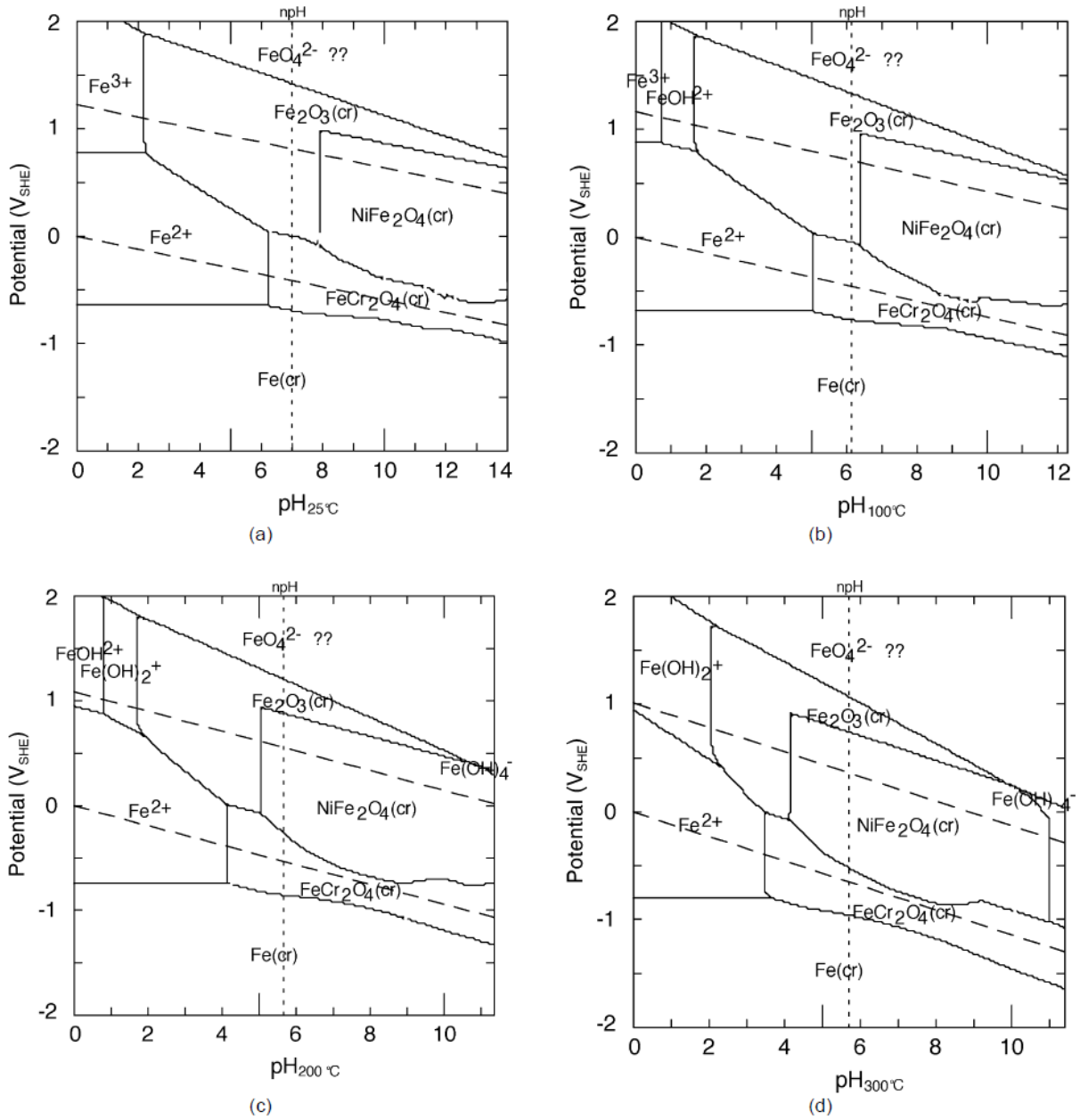
Figure 2-14: **Pourbaix diagrams for iron species in the ternary system of Fe-Cr-Ni at: (a) 25°C, (b) 100°C, (c) 200°C, and (d) 300°C and [Fe(aq)]tot = [Cr(aq)]tot = [Ni(aq)]tot = 10^{-6} molal [31].**
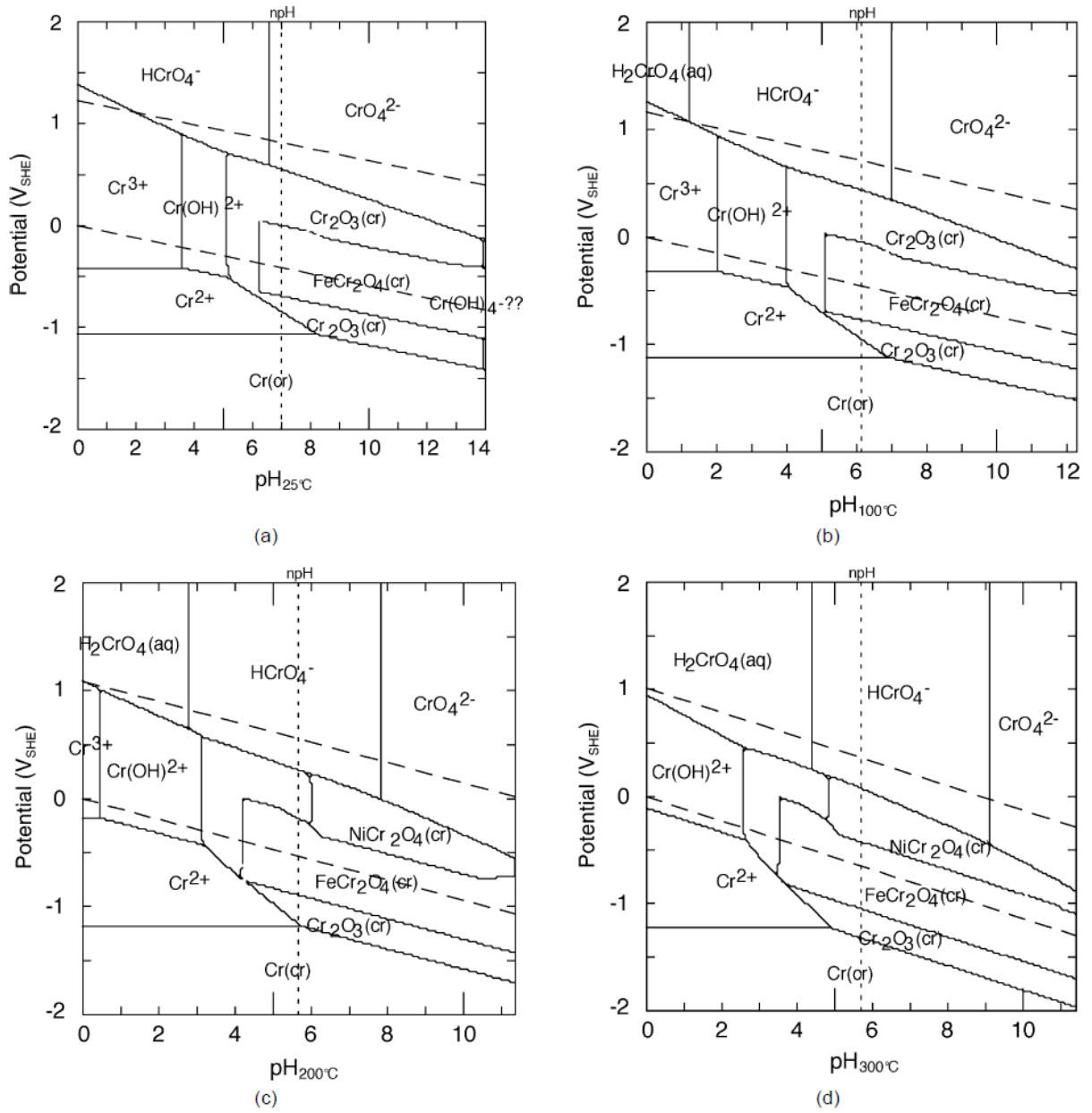
Figure 2-15: **Pourbaix diagrams for chromium species in the ternary system of Fe-Cr-Ni at: (a) 25°C, (b) 100°C, (c) 200°C, and (d) 300°C and [Fe(aq)]tot = [Cr(aq)]tot = [Ni(aq)]tot = 10^{-6} molal [31].**
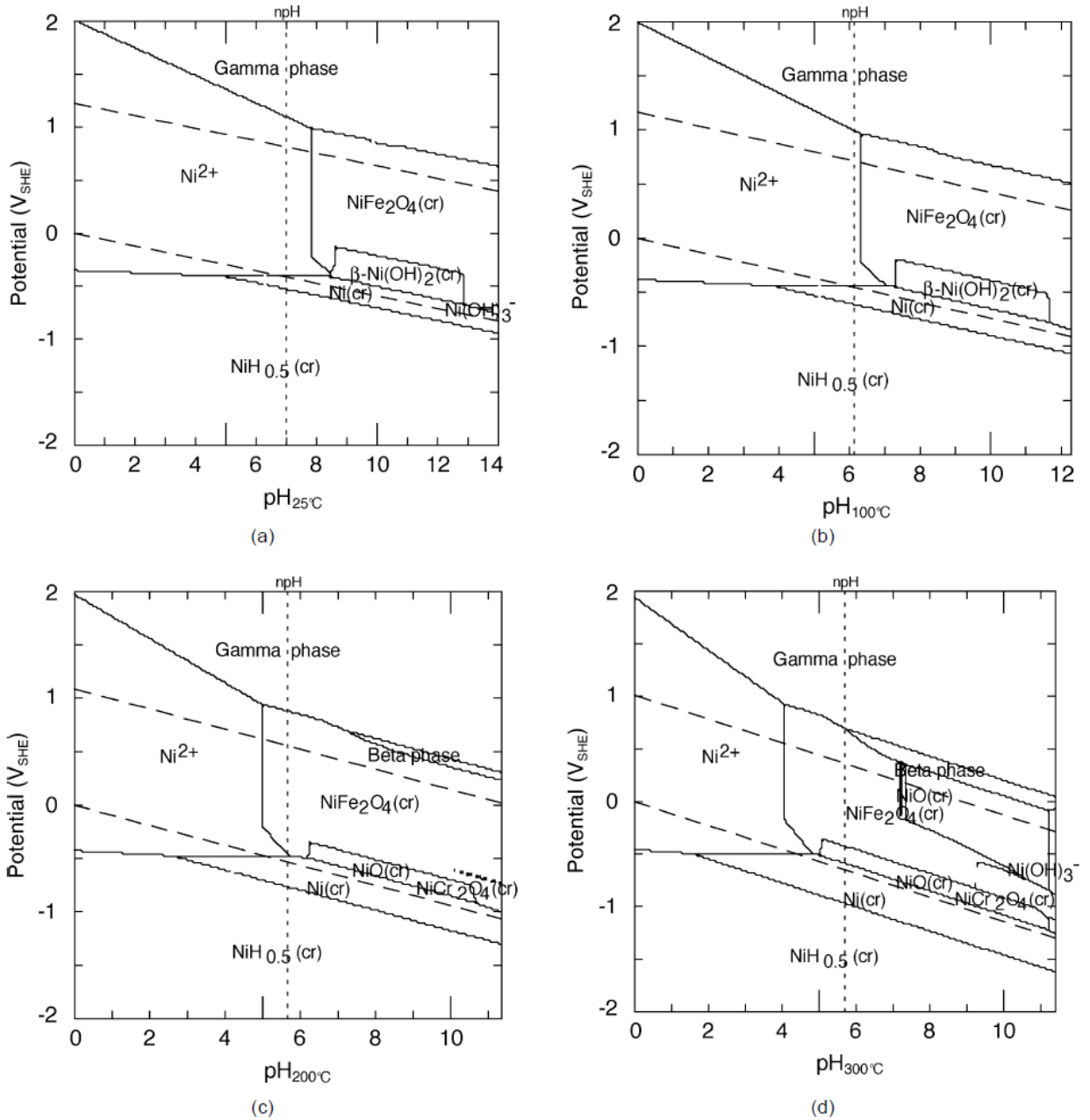
Figure 2-16: Pourbaix diagrams for nickel species in the ternary system of Fe-Cr-Ni at: (a) 25°C, (b) 100°C, (c) 200°C, and (d) 300°C and [Fe(aq)]tot = [Cr(aq)]tot = [Ni(aq)]tot = 10^{-6} molal [31].

2.4.3   Corrosion of Fe-Cr-Ni alloys

Oxide film formation and corrosion of Fe-Cr-Ni alloys in general and Alloy 800 in particular have been investigated extensively. A few of these studies that focus on the

corrosion of Fe-Cr-Ni alloys in the nuclear industry and describe oxide film formation are presented here.

Li et al. (2013) [32] studied corrosion of Alloy 800 and 690 in simulated primary water by means of electrochemical experiments. Their results show that increases in pressure and temperature shift the corrosion potential toward more negative values for both Alloy 690 and Alloy 800. They concluded that Alloy 690 shows a better corrosion resistance than Alloy 800 under their experimental conditions.

Le Canut et al. (2004) [33] used electrochemical techniques to compare the corrosion resistance of Ni-based alloys in sulphate solution at 320 °C, at neutral and slightly alkaline pHs. They found that the passive layers are more stable in neutral conditions. They attributed this observation to the formation of more stable chromium oxide on the surface at near neutral pH. According to their presented results, alloys 600TT and 690 showed the best passivity. Their results also show that at alkaline pH, the passivation currents were higher than those obtained at neutral pH and the alloys have a similar behaviour. Based on their results, they claimed that the reduction of sulphates to sulphides is possible.

Crum and Scarberry (1982) [34] studied corrosion of Alloy 690 in a PWR steam generator environment. Their tests in nitric acid and nitric hydrofluoric acid demonstrate that Alloy 690, with its higher chromium content than Alloy 600, shows a very good resistance to highly oxidizing environments. Their extensive laboratory testing indicates that the alloy is very resistant to cracking in water over a wide range of high temperatures and oxygen concentrations, in the presence of crevices and lead or chloride contamination. The analysis by the authors confirms that Alloy 690 releases a negligible amount of material when exposed to high velocity water at elevated temperatures. Their SCC experiments show that in constant extension rate tests, Alloy 690 resists crack propagation in a deaerated sodium hydroxide environment better than Alloy 600. Based on long time-duration experiments, they also found a greater resistance of Alloy 690 to intergranular attack in deaerated corrosive solutions than Alloy 600. Finally, they suggested that Alloy 690 offers the necessary resistance to the highly oxidizing environments and high temperature oxidation conditions for radioactive waste disposal involving nitric hydrofluoric acid dissolution and vitrification.

Crum (1986) [35] also studied the effects of heat treatment, carbon content, and microstructure on the SCC of Alloy 690 and 600 and found the same results as presented in 1982.

Wang et al. (2016) [36] examined the effects of temperature on the electrochemical behaviour and oxide film properties of Alloy 800 in hydrogenated high temperature water. According to their results, the corrosion resistance of Alloy 800 passes through a local minimum at 250 °C. They found that the kinetic controlling step of the growth of oxide films changes from the diffusion of ions in the aqueous phase to the growth of a Cr-rich barrier layer at 200–300 °C. Finally, they proposed a modified model to explain the effect of temperature on the oxide film properties on Alloy 800 in hydrogenated high temperature water.

Marcus and Grimal (1992) [37] investigated the surface compositions of two Ni-Cr-Fe alloys (Ni-21Cr-8Fe (at%) single crystal and Ni-17Cr-10Fe) by angle-resolved electron spectroscopy for chemical analysis (ESCA), after polarization in the passive state or in the active state in 0.05 M H_2SO_4. They found that the passive layer formed on Ni-21Cr-8Fe (100) has a bilayer structure. The inner layer is an oxide film and the outer part is made of a hydroxide layer. In terms of film composition, their results indicate that the film is enriched with chromium oxide and hydroxide. The composition of the inner oxide layer is determined to be 96% Cr_2O_3 and 4% Fe_2O_3 and there was no detectable Ni^{2+}. The outer layer is composed completely of chromium hydroxide. They observed that the thickness increases when the applied potential increases. They found the same result for the Ni-17Cr-10Fe alloy, except that the film was slightly thicker. Their results reveal that the first metallic plane under the passive film is enriched in Cr (~43%). When the applied potential is in the active region, there is a monolayer on the surface that contains all three element cations. However, it is still enriched in Cr^{3+}. In this case they observed a higher chromium enrichment under the passive film and attributed it to the selective dissolution of Fe and Ni that happens on this alloy.

Sik Hwang et al., (1997) [38] studied the effects of Pb on the passive film of Alloy 600 using polarization and immersion tests. Using the polarization technique, they observed anodic dissolution behavior in water with up to 500 ppm of PbO at pH 4 and pH 10 at 90°C.

Their results indicate that as Pb concentration increased, the critical current densities of Alloy 600 increased at both pH 4 and pH 10. Their immersion tests at 250 °C with lead concentrations of 0, 25, and 250 ppm suggest that at pH 10, the outermost surface films were enriched in Cr and depleted in Ni with increased levels of Pb, but the inner layer showed the opposite trend. The ICP solution analysis results indicated that higher concentrations of Ni were found with increased levels of Pb, which suggests that Pb facilitates Ni dissolution.

The effects of cold work on the oxidation behaviour and carburization resistance of Alloy 800 were investigated by Leistikow et al., (1987) [39]. Their results indicate the role of the grain boundaries as easy diffusion paths for Cr and Mn to the alloy/oxide interface on the structure of the oxide layer formed on Alloy 800 at 600 °C in superheated steam. In their work the number of grain boundaries increased by applying 10-90% cold work and the consequence was a higher fraction of Cr and Mn in the oxide that forms on the surface. They observed a linear relationship between the oxide growth rate and the alloy grain size.

Faichuk (2013) [40] explored corrosion and the oxide film properties of Alloy 600 and Alloy 800. Her work indicates that Alloy 800 is more corrosion resistant than Alloy 600. This observation was attributed to the easier formation of a Cr_2O_3 barrier layer due to the higher Fe content. For Alloy 600, the more noble Ni is not so readily segregated to the outer surface which results in the formation of a thinner, less protective barrier layer.

Nickchi and Alfantazi (2010 - 2013) [41-44], in a series of works, investigated the effect of sulphate on corrosion of Alloy 800 in hydrogen peroxide-containing solutions at temperatures between 25-200 °C. Their electrochemical investigations are an indication of possibly active behaviour after 24 h corrosion in 25 mM sodium sulphate solution in the absence of hydrogen peroxide. However, the alloy undergoes active–passive transition in solutions containing 10^{-4} M hydrogen peroxide. The polarization resistance data demonstrated that the passive film continues thickening after corrosion potential stabilization in the presence of H_2O_2.

Xia et al. (2014) [45] studied the effect of pH on the sulphur-induced passivity degradation of Alloy 800. Their experimental results reveal the significance of the solution pH on the effect of impurities containing sulphur at the reduced or intermediate oxidation

level (S^x) on the passivity of Alloy 800. Impurities containing sulphur at the reduced or intermediate oxidation level would cause Alloy 800 to lose its passivity and become active in an acidic crevice chemistry. Experimental evidence also indicates that the solution pH alters the semiconductor type of the surface film from n-type in neutral crevice solutions to p-type in alkaline crevice solutions.

Hickling and Wieling (1981) [46] investigated the resistance of Alloy 800 to pitting corrosion at elevated temperatures. They suggest that for the SG, the electrochemical data indicate that a larger margin of resistance to pitting attack is achieved by using Alloy 800 rather than 600. Their experimental results indicate that to prevent pitting corrosion the SG secondary water chemistry must be strictly controlled, and maintaining low oxygen levels in the water must be considered at least as important as the control of chloride contamination. An important conclusion from their work is that the danger of pitting attack in PWR SG may be at a maximum at temperatures considerably below those in normal operating conditions. Thus, particular attention should be paid to water chemistry during periods of intermediate temperatures.

Edwards and McIntyre (2013) [47] studied oxides on the Alloy 800 surface in dilute O_2 gas at a temperature of 300 °C. They observed a multi-layered oxide film composed of an exterior γ-Fe_2O_3 with a Cr_2O_3 layer at the oxide–metal interface. This oxide film also contains significant concentrations of $NiCr_2O_4$. They could also detect minor concentrations of another spinel oxide, $NiFe_2O_4$. According to their analysis, the kinetics of oxide growth were found to follow a direct logarithmic relationship suggesting that the oxide would be suitably protective.

Huang et al. (2009) [48] investigated the influence of pH on the electrochemical properties of passive films formed on Alloy 690 in high temperature aqueous environments. They observed that the chemical compositions and electronic structures of the passive films are strongly pH-dependent. According to their results, the passive film is a mixture of Cr_2O_3 and $FeCr_2O_4$ below the flat band potential of nickel oxide and $NiFe_2O_4$ above this potential.

Persaud et al. [49-55], in a series of works, studied the effect of different anions and the presence of hydrogen on the uniform, SCC and internal corrosion of Ni-based alloys, using electrochemical experiments and surface analysis techniques. Their findings indicate that in a mixture of chloride and sulfate anions, sulfate acts as an aggressive anion for corrosion of Ni and Ni-based alloys. It was shown that Alloy 800 is susceptible to SCC while Ni and Ni-rich alloys show faster general corrosion. They found that sulfate reduction at the tip of a crack is possible and sulphur formation is more favourable than oxide formation in the crack. Their studies exposing the alloys to high temperature environmenst in the presence of hydrogen resulted in expulsion of Ni to the surface and internal oxidation of Cr at the grain boundaries. The thickness of the oxide depends on the alloy chemical composition but it was suggested that this chromium oxide formation at the grain boundaries is responsible for the alloy embrittlement and intergranular progression of cracks in SCC.

McIntyre et al. [56] found that because of the pH change in the secondary system water chemistry, different alloys show different behaviours. Monel 400, which does not have enough chromium to form a chromium oxide layer on the surface, cannot restrict transport of Ni to the solution and sulphide crystals grows on the surface of the Monel 400 alloy even when subjected to a period of mildly acidic pH. However, for Alloy 600, 800 and 690, the initial acid exposure resulted in the growth of a chromium-rich surface corrosion product film on all alloys and the precipitation of nickel-rich sulphates. When pH increased to a higher value, the alloy again had chromium-rich surface oxides but also exhibited sulphide crystallites adhering to the base oxide, particularly for Inconel 600. They attributed the tendency to retain these sulphides to the porosity of the protective oxide through which nickel is transported to the solution.

Marchetti et al. [57-65], in a series of works, studied general corrosion and oxide formation on Fe-Cr-Ni alloys in primary coolant water conditions and presented a kinetic model based on their results, focusing on the link between the alloy subsurface defects density and the shape of the oxidation kinetic curves.

There are also numerous studies on the corrosion of Fe-Cr-Ni alloys in the SCW environment. Choudhary et al. [66] reported a reduction in the dissolved hydrogen level and

the apparent corrosion rate when the Ni content of an alloy increased. Data presented by Steeves et al. [67] reveals that the oxidation mechanism changes with temperature, with electrochemical oxidation occurring at subcritical temperatures and direct chemical oxidation at supercritical temperatures. They also demonstrated that the corrosion rate goes through a local maximum around the critical point but that the overall alloy corrosion rate increases with increasing temperature, as would be expected.

Tan et al. [23, 68-70] reported that when Alloy 800 with different treatments (as-received and grain boundary treated (GBE)) are exposed to SCW corrosion conditions, at different temperatures and oxygen content for different times, oxidation was observed as the primary corrosion behavior of the alloy with significantly mitigated oxide exfoliation on the GBE-treated samples compared to that on the as-received samples. They also observed larger weight gains on the treated samples with a near linear rate law at 500 °C and possibly a cubic rate law at 600 °C for the growth of the oxide scales. They suggested an outer Fe-enriched oxide on top of an inner Cr-enriched oxide layer with semi-continuous pure Ni at the interface of metal and oxide. This is very consistent with what Sun et al., [71], Rodriguez and Chidambaram [72] and Svishchev et al. [73] observed when stainless steel 316 (316 SS) was exposed to the SCW environment under different conditions. The same oxide layer structure has been reported for other alloying systems under SCW corrosion [74-87]

Choudhry et al. [88] presented an online monitoring study for oxide formation and dissolution on Alloy 800 in SCW by measuring oxygen, hydrogen and metal release to the solution. Their results suggest that oxide film formation on Alloy 800H can be divided into five distinct stages. They noticed that the effect of flow rate on the metal release was small relative to the effect of temperature for Fe, Ni and Mn, but significant for Cr and Al. Their data show that the formation of a steady-state film requires several hundred hours, and the time required increases with increasing temperature.

In general, for the use of Fe-Cr-Ni alloys in SCW conditions, it has been shown that stainless steel 300-series alloys have a comparable corrosion rate with that of Ni-based alloys up to 550 °C but their corrosion resistance increases rapidly as temperature increases [89]. It was also shown that the corrosion behaviour of these alloys under SCW can be simulated by

doing experiments under 100% humidity steam environment, albeit with slower rates [90, 91].

2.5   Review of current oxide growth models

Several corrosion models have been developed for predicting oxide growth rates and mechanisms on the surface of metals and alloys. To obtain the rate of corrosion under a given driving force (V), many of these models focus on solving the transport rate equations for individual charge carriers (interstitial cations and anions, cation and anion vacancies, and electrons and holes) across the oxide film, as well as the rates of creation of these charge species at the respective interfaces (i.e. electrochemical redox reaction rates). Since the rate of charge transport (charge flux) depends on the electric field gradient (electric potential), the electrochemical potentials of the metal and the oxide and the solution phases are important parameters in determining the corrosion rate. These potentials may change with time as corrosion progresses. In these models, it is considered that the driving force for oxide formation in a metal/oxide/electrolyte system comprises three parts (Figure 2-17): (i) the potential drop at the metal/oxide interface ($\varphi_{m/f}$) that controls the internal interfacial reactions, (ii) the potential drop at the oxide/electrolyte interface ($\varphi_{f/s}$) that controls the external interfacial reactions and (iii) the potential drop in the oxide layer (φ_f) that controls the transport mechanisms across the oxide film. Thus, the oxide layer is the result of complex processes combining transport through the oxide and interfacial reactions. Four of these models are reviewed here.

Electronic potential
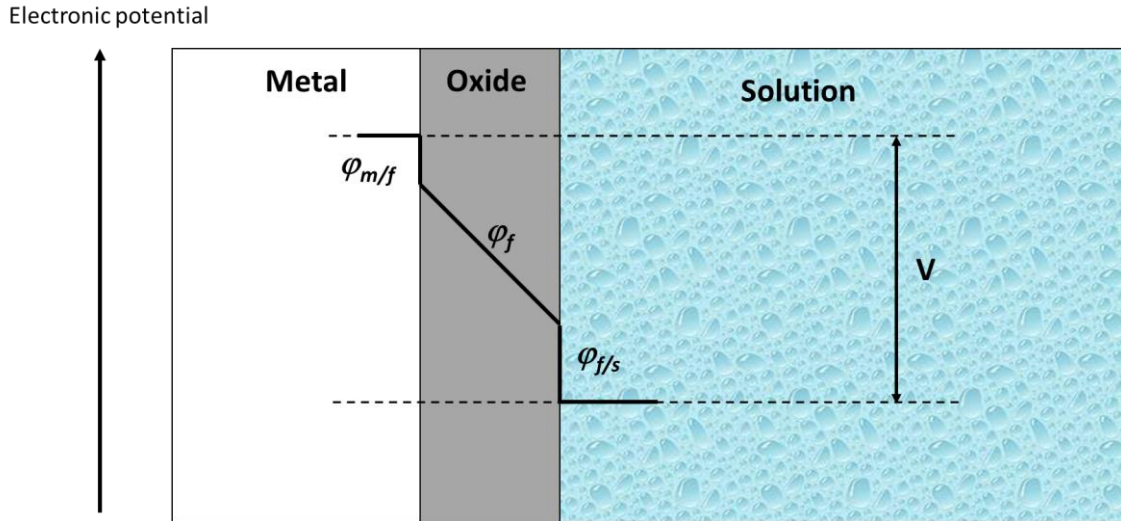
Figure 2-17: **Scheme of the potential drop in the metal/oxide/solution system [92]. In this figure V is the driving force for corrosion, $\varphi_{m/f}$ is the potential derop at the metal / film interface, $\varphi_{f/s}$ is thepotential derop at the film and solution interface and φ_f is the potential dero inside the film.**

2.5.1 Cabrera-Mott model

This is one of the first models developed for oxide film formation on metal alloys [93-96]. There are three main assumptions in this model:

1. They consider that the oxide grows by the interstitial transport of cations across the oxide film (transport (I_M) in Figure 2-18) to the oxide/solution interface, which then react with the electrolyte (reaction (g) in Figure 2-18).

2. The electric field ε set up in the oxide film controls the activation energy of the rate-limiting step ($\varepsilon = \varphi_{f} / x$).

3. For thick oxide films that have a weak electric field a parabolic growth law ($x=\sqrt{Et}$, where E is a constant) is used because of the assumption that the limiting step is the transport of cations through the oxide (transport I_M in Figure 2-18). For thin oxide films (strong electric field) the oxide growth law is logarithmic because of the slow rate of injection of cations at the

43

metal/oxide interface (reaction (c) in Figure 2-18). In this case, the rate of oxide growth is calculated as: $x^{-1} = A - B \ln(t)$. (A and B are constants)

Some of the limitations of this model are:

1. The model has initially been developed to describe oxides formed in air. Thus, the potential drop at the oxide/solution interface that is responsible for the dissolution of the oxide film according to reaction (i) in Figure 2-18, is not considered. This means that in this model the pH of the solution does not affect the oxide growth kinetics, although it is known to affect it.

2. The authors assume that oxide thickening reduces the activation energy for the rate-limiting step but does not affect the potential drop at the metal/oxide interface.

3. This model is only applicable for the pure metals and cannot be applied to alloys.
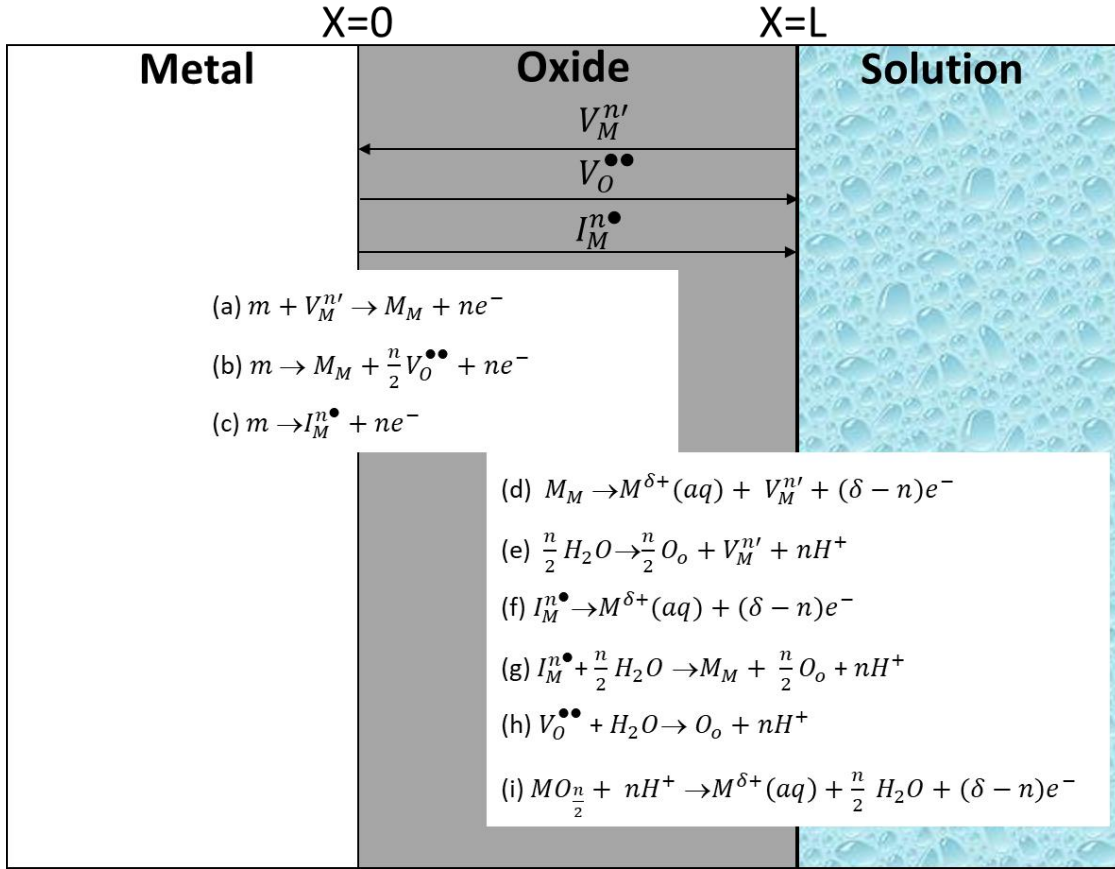
Figure 2-18: **Scheme describing the reaction and transport processes involved in the system metal/oxide/electrolyte during the growth of the oxide layer [92].**

The Fehlner-Mott model [96] is a modified Cabrera-Mott model with similar assumptions. The modifications to the model are as follows: (a) The transport of interstitial anions across the oxide film is assumed to be responsible for the oxide growth. (b) The transport of the anions in the film is assumed to be the only rate-limiting step and it is assisted by the electric field. (c) The electric field is assumed to be constant and to not vary with the oxide thickness. However, the activation energy of the transport of anions across the film (the rate-limiting step) is considered to increase linearly with the oxide thickness ($W_A = W^{\circ} + \mu x$, where W° and μ are constants for a given oxide structure) as was originally proposed by Eley and Wilkinson in 1960 [97]. This assumption of activation energy increasing linearly with the oxide thickness yields a logarithmic growth law:

$$x = A + B \cdot \ln{(t + t_0)} \tag{2-19}$$

where A and B are parameters depending on μ and t_0. The same limitations for the Cabrera-Mott model apply for this model. One of the main drawbacks of this model is that it does not allow for an accurate description of the behaviour of anodically-formed oxide films. In this model, it is assumed that the electric field is not dependent on the oxide thickness ($\varepsilon=$ constant). Also, no interfacial potential is considered; a more accurate approach for anodically-formed oxide films is to define the electric field as $\varepsilon = \frac{V_{app}}{x}$ where V_{app} is the applied potential and x is the oxide thickness. In general, the assumptions of this model do not reflect a correct physical description of the mechanisms involved.

2.5.2 Point Defect Model (PDM)

This model was initially developed in 1981 by Macdonald et al. to model the growth of oxide films formed in electrochemical reactions. This model was the first to include interfacial potential drops in the description of anodic oxide film growth on metals. It was then improved to take into account different factors affecting oxide formation, oxide dissolution and localized corrosion [98-121]. In its original version [119, 120] the main assumptions of this model are:

a. The mechanism of oxide growth involves the transport of oxygen vacancies from the metal / oxide interface to the oxide / solution interface (V_O in Figure 2-18). This process to be considered as the rate limiting step for oxide growth.

b. The oxide dissolution occurs via the diffusion of interstitial cations and / or cation vacancies (f and d on Figure 2-18, respectively).

c. The electric field does not change across the oxide ($\varepsilon =$ constant).

In this case, the oxide growth law is formulated as:

$$x = \frac{1}{2K}\left(\ln(2K\,A\,(B-1)) + \ln t\right) \qquad (2\text{-}20)$$

Where A, B and K are constants. In this model, the potential drops at the interfaces are assumed to be functions of the pH and the applied potential V_{app}. This model was later

extended for interfacial controlled oxide growth [121] by implementing another logarithmic law, a function of pH and the applied potential (V_{app}). The modified oxide growth law is then:

$$x = x_{t=0} + \frac{1}{b} ln(1 + Ab \exp[-bx_{t=0}] \, t) \tag{2-21}$$

In this model oxide dissolution at the oxide/electrolyte interface, reaction (i) in Figure 2-18 is also considered. The oxide chemical dissolution rate is formulated as:

$$v = k_s[H^+]^m \tag{2-20}$$

where k_s is the rate constant that depends on the oxide/electrolyte interface potential drop and m the order of the reaction.

2.5.3 Mixed conduction model (MCM)

The PDM model was modified by Bojinov et al. to work for alloying systems in order to develop the mixed conduction model (MCM). This model emphasizes the coupling between ionic and electronic defects in quasi-steady-state passive films [122-139]. The electronic properties of the oxide layer can be determined by this model as well as the main kinetics and transport parameters. These parameters are then used to calculate the steady-state current density, the oxide film impedance response and the time dependent oxide thickness on many alloys. According to the MCM model, the passive film is considered as a doped n-type–insulator-p-type semiconductor junction. They suggested that at a high positive potential the concentration of ionic defects and electron holes reaches a critical value for the film to act as a conductor. At this potential, oxidation of chromium oxide to Cr^{VI} and / or oxygen evolution happens on the film surface. The electronic conductivity is formulated for both DC and AC experiments. For DC it is:

$$\sigma_e \propto \mu_e F c_{min} \tag{2-21a}$$

$$c_{min} = 2[\frac{k_3 k_{1,i}}{k_1 k_{3,i}}]^{0.5} \exp\left(-\frac{L}{2a}\right) + \frac{k_{1,i}a}{D'_i} + \frac{k_3 a}{D'_M} \tag{2-21b}$$

In these equations μ_e is the mobility of electronic charge carrier, k is the rate constant of the reaction(s) involved in the process, L is the thickness of the film or of the space charge layer, a is atomic jump distance and D_i and D_M are diffusion coefficient of interstitial cations and cation vacancies respectively. The definitions of the parameters can be found in [139]. For AC conditions, it is estimated as:

$$\sigma_e = \left(\frac{F^2 D_e}{RT}\right) k_3 \left[\left(k_1^{-1} - \frac{a}{D_M'}\right) \exp\left(-\frac{L-x}{a}\right) + \frac{a}{D_M'}\right] \tag{2-22}$$

Where x is distance within the film, and D_e is diffusion coefficient of electron. The rest of the parameters are similar to the DC case (for the meaning of each parameter refer to [139]).

In the MCM model, like the PDM model, the system is assumed to be at quasi-steady-state. As discussed previously for PDM, this model also considers that the interfacial potential drop at the oxide/film interface and the electric field in the oxide remain constant during oxide growth, which is valid for the stationary condition.

2.5.4   Generalized Model for Oxide Film Growth

Seyeux et al. present a "generalized model" [92, 140] for the kinetics of oxide growth. In this model, they included the evolution of the interfacial potential drops as well as the variation of the electric field in the growing oxide during the film growth. According to the authors, this new model can describe the growth of oxide films on alloys under non-steady-state conditions. In this model, two different conditions are considered, oxide growth controlled by charge transport through the oxide, and controlled by injection of metal cations at the metal oxide interface. In the case of the transport-controlled condition, the flux of movement of each species is given by:

$$J_i = q_i \frac{F\varphi_f(x)}{RTx} D_i^* \frac{C_i|_{m/f} \exp\left[q_i \frac{F[\varphi_f^0 + \Delta V(1 - \alpha f(x))]}{RT}\right] - C_i|_{f/s}}{\exp\left[q_i \frac{F[\varphi_f^0 + \Delta V(1 - \alpha f(x))]}{RT}\right] - 1} \tag{2-23}$$

Where $C_i|_{m/f}$ and $C_i|_{f/s}$ are concentrations of species i at the metal/oxide and oxide /electrolyte interfaces, respectively. $\varphi_f(x)$ is oxide potential drop, x is oxide thickness, α is a positive constant less than 1, ΔV is potential variation, q_i and D_i^* are charge and diffusion coefficient of species i. When the oxide growth is controlled by cation injection, the rate of growth is given by:

$$\frac{dx}{dt} = \frac{\Omega}{N_V} \vartheta C_m^M \exp\left(-\frac{W_I^M - en\varphi_{m/f}}{kT}\right) \tag{2-24}$$

Ω is molar volume of oxide per Cr cation, Nv is Avogadro's number, C_m^M is concentration of M in the metal, ϑ is vibration frequency of M and W_I^M is the activation energy of the reaction. They also formulated the rate of cation dissolution as:

$$v_{diss} = k^0 \exp\left(-\frac{E_A}{kT} + \frac{e(\varphi_{f|s}^o(d_i) + \alpha f(x)\Delta V)}{kT}\right)[H^+]^m \tag{2-25}$$

The parameters are defined in [92].

None of the above-mentioned models express the potentials that control the charge transport rates as a function of experimentally quantifiable potentials such as E_{corr} or E_{rdx}^{eq}. The models assign different rates for the transport of different charge carriers across the solid oxide phase (ions, ion vacancies, electrons and holes). The individual transport rate parameters are difficult to verify, and this limits the predictive capabilities and the application ranges of these models. Oddly, mass and charge balance for the overall corrosion process, clear physical requirements, are not generally invoked in these models.

2.6   Radiation and Water Radiolysis

2.6.1   Radiation Chemistry

This thesis examines the effect of ionizing radiation on the corrosion of Alloy 800. Hence, this section provides a brief overview of the chemistry induced in water by ionizing radiation.

Radiation chemistry is the study of the chemical effects produced in a system when exposed to high-energy ionizing radiation. Ionizing radiation includes high-energy charged particles (e.g., α and β particles), fast electrons from accelerators, and electromagnetic radiation (e.g., x-rays and γ-rays). The most common sources of ionizing radiation are nuclear fission and radioactive isotope decay, but ionizing radiation can also be created by high energy particle accelerators. The energy of a radiation particle or photon emitted from a radionuclide is characteristic of the nuclide [141]. For example, the γ-rays emitted during the β-decay of ^{60}Co have energies of 1.332 MeV and 1.173 MeV. The energy of β particles and photons from radionuclide decay typically range from 0.1 MeV to 5 MeV[141]. Particles with this energy cannot induce nuclear reactions but the energy is much higher than that required to ionize atoms and molecules (typically 10s of eV).

When radiation interacts with matter it leaves a track of ionized particles and hence is known as ionizing radiation. The main energy transfer mechanism from a radiation particle or photon to an interacting solvent medium is an inelastic collision whose probability depends on the electron density of the solvent molecules. The rate of energy loss from the radiation particle (or the rate of energy absorbed by the coolant) is nearly independent of the initial energy of the radiation particle or photon. In determining the chemical effects of ionizing radiation on a medium it is the energy transfer rate per unit mass of the medium that counts. This is referred to as the linear energy transfer (LET) rate. The LET rate depends on the type of radiation and the interacting medium. For a given medium, it is higher for α-particles (due to their large size and charge), lower for β-particles, and lowest for γ-photons [142].

The different LET rates result in different average penetration depths. The depth depends on the mass density (and more importantly the electron density) of the medium. For water at room temperature the penetration depths are: 20 – 25 μm for α-particles, 0.5 – 1.0 cm for β-particles, and tens of cm for γ-photons. These depths are the distances into the medium at which the incident energy flux is reduced by 50%. For α-radiation, the incident energy is deposited in a small volume very near the radiation source, while for β and γ the energy is deposited throughout the medium. Alpha particles are considered high LET radiation while β and γ are considered low LET radiation. Because α-particles can be

'stopped' by thin layers of material and because they deposit their energy in very small volumes, they play little role in the radiolysis of water systems. Alpha radiation is largely confined to nuclear fuel and fuel cladding in a nuclear reactor. Hence in the following discussion we only focus on the interaction of low LET radiation with water. The total radiation energy depends on not only the energy of individual particles or photons but also on the number of the particles/photons. The estimated radiation flux (or radiation dose rate) of low LET radiation to the coolant in the core of a nuclear reactor ranges from 1000 to 4500 kGy·h^{-1} (1 Gy = 1 J·kg^{-1}) [143]. The LET rate is important in determining the density of ions and electronically excited molecules that are formed along the radiation track. Since this density can affect further collision/reactions of species in the track, it will have consequences on the yields of radiolysis products that reach the bulk phase (after diffusing out of the localized zone near the track) where they can undergo bulk chemical reactions.

Due to their high initial energy, each β-particle or γ-photon undergoes many collisions while it loses energy. Eventually the collisions will reduce the energy of the residual electrons to the average kinetic energy of the medium being irradiated and the electrons are "thermalized". The high energy β or γ interactions do not depend on the chemical nature of the target matter; to a first order they only depend on the relative abundance of electrons in the interacting matter. This is an important consideration when irradiating dilute solutions. The total mass of the solutes in such solutions is very much less than the mass of the surrounding water. Hence, the probability of an incident β particle or γ photon interacting with a solute molecule is very small compared to the probability of interacting with a water molecule. For this reason, chemical processes induced by low LET radiation of solutions are often referred to as solvent-oriented processes (as opposed to solute-oriented processes).

Ionizing radiation transfers its energy to an interacting medium mainly by colliding non-discriminately with the electrons bound to atoms and molecules in the medium. The difference between β and γ-radiation lies mainly in the different nature of the interactions. For β particles the energy is transferred directly via inelastic collisions between the incident fast electron and the quasi-stationary bound electrons. Such collisions can result in the ejection of a secondary electron from the target molecule leaving behind an ionized and

excited molecule (or atom). For γ-radiation the interaction is more complicated. It involves a photo-electron process called Compton scattering which results in a lower energy photon and an ejected electron [142, 144-146]. The Compton-scattered electron (a high energy 'primary' electron) behaves very much like a β-particle in its subsequent collisions with medium molecules and this is why the chemical effects induced by both β and γ radiation in water (for the same absorbed energy) are essentially the same. The probability of a Compton scattering event is much lower than the probability of an electron scattering event (because the latter is a direct charge-charge interaction). This allows gamma rays to penetrate a medium much more deeply than a β-particle with the same incident energy. However, once a γ-photon produces a high energy secondary electron, the subsequent radiation deposition is the same for β and γ. Hence, we do not distinguish between them in their chemical impacts on solutions and refer to both as a radiation particle hereafter.

The average energy transferred from a radiation particle to a water molecule, per collision, typically ranges from 60 to 100 eV [142, 147]. This amount of energy is a very small fraction of the initial energy of the radiation particle so that individual collisions do not slow the particle much or change its path direction appreciably. The radiation particle moves in a straight line that is described as a radiation track. The initial consequence of each energy transfer collision is ionization and/or electronic excitation of a water molecule. The result is creation of ion pairs ($H_2O^{\bullet+}$ and e^-_{hot}) or electronically excited water molecules (H_2O^*) along the radiation track. The electron of this ion pair is labelled as 'hot' because it has a kinetic energy that is sufficient to excite or ionize one or more neighbouring water molecules (the 60 - 100 eV transferred in a collision is well in excess of the ionization energy of a water molecule (12.6 eV) [144]). Secondary (or even tertiary) ionization caused by this 'hot' electron will occur very near the location of the first ionization that created the 'hot' electron (because the 'hot' electron kinetic energy is low, it won't move very far). This results in clusters of 2-3 ion pairs (or excited water molecules) along the radiation track. This cluster is referred to as a "spur" and is illustrated in Figure 2-19 [142, 147]. Any electronically excited water molecules that arise because of a 'hot' electron impact have the option of being stabilized (by radiative decay and de-excitation collisions with other water

molecules), dissociating into an ion pair (with a low kinetic energy), or separating into free radical fragments (such as •OH and •H).
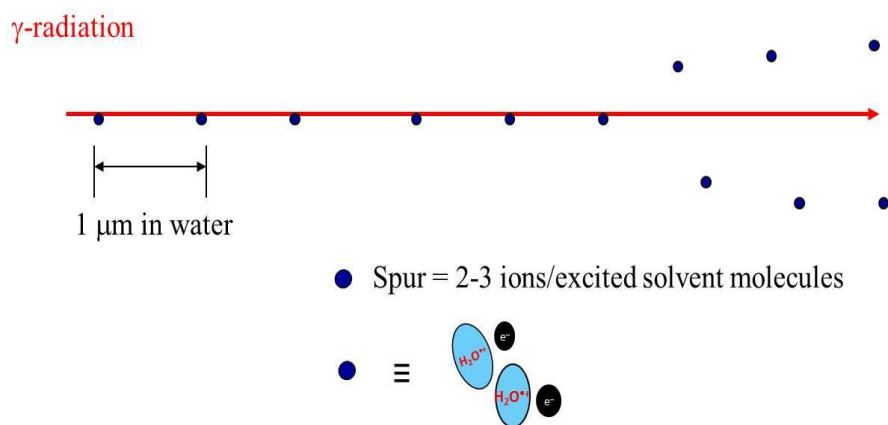
Figure 2-19: **The radiation track of a fast electron showing spurs (spur size not to scale) [21].**

The density of spurs along a radiation track is an important parameter in determining the chemical yields of radiolysis products. The spur density depends mainly on the collision rate of the radiation particle with the bound electrons in the water molecules. If the spurs are close enough together the ions and radicals in a spur can interact with those of an adjacent spur before they diffuse into the bulk water phase. Also, if the spur density is sufficiently high, these interactions can lead to a lower net decomposition rate of water (per absorbed energy unit) and a higher ratio of molecular to radical primary radiolysis products.

Figure 2-20 illustrates in detail the process breakdown of water into radiolysis products in the presence on ionizing radiation and subsequent reactions starting from the instantaneous interaction of a radiation particle with a molecule to the formation of the primary radiolysis products. Ionizing radiation initially produces a series of spurs of 2-3 ion pairs (electrons and water cations) or excited water molecules along a radiation track. As these species diffuse out, expanding the spurs, they can undergo dissociation, recombination

and ion-molecule reactions to form radical and molecular products as schematically represented in Figure 2-20.
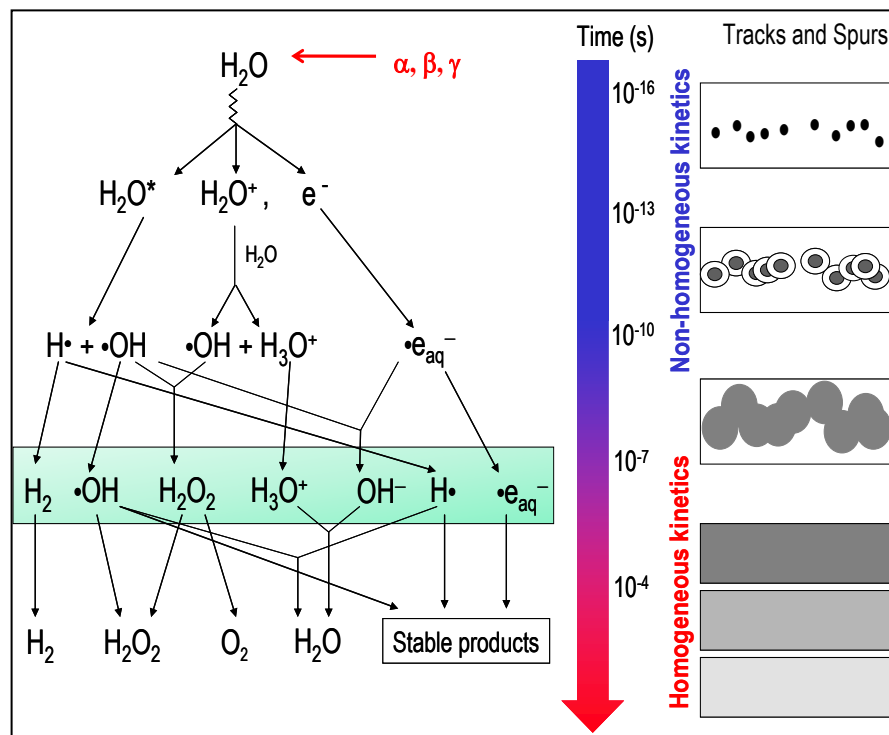
Figure 2-20: **Schematic of water radiolysis as a function of time following absorption of a single pulse of radiation energy. The figure on the right hand panel shows the expansion of spurs with time.**

The distribution of the radiolysis products in the solution is initially inhomogeneous but it becomes homogeneous as the spurs expand. The homogeneous distribution is reached in less than 10^{-6} s in water. This time is shorter than the time required for bulk aqueous phase chemistry to take place. For this reason, the products formed at this stage are referred to as the primary radiolysis products, even though they are not the very first species created by the interaction of a radiation particle. The chemical yields per absorbed energy at this stage are known as the primary radiolysis yields, commonly referred to as G-values ($\mu mol \cdot J^{-1}$). For gamma-radiolysis of water the primary yields (G values in units of $\mu mol \cdot J^{-1}$) at different temperatures are listed in Table 2-4 [142].

Table 2-4: The primary yields (μmol·J⁻¹) from γ-radiolysis of liquid water at different temperatures [21].

Temperature (°C)	$G(e_{aq})$	$G(H_2)$	$G(H)$	$G(OH)$	$G(H_2O_2)$
25	0.275	0.044	0.06	0.281	0.071
50	0.285	0.045	0.064	0.307	0.067
100	0.310	0.047	0.071	0.357	0.059
150	0.331	0.049	0.08	0.407	0.051
200	0.346	0.051	0.094	0.457	0.043
250	0.351	0.056	0.118	0.512	0.035
300	0.343	0.064	0.156	0.574	0.043
350	0.319	0.076	0.211	0.645	0.019

After formation, the primary radiolysis products continue to react with each other, solvent water ions (H^+ and OH^-), water molecules and, if present, solute species. These subsequent processes following the attainment of the homogeneous "out-of-spur" distribution of the radiolysis products can be described very effectively by classical reaction kinetic rate equations. Nevertheless, the chemical system is still very complex because of the number of primary radiolysis products, the large number of reactions that can occur and the coupling of these reactions, as schematically shown in Figure 2-21. About 50 elementary reactions are required to describe the radiolysis kinetics of the pure water system.

In the case of continuous irradiation over a time period that is long compared to chemical reaction rates (>ms), primary radiolysis products are produced continuously and their concentrations reach a steady state on a time scale of seconds [142, 148, 149]. The reactions of secondary radiolysis products, the reverse reactions of acid-base equilibria of various radiolysis products and cyclic reactions contribute significantly to the net radiolysis kinetics and the steady-state concentrations. In most practical environments where there is a radiation source present, irradiation will be continuous and the pseudo-steady-state concentrations of radiolysis products will dictate the effect of irradiation on the system (such as the rate of corrosion or degradation of nuclear reactor structural materials in or near a reactor core). Solid/liquid interfacial reactions such as corrosion generally occur over much

longer time scales (hours to years). Thus, the rates of the interfacial reactions are dictated by the long-term steady-state concentrations of reactive species.
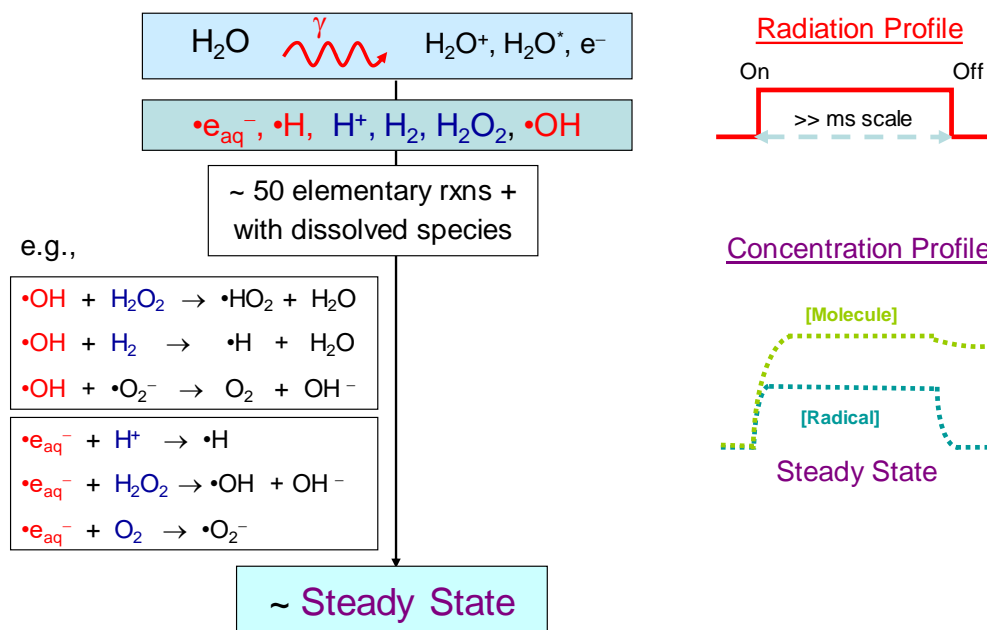
Figure 2-21: Schematic of water radiolysis reaction mechanism under long-term (>ms) continuous irradiation.

To determine the effect of pH and temperature on the net radiolytic production of H_2, O_2 and H_2O_2 and to establish the relationship between the measurable quantities (concentrations of the molecular products) and non-measurable quantities (the concentrations of radical species) a computational model has been developed [149].

Model calculations predict the effect of pH on the net radiolysis under deaerated conditions at 25 °C and 150 °C with dose rate 4.5 kG·h^{-1} as shown in Figure 2-22 and Figure 2-23. These figures show the time evolution of the chemistry in water when exposed to a continuous flux of radiation that is turned on at time 0. The model results show that the radiolysis product behaviours at pH$_{25°C}$ 6.0 and 10.6 are the same at short times (< 10 µs) but diverge considerably at longer times (> 1 s). This is because the short-term chemistry is

mostly determined by the primary radiolysis rate while longer term chemistry involves more chemical reactions.
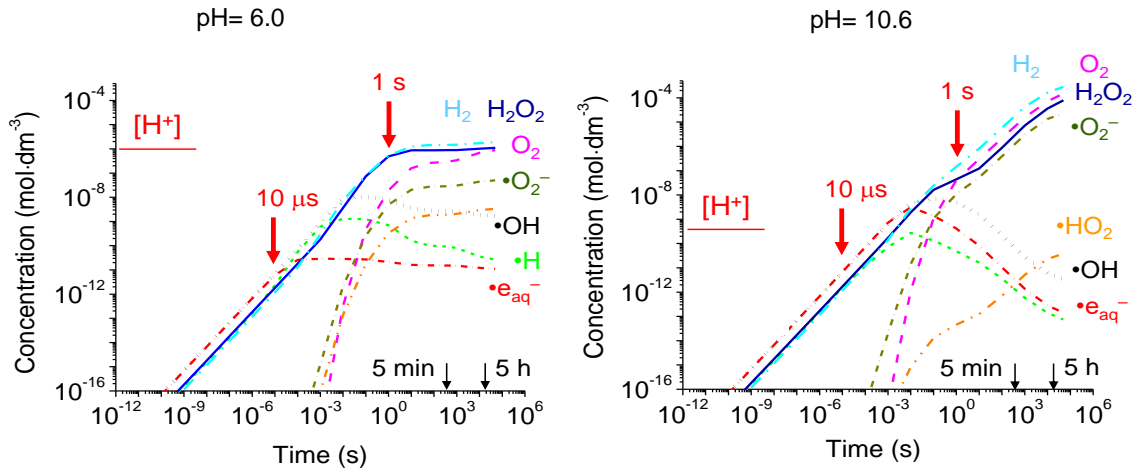
Figure 2-22: **Model simulation results that illustrate the effect of pH on radiolysis chemistry in deaerated water at a dose rate of 4.5 kG·h⁻¹ at 25 ºC [149].**
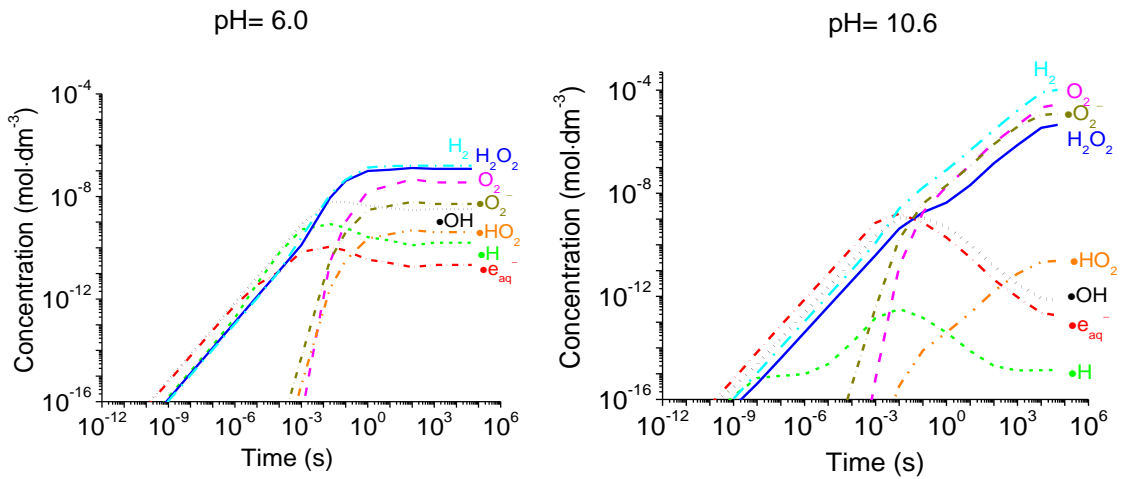
Figure 2-23: **Model simulation results that illustrate the effect of pH on radiolysis chemistry in deaerated water at a dose rate of 4.5 kG·h⁻¹ at 150 ºC [149].**

The primary radiolysis rate is obtained from,

$$i = \frac{d[i]}{dt} = D_R . G_i . \rho \qquad (2\text{-}26)$$

57

where D_R is the absorbed dose rate in units of $Gy \cdot s^{-1}$ where 1 Gy (Gray) = $1\ J \cdot kg^{-1}$, G_i is the G-value of species i in units of $\mu mol \cdot J^{-1}$, and ρ is the density of water in units of $kg \cdot dm^{-3}$. At a given temperature, the $G_i \cdot \rho \cdot D_R$ values are independent of pH. This explains the similarities in the concentrations of the primary radiolysis products at the two different pHs at early times.

The concentrations of the primary radiolysis products deviate from a linear dependence on time after 1 ms. The model results show that the onset of the deviation occurs earlier at pH 6.0 than at pH 10.6. This effect of pH on the long-term behaviour arises mainly from a change in the rate of the reaction of $\bullet e_{aq}^-$ with H^+:

$$\bullet e_{aq}^- + H^+ \leftrightarrows \bullet H \ pK_a \text{ of } \bullet H = 9.6 \tag{2-27}$$

At pH < 9.6, the pK_a of $\bullet$H, this reaction is very fast and is the main loss path for $\bullet e_{aq}^-$ at long times. The main production path for $\bullet e_{aq}^-$ is the primary radiolysis yield. Under these conditions, $[\bullet e_{aq}^-]$ reaches steady state relatively quickly and its pseudo-steady-state concentration is relatively small.

At pH > 9.6, the net rate of reaction 2-27 is extremely small. Thus, $\bullet e_{aq}^-$ accumulates until the concentration of the secondary product O_2 reaches a sufficient level to react with $\bullet e_{aq}^-$ at an appreciable rate:

$$O_2 + \bullet e_{aq}^- \rightarrow \bullet O_2^- \ k_{2\text{-}28} = 2.22 \times 10^{10}\ mol^{-1} \cdot dm^3 \cdot s^{-1} \tag{2-28}$$
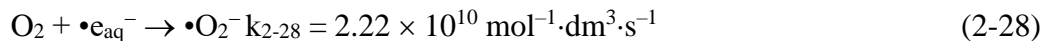
This reaction, however, produces $\bullet O_2^-$ which can react with another primary radiolysis product, $\bullet$OH, reforming O_2:

$$\bullet OH + \bullet O_2^- \rightarrow O_2 + OH^- \ k_{2\text{-}29} = 8.0 \times 10^9\ mol^{-1} \cdot dm^3 \cdot s^{-1} \tag{2-29}$$
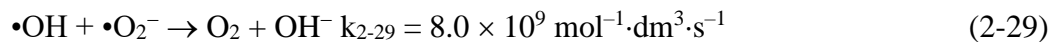
Once the reaction cycle between reactions (2-28) and (2-29) is established, $\bullet$OH and $\bullet e_{aq}^-$ are continually removed and their concentrations decrease steadily. Since the molecular radiolysis products H_2 and H_2O_2 are removed primarily via reactions with the radical species, the decreases in $[\bullet OH]$ and $[\bullet e_{aq}^-]$ result in an increase in $[H_2]$ and $[H_2O_2]$.

58

With increase in temperature the rate of thermal decomposition of H_2O_2 increases. The thermal decomposition can occur via two reaction pathways:

$$2 \ H_2O_2 \rightarrow O_2 + H_2O \tag{2-30}$$

$$H_2O_2 \rightarrow 2 \ \bullet OH \tag{2-31}$$

Due to faster decomposition, the pseudo-steady-state concentration of H_2O_2 is reached at an earlier time and is lower at 150 °C than at 25 °C.

2.6.2 Radiation Induced Nanoparticle Formation

Gamma-radiation decomposes water to yield a range of redox active species and the chemical yields per unit energy input of the radical species are very high, and cannot be obtained by other thermal processes. Radiolysis is a promising new technique that can be applied to the synthesis of metal oxide nanoparticles and thin films to provide superior control of the size and morphology of the particles. Because γ-radiation penetrates deeply in water, it generates a uniform homogeneous distribution of radiolysis products that, in turn, leads to the simultaneous generation of homogeneously distributed nucleation sites. This leads to the formation of nanoparticles with a narrow, uniform size distribution. Radiation-induced nanoparticle formation is also considered a cleaner technique since the addition of chemical additives or stabilizers is not required for particle formation or size control. Important consequences of this are the generation of redox active species without altering the metal-cation solubility in the solution and without unwanted waste products. This eliminates the need for other chemical agents that can interfere with the particle growth kinetics.

Wren et al. have reported the mechanism of γ-radiation-induced formation and growth of metal-oxide nanoparticles from initially dissolved metal cations in aqueous solutions (γ-FeOOH and Fe_3O_4 from Fe^{2+}, Co_3O_4 from Co^{2+}, and Cr_2O_3 from Cr^{6+}) [150-155]. In these studies, the strong oxidizing power of $\bullet OH$ and H_2O_2 or the strong reducing power of $\bullet e_{aq}^-$, and the difference in the solubility of the oxidation products are utilized for metal oxide nanoparticle formation. Depending on the equilibrium potential of the redox

reactions involved, either the oxidizing or reducing water radiolysis products are utilized for the generation of nucleation sites and particle growth. In the case of chromium oxide, the reducing power of $\bullet e_{aq}^-$ is used whereas for the iron and cobalt systems the oxidizing powers of $\bullet OH$ and H_2O_2 are employed.

2.7   References

[1] F. Cattant, D. Crusset, D. Féron, Corrosion issues in nuclear industry today, Materials Today, 11 (2008) 32-37.

[2] J. Chen, Q. Xiao, Z. Lu, X. Ru, H. Peng, Q. Xiong, H. Li, Characterization of interfacial reactions and oxide films on 316L stainless steel in various simulated PWR primary water environments, Journal of Nuclear Materials, 489 (2017) 137-149.

[3] W. Garland, The Essential CANDU, University Network of Excellence in Nuclear Engineering (UNENE), (2014).

[4] R.M. Cornell, U. Schwertmann, The Iron Oxides: Structure, Properties, Reactions, Occurrences and Uses, Wiley, 2003.

[5] A.J. Davenport, L.J. Oblonsky, M.P. Ryan, M.F. Toney, The Structure of the Passive Film That Forms on Iron in Aqueous Environments, Journal of The Electrochemical Society, 147 (2000) 2162-2173.

[6] L. Wang, T. Maxisch, G. Ceder, Oxidation energies of transition metal oxides within the GGA+U framework, Physical Review B, 73 (2006) 195107.

[7] D.A. Robinson, Calculation of the Dielectric Properties of Temperate and Tropical Soil Minerals from Ion Polarizabilities using the Clausius–Mosotti Equation, Soil Science Society of America Journal, 68 (2004) 1780-1785.

[8] T. Misawa, The thermodynamic consideration for Fe-H_2O system at 25°C, Corrosion Science, 13 (1973) 659-676.

[9] P. Schmuki, M. Büchler, S. Virtanen, H. Böhni, R. Müller, L.J. Gauckler, Bulk Metal Oxides as a Model for the Electronic Properties of Passive Films, Journal of The Electrochemical Society, 142 (1995) 3336-3342.

[10] J.P. Glusker, M. Lewis, M. Rossi, Crystal Structure Analysis for Chemists and Biologists, Wiley, 1994.

[11] S.S. Kulkarni, C.D. Lokhande, Structural, optical, electrical and dielectrical properties of electrosynthesized nanocrystalline iron oxide thin films, Materials Chemistry and Physics, 82 (2003) 151-156.

[12] P. Patil, L. Kadam, Preparation and characterization of spray pyrolyzed nickel oxide (NiO) thin films, Applied surface science, 199 (2002) 211-221.

[13] S. Pizzini, R. Morlotti, Thermodynamic and transport properties of stoichiometric and nonstoichiometric nickel oxide, Journal of The Electrochemical Society, 114 (1967) 1179-1189.

[14] S. Dudarev, G. Botton, S. Savrasov, C. Humphreys, A. Sutton, Electron-energy-loss spectra and the structural stability of nickel oxide: An LSDA+ U study, Physical Review B, 57 (1998) 1505.

[15] P. Jeevanandam, Y. Koltypin, A. Gedanken, Synthesis of nanosized α-nickel hydroxide by a sonochemical method, Nano Letters, 1 (2001) 263-266.

[16] P. Oliva, J. Leonardi, J. Laurent, C. Delmas, J. Braconnier, M. Figlarz, F. Fievet, A. De Guibert, Review of the structure and the electrochemistry of nickel hydroxides and oxy-hydroxides, Journal of Power Sources, 8 (1982) 229-255.

[17] P.V. Kamath, M. Dixit, L. Indira, A. Shukla, V.G. Kumar, N. Munichandraiah, Stabilized α-Ni(OH)$_2$ as Electrode Material for Alkaline Secondary Cells, Journal of the Electrochemical Society, 141 (1994) 2956-2959.

[18] C. Greaves, M. Thomas, Refinement of the structure of deuterated nickel hydroxide, Ni(OD)$_2$, by powder neutron diffraction and evidence for structural disorder in samples with high surface area, Acta Crystallographica Section B: Structural Science, 42 (1986) 51-55.

[19] A. Szytula, A. Murasik, M. Balanda, Neutron diffraction study of Ni(OH)$_2$, physica status solidi (b), 43 (1971) 125-128.

[20] D. Marijan, M. Gojić, Electrochemical study of the chromium electrode behaviour in borate buffer solution, Journal of Applied Electrochemistry, 32 (2002) 1341-1346.

[21] M. Behazin, "Radiation Induced Corrosion of Stellite-6" (2014). Electronic Thesis and Dissertation Repository. 2434.

[22] R. Cheng, B. Xu, C. Borca, A. Sokolov, C.-S. Yang, L. Yuan, S.-H. Liou, B. Doudin, P.A. Dowben, Characterization of the native Cr$_2$O$_3$ oxide surface of CrO$_2$, Applied Physics Letters, 79 (2001) 3122-3124.

[23] L. Tan, T.R. Allen, Y. Yang, Corrosion behavior of alloy 800H (Fe–21Cr–32Ni) in supercritical water, Corrosion Science, 53 (2011) 703-711.

[24] B. Beverskog, I. Puigdomenech, Revised Pourbaix diagrams for nickel at 25–300 °C, Corrosion Science, 39 (1997) 969-980.

[25] M. Pourbaix, Atlas of Electrochemical Equilibria in Aqueous Solutions, National Association of Corrosion Engineers, 1966.

[26] J. Chivot, L. Mendoza, C. Mansour, T. Pauporté, M. Cassir, New insight in the behaviour of Co–H$_2$O system at 25–150 °C, based on revised Pourbaix diagrams, Corrosion Science, 50 (2008) 62-69.

[27] F. Tack, O. Callewaert, M. Verloo, Metal solubility as a function of pH in a contaminated, dredged sediment affected by oxidation, Environmental pollution, 91 (1996) 199-208.

[28] H.-X. You, H.-B. Xu, Y. Zhang, S.-L. Zheng, Y.-Y. Gao, Potential—pH diagrams of Cr-H$_2$O system at elevated temperatures, Transactions of Nonferrous Metals Society of China, 20 (2010) s26-s31.

[29] B. Beverskog, I. Puigdomenech, Revised Pourbaix diagrams for iron at 25–300 °C, Corrosion Science, 38 (1996) 2121-2135.

[30] C.F. Baes, R.E. Mesmer, The Hydrolysis of Cations, Robert E. Krieger, 1986.

[31] B. Beverskog, I. Puigdomenech, Pourbaix diagrams for the ternary system of iron-chromium-nickel, CORROSION, 55 (1999) 1077-1087.

[32] X. Li, J. Wang, E.-H. Han, W. Ke, Corrosion behavior for Alloy 690 and Alloy 800 tubes in simulated primary water, Corrosion Science, 67 (2013) 169-178.

[33] J.-M. Le Canut, S. Maximovitch, F. Dalard, Electrochemical characterisation of nickel-based alloys in sulphate solutions at 320° C, Journal of Nuclear Materials, 334 (2004) 13-27.

[34] J.R. Crum, R.C. Scarberry, Corrosion Testing of INCONEL Alloy 690 for PWR steam generators, Journal of Materials for Energy Systems, 4 (1982) 125-130.

[35] J. Crum, Stress corrosion cracking testing of Inconel alloys 600 and 690 under high-temperature caustic conditions, CORROSION, 42 (1986) 368-372.

[36] J.Z. Wang, J.Q. Wang, E.H. Han, Influence of temperature on electrochemical behavior and oxide film property of Alloy 800 in hydrogenated high temperature water, Materials and Corrosion, 67 (2016) 796-803.

[37] P. Marcus, J. Grimal, The anodic dissolution and passivation of NiCrFe alloys studied by ESCA, Corrosion Science, 33 (1992) 805-814.

[38] S.S. Hwang, U.C. Kim, Y.S. Park, The effects of Pb on the passive film of Ni-base alloy in high temperature water, Journal of Nuclear Materials, 246 (1997) 77-83.

[39] S. Leistikow, I. Wolf, H. Grabke, Effects of cold work on the oxidation behavior and carburization resistance of Alloy 800, Materials and Corrosion, 38 (1987) 556-562.

[40] M. Faichuk, "Characterization of the Corrosion and Oxide Film Properties of Alloy 600 and Alloy 800" (2013). Electronic Thesis and Dissertation Repository. 1777.

[41] T. Nickchi, A. Alfantazi, Effect of Buffer Capacity on Electrochemical Corrosion Behavior of Alloy 800 in Sulfate Solutions, Corrosion, The Journal of Science and Engineering, 68 (2012) 015003-015001-015003-015011.

[42] T. Nickchi, A. Alfantazi, Corrosion characteristics of alloy 800 in aqueous solutions up to 200 C, Journal of The Electrochemical Society, 160 (2013) C64-C76.

[43] T. Nickchi, A. Alfantazi, Electrochemical corrosion behaviour of Incoloy 800 in sulphate solutions containing hydrogen peroxide, Corrosion Science, 52 (2010) 4035-4045.

[44] T. Nickchi, A. Alfantazi, Kinetics of passive film growth on Alloy 800 in the presence of hydrogen peroxide, Electrochimica Acta, 58 (2011) 743-749.

[45] D.-H. Xia, Y. Behnamian, H.-N. Feng, H.-Q. Fan, L.-X. Yang, C. Shen, J.-L. Luo, Y.-C. Lu, S. Klimas, Semiconductivity conversion of Alloy 800 in sulphate, thiosulphate, and chloride solutions, Corrosion Science, 87 (2014) 265-277.

[46] J. Hickling, N. Wieling, Electrochemical investigations of the resistance of Inconel 600, Incoloy 800, and Type 347 stainless steel to pitting corrosion in faulted PWR secondary water at 150 to 250 C, CORROSION, 37 (1981) 147-152.

[47] M.W. Edwards, N.S. McIntyre, Gas Phase Initial Oxidation of Incoloy 800 Surfaces, Oxidation of Metals, 79 (2013) 179-200.

[48] J. Huang, X. Wu, E.-H. Han, Influence of pH on electrochemical properties of passive films formed on Alloy 690 in high temperature aqueous environments, Corrosion Science, 51 (2009) 2976-2982.

[49] S. Persaud, A. Carcea, R. Newman, An electrochemical study assisting the interpretation of acid sulfate stress corrosion cracking of NiCrFe alloys, Corrosion Science, 90 (2015) 383-391.

[50] S. Persaud, A. Carcea, J. Huang, A. Korinek, G. Botton, R. Newman, Analytical electron microscopy of a crack tip extracted from a stressed Alloy 800 sample exposed to an acid sulfate environment, Micron, 61 (2014) 62-69.

[51] S. Persaud, S. Ramamurthy, R. Newman, Internal oxidation of alloy 690 in hydrogenated steam, Corrosion Science, 90 (2015) 606-613.

[52] B. Langelier, S. Persaud, R. Newman, G. Botton, An atom probe tomography study of internal oxidation processes in Alloy 600, Acta Materialia, 109 (2016) 55-68.

[53] S. Persaud, S. Ramamurthy, A. Korinek, G. Botton, R. Newman, The influence of the high Fe and Cr contents of Alloy 800 on its inter-and intragranular oxidation tendency in 480° C hydrogenated steam, Corrosion Science, 106 (2016) 117-126.

[54] S. Persaud, J. Smith, A. Korinek, G. Botton, R. Newman, High resolution analysis of oxidation in Ni-Fe-Cr alloys after exposure to 315° C deaerated water with added hydrogen, Corrosion Science, 106 (2016) 236-248.

[55] S. Persaud, A. Korinek, J. Huang, G. Botton, R. Newman, Internal oxidation of Alloy 600 exposed to hydrogenated steam and the beneficial effects of thermal treatment, Corrosion Science, 86 (2014) 108-122.

[56] N.S. McIntyre, R.D. Davidson, T.L. Walzak, A.M. Brennenstuhl, F. Gonzalez, S. Corazza, The corrosion of steam generator surfaces under typical secondary coolant conditions: Effects of pH excursions on the alloy surface composition, Corrosion Science, 37 (1995) 1059-1083.

[57] T. Dieudonné, L. Marchetti, M. Wery, F. Miserque, M. Tabarant, J. Chêne, C. Allely, P. Cugy, C.P. Scott, Role of copper and aluminum on the corrosion behavior of austenitic Fe–Mn–C TWIP steels in aqueous solutions and the related hydrogen absorption, Corrosion Science, 83 (2014) 234-244.

[58] M. Dumerval, S. Perrin, L. Marchetti, M. Sennour, F. Jomard, S. Vaubaillon, Y. Wouters, Effect of implantation defects on the corrosion of 316L stainless steels in primary medium of pressurized water reactors, Corrosion Science, 107 (2016) 1-8.

[59] S. Guillou, C. Cabet, C. Desgranges, L. Marchetti, Y. Wouters, Influence of Hydrogen and Water Vapour on the Kinetics of Chromium Oxide Growth at High Temperature, Oxidation of Metals, 76 (2011) 193-214.

[60] H. Lefaix-Jeuland, L. Marchetti, S. Perrin, M. Pijolat, M. Sennour, R. Molins, Oxidation kinetics and mechanisms of Ni-base alloys in pressurised water reactor primary conditions: Influence of subsurface defects, Corrosion Science, 53 (2011) 3914-3922.

[61] L. Marchetti, S. Perrin, F. Jambon, M. Pijolat, Corrosion of nickel-base alloys in primary medium of pressurized water reactors: New insights on the oxide growth mechanisms and kinetic modelling, Corrosion Science, 102 (2016) 24-35.

[62] L. Marchetti, S. Perrin, O. Raquet, M. Pijolat, Corrosion mechanisms of Ni-base alloys in pressurized water reactor primary conditions, in: Materials Science Forum, Trans Tech Publ, 2008, pp. 529-537.

[63] L. Marchetti, S. Perrin, Y. Wouters, F. Martin, M. Pijolat, Photoelectrochemical study of nickel base alloys oxide films formed at high temperature and high pressure water, Electrochimica Acta, 55 (2010) 5384-5392.

[64] M. Sennour, L. Marchetti, F. Martin, S. Perrin, R. Molins, M. Pijolat, A detailed TEM and SEM study of Ni-base alloys oxide scales formed in primary conditions of pressurized water reactor, Journal of Nuclear Materials, 402 (2010) 147-156.

[65] M. Sennour, L. Marchetti, S. Perrin, R. Molins, M. Pijolat, O. Raquet, Characterization of the oxide films formed at the surface of Ni-base alloys in pressurized water reactors primary coolant by transmission electron microscopy, in: Materials Science Forum, Trans Tech Publ, 2008, pp. 539-547.

[66] K.I. Choudhry, D.T. Kallikragas, I.M. Svishchev, Hydrogen Release Rate and Corrosion Measurements on Alloy 800H and Stainless Steel 316 in Supercritical Water Conditions, in: S. Penttilä (Ed.) The 7th International Symposium on Supercritical Water-Cooled Reactors ISSCWR-7, VTT Technical Research Centre of Finland Ltd, Helsinki, Finland, 2015, pp. 1-7.

[67] G. Steeves, W. Cook, Development of Kinetic Models for the Long-Term Corrosion Behavior of Candidate Alloys for the Canadian SCWR, Journal of Nuclear Engineering and Radiation Science, 3 (2017) 031001-031001-031007.

[68] L. Tan, X. Ren, K. Sridharan, T.R. Allen, Corrosion behavior of Ni-base alloys for advanced high temperature water-cooled nuclear plants, Corrosion Science, 50 (2008) 3056-3062.

[69] L. Tan, K. Sridharan, T.R. Allen, The effect of grain boundary engineering on the oxidation behavior of INCOLOY alloy 800H in supercritical water, Journal of Nuclear Materials, 348 (2006) 263-271.

[70] L. Tan, K. Sridharan, T.R. Allen, R.K. Nanstad, D.A. McClintock, Microstructure tailoring for property improvements by grain boundary engineering, Journal of Nuclear Materials, 374 (2008) 270-280.

[71] M. Sun, X. Wu, Z. Zhang, E.-H. Han, Oxidation of 316 stainless steel in supercritical water, Corrosion Science, 51 (2009) 1069-1072.

[72] D. Rodriguez, D. Chidambaram, Oxidation of stainless steel 316 and Nitronic 50 in supercritical and ultrasupercritical water, Applied Surface Science, 347 (2015) 10-16.

[73] I.M. Svishchev, R.A. Carvajal-Ortiz, K.I. Choudhry, D.A. Guzonas, Corrosion behavior of stainless steel 316 in sub- and supercritical aqueous environments: Effect of LiOH additions, Corrosion Science, 72 (2013) 20-25.

[74] G.S. Was, P. Ampornrat, G. Gupta, S. Teysseyre, E.A. West, T.R. Allen, K. Sridharan, L. Tan, Y. Chen, X. Ren, C. Pister, Corrosion and stress corrosion cracking in supercritical water, Journal of Nuclear Materials, 371 (2007) 176-201.

[75] P. Kritzer, Corrosion in high-temperature and supercritical water and aqueous solutions: a review, The Journal of Supercritical Fluids, 29 (2004) 1-29.

[76] Q. Zhang, R. Tang, K. Yin, X. Luo, L. Zhang, Corrosion behavior of Hastelloy C-276 in supercritical water, Corrosion Science, 51 (2009) 2092-2097.

[77] K.I. Choudhry, S. Mahboubi, G.A. Botton, J.R. Kish, I.M. Svishchev, Corrosion of engineering materials in a supercritical water cooled reactor: Characterization of oxide scales on Alloy 800H and stainless steel 316, Corrosion Science, 100 (2015) 222-230.

[78] M. Fulger, D. Ohai, M. Mihalache, M. Pantiru, V. Malinovschi, Oxidation behavior of Incoloy 800 under simulated supercritical water conditions, Journal of Nuclear Materials, 385 (2009) 288-293.

[79] G.S. Was, S. Teysseyre, Z. Jiao, Corrosion of Austenitic Alloys in Supercritical Water, CORROSION, 62 (2006) 989-1005.

[80] S. Mahboubi, G.A. Botton, J.R. Kish, On the Oxidation Resistance of Alloy 800HT Exposed in Supercritical Water (SCW), CORROSION, 71 (2015) 992-1002.

[81] X. Ru, R.W. Staehle, Historical Experience Providing Bases for Predicting Corrosion and Stress Corrosion in Emerging Supercritical Water Nuclear Technology: Part 1— Review, CORROSION, 69 (2013) 211-229.

[82] Q.J. Peng, S. Teysseyre, P.L. Andresen, G.S. Was, Stress Corrosion Crack Growth in Type 316 Stainless Steel in Supercritical Water, CORROSION, 63 (2007) 1033-1041.

[83] S. Mahboubi, G.A. Botton, J.R. Kish, Technical Note: Corrosion Resistance of Alloy 33 (Fe-33Cr-32Ni) in Supercritical Water, CORROSION, 71 (2015) 1064-1070.

[84] Y. Yang, Q. Yan, R. Ma, F. Zhu, L. Zhang, C. Ge, Corrosion Behavior of Modified UNS N08367 Austenitic Steel in Supercritical Water, CORROSION, 66 (2010) 096002-096002-096005.

[85] X. Ren, K. Sridharan, T.R. Allen, Corrosion Behavior of Alloys 625 and 718 in Supercritical Water, CORROSION, 63 (2007) 603-612.

[86] S. Mahboubi, Y. Jiao, W. Cook, W. Zheng, D.A. Guzonas, G.A. Botton, J.R. Kish, Stability of Chromia (Cr2O3)-Based Scales Formed During Corrosion of Austenitic Fe-Cr-Ni Alloys in Flowing Oxygenated Supercritical Water, CORROSION, 72 (2016) 1170-1180.

[87] Y. Behnamian, A. Mostafaei, A. Kohandehghan, B. Zahiri, W. Zheng, D. Guzonas, M. Chmielus, W. Chen, J.L. Luo, Corrosion behavior of alloy 316L stainless steel after exposure to supercritical water at 500 °C for 20,000 h, The Journal of Supercritical Fluids, 127 (2017) 191-199.

[88] K.I. Choudhry, D.A. Guzonas, D.T. Kallikragas, I.M. Svishchev, On-line monitoring of oxide formation and dissolution on alloy 800H in supercritical water, Corrosion Science, 111 (2016) 574-582.

[89] L. Zhang, Y. Bao, R. Tang, Selection and corrosion evaluation tests of candidate SCWR fuel cladding materials, Nuclear Engineering and Design, 249 (2012) 180-187.

[90] S. Hariharan, M. Momeni, V. Subramanian, J.J. Noel, J. Joseph, J.C. Wren, The Influence of Water Radiolysis on Corrosion By Supercritical Water, in: Meeting Abstracts, The Electrochemical Society, 2015, pp. 682-682.

[91] H. Subramanian, V. Subramanian, M. Momeni, James J. Noël, J.M. Joseph, D.A. Guzonas, J.C. Wren, The Effect of Water Radiolysis on Corrosion in High-temperature Steam, in: 17th International Conference on Environmental Degradation of Materials in Nuclear Power Systems - Water Reactors, Ottawa, ON, Canada, 2015.

[92] A. Seyeux, V. Maurice, P. Marcus, Oxide Film Growth Kinetics on Metals and Alloys: I. Physical Model, Journal of The Electrochemical Society, 160 (2013) C189-C196.

[93] N. Mott, The theory of the formation of protective oxide films on metals.—III, Transactions of the Faraday Society, 43 (1947) 429-434.

[94] N. Mott, The theory of the formation of protective oxide films on metals, II, Transactions of the faraday society, 35 (1940) 472-483.

[95] N. Mott, A theory of the formation of protective oxide films on metals, Transactions of the faraday Society, 35 (1939) 1175-1177.

[96] N. Cabrera, N. Mott, Theory of the oxidation of metals, Reports on progress in physics, 12 (1949) 163.

[97] D.D. Eley, P.R. Wilkinson, Adsorption and Oxide Formation on Aluminium Films, Proceedings of the Royal Society of London. Series A. Mathematical and Physical Sciences, 254 (1960) 327-342.

[98] D. Macdonald, Passivity: enabler of our metals based civilisation, Corrosion Engineering, Science and Technology, 49 (2014) 143-155.

[99] D. Ellerbrock, D.D. Macdonald, Passivity of titanium, part 1: film growth model diagnostics, Journal of Solid State Electrochemistry, 18 (2014) 1485-1493.

[100] F. Mao, C. Dong, S. Sharifi-Asl, P. Lu, D.D. Macdonald, Passivity breakdown on copper: influence of chloride ion, Electrochimica Acta, 144 (2014) 391-399.

[101] P. Lu, G.R. Engelhardt, B. Kursten, D.D. Macdonald, The kinetics of nucleation of metastable pits on metal surfaces: the Point Defect Model and its optimization on data obtained on stainless steel, carbon steel, iron, aluminum and Alloy-22, Journal of The Electrochemical Society, 163 (2016) C156-C163.

[102] D.D. Macdonald, X. Lei, Theoretical Interpretation of Anion Size Effects in Passivity Breakdown, Journal of The Electrochemical Society, 163 (2016) C738-C744.

[103] F. Mao, P. Lu, D.D. Macdonald, Diagnosis of the Mechanism of Anodic Oxide Film Growth on Platinum in KOH, Zeitschrift für Physikalische Chemie, 230 (2016) 79-95.

[104] X. Lei, Y. Feng, J. Zhang, A. Fu, C. Yin, D.D. Macdonald, Impact of Reversed Austenite on the Pitting Corrosion Behavior of Super 13Cr Martensitic Stainless Steel, Electrochimica Acta, 191 (2016) 640-650.

[105] P. Lu, S. Sharifi-Asl, B. Kursten, D.D. Macdonald, The Modelling of Pitting Corrosion of Carbon Steel in High Level Nuclear Waste Supercontainer, Meeting Abstracts, MA2015-02 (2015) 716.

[106] P. Lu, G. Engelhardt, D.D. Macdonald, The Kinetics of the Metastable Pit Nucleation on Metal Surfaces, Meeting Abstracts, MA2016-02 (2016) 1156.

[107] D.D. Macdonald, On the formation of voids in anodic oxide films on aluminum, Journal of the Electrochemical Society, 140 (1993) L27-L30.

[108] L. Zhang, D.D. Macdonald, E. Sikora, J. Sikora, On the kinetics of growth of anodic oxide films, Journal of the Electrochemical Society, 145 (1998) 898-905.

[109] D.D. Macdonald, On the existence of our metals-based civilization I. Phase-space analysis, Journal of the Electrochemical Society, 153 (2006) B213-B224.

[110] D.D. Macdonald, K.M. Ismail, E. Sikora, Characterization of the passive state on zinc, Journal of the Electrochemical Society, 145 (1998) 3141-3149.

[111] D.D. Macdonald, M. Urquidi-Macdonald, Theory of Steady-State Passive Films, Journal of the Electrochemical Society, 137 (1990) 2395-2402.

[112] D.D. Macdonald, Passivity–the key to our metals-based civilization, Pure and Applied Chemistry, 71 (1999) 951-978.

[113] D. Macdonald, G. Englehardt, The point defect model for bi-layer passive films, ECS Transactions, 28 (2010) 123-144.

[114] O. Pensado-Rodriguez, J.R. Flores, M. Urquidi-Macdonald, D.D. Macdonald, Electrochemical behavior of lithium in alkaline aqueous electrolytes. II. Point defect model, Journal of the Electrochemical Society, 146 (1999) 1326-1335.

[115] R. Narayanan, S. Seshadri, Point defect model and corrosion of anodic oxide coatings on Ti–6Al–4V, Corrosion Science, 50 (2008) 1521-1529.

[116] D.D. Macdonald, The history of the point defect model for the passive state: a brief review of film growth aspects, Electrochimica Acta, 56 (2011) 1761-1772.

[117] D.D. Macdonald, The point defect model for the passive state, Journal of the Electrochemical Society, 139 (1992) 3434-3449.

[118] C. Chao, L. Lin, D. Macdonald, A point defect model for anodic passive films III. Impedance response, Journal of the electrochemical society, 129 (1982) 1874-1879.

[119] L. Lin, C. Chao, D. Macdonald, A point defect model for anodic passive films II. Chemical breakdown and pit initiation, Journal of the Electrochemical Society, 128 (1981) 1194-1198.

[120] C. Chao, L. Lin, D. Macdonald, A point defect model for anodic passive films I. Film growth kinetics, Journal of the Electrochemical Society, 128 (1981) 1187-1194.

[121] D.D. Macdonald, S.R. Biaggio, H. Song, Steady-State Passive Films: Interfacial Kinetic Effects and Diagnostic Criteria, Journal of The Electrochemical Society, 139 (1992) 170-177.

[122] I. Betova, M. Bojinov, P. Kinnunen, K. Mäkelä, T. Saario, Conduction mechanism in oxide films on ferrous alloys studied by impedance spectroscopy in symmetrical and asymmetrical configurations, Journal of Electroanalytical Chemistry, 572 (2004) 211-223.

[123] M. Bojinov, I. Betova, R. Raicheff, A model for the transpassivity of molybdenum in acidic sulphate solutions based on ac impedance measurements, Electrochimica acta, 41 (1996) 1173-1179.

[124] M. Bojinov, I. Betova, R. Raicheff, Kinetics of formation and properties of a barrier oxide film on molybdenum, Journal of Electroanalytical Chemistry, 411 (1996) 37-42.

[125] I. Betova, M. Bojinov, T. Laitinen, K. Mäkelä, P. Pohjanne, T. Saario, The transpassive dissolution mechanism of highly alloyed stainless steels: II. Effect of pH and solution anion on the kinetics, Corrosion science, 44 (2002) 2699-2723.

[126] D. Pavlov, M. Bojinov, T. Laitinen, G. Sundholm, Electrochemical behaviour of the antimony electrode in sulphuric acid solutions—II. Formation and properties of the primary anodic layer, Electrochimica acta, 36 (1991) 2087-2092.

[127] M. Bojinov, G. Fabricius, T. Laitinen, K. Mäkelä, T. Saario, G. Sundholm, Conduction Mechanism of the Anodic Film on Fe-Cr Alloys in Sulfate Solutions, Journal of the Electrochemical Society, 146 (1999) 3238-3247.

[128] M. Bojinov, P. Kinnunen, K. Lundgren, G. Wikmark, A mixed-conduction model for the oxidation of stainless steel in a high-temperature electrolyte estimation of kinetic parameters of oxide layer growth and restructuring, Journal of The Electrochemical Society, 152 (2005) B250-B261.

[129] M. Bojinov, T. Laitinen, K. Mäkelä, T. Saario, Conduction mechanism of the passive film on iron based on contact electric impedance and resistance measurements, Journal of The Electrochemical Society, 148 (2001) B243-B250.

[130] M. Bojinov, A. Galtayries, P. Kinnunen, A. Machet, P. Marcus, Estimation of the parameters of oxide film growth on nickel-based alloys in high-temperature water electrolytes, Electrochimica acta, 52 (2007) 7475-7483.

[131] M. Bojinov, Modelling the formation and growth of anodic passive films on metals in concentrated acid solutions, Journal of Solid State Electrochemistry, 1 (1997) 161-171.

[132] B. Beverskog, M. Bojinov, A. Englund, P. Kinnunen, T. Laitinen, K. Mäkelä, T. Saario, P. Sirkiä, A mixed-conduction model for oxide films on Fe, Cr and Fe–Cr alloys in high-temperature aqueous electrolytes—I. Comparison of the electrochemical behaviour at room temperature and at 200° C, Corrosion science, 44 (2002) 1901-1921.

[133] M. Bojinov, G. Fabricius, P. Kinnunen, T. Laitinen, K. Mäkelä, T. Saario, G. Sundholm, The mechanism of transpassive dissolution of Ni–Cr alloys in sulphate solutions, Electrochimica Acta, 45 (2000) 2791-2802.

[134] B. Beverskog, M. Bojinov, P. Kinnunen, T. Laitinen, K. Mäkelä, T. Saario, A mixed-conduction model for oxide films on Fe, Cr and Fe–Cr alloys in high-temperature aqueous electrolytes—II. Adaptation and justification of the model, Corrosion Science, 44 (2002) 1923-1940.

[135] M. Bojinov, I. Betova, G. Fabricius, T. Laitinen, T. Saario, The stability of the passive state of iron–chromium alloys in sulphuric acid solution, Corrosion Science, 41 (1999) 1557-1584.

[136] M. Bojinov, G. Fabricius, P. Kinnunen, T. Laitinen, K. Mäkelä, T. Saario, G. Sundholm, Electrochemical study of the passive behaviour of Ni–Cr alloys in a borate solution—a mixed-conduction model approach, Journal of Electroanalytical Chemistry, 504 (2001) 29-44.

[137] I. Betova, M. Bojinov, T. Laitinen, K. Mäkelä, P. Pohjanne, T. Saario, The transpassive dissolution mechanism of highly alloyed stainless steels: I. Experimental results and modelling procedure, Corrosion Science, 44 (2002) 2675-2697.

[138] M. Bojinov, The ability of a surface charge approach to describe barrier film growth on tungsten in acidic solutions, Electrochimica acta, 42 (1997) 3489-3498.

[139] M. Bojinov, G. Fabricius, T. Laitinen, K. Mäkelä, T. Saario, G. Sundholm, Coupling between ionic defect structure and electronic conduction in passive films on iron, chromium and iron–chromium alloys, Electrochimica Acta, 45 (2000) 2029-2048.

[140] K. Leistner, C. Toulemonde, B. Diawara, A. Seyeux, P. Marcus, Oxide film growth kinetics on metals and alloys II. Numerical simulation of transient behavior, Journal of The Electrochemical Society, 160 (2013) C197-C205.

[141] D.R. Lide, CRC Handbook of Chemistry and Physics, 85th Edition, Taylor & Francis, 2004.

[142] J.W.T. Spinks, R.J. Woods, An introduction to radiation chemistry, Wiley, 1990.

[143] D. Janik, I. Janik, D.M. Bartels, Neutron and β/γ Radiolysis of Water up to Supercritical Conditions. 1. β/γ Yields for H2, H• Atom, and Hydrated Electron, The Journal of Physical Chemistry A, 111 (2007) 7777-7786.

[144] I. Draganic, The Radiation Chemistry of Water, Elsevier Science, 2012.

[145] J.H. O'Donnell, D.F. Sangster, Principles of Radiation Chemistry, Elsevier, 1970.

[146] M.A.J. Rodgers, Radiation chemistry: principles and applications, VCH Publishers, 1987.

[147] J. Wren, Steady-state radiolysis: effects of dissolved additives, in: Nuclear Energy and the Environment, ACS Publications, 2010, pp. 271-295.

[148] P.A. Yakabuskie, J.M. Joseph, J.C. Wren, The effect of interfacial mass transfer on steady-state water radiolysis, Radiation Physics and Chemistry, 79 (2010) 777-785.

[149] J.M. Joseph, B.S. Choi, P. Yakabuskie, J.C. Wren, A combined experimental and model analysis on the effect of pH and O_2 (aq) on γ-radiolytically produced H_2 and H_2O_2, Radiation Physics and Chemistry, 77 (2008) 1009-1020.

[150] L. Alrehaily, J. Joseph, M. Biesinger, D. Guzonas, J. Wren, Gamma-radiolysis-assisted cobalt oxide nanoparticle formation, Physical Chemistry Chemical Physics, 15 (2013) 1014-1024.

[151] L. Alrehaily, J. Joseph, A. Musa, D. Guzonas, J. Wren, Gamma-radiation induced formation of chromium oxide nanoparticles from dissolved dichromate, Physical Chemistry Chemical Physics, 15 (2013) 98-107.

[152] P. Yakabuskie, J. Joseph, P. Keech, G. Botton, D. Guzonas, J. Wren, Iron oxyhydroxide colloid formation by gamma-radiolysis, Physical Chemistry Chemical Physics, 13 (2011) 7198-7206.

[153] L. Alrehaily, J. Joseph, J. Wren, Radiation-Induced Formation of Chromium Oxide Nanoparticles: Role of Radical Scavengers on the Redox Kinetics and Particle Size, The Journal of Physical Chemistry C, 119 (2015) 16321-16330.

[154] L. Alrehaily, J. Joseph, J. Wren, Radiation-induced formation of Co_3O_4 nanoparticles from Co^{2+}(aq): probing the kinetics using radical scavengers, Physical Chemistry Chemical Physics, 17 (2015) 24138-24150.

[155] T. Sutherland, C. Sparks, J. Joseph, Z. Wang, G. Whitaker, T. Sham, J. Wren, Effect of ferrous ion concentration on the kinetics of radiation-induced iron-oxide nanoparticle formation and growth, Physical Chemistry Chemical Physics, 19 (2017) 695-708.

Chapter 3

Experimental Techniques and Procedures

This chapter describes the electrochemical methods, surface analysis techniques, solution analysis techniques and general experimental procedures used in this research. Any additional experimental details and information that are specific to each chapter are provided in the appropriate experimental sections of those chapters.

3.1 Electrochemical Techniques

3.1.1 Electrochemical cell setup

A standard three-electrode electrochemical cell design consisting of a working electrode (WE), a counter electrode (CE) and a reference electrode (RE) was used in this study (Figure 3-1). A potentiostat is used to control and measure the potential and current.
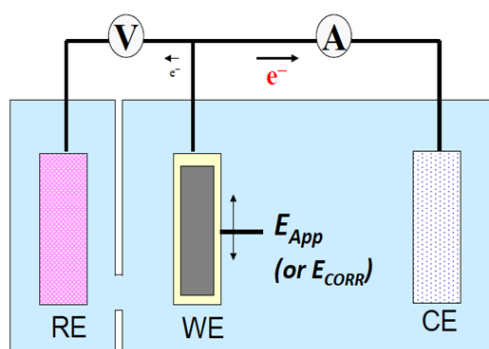
Figure 3-1: **Schematic of three-electrode electrochemical cell**

In the electrochemical cell the current of the reaction under investigation passes between the WE (the electrode of interest, in this case, Alloy 800) and the CE. The CE should

73

have high activity, negligible by-product production and a larger surface area compared to the working electrode. For these reasons platinum mesh is a common choice for the CE and was used in this work. The RE is a stable electrode of known potential against which the potential of the WE can be controlled or measured. In the potentiostat, the WE and RE are connected through a circuit with a high impedance voltmeter that ensures negligible current flows through the external measurement circuit between the WE and RE [1]. Therefore, the potential of the RE remains stable.

3.1.2 Linear Polarization Resistance (LPR) Measurements

The relationship between the applied potential and the corrosion current (I_{CORR}) when Wagner-Traude equation is applicable is known to be as following (Eq 2-8b).

$$I = I_{CORR} \left[exp \left(\frac{2.303\ (E - E_{CORR})}{\beta_a} \right) - exp \left(\frac{-2.303\ (E - E_{CORR})}{\beta_c} \right) \right] \tag{3-1}$$

where β_a and β_c are the anodic and cathodic Tafel slopes, respectively. Figure 3-2 shows the data for conditions that above equation is applicable [2].
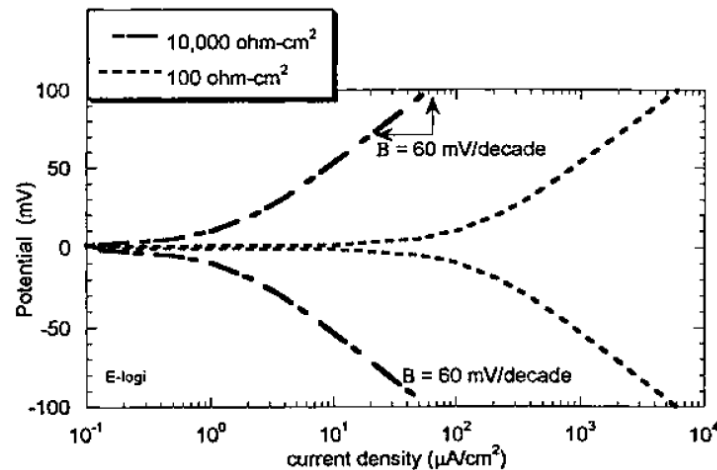
Figure 3-2: **E-log(i_app) data for two hypothetical corroding surfaces with two different resistances [2]**

74

If the applied potential is within the ±10 mV vs. E_{CORR}, according to Stern-Geary [3] the above Eq can be simplified to a linear relation expressing the kinetics of the charge transfer process as:

$$R_P = \left[\frac{\Delta E}{\Delta I_{APP}}\right]_{E-E_{CORR}\rightarrow0} = \left(\frac{\beta_a\,\beta_c}{2.303\,I_{CORR}\,(\beta_a + \beta_c)}\right) \tag{3-2}$$

where R_P is the linear polarization resistance and is inversely proportional to the corrosion current (rate).

3.2   Surface Analysis Techniques

A combination of spectroscopic techniques (Raman spectroscopy, X-ray Photoelectron spectroscopy, Auger electron spectroscopy) and scanning electron microscopy were used in this study to characterize the composition and morphology of the oxides formed on the metal substrate after electrochemical or radiation experiments. The principles behind these techniques are described below.

3.2.1   Raman Spectroscopy

Raman spectroscopy is a surface analytical method used to probe the composition of materials that are Raman active. The instrumentation of the Raman spectrometer consists of a laser source, a sample-illumination system and a suitable detector. The laser produces a beam of monochromatic light that passes through a sophisticated optical network in the spectrometer, which is designed to align, collimate and attenuate the power of the beam. A microscope is used to mount the sample on the stage and to locate and focus the laser beam on the areas of interest on the sample. When the beam strikes the sample, it can polarize it causing to emit photons that pass as a beam back into the optical network for detection and analysis [4]. A charge coupled device (CCD) array detector is used to detect the optical signals. The data from the CCD is read, stored, and processed by a computer.

The incident radiation is scattered by certain molecules and the scattered light is detected. Scattering involves a distortion of electrons distributed around a bond in a

molecule, followed by reemission of the radiation as the bond returns to its normal state. When this excitation occurs, the molecule can scatter the light elastically or inelastically. Most of the interaction results in elastic, or Rayleigh scattering. In this process, the molecule absorbs the incident photon, and is excited to a virtual energy state, but returns to the same ground vibrational state by re-emitting a photon with the same amount of energy as shown in Figure 3-3a. The molecule may also relax back to its original electronic state, but in a different vibrational or rotational state. This results in the emission of a photon with different energy than the incoming light. If the energy is lower than the incident photon energy, the shift in the frequency of light is called a Stokes shift (Figure 3-3b). If it is higher than the incident photon energy, it is called an Anti-Stokes shift [5, 6], Figure 3-3c.

3.2.2 **Scanning Electron Microscopy**

Scanning electron microscopy (SEM) is used for examination and analysis of microstructure and morphology. A high-resolution beam of electrons is directed onto the sample surface and the reflected electron intensity is measured and displayed on a cathode-ray screen to produce an image. The resolution of an image taken by SEM is much higher than that of an optical microscope, and images with a much greater depth of field are formed. Samples are analyzed in a vacuum chamber in order to give both incident and resulting scattered electrons free passage from the source to the sample and from the sample to the detector. The incident electrons typically have an energy ranging from a few hundred eV to 40 keV. They are focused by one or two condenser lenses into a beam with a very fine focal spot, typically sized from 0.4 to 5 nm in diameter. The beam passes through pairs of scanning coils or pairs of deflector plates which deflect the beam either horizontally or vertically so that a faster scan can be used to image a rectangular area of the sample [7, 8]. When the incident electron beam hits the surface, scattering and absorption cause energy loss of the incident beam within a certain volume of the sample, known as the interaction volume. This volume is dependent on the beam energy, and the atomic number and density of the atoms in the sample. Within this interaction volume, energy exchange between the beam and the sample takes place. High energy electrons from elastic scattering and lower energy secondary electrons formed by inelastic scattering can be detected. After suitable amplification, the

detected electrons can be used to modulate the intensity of the scanning image on display video screen.

(a) Virtual Energy State

$E_0 = h\nu$

$E = h\nu'$

1st Excited Vibrational State

$E_0 = E$

Ground Vibrational State

(b) Virtual Energy State

$E_0 = h\nu$

$E = h\nu'$

1st Excited Vibrational State

$E_0 > E$

Ground Vibrational State

(c) Virtual Energy State

$E_0 = h\nu$

$E = h\nu'$

1st Excited Vibrational State

$E_0 < E$

Ground Vibrational State
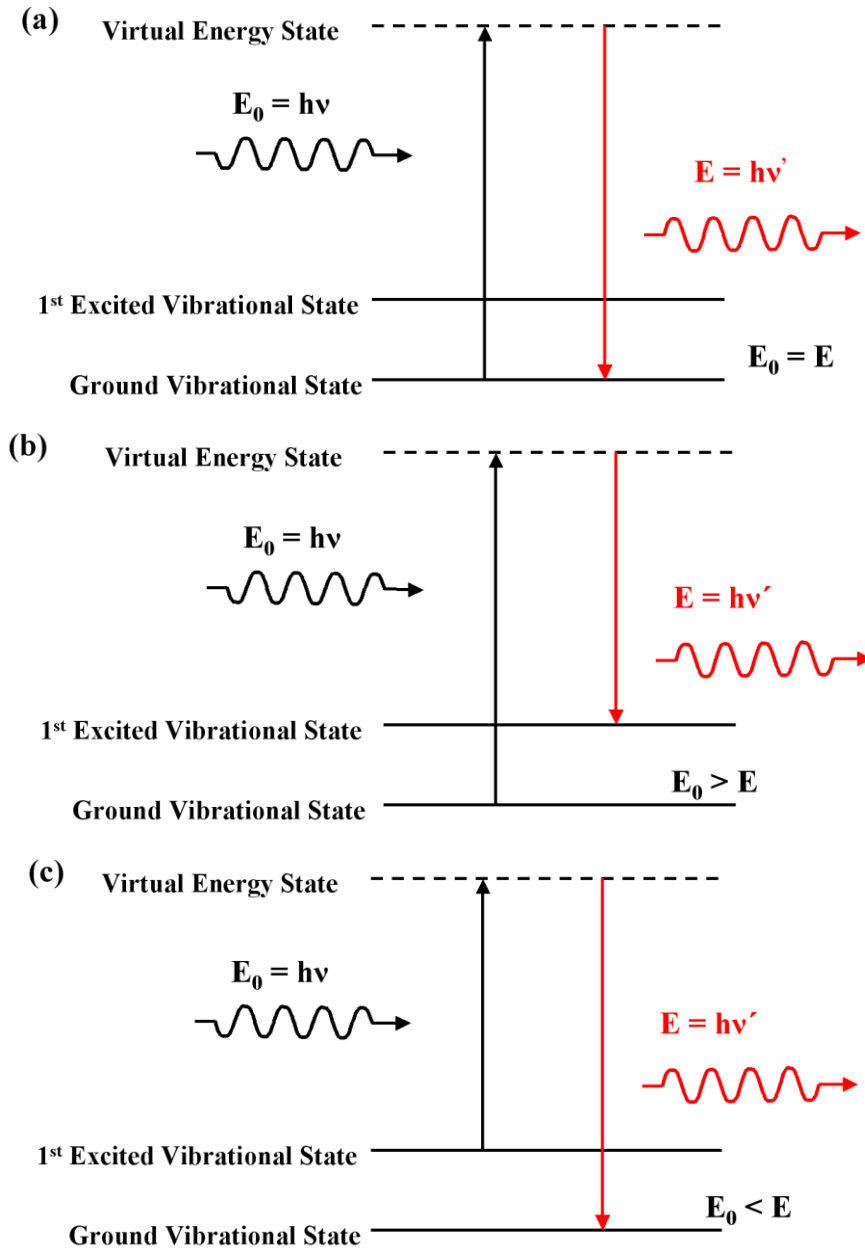
Figure 3-3: Illustration of Rayleigh Scattering (a), Stokes Scattering (b) and Anti-Stokes Scattering (c).

When a sample surface is subjected to a focused beam of electrons, various processes such as elastic and inelastic scattering can occur. Incident electrons can interact with the atoms on the surface of the sample and eject secondary electrons and photons (characteristic X-rays). These electrons are lower in energy than those in the incident beam (inelastic scattering), and only arise from the top few nanometers of the sample surface. Measurements of secondary electrons are used to study the sample topography and morphology. Due to varying distances from the detector, secondary electrons from areas of higher points on the sample surface are more likely to be detected than electrons from lower points. The varying signal strengths of the secondary electrons results in a brightness contrast in the image that gives the micrograph depth perspective.

Characteristic X-rays are used for elemental analysis. This technique is called energy dispersive X-ray spectrometry (EDX). Qualitative analysis involves the identification of the lines in the spectrum and is fairly straightforward owing to the simplicity of X-ray spectra [9].

Electrons from the elastic scattering of the beam with the specimen are called backscattered electrons. The escape depth of backscattered electrons can be greater than that of secondary electrons and consequently resolution of surface topographical characteristics can suffer. However, backscattered electrons have the advantage over secondary electrons that they are sensitive to the atomic mass of the nuclei they scatter from [8]. As a result, heavier elements which backscatter more efficiently appear brighter than lighter elements in a backscattered electron image. The combined use of both secondary and backscattered electron imaging modes provides valuable information not typically available through either imaging method alone.

Secondary electrons and backscattered electrons are commonly used for imaging samples: secondary electrons are most valuable for showing morphology and topography on samples and backscattered electrons are most valuable for illustrating contrasts in composition in multiphase samples.

3.2.3 **X-Ray Photoelectron Spectroscopy**

X-ray photoelectron spectroscopy (XPS) is a quantitative spectroscopic technique that can measure the elemental composition, chemical state, and electronic state of the elements within the first 1–30 monolayers of a surface. Because XPS only measures the properties of a few nm of a surface, it can be used to determine elemental composition as a function of depth by combining it with ion etching to progressively remove surface layers. Spectra are obtained by irradiating a sample with X-rays of known energy, hν, and causing photoelectrons, a core electron, to be emitted from the sample surface. The kinetic energies (KE) of the photoelectrons are related to the ionization energy (or binding energy, BE) of a particular element and the work function of the spectrometer, ϕ_{sp}, (typically 4-5 eV) by equation 3-3 [10],

$$KE = h\upsilon - BE - \Phi_{sp} \qquad\qquad (3\text{-}3)$$

Since the binding energy is characteristic of the element from which it was ejected, measurements of the photoelectron energy and can be used to identify all elements in the periodic table with the exception of He and H. A typical XPS spectrum is a plot of the measured photoelectron intensity as a function of the binding energy of the electrons detected. Each element produces a set of XPS peaks or lines at characteristic binding energy values. These peaks correspond to ejection of electrons from different orbitals of an atom and the binding energies correspond to energies of those orbitals (Figure 3-4). The peak locations and areas can be used (with appropriate sensitivity factors) to determine the composition of the surface. The shape of each peak and the binding energy can be slightly altered by the chemical environment of the emitting atom as well (e.g., oxidation state) [11]. The sizes of the peaks are directly related to the amount of a particular element within the sample volume that is irradiated.
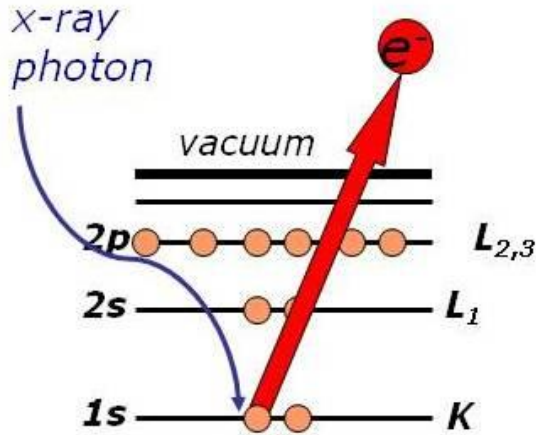
Figure 3-4: Schematic demonstrating the principles of XPS and the ejection of a photoelectron.

3.2.3.1   **XPS results analysis**

For the relative enrichments, the atomic fractions of Cr, Fe and Ni in the surface layer, $[M]_{surf}$, obtained from the survey spectra were first normalized for their atomic abundances in the alloy, $[M]_{bulk}$ to obtain the surface-to-bulk atomic ratios for individual elements. The surface-to-bulk atomic ratios, $[M]_{surf}/[M]_{bulk}$, were then compared to that of Cr, $[Cr]_{surf}/[Cr]_{bulk}$. The final ratio, $([M]_{surf}/[M]_{bulk})/([Cr]_{surf}/[Cr]_{bulk})$, represents the relative enrichment in the surface layer of element M with respect to Cr:

$$ER = \left(\frac{[M]_{surf}}{[M]_{bulk}}\right)\bigg/\left(\frac{[Cr]_{surf}}{[Cr]_{bulk}}\right) \tag{3-4}$$

This ratio is referred to as an enrichment ratio (ER) hereafter. The ER for the reference element, Cr is always 1.0, and a ratio less than 1.0 for Fe or Ni means that there is depletion of Fe or Ni, or conversely enrichment of Cr, in the surface layer, relative to the bulk alloy composition.

To obtain the composition of oxidation states, high resolution XPS spectra were deconvoluted using reference spectra taken from well-characterized powder samples. Detailed descriptions of binding energies and the spectral deconvolution method can be found elsewhere [11]. For chromium, contributions of Cr^0, Cr_2O_3, $Cr(OH)_3$ and Cr^{VI} to the Cr-2p spectra were considered. For iron those from Fe^0, FeO, Fe_3O_4 (mixed Fe^{II}/Fe^{III} oxide),

80

Fe_2O_3 and FeOOH to the Fe-2p spectra and for nickel those of Ni^0, NiO and $Ni(OH)_2$ to the Ni-2p spectra were considered. The distinguishing of metal oxide from metal hydroxide was further aided by deconvolution of the O-1s and C-1s spectra.

3.2.4 Auger Electron Spectroscopy

Auger electron spectroscopy (AES) is one of the most commonly used analytical techniques to measure the chemical composition of the first few monolayers of a surface. It can have a sensitivity on the order of 0.1 atomic % and a spatial resolution on the order of 10 nm [7]. Auger spectroscopy involves a three-electron process (Figure 3-5). This process is initiated by ejection of a core electron of an atom by incident high-energy electrons (typically with energy between 3 and 30 keV). The vacancy leaves the atom in an electronically excited state. The excited atom can lose energy in one of two ways. Firstly, an electron from a higher energy orbital drops down to fill the vacancy. This is accompanied by either the ejection of a photon of the appropriate energy, or by the ejection of another electron. Since the differences in energies of the orbitals involved are typically high, the ejected photon has a high energy (in the X-ray region). The measurement of these X-rays is known as X-ray fluorescence (XRF) spectroscopy. The kinetic energy of an ejected secondary electron (a so-called Auger electron) is also characteristic of the source atom. The Auger electron energy (E_{Auger}) is related to the electronic orbital energies of an atom by,

$$E_{Auger} = BE_b - E_b (L_1) - E_b (L_{23}) \tag{3-5}$$

where BE_b is the binding energy of the 1s orbital (core electron), while $E_b(L_1)$ and $E_b(L_{2,3})$ are the binding energies of the first and second outer orbitals, respectively. Since the atomic energy levels are characteristic of an atom, measurement of the energies of the X-rays and the Auger electrons can determine the atoms that are present. Like XPS, the Auger X-ray and electron energies can be influenced by the chemical environment of the atom and give information on properties like the oxidation state.

Similar to XPS, Auger spectroscopy can be used to analyze elemental composition as a function of depth by combining it with surface etching. For this technique bombardment

with a well-focused ion beam (Ar$^+$) to remove successive surface layers is used. After ablation each layer is analyzed for the individual components [10].
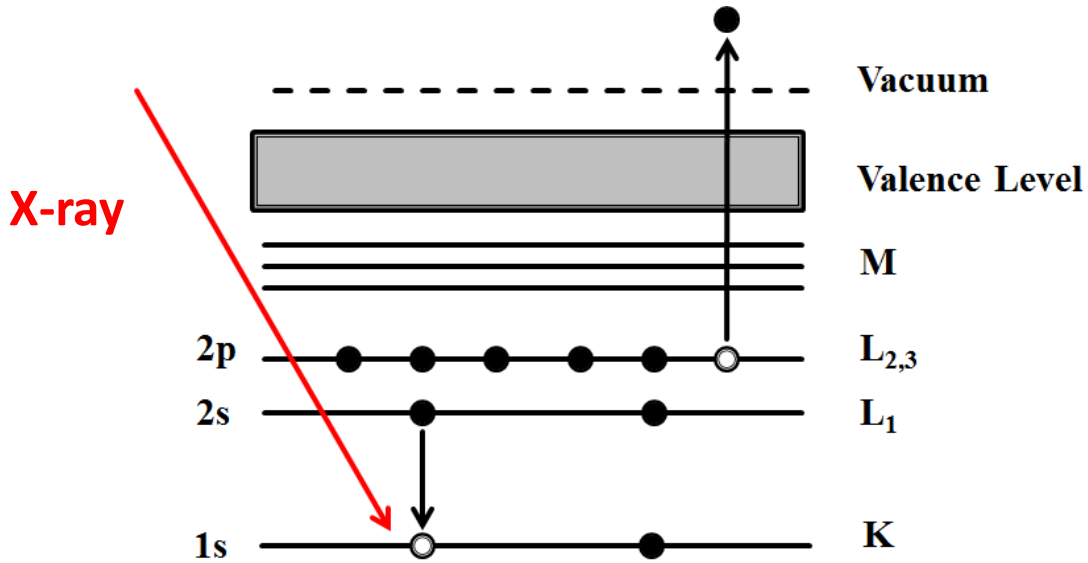
Figure 3-5: Schematic demonstrating the principles of AES and the ejection of an Auger electron.

3.3   Solution Analysis Techniques

The concentration of metal ions dissolved into the test solution after each experiment were determined using ICP-MS and ICP-OES techniques.

3.3.1   Inductively-Coupled Plasma Mass Spectrometry

Inductively-coupled plasma mass spectrometry (ICP-MS) combines a high temperature ICP (inductively-coupled plasma) source with a mass spectrometer to determine the levels of trace elements in a sample [12]. An ICP-MS system consist of four main processes: (1) sample introduction and aerosol generation, (2) ionization by an argon plasma source, (3) mass discrimination, and (4) ion detection [13], Figure 3-6. In the first phase, digested solutions are introduced by a peristaltic pump and nebulized in a spray chamber. The resultant aerosol particles are carried by a noble gas to a plasma region. In the plasma

region, inductive coupling of energy from a microwave power supply coil heats the gas stream to a temperature sufficiently high to vaporize and ionize the droplets creating plasma. The ionization inside the plasma produces both simple and complex (polyatomic) ions. These include dissociation products of water and the components of the solutes in a solution sample. The ions produced are extracted from the plasma into a mass spectrometer (frequently a small quadrupole unit). The ionic stream flows through the quadrupole mass spectrometer and is separated based on atomic mass. The selected ions are collected by a detector which provides an output signal. Based on the distribution of the mass fragments that are detected, the composition of the sample can be determined. The magnitude of the signal can be related to the quantity of the different compounds in the sample.
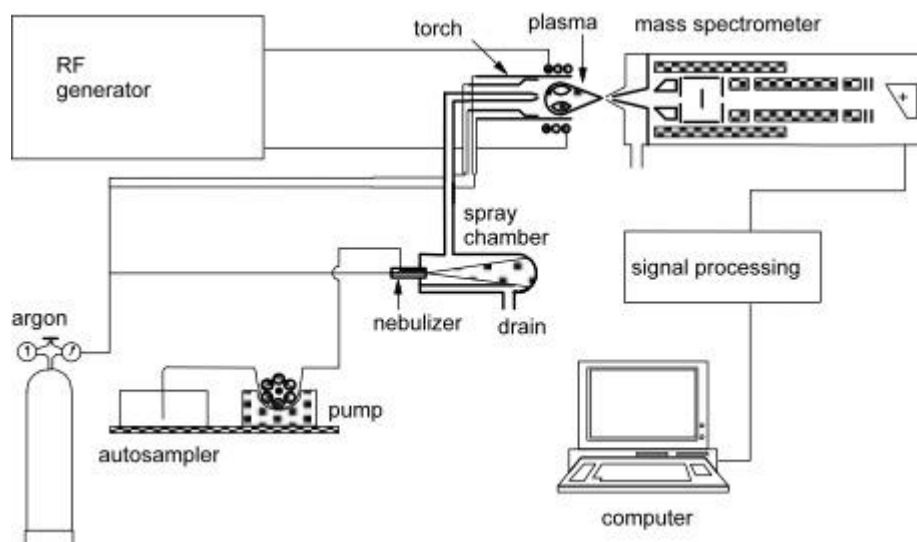
Figure 3-6: Illustration of inductively coupled plasma mass spectrometry (ICP-MS).

3.3.2 **Inductively-Coupled Plasma Optical Emission Spectrometry**

In ICP-OES, the light emitted by the excited atoms and ions in the plasma is measured to obtain information about the sample, Figure 3-7. Because the excited species in the plasma emit light at several different wavelengths, the emission from the plasma is polychromatic. This polychromatic radiation must be separated into individual wavelengths so the emission from each excited species can be identified and its intensity can be measured without interference from emission at other wavelengths.

83
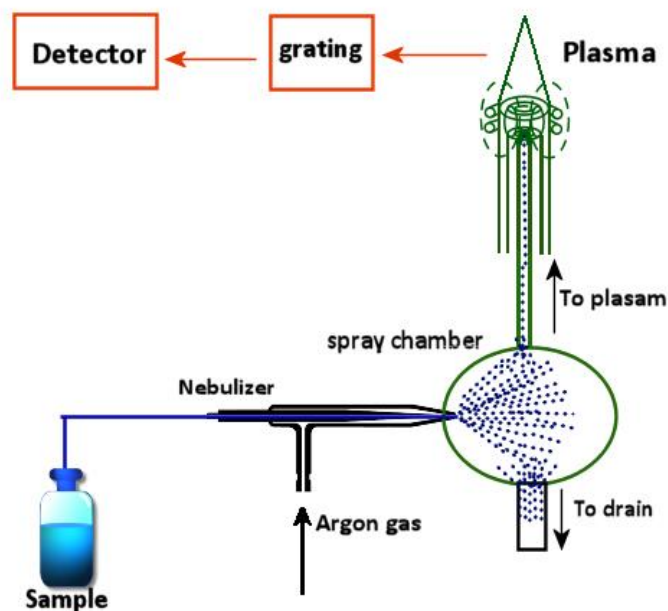
Figure 3-7: Illustration of inductively coupled plasma Optical Emission Spectrometry (ICP-OES).

The separation of light according to wavelength is generally done using a monochromator, which is used to measure light one wavelength at a time, or a polychromator, which can be used to measure light of several different wavelengths at once. The actual detection of the light, once it has been separated from other wavelengths, is done using a photosensitive detector such as a photo-multiplier tube (PMT) or advanced detector techniques such as a charge-injection device (CID) or a charge-coupled device (CCD) [14].

3.4 Experimental Procedures

3.4.1 Material and Solution Preparation

The working electrode in all experiments was Alloy 800 purchased from Goodfellow Inc. and had a composition (in wt.%) of Cr: 22, Ni: 32.5 and Fe: 43. A 10 mm diameter Alloy 800 rod was cut into cylindrical pieces. For the aqueous corrosion studies, these coupons

were 3 mm thick and 10 mm in diameter, giving each coupon a total surface area of 2.12 cm^2, and for the electrochemical studies the electrode was set in an epoxy resin within a polytetrafluoroetheylene (PTFE) cylinder so that only the flat front face (0.708 cm^2) was exposed to the electrolyte solution in the cell. Prior to each experiment, the working electrode was polished manually with 180, 400, 800 and 1200 grit silicon carbide papers. This was followed by polishing on a Texmet microcloth (Buehler) with a 1 μm MetaDi Supreme diamond paste suspension (Buehler) and lastly sonication in an acetone/methanol mixture for 5 min to remove polishing residues. The electrode was then rinsed with Type 1 water and dried with argon.

All solutions were prepared using water from a NANOpure Diamond UV ultrapure water system (Barnstead International) which removes dissolved organic and inorganic impurities. The resulting purified water had a consistent resistivity of 18.2 MΩ·cm. Borate buffer solutions (0.01M) were prepared using $Na_2B_4O_7$ (analytical grade, EMD Inc.). The solution pH was adjusted to 10.6 by adding the required amount of 2 M sodium hydroxide (NaOH) solution and pH 6.0 and 8.4 by adding boric acid (H_3BO_3, analytical grade, Caledon Laboratories Ltd.). All solutions were purged with argon gas for an hour prior to the electrochemical tests.

3.4.2 Electrochemical Setup

The Electrochemical tests at room temperature and 80 ^{o}C were carried out using a standard 3-electrode electrochemical cell (Figure 3-8). The working electrode used was the Alloy 800 sample under study; the counter electrode was a platinum mesh, and the reference electrode was saturated calomel electrode (SCE) for room temperature and saturated Ag/AgCl for 80 ^{o}C tests, respectively. The working electrode was cathodically cleaned for 5 minutes prior to the start of an experiment. This cleaning process helps to get rid of any organic compounds on the sample's surface. For all the experiments, the borate buffer solution was purged with argon gas for an hour to remove the oxygen in the solution.

A Solartron potentiostat (either model 1480 or 1287) and a Solartron model 1252 frequency response analyzer were used in all electrochemical measurements. Corrware™

and Zplot™ software (Scribner and Associates) were used for experiment control and data analysis.
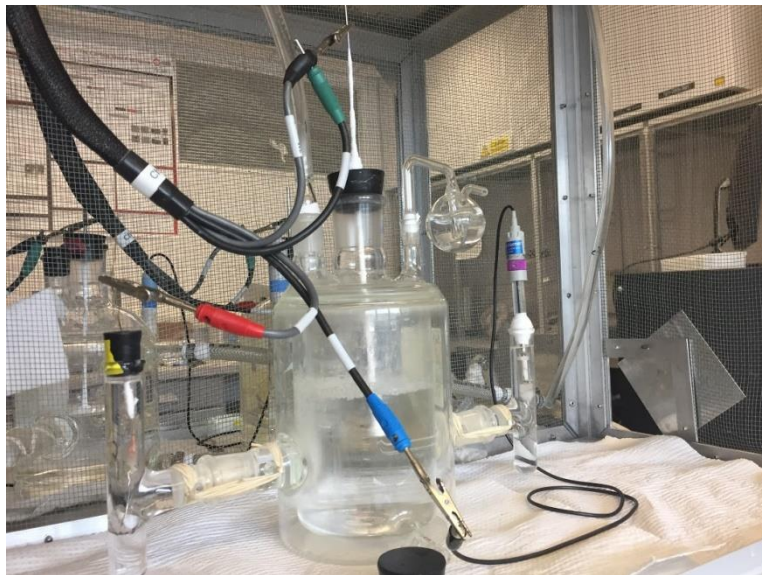
Figure 3-8: Standard three-electrode electrochemical cell.

For the electrochemical experiments at temperature $T \geq 100$ °C, an autoclave made of stainless steel 316L equipped with a high temperature reference electrode, a titanium rod for WE connection and a platinum mesh for CE were used (Figure 3-9). The design of the cell is similar to that of the low temperature cell. An Ag/AgCl electrode was used for unirradiated tests at 80 °C $\leq T \leq$ 250 °C. For electrochemical tests performed under radiation a Hg/HgO reference electrode (Radiometer Analytical) in a 1.0 M KOH solution was employed. The Hg/HgO electrode has been found to be more resistant to radiation than either the SCE or Ag/AgCl electrodes. It has a potential of 0.112 V vs. a standard hydrogen electrode (SHE). All potentials measured in these tests are adjusted to the SCE scale (0.242 V vs. SHE).

Figure 3-9: Electrochemistry autoclave used for experiments above 100 °C

3.4.2.1 **High-Temperature reference electrode**

For high temperature electrochemistry, a high temperature/high pressure saturated external Ag/AgCl reference electrode was used. The part of the reference electrode that contains Ag wire (reference electrode) was continuously cooled by a fan during the experiment to make sure the reference electrode remained at room temperature.

Bogaerts (2016) [15] proposed the following equation for potential conversion:

$$E_{SHE}{}^{T} = E_{meas} + E_{correction} \tag{3-6a}$$

$$E_{correction} = E_{Ag/AgCl}{}^{25\ \circ C} - [70 + 1.20\ (\Delta T - 75)]\ (mV) \tag{3-6b}$$

At which $E_{SHE}{}^{T}$ is the potential vs. standard hydrogen electrode at temperature T, E_{meas} is the potential measured by the instrument, $E_{correction}$ is the correction potential (taking into account all the thermal liquid junction phenomena), determined as a function of the

87

temperature difference ($\Delta T = T - 25\ °C$) across a cooled salt bridge and $E_{Ag/AgCl}^{25\ °C}$ is the potential of the Ag/AgCl electrode at 25 °C. The author showed the validity of this conversion over a range of pH (7 - 10.5) and up to 4 M KCl.

Bratsch (1989) [16], You, et al., (2010) [17] showed that the standard potential for hydrogen reduction reaction does not change with temperature. Thus:

$$E_{SHE}^{T} = E_{SHE}^{25\ °C} \tag{3-7}$$

and the difference between the saturated calomel electrode (SCE) and SHE is presented as:

$$E_{SHE}^{25\ °C} = E_{SCE}^{25\ °C} - 242\ (\text{mV}) \tag{3-8}$$

The measured potential at temperature T using the high temperature-high pressure saturated external Ag/AgCl reference electrode can be converted to the $E_{SCE}^{25\ °C}$ using equations 3-6 to 3-8.

3.4.3 Radiation exposure tests

All radiation experiments were conducted in a MDS Nordion Gammacell 220 Excel Cobalt-60 irradiator. The autoclave was positioned inside the gamma cell sample chamber, and the chamber lowered into the irradiation zone, centred within a cylinder bounded by 11 tubular pencils containing ^{60}Co.

The ^{60}Co radiation source has a half-life of 5.3 years and emits two characteristic γ-photons with energies of 1.332 MeV and 1.173 MeV [6].

$$^{60}\text{Co} \rightarrow\ ^{60}\text{Ni} + 2\ \gamma\text{-photons} + \beta\text{-particle} \tag{3-9}$$
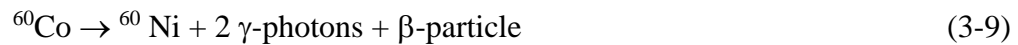
A β-particle is also emitted with energy of 0.318 MeV, but this particle is easily blocked from entering the irradiation chamber by the metal shielding around the chamber. The absorbed radiation dose rate in the irradiation chamber during the experiments was 3.1-3.3 kGy·h^{-1}, where 1 Gy = 1 J absorbed per kg of water, determined using Fricke Dosimetry.

3.4.3.1 **Fricke Dosimetry**

A Fricke dosimeter is a chemical dosimeter used to quantify the amount of energy deposited by ionizing radiation in the irradiated system. The Fricke dosimeter consists of an aerated solution of 1 mM $FeSO_4$ under acidic conditions (0.4 M H_2SO_4). Under these conditions, Fe^{2+} will be oxidized to Fe^{3+} by the oxidizing radiolysis products as shown in the reaction scheme below (Figure 3-10).
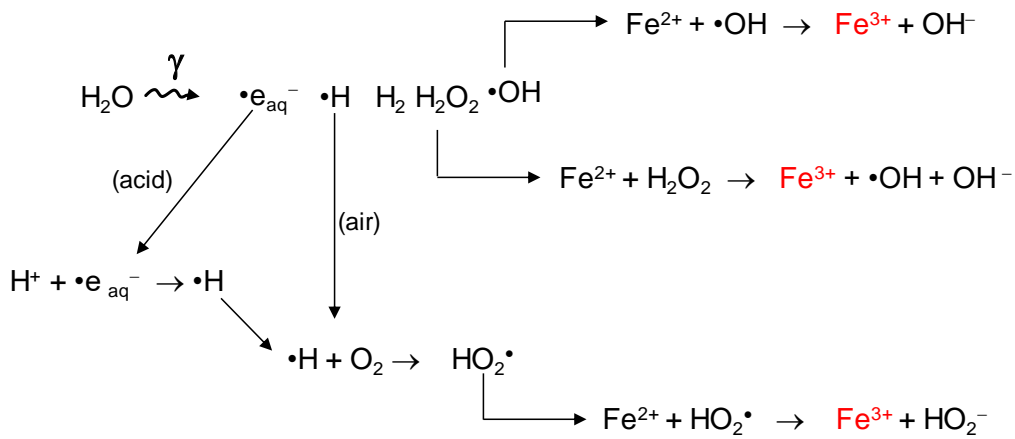
Figure 3-10: Schematic representation of the reactions occurring during Fricke dosimetry.

The rate of oxidation of Fe^{2+} to Fe^{3+} is determined by the rate of generation of the oxidizing radiolysis products. A known volume of the Fricke solution is irradiated using the gamma cell for a fixed amount of time (60 s). The amount of Fe^{3+} produced is determined by measuring the absorbance at 304 nm and the dose is calculated from Eq 3-16.

$$Dose(Gy) = \frac{9.648*10^6*\Delta A_{304}}{\varepsilon_{304}l\rho G(products)} \qquad (3\text{-}10)$$

where ΔA_{304} is the difference in the absorbance of the irradiated sample and a sample that was not irradiated, ε_{304} is the molar extinction coefficient of Fe^{3+} at 304 nm, l is the length of the UV-Vis cuvette that the light passes through, ρ is the density of the dosimeter solution (1.024 g/cm^3), $G(products)$ is the known dose required (15.5) to generate the

species necessary to produce the observed [$Fe^{3+}_{(aq)}$], t is time, and 9.648×10^6 is a proportionality constant [18].

3.4.4 Coupon exposure experiments at T ≥ 150 °C

For coupon exposure experiments the test samples were prepared inside an argon-filled glove box. The freshly polished coupons were held on a specially designed sample holder in quartz vials (for experiment performed at T ≥ 150 °C) and the desired volume of argon-purged buffer solution was added to the vials. The coupons were fully immersed in the solution and the vials were capped under argon with PTFE septa. The sample vials were placed in a 300 mL AISI 316 stainless steel autoclave purchased from Parr Instrument Company. The autoclave was heated to the desired temperature before being lowered into the irradiation zone.

The corrosion studies in saturated steam at 285 °C were carried out in a 300 mL AISI 316 stainless steel autoclave. The test specimens were arranged in a pre-oxidized zirconium specimen holder. At the time of closure, the autoclave contained 20 mL (only 7% of the autoclave volume) of liquid Type 1 water (Barnstead International NANOpure Diamond UV, 18.2 MΩ·cm) to ensure no exposure of the test specimen to the condensed phase during the experiments. The gaseous headspace of the vessel was filled with either ultra-high purity Ar (99.999%, Praxair), 35% O_2 + 65% Ar or a 50% O_2 + 65% Ar mixture (Praxair), which was introduced by sparging within the partially closed vessel for 90 min before the autoclave was sealed. The experiments were carried out either during exposure to gamma-radiation or without radiation on the lab bench. The duration of each exposure was 5 h.

3.4.5 Post-test surface analysis

The surfaces of test coupons or working electrodes were analyzed by SEM, XPS, and AES after each electrochemical experiment or coupon exposure test under irradiation. A LEO (Zeiss) 1540XB focused ion beam (FIB)/SEM/EDX was used to examine the morphology and carry out quantitative analysis of the surfaces. The chemical compositions of the surface layers were determined from XPS spectra acquired using a KRATOS Axis Nova spectrometer using monochromatic Al K(α) radiation and operating at 210 W, with a

base pressure of 10^{-8} Pa. The analysis depth of this instrument was approximately < 9 nm. The analysis spot size was typically 400 µm × 700 µm and both low-resolution (or survey spectra) and high-resolution spectra were obtained. The survey spectra were recorded with a pass energy of 160 eV to verify spatial composition and cleanliness. High resolution spectra were obtained using a pass energy of 20 eV and a step size of 0.05 eV over the, Ni $2p_{3/2}$ (852.6 ± 10.6 eV), Cr $2p_{3/2}$ (582.4 ± 12.6 eV), Fe $2p_{3/2}$ (720.0 ± 20.0 eV), O 1s (532.0 ± 8.0 eV), and C 1s (286.7 ± 8.5 eV) regions (calibration set point of 284.8 eV from adventitious carbon) [10]. The high-resolution spectra were deconvoluted using standard peaks generated from reference materials. All XPS spectral analyses were performed using CasaXPS software (version 2.3.14).

Raman scattering measurements were performed using a Renishaw model 2000 Raman spectrometer (Renishaw PLC, UK), equipped with a MellesGriot 35 mW HeNe laser with an excitation wavelength of 633 nm and a focused beam of ~2 µm diameter. The laser power was reduced to 25% to avoid laser-heating effects, since small changes in temperature can easily produce minor changes in the frequency and width of Raman lines.

AES combined with argon ion sputtering provided a depth profile of the chemical composition of surface oxides. Auger spectra were obtained using a Phi 660 AES instrument with excitation energy of 5 keV and sputtering was accomplished using an Ar^+ ion beam. The AES scans for Fe, Cr, Ni, C, and O were performed as a function of sputter time. The AES intensities were calibrated using standard samples under the same sputtering conditions to convert the measured intensities into mole fractions and the sputter time into sputter depth. The sputter rate used for this study was 9 nm·min^{-1} for thin oxides and 30 nm·min^{-1} for thicker oxides.

3.4.6 Solution Analysis

The test solutions from each coupon exposure test (8.5 ml) were collected after each experiment for solution analysis. ICP-MS and ICP-OES were used to measure the amount of dissolved Fe, Ni and Cr in solution after each corrosion test. The detection limits of the ICP mass spectrometer for Fe, Ni and Cr were 10 µg·L^{-1}, 2.5 µg·L^{-1} and 0.2 µg·L^{-1} respectively.

The detection limits of the ICP-OES for Fe, Ni and Cr were 2 $\mu g \cdot L^{-1}$, 5 $\mu g \cdot L^{-1}$ and 2 $\mu g \cdot L^{-1}$, respectively. The pHs of the solutions were also measured after each experiment.

3.3. References

[1] K.J. Vetter, Electrochemical kinetics : theoretical and experimental aspects, Academic Press, 1967.

[2] R.G. Kelly, J.R. Scully, D. Shoesmith, R.G. Buchheit, Electrochemical techniques in corrosion science and engineering, CRC Press, 2002.

[3] M. Stern, A.L. Geary, Electrochemical polarization I. A theoretical analysis of the shape of polarization curves, Journal of the electrochemical society, 104 (1957) 56-63.

[4] D.A. Skoog, F.J. Holler, S.R. Crouch, Principles of Instrumental Analysis, Thomson Brooks/Cole, 2007.

[5] R.L. McCreery, Raman Spectroscopy for Chemical Analysis, Wiley, 2005.

[6] E. Smith, G. Dent, Modern Raman Spectroscopy: A Practical Approach, Wiley, 2013.

[7] J. O'Connor, B.A. Sexton, R.S.C. Smart, Surface Analysis Methods in Materials Science, Springer, 2003.

[8] R.F. Egerton, Physical Principles of Electron Microscopy: An Introduction to TEM, SEM, and AEM, Springer International Publishing, 2016.

[9] D. Bell, A. Garratt-Reed, Energy Dispersive X-ray Analysis in the Electron Microscope, Taylor & Francis, 2003.

[10] J.T. Grant, Analysis of surfaces and thin films by using auger electron spectroscopy and X-ray photoelectron spectroscopy, Journal of the Korean Physical Society, 51 (2007) 925-932.

[11] M.C. Biesinger, B.P. Payne, A.P. Grosvenor, L.W. Lau, A.R. Gerson, R.S.C. Smart, Resolving surface chemical states in XPS analysis of first row transition metals, oxides and hydroxides: Cr, Mn, Fe, Co and Ni, Applied Surface Science, 257 (2011) 2717-2730.

[12] F. Vanhaecke, P. Degryse, Isotopic analysis: fundamentals and applications using ICP-MS, John Wiley & Sons, 2012.

[13] A. Montaser, Inductively Coupled Plasma Mass Spectrometry, Wiley, 1998.

[14] C.B. Boss, K.J. Fredeen, Concepts, instrumentation and techniques in inductively coupled plasma optical emission spectrometry, Perkin Elmer Norwalk, 1999.

[15] W.F. Bogaerts, Reference Electrodes for electrochemical measurements in high-temperature high-pressure aqueous environments—Review of potential corrections for 'external' reference systems, Electrochimica Acta, 212 (2016) 102-112.

[16] S.G. Bratsch, Standard electrode potentials and temperature coefficients in water at 298.15 K, Journal of Physical and Chemical Reference Data, 18 (1989) 1-21.

[17] H.-X. You, H.-B. Xu, Y. Zhang, S.-L. Zheng, Y.-Y. Gao, Potential—pH diagrams of Cr-H_2O system at elevated temperatures, Transactions of Nonferrous Metals Society of China, 20 (2010) s26-s31.

[18] A. Mozumder, Fundamentals of Radiation Chemistry, Elsevier Science, 1999.

Chapter 4

Effects of pH and γ-Radiation on Corrosion of Alloy 800 in Deaerated Borate Buffer at Ambient Temperatures

4.1   Introduction

Nickel-chromium-iron alloys such as Alloy 800 are used in nuclear power plant components such as thin-walled heat exchange tubing and piping [1]. In nuclear reactors these alloys are exposed to γ-radiation and a range of water chemistries [2]. Corrosion of these alloys can release dissolved metal ions into the coolant. Corrosion products released into the reactor coolant circulate through the reactor core and can be deposited on surfaces in the reactor core where they can be neutron activated producing radioactive species. If these radioactive species become re-suspended in the coolant, they can migrate out of the core and deposit on piping and components located outside the biological shield of the reactor core where they will pose a radiological hazard to plant workers.

When exposed to gamma radiation water decomposes to produce redox-active species which can interact very effectively with metallic corrosion products, changing their oxidation states. The solubility of hydrated metal species varies considerably depending on their oxidation state and pH. This study investigates the effect of pH and gamma radiation on the corrosion of Alloy 800 in deaerated water at ambient temperatures (room temperature and 80 °C).

4.2   Experimental

Two sets of tests, coupon-exposure tests and electrochemical tests, were performed to investigate the combined effects of pH and γ-radiation on Alloy 800 corrosion. The setup and the analyses performed in these tests are schematically illustrated in Figure 4-1. The tests were conducted primarily at 80 °C but some were conducted at room temperature (normally

21 °C). The solutions in all of the tests were 0.01 M sodium borate ($Na_2B_4O_7.10H_2O$) purged with argon.
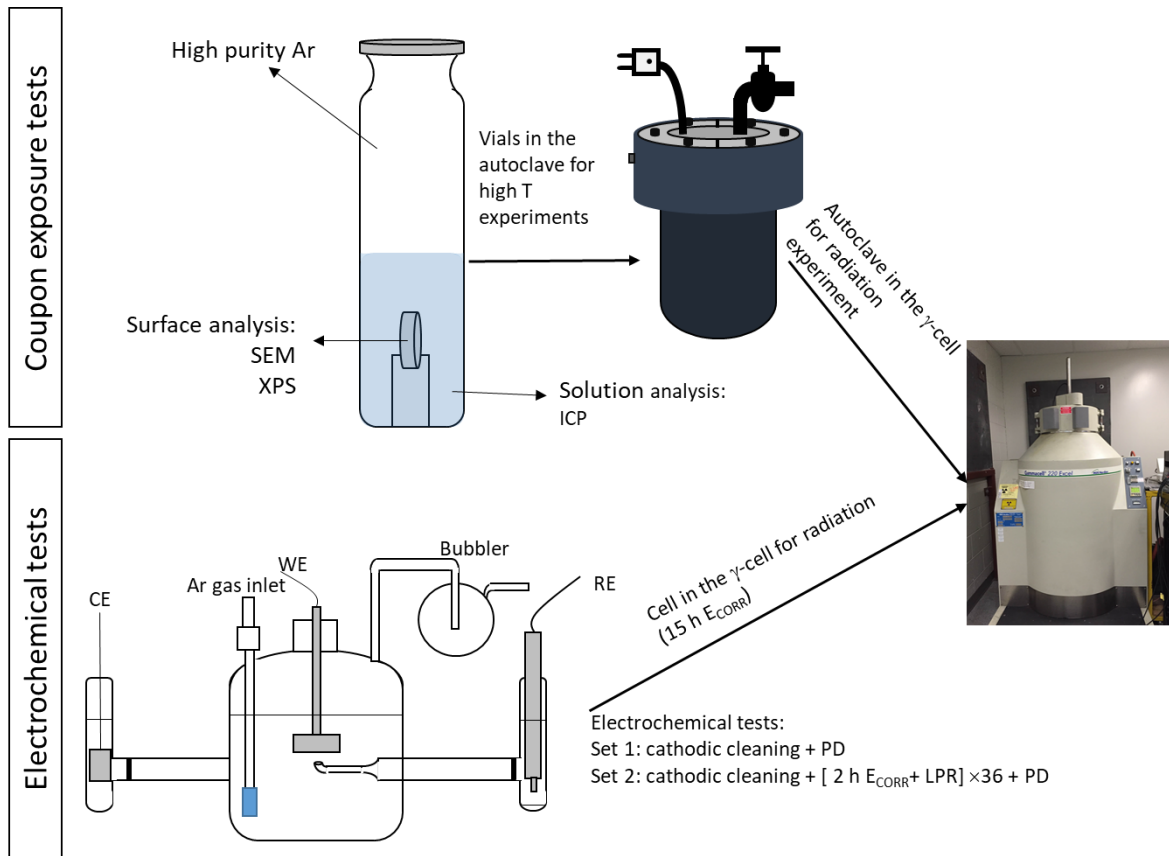
Figure 4-1: **Schematic of the experimental setup for the study on the effects of pH and γ-radiation on Alloy 800 corrosion at 21 °C and 80 °C.**

The coupon exposure test cell was assembled in an Ar-purged glove box as described in Chapter 3. A polished coupon with 2.5 cm^2 total surface area was fully immersed in a 8.5 mL solution in a sealed quartz vial. The vial was then placed in an autoclave. The autoclave assembly was heated to 80 °C, and the corrosion test began. For irradiation tests the autoclave heated to 80 °C was placed in the Cobalt-60 γ-irradiator (MDS Nordion Gammacell 220 Excel). After 3-d coupon exposure test either with or without radiation present, post-test analyses were performed for the solution and the coupon surface. The solutions were analyzed for dissolved metal ions using inductively-coupled plasma mass spectrometry (ICP-MS). The morphology of the coupon surface was examined by scanning electron microscope (SEM), and the distribution and oxidation states of the three metal elements in the top ~ 8

nm surface layer was investigated by X-ray photoelectron spectroscopy (XPS). A detailed description of these techniques is given in Chapter 3.

The electrochemical analyses performed in this study were open-circuit potential (E_{CORR}), linear polarization resistance (LPR) and potentiodynamic polarization (PD) measurements. These analyses were carried out in a 3-electrode electrochemical cell. For the electrochemical tests the Alloy 800 working electrode with surface area of 0.785 cm^2 was exposed to the deaerated solution containing 0.01 M sodium borate. The preparation of the electrodes, electrolyte solutions, and the set-up of the electrochemical cell are described in detail in Chapter 3.

Prior to each electrochemical measurement, the working electrode was cathodically cleaned for 5 min to remove any air-formed oxides or any organic impurities from the alloy surface. This was followed by either E_{CORR} measurement for 72 h or by performing a potentiodynamic scan. The PD scan was performed over the potential range from the cleaning potential to a sufficiently high anodic potential (higher than the range of corrosion potential) with a scan rate of 1 mV/s. The E_{CORR} measurement was interrupted periodically (every 2 h) to carry out an LPR measurement. The linear polarization was carried out in the potential range of ±10 mV vs. E_{CORR}. After the E_{CORR} /LPR measurements, a PD scan was performed from (E_{CORR} − 0.3 V) to a potential above E_{CORR} with a scan rate of 1 mV/s.

4.3   Results

4.3.1   3-d Coupon Exposure Tests

Figure 4-2 compares the dissolved metal concentrations and the morphologies of the corresponding surfaces. For corrosion without γ-radiation present, the dissolved concentration of a given metal element depends on pH. Each metal element has a different pH dependence; the dissolved concentration of Cr increases with an increase in pH, that of Fe is nearly independent of pH, while that of Ni is at its minimum at pH 8.4.

Gamma-radiation increases the dissolved concentrations of all three metals at all three pHs, except for the case of Fe at pH 6.0. With γ-radiation the pH dependence of dissolved concentration also varies with metal. The dissolved concentration of Cr shows the same pH dependence as that observed without radiation. However, those of Fe and Ni are different; with radiation present the concentration of Fe increases with pH, while that of Ni decreases.

The SEM micrographs of the corresponding surfaces show that the surface of the coupon corroded for 3 d at pH 6.0 with radiation present is smoother, and the number density of granular particles deposited on the surface is lower, than those corroded without γ-radiation. The higher dissolved Ni concentration and the smoother surface indicates that the 3-d corrosion of Alloy 800 at pH 6.0 involves primarily metal dissolution with negligible formation of oxide/hydroxide deposits, and that γ-radiation predominantly increases Ni dissolution. The observation of the lower dissolved Fe concentration and the higher number density of granular particles at pH 6.0 without than with radiation indicates that the granular particles may be formed by precipitation of Fe ions dissolved at earlier times – see discussion in 4.3.

The surface of the coupon corroded for 3 d at pH 10.6 without radiation present is very smooth, smoother than the surfaces corroded at pH 6.0 and pH 8.4. However, the surface of the coupon corroded at pH 10.6 with radiation present is covered extensively with oxide particles. The smoother surface and the significantly lower dissolved Ni concentration at pH 10.6 than at the two lower pHs without than with radiation present indicate that the oxide on the surface at pH 10.6 is uniform and compact. The earlier formation of a uniform and compact oxide layer suppresses Ni dissolution early, lowering the overall Ni dissolution over 3 d. The higher dissolved Fe and Cr but the lower dissolved Ni concentrations, combined with the higher density of granular particles, suggest that γ-radiation at pH 10.6 may promote the formation of an underlying uniform and compact oxide layer. Alloy 800 corrosion at pH 8.4 with or without radiation present shows a behaviour somewhere between those observed at pH 6.0 and pH 10.6.
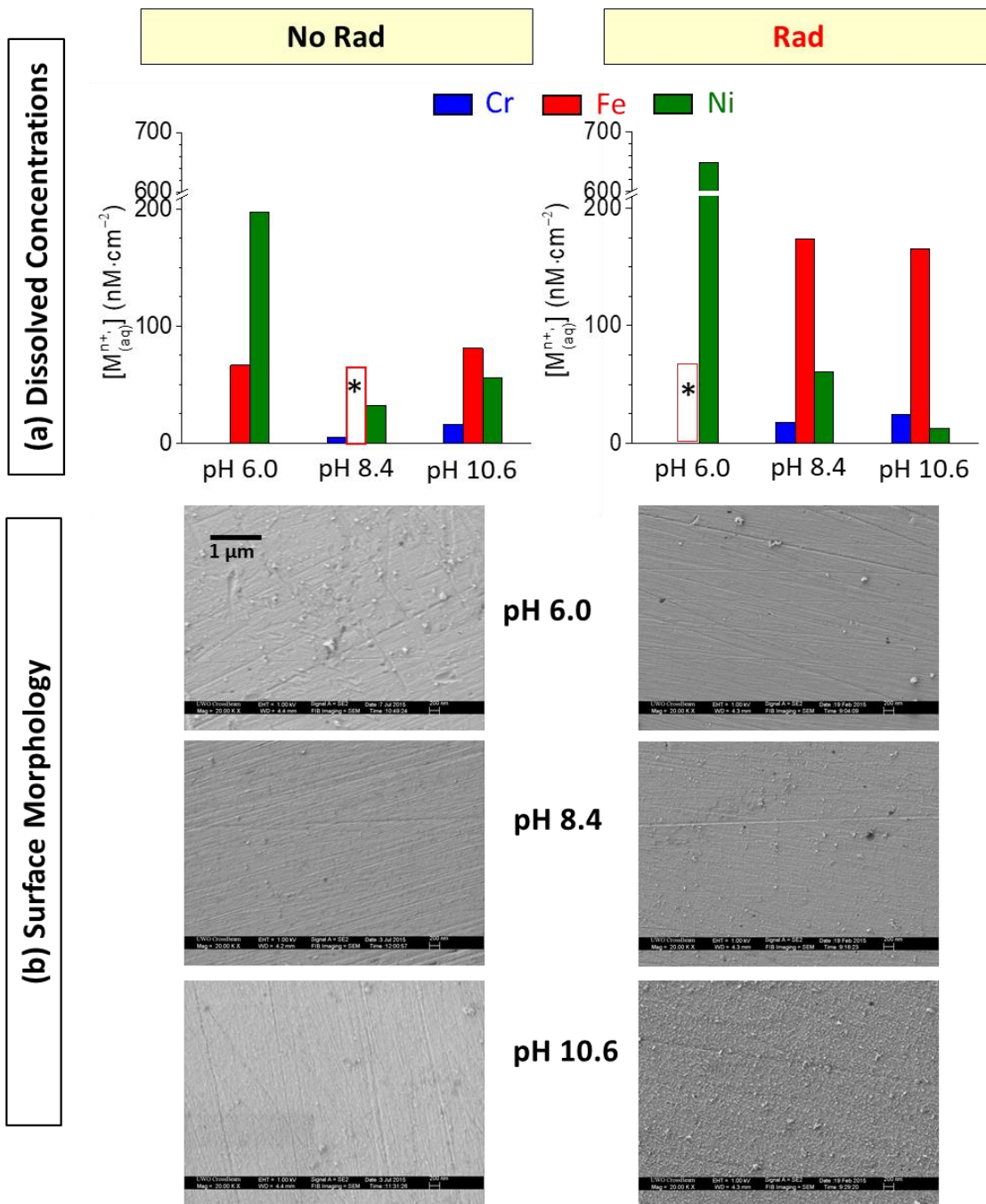
Figure 4-2: **(a) Dissolved concentrations of Cr, Fe and Ni species determined by ICP-MS analysis and (b) SEM micrographs of the surfaces of the corresponding coupons. These results were obtained after 3-d corrosion of the coupons in Ar-purged solutions at three different pHs with or without γ-radiation present (labeled as Rad and No Rad, respectively). Fe dissolved concentration marked with * for pH 8.4 No Rad and pH 6.0 Rad were below the detection limit (10 μg/l).**

The top 8 nm surface layers were investigated by XPS. Both the low-resolution survey spectra over a wide binding energy range of 0 to 1200 eV and the high-resolution spectra over the binding energy ranges of Cr-2p$_{3/2}$, Fe-2p$_{3/2}$, Ni-2p$_{3/2}$, O-1s and C-1s were taken. Examples of the raw XPS spectra are shown in Figure 4-3. The survey spectra were used to determine the relative enrichments of metal elements in the surface layer. The high-resolution spectra of different elements were used to determine the composition of individual metals and their oxidation states in the top layer.

For the relative enrichments, the atomic fractions of Cr, Fe and Ni in the surface layer obtained from the survey spectra ($[M]_{surf}$ where M = Cr, Fe or Ni) were first normalized for their atomic abundances in the alloy phase ($[M]_{bulk}$) in order to obtain the surface-to-bulk atomic ratios for individual elements. The surface-to-bulk atomic ratios ($[M]_{surf}/[M]_{bulk}$) were then compared to that of Cr ($[Cr]_{surf}/[Cr]_{bulk}$). The final ratio, ($[M]_{surf}/[M]_{bulk}$) to ($[Cr]_{surf}/[Cr]_{bulk}$), represents the relative enrichment of element M with respect to Cr:

$$ER_{M/Cr} = \left(\frac{[M]_{surf}}{[M]_{bulk}}\right) \Big/ \left(\frac{[Cr]_{surf}}{[Cr]_{bulk}}\right) \qquad \text{where M = Cr, Fe, or Ni} \qquad (4\text{-}1)$$

This ratio is referred to as simply enrichment ratio ($ER_{M/Cr}$) hereafter. The $ER_{Cr/Cr}$ of the reference element, Cr, is always 1.0. An enrichment ratio for Fe or Ni ($ER_{Fe/Cr}$ or $ER_{Ni/Cr}$) less than 1.0 means that there is depletion of Fe or Ni, or conversely enrichment of Cr in the surface layer, relative to the bulk alloy composition. An $ER_{Fe/Cr}$ or $ER_{Ni/Cr}$ value higher than 1.0 means enrichment of Fe or Ni, or conversely depletion of Cr, in the surface layer relative to the bulk alloy composition.
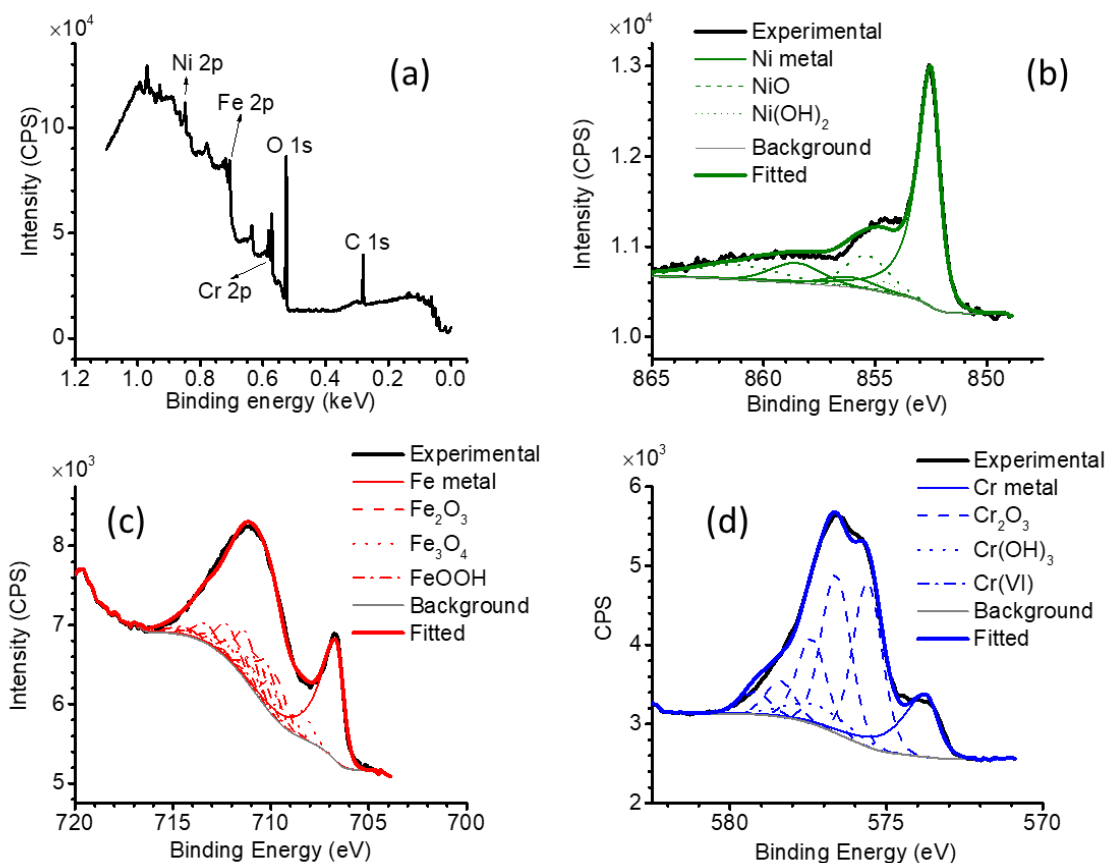
Figure 4-3: XPS spectra taken from an Alloy 800 surface corroded for 3 d in deaerated water at pH 6.0 at 80 °C under γ-irradiation: (a) the survey spectrum in the binding energy range of 0 to 1200 eV, and the high-resolution spectra of (b) the Ni $2p_{3/2}$ band, (c) the Fe $2p_{3/2}$ band and (d) the Cr $2p_{3/2}$ band. The high-resolution spectra also show the deconvoluted spectra of individual components, each consisting of multiple peaks.

The relative enrichment analysis results are compared with the corresponding dissolved metal concentrations in Figure 4-4. Also shown in Figure 4-4 are the composition of oxidation states of individual metal elements obtained by deconvoluting the high-resolution XPS using the reference spectra of standard oxide powder samples. Detailed descriptions of binding energies and the spectral deconvolution method can be found elsewhere [3]. For chromium, contributions of Cr^0, Cr_2O_3, $Cr(OH)_3$ and Cr^{VI} to the Cr-$2p_{3/2}$ spectra were considered. For iron, those of Fe^0, FeO, Fe_3O_4 (mixed Fe^{II}/Fe^{III} oxide), Fe_2O_3 and FeOOH to the Fe-$2p_{3/2}$ spectra and for nickel those of Ni^0, NiO and $Ni(OH)_2$ to the Ni-$2p_{3/2}$ spectra were considered. The determination of the oxide and hydroxide fractions was

further aided by deconvolution of the O-1s and C-1s spectra (results not shown). Examples of the deconvoluted spectra and their composite spectra are compared with the observed spectra in Figure 4-3.

After 3-d corrosion at pH 6.0 without radiation present, the dissolved concentration is largest to smallest in the order of Ni, Fe and Cr. The enrichment ratio in the top 8 nm layer is smallest to largest in the order of Ni, Fe and Cr, while the metallic fraction (M^0) in the top layer is largest to smallest. These results indicate that the 3-d corrosion of Alloy 800 at pH 6.0 without radiation present has led to mostly dissolution of mostly Ni and some Fe. The solubility of Ni^{2+} is lower than that of Fe^{2+} but higher than that of Fe^{3+} as shown in Figure 4-5. These results are consistent with the observation of the granular particles on the uniform underlying surface seen by SEM (Figure 4-2) if the granular particles are mostly Fe_3O_4 and the underlying layer is composed of Cr_2O_3 and $FeCr_2O_4$. A few monolayers of the surfaces of oxides and metals submerged in water would be hydrated and hydrolyzed. Hence, the observed hydroxide fractions of all three metal elements in the top 8 nm layer are not negligible, particularly for Fe and Ni. The large Ni metallic (Ni^0) fraction further supports negligible formation of Ni^{II} oxide/hydroxide after 3-d corrosion at pH 6.0.
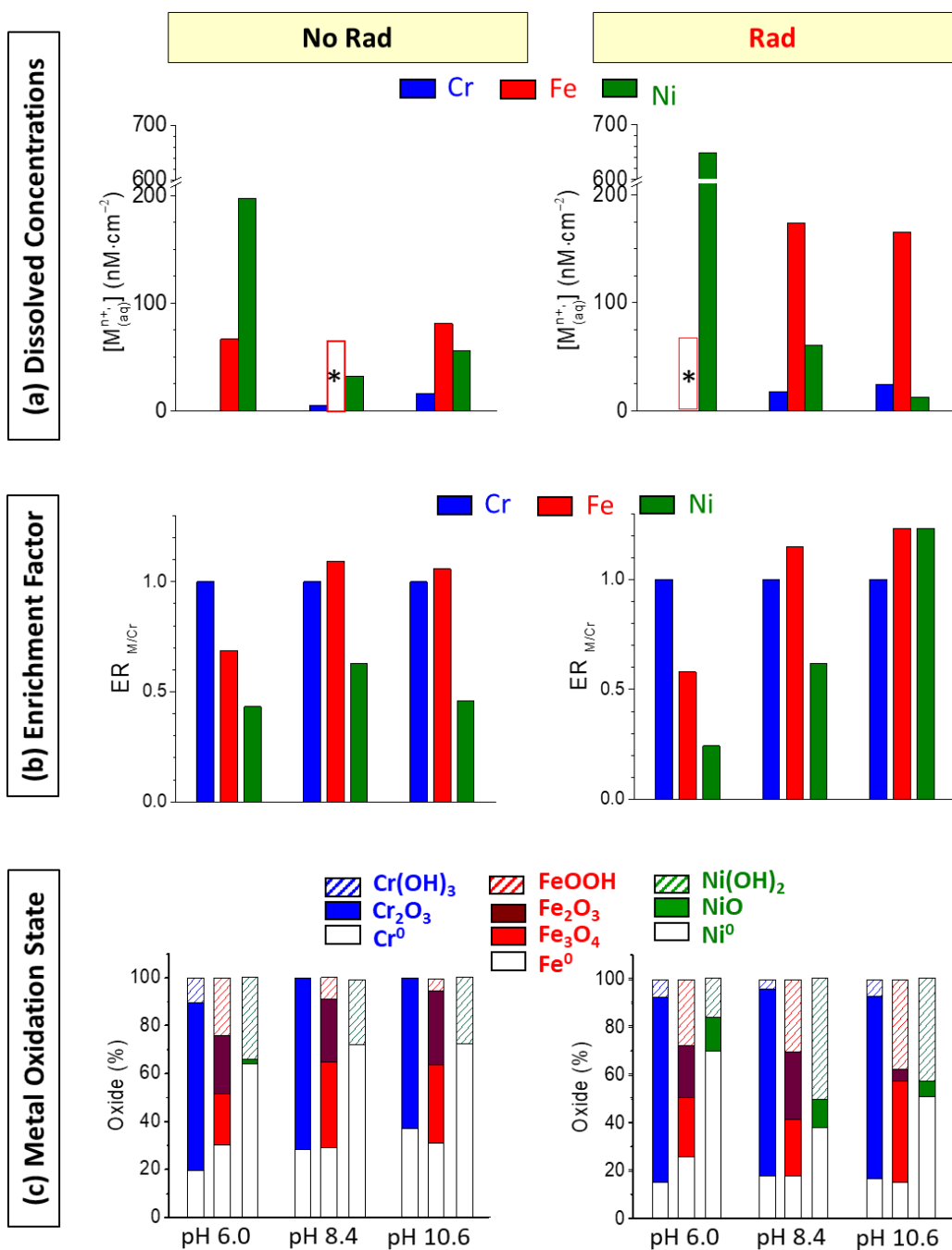
Figure 4-4: (a) Dissolved concentrations of Cr, Fe and Ni species determined by ICP-MS analysis and (b) enrichment ratios ($ER_{M/Cr}$) and (c) compositions of metal oxidation states in the top ~8 nm surface layer.
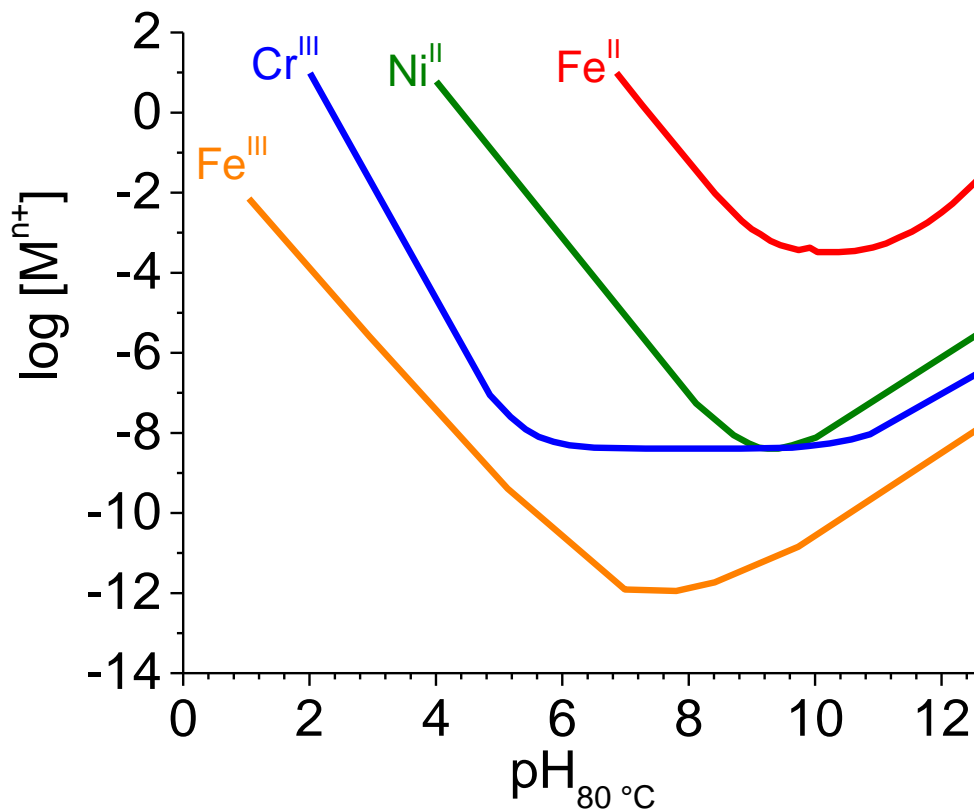
Figure 4-5: pH-dependent solubility of Fe^{II}, Fe^{III}, Ni^{II} and Cr^{III} at 80 °C. The solubilities are calculated from the thermodynamics data presented in [4-7].

The pH has different effects on dissolved concentration, enrichment ratio and surface composition of oxidation-states for different metal elements. For Cr, both the dissolved concentration and the metallic fraction in the surface layer increase with pH. For Fe and Ni, the dissolved concentration is lowest, and the enrichment ratio is highest, at pH 8.4. However, the metallic fraction in the surface layer is nearly independent of pH for Fe while it increases with pH for Ni. The hydroxide or oxyhydroxide fraction decreases with pH for all three metals. The fraction of Cr^{III} in the hydroxide form ($Cr(OH)_3$) in the surface layer is negligible, indicating negligible exposure of the surfaces of Cr^0 or Cr^{III} oxides to water. For Fe, while the sum of oxide and hydroxide fractions is nearly independent of pH the fraction of Fe^{II}/Fe^{III} and Fe^{III} oxides increases and the fraction of Fe^{III} oxyhydroxide (FeOOH) decreases with pH. For Ni, Ni^{II} is all in the form of hydroxide ($Ni(OH)_2$) at all three pHs.

These results suggest that although the rates of dissolution for all three metals are initially higher at a higher pH, a protective Fe-oxide layer is formed earlier which suppresses the oxidation of Ni^0 to $Ni^{2+}_{(aq)}$ earlier. The solubility of Fe^{3+} is lowest at pH 8.4 (Figure 4-5). The lower Fe and Ni dissolution at pH 8.4 than at the other two pHs can therefore be attributed to the earlier formation of the mixed Fe^{II}/Fe^{III} oxide (Fe_3O_4) and its conversion to Fe^{III} oxide/oxyhydroxide at pH 8.4. As the iron oxides cover the surface, further dissolution of Cr^{III} from chromium oxide/hydroxide, and oxidation of Ni^0 to Ni^{II} which dissolves into solution, are restricted.

For corrosion at pH 6.0 with radiation present, the relative values observed for dissolved concentration, enrichment ratio and metallic fraction of the three metals followed the same order observed for corrosion without radiation present. Of the three metals, Ni shows the highest dissolved concentration, lowest enrichment ratio and highest metallic fraction. Gamma-radiation at pH 6.0 increases the concentration of Ni ions dissolved over 3-d and consequently lowers the enrichment ratio and the metallic fraction of Ni in the surface layer. Gamma-radiation at pH 6.0 has smaller effects on those of Fe and Cr. These results indicate that γ-radiolysis makes the solution environment more oxidizing and increases metal oxidation rates, and hence the overall dissolution rates of metal cations, particularly that of Ni^{II}.

The effect of pH on Alloy 800 corrosion with radiation present is different from that observed without radiation present. With radiation present, the dissolved concentration decreases while the enrichment ratio increases, steadily with pH for Ni. On the other hand, the metallic fraction is lowest while the hydroxide fraction is highest at pH 8.4. For Fe, the enrichment ratio increases while the metallic fraction and the oxyhydroxide fraction decrease with pH. For Cr, the dissolved concentration increases, while the metallic fraction in the surface layer remains nearly constant, with pH.

The metallic fractions of all three elements at a given pH are lower on the coupon corroded with radiation than those on the coupon corroded without radiation, except for the slight increase for Ni at pH 6.0. The decrease in metallic fraction or the increase in the fraction of metal cations is mostly due to an increase in the fraction of the hydroxide and not the oxides of the metal cations (except for NiO).

4.3.2 **Electrochemical Experiments**

The 3-d, 80 °C coupon exposure tests show that the dissolved concentrations of individual metals, and the elemental and chemical compositions of oxides present on the surface depend on the pH of the solution and whether γ-radiation is present or not. To investigate how the corrosion might have progressed over the 3 d that produced the results, electrochemical analyses, E_{CORR} and LPR measurements and PD scans were performed as a function of time. The electrochemical analyses of Alloy 800 corrosion over 72 h without radiation present were performed at three different pHs (6.0, 8.4 and 10.6) and at 21 °C and 80 °C. With radiation present the analyses were performed for a shorter duration (15 h) and only at room temperature due to concerns over the long-term stability of the reference electrode.

The E_{CORR} and the PD scan results obtained without radiation present are shown in Figure 4-6. The linear polarization results will be presented in the following section where the electrochemical analysis results are discussed.
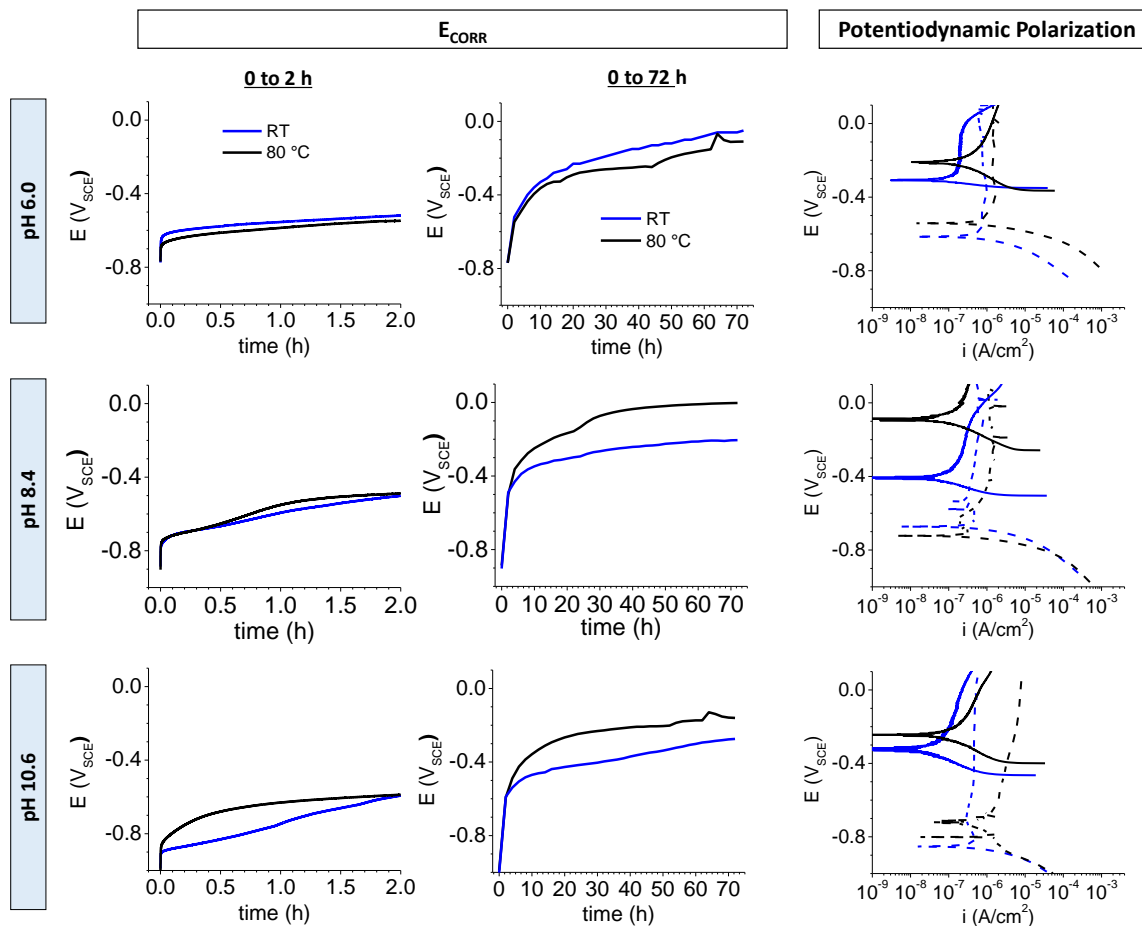
Figure 4-6: E_{CORR} **as a function of time, and potentiodynamic polarization curves taken immediately after cathodic cleaning (broken lines) and after 72-h** E_{CORR} **measurements (solid lines). The** E_{CORR} **is plotted in two different time scales. The black lines represent the data obtained at 80 °C and the blue lines represent those obtained at 21 ⁰C.**

4.3.2.1   Evolution of E_{CORR} over 72-h Corrosion

Corrosion is an interfacial charge transfer (or electrochemical) process, involving metal oxidation coupled with solution reduction via interfacial transfer of ions and electrons. Although E_{CORR} does not provide direct information on the corrosion rate, it can provide information on the types of metal oxidation reaction that can occur and hence the types of oxide that can be formed. Without any externally applied potential, the rate of overall electrochemical oxidation occurring at any given time must be the same as that of overall electrochemical reduction due to charge and mass conservation. Mass and charge conservation may not apply to microscopic space and time domains, but the electrochemical

analyses performed here measure macroscopic properties of corrosion reactions. This condition dictates the E_{CORR} of a corroding system at any given time because there is only one potential at which the overall oxidation (or anodic) current can be the same as the overall reduction (or cathodic) current [8].

A layer of oxide may initially be present on the alloy surface. As corrosion progresses, corrosion products (dissolved metal cations) may also deposit and grow metal hydroxide/oxide on the surface. Oxide present on the corroding surface is a reaction potential barrier for metal oxidation. As oxide grows and converts to different oxide, the magnitude of the potential barrier (the activation energy) changes. If one can establish the magnitude of the potential barrier for metal oxidation as a function of oxide thickness, the evolution of oxide growth rate and its effect on the evolution of overall corrosion rate may be extracted from the E_{CORR} observed as a function of time [8, 9].

It is not the absolute value of E_{CORR}, but the difference between E_{CORR} and the equilibrium potential (E_{eq}) of a specific redox reaction, that determines whether the redox reaction can occur or not and the rate of the redox reaction. The difference between E_{CORR} and the E_{eq} of a redox reaction is commonly referred to as overpotential ($\eta = E_{CORR} - E_{eq}$), and is the driving force for the redox reaction. That is, net metal oxidation will proceed only if the E_{CORR} of the corroding system at the time is higher than the equilibrium potential (E_{eq}) of the metal oxidation half-reaction and is lower than the E_{eq} of the solution reduction half-reaction.

Alloy 800 contains multiple metal elements and each metal can also undergo many different oxidation reactions coupled with solution reduction reactions. The metal oxidation and solution reduction half-reactions that can occur during Alloy 800 corrosion within the potential range of water stability and their E_{eq} values at 25 °C are listed in Table 4-1. The equilibrium potentials at the three pHs studied were calculated using the Nernst equation and the standard reduction potentials of these reactions [4, 5, 7].

Table 4-1: Redox half-reactions involving metal and solution species that can occur during corrosion of Alloy 800 and their equilibrium potentials at different pH.

Rxn#	Metal Redox Half Reactions	E_{eq} (V_{SCE}) at 25 °C*		
		pH$_{25°C}$		
		6.0	**8.4**	**10.6**
Ox0	$2\,Cr^0 + 6\,OH^- \rightarrow Cr_2O_3 + 3\,H_2O + 6\,e^-$	−1.187	−1.329	−1.458
Ox1	$Fe^0 + Cr_2O_3 + 2\,OH^- \rightarrow FeCr_2O_4 + 2\,e^-$	−0.885	−1.027	−1.157
Ox2	$Fe^0 + 2\,OH^- \rightarrow Fe(OH)_2 + 2\,e^-$	−0.701	−0.843	−0.973
Ox3	$3\,Fe(OH)_2 + 2\,OH^- \rightarrow Fe_3O_4 + 4\,H_2O + 2\,e^-$	−0.621	−0.762	−0.893
Ox4	$Fe(OH)_2 + OH^- \rightarrow \gamma\text{-}FeOOH + H_2O + e^-$	−0.349	−0.491	−0.622
Ox5	$2\,Fe_3O_4 + 2\,OH^- \rightarrow 3\,\gamma\text{-}Fe_2O_3 + H_2O + 2\,e^-$	−0.223	−0.364	−0.495
Ox6	$Fe_3O_4 + OH^- + H_2O \rightarrow 3\,\gamma\text{-}FeOOH + e^-$	0.193	0.050	−0.079
Ox7	$Ni^0 + 2\,OH^- \rightarrow Ni(OH)_2 + 2\,e^-$	−0.517	−0.659	−0.789
Ox8	$Ni^0 + H_2O \rightarrow NiO + 2\,H^+ + 2\,e^-$	−0.482	−0.623	−0.754
Ox9	$Cr^0 + 3\,H_2O \rightarrow Cr(OH)_3 + 3\,H^+ + 3\,e^-$	−1.115	−1.297	−1.428
Ox10	$Cr(OH)_3 + H_2O \rightarrow CrO_4^{2-} + 5\,H^+ + 3\,e^-$	0.339	0.253	0.175
	Solution Redox Half-Reaction**			
Red1	$2\,H_2O + 2\,e^- \rightarrow H_2 + 2\,OH^-$	−0.596	−0.612	−0.742
Red2	$H_2O_2 + 2\,e^- \rightarrow 2\,OH^-$	1.119	0.977	0.847
Red3	$O_2 + H_2O + 2\,e^- \rightarrow H_2O_2 + 2\,OH^-$	0.369	0.227	0.097
Red4	$O_2 + 2\,H_2O + 4\,e^- \rightarrow 4\,OH^-$	0.515	0.373	0.242

* The equilibrium potentials were calculated using the Nernst equation and the standard reduction potentials reported for these reactions [4, 5, 7, 10, 11].

** The equilibrium potentials for solution reduction reactions are for H_2 at 5.50×10^{-5} atm that more closely represents the Ar-purged solution environment, and [H_2O_2] and [O_2] at 10^{-4} M that more closely represent the steady-state radiolysis environment [12, 13]

Not listed in the table are the redox half-reactions that involve dissolved metal cations ($M^{n+}_{(aq)}$ such as $Fe^{2+}_{(aq)}$, $Ni^{2+}_{(aq)}$ and $Cr^{3+}_{(aq)}$) because their E_{eq} values depend on the dissolved concentrations of these cations, which are continuously shifting as corrosion progresses. The higher the dissolved concentration is, the higher the E_{eq} will be. If the dissolved concentration of $M^{n+}_{(aq)}$ is at its saturation limit the E_{eq} for a redox reaction involving $M^{n+}_{(aq)}$ will be the same as the E_{eq} of the metal oxidation leading to its hydroxide ($M(OH)_n$) because of the hydrolysis equilibrium of the metal cation:

$$M^{n+}_{(aq)} + n\,OH^- \leftrightarrows M(OH)_x^{(n-x)+}_{(aq)} + (n\text{-}x)\,OH^- \leftrightarrows M(OH)_{x(s)} + (n\text{-}x)\,OH^- \quad (4\text{-}2)$$
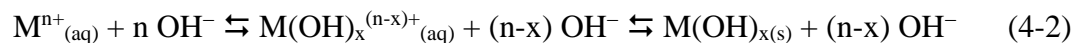
For example, at a given pH the E_{eq} of ($Fe^0 \leftrightarrows Fe^{2+}_{(aq)} + 2\ e^-$) when [$Fe^{2+}_{(aq)}$] is at its saturation limit is the same as E_{eq} of ($Fe^0 + 2\ OH^- \leftrightarrows Fe(OH)_2 + 2\ e^-$) because of the hydrolysis equilibrium of ferrous ions ($Fe^{2+}_{(aq)} + 2\ OH^- \leftrightarrows Fe(OH)_2$). Note that the E_{eq} values of metal and solution redox-half reactions all decrease by 59 mV per one pH unit increase (for one proton transfer per one electron transfer).

Some of the metal oxidation half-reactions that can occur during Alloy 800 corrosion and their E_{eq} values are also shown in Figure 4-7. Because the chemical activity of solid species is 1.0, the E_{eq} values of the metal redox half-reactions that involve only solid species (metals and oxides) all have the same pH dependence, all decreasing by 59 mV per pH unit increase. Hence, different potential axes for different pHs are used in the potential diagram. Plotted this way, the E_{eq} values at different pHs all appear on the same place on the pH-dependent potential scales.

The oxidation reactions involving only chromium species are not shown in Figure 4-7. The E_{eq} of Cr^0 oxidation to Cr_2O_3 is lower than that of Fe^0 in the presence of Cr_2O_3 to $FeCr_2O_4$, and the E_{eq} of the oxidation of Cr^{III} (Cr_2O_3 and $Cr(OH)_3$) to Cr^{VI} ions (e.g., $Cr_2O_7^{2-}$) is higher than the E_{eq} of Fe_3O_4 oxidation to γ-FeOOH. Note that Cr_2O_3 is easily formed by air oxidation and possibly during cathodic cleaning and hence, a thin layer of Cr_2O_3 is likely to be present on the surface prior to corrosion. Due to its insulating nature, the Cr_2O_3 layer is not expected to grow thicker during corrosion but as the Cr^{III} is hydrated and dissolves into solution, Cr^0 can be oxidized to Cr_2O_3 to maintain the layer at a steady-state thickness with minimal change.

Figure 4-6 shows that upon removal of the externally applied potential for cathodic cleaning, E_{CORR} rises nearly instantly (within a minute) to a certain value before it increases at a much slower rate. The E_{CORR} at which the slow increase begins are approximately –0.65, –0.77 and –0.90 V_{SCE} at pH 6.0, 8.4 and 10.6 at 21 °C, and –0.68, –0.77 and –0.87 V_{SCE} at 80 °C. These potentials will be referred to as the initial E_{CORR} (E_{CORR} (0 h)). The observed E_{CORR} ranges, from the initial (E_{CORR} (0 h)) to the final E_{CORR} (E_{CORR} (72 h)), are indicated on the pH-dependent potential scales in Figure 4-7.
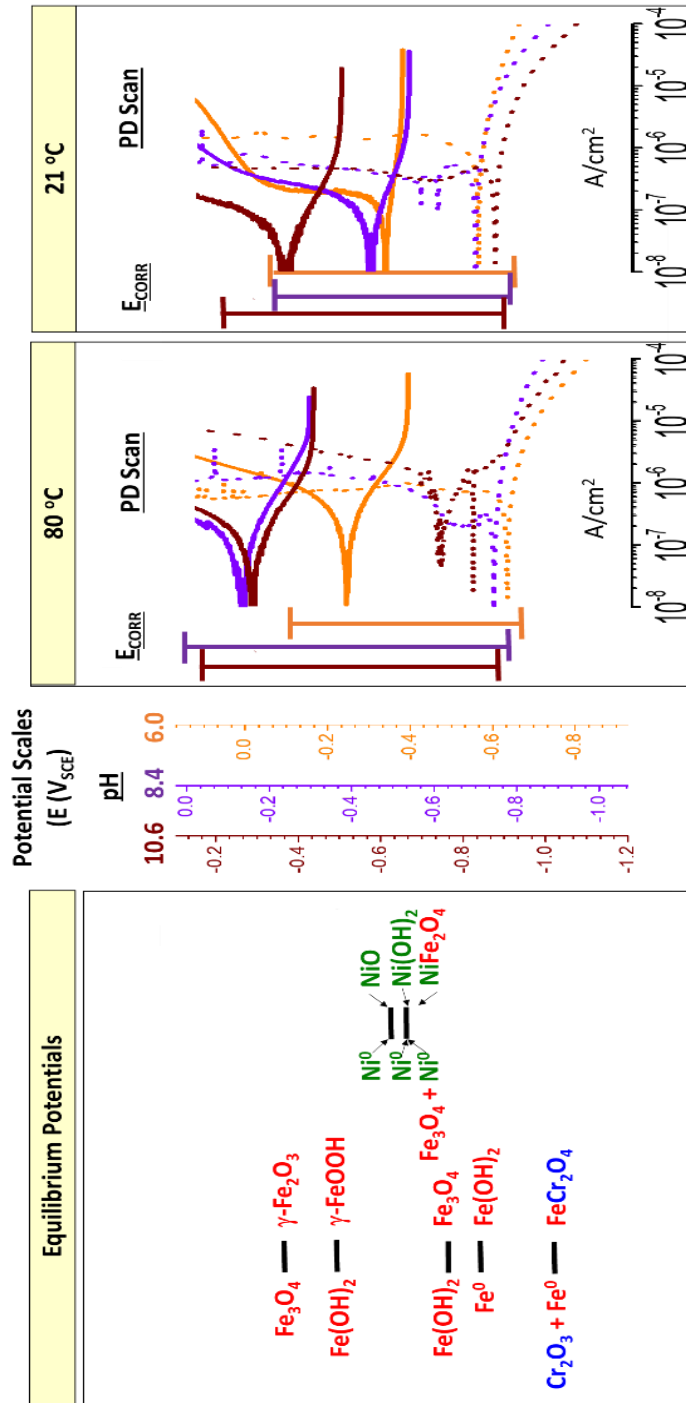
Figure 4-7: Equilibrium potentials of redox half-reactions of iron, nickel and chromium species, and the observed E_{CORR} ranges (from E_{CORR} (0 h) to E_{CORR} (72 h)) and potentiodynamic (PD) polarization curves. Different potential scales are used depending on pH. In the E_{eq} diagram the E_{eq} values are indicated by black bars, and the corresponding redox couples are shown both sides of the bars. The PD polarization curves taken at 0 h and 72 h are shown with dotted and solid lines, respectively.

Some metal oxidation followed by dissolution may occur in the initial rapid transient period prior to establishing the initial E_{CORR}. However, the change in the double layer structure (or the IR drop) in the interfacial region contributes significantly to the change in E_{CORR} in this short period. Hence, the initial transient E_{CORR} behaviour will not be discussed.

The initial E_{CORR} values all lie above the E_{eq} of the oxidation half-reaction of Fe^0 in the presence of Cr_2O_3 to $FeCr_2O_4$. The difference between $E_{CORR}(0\ h)$ and the E_{eq} of Fe^0 oxidation to $FeCr_2O_4$ (i.e., the overpotential for Fe^0 oxidation to $FeCr_2O_4$) is larger at a higher pH. This pH dependence is stronger at 80 ^oC than at 21 ^oC, and the E_{CORR} (0 h) at pH 10.6 at 80 ^oC approaches the E_{eq} of Fe^0 to $Fe(OH)_2$.

4.3.2.2   **Potentiodynamic Polarization at 0 h versus at 72 h**

The voltammograms obtained during the PD scans presented in Figure 4-6 are also replotted on the pH-dependent potential scales in Figure 4-7. The potential at which the current switches from negative to positive during the PD scan will be referred to as the potential of zero current ($E_{i=0}$). The $E_{i=0}$ during the PD scan obtained immediately after cathodic cleaning will be referred to as $E_{i=0}(0\ h)$ and that obtained following 72-h corrosion $E_{i=0}(72\ h)$.

At all studied pHs, the $E_{i=0}(0\ h)$ is close to the E_{eq} of Fe^0 oxidation to $Fe(OH)_2$ ($E_{eq}(Fe^0 \leftrightarrows Fe(OH)_2)$). Note that at pH 10.6 at 80 ^oC, there are two potentials at which the current switches from negative to positive. The lower of the two is closer to the E_{CORR} (0 h) while the second $E_{i=0}(0\ h)$ lies above the E_{eq} of the oxidation of Ni to $Ni(OH)_2$ (E_{eq} (Ni $\leftrightarrows$ $Ni(OH)_2$)).

These observations indicate that irrespective of pH, temperature or radiation environment the initial corrosion process is mainly the oxidation of Fe^0 in the presence of Cr_2O_3 to $FeCr_2O_4$, and the metal cations on the surfaces of the oxides are hydrated ($Cr^{3+}_{(aq)}$ and $Fe^{2+}_{(aq)}$) and diffuse into the bulk solution phase. The concentration of $Fe^{2+}_{(aq)}$ near the surface at a given time will be determined by the combination of the rates of Fe^0 oxidation to $FeCr_2O_4$, and the surface hydration of Fe^{II} from the oxide followed by hydrolysis and diffusion of the hydrated $Fe^{2+}_{(aq)}$.

That E_{CORR} (0 h) is lower than $E_{eq}(Fe^0 \leftrightarrows Fe(OH)_2)$ indicates that it takes much longer than a minute to saturate the solution near the surface with $Fe^{2+}_{(aq)}$ and hence, it takes longer for $Fe^{2+}_{(aq)}$ to hydrolyze to $Fe(OH)_2$. The observation that the $E_{CORR}(0\ h)$ at pH 10.6 at 80 ^oC

is closer to $E_{eq}(Fe^0 \leftrightarrows Fe(OH)_2)$ further suggests that the saturation concentration is reached very fast at pH 10.6.

The surface hydration and hydrolysis of transition metal cations from their metal oxides are known to increase with pH [14]. On the other hand, the solubility of $Fe^{2+}_{(aq)}$ decreases with pH within the studied pH range [14]. The net effect of pH is a faster approach to the saturation limit and hence the earlier formation of $Fe(OH)_2$. Increasing temperature from 21 °C to 80 °C increases both the solubility of $Fe^{2+}_{(aq)}$ and the rate of its hydrolysis to $Fe(OH)_2$. However, the latter rate is more sensitive to temperature and hence, the fastest formation of $Fe(OH)_2$ occurs at pH 10.6 and 80 °C.

Under all conditions E_{CORR} continues to increase with time. The final E_{CORR} values reached after 72-h corrosion (E_{CORR}(72 h)) are all below the E_{eq} of the oxidation of Cr^{III} to Cr^{VI} species (which is higher than that of Fe_3O_4 to γ-FeOOH and hence is not shown in Figure 4-7). However, the final E_{CORR} values are all above the E_{eq} of the oxidation of Ni^0 to Ni^{II} species ($NiFe_2O_4$, $Ni(OH)_2$ and NiO), indicating that the Ar-purged environment is oxidizing enough to form Ni^{II} oxide/hydroxide on Alloy 800 surface from which $Ni^{2+}_{(aq)}$ can dissolve out.

The final E_{CORR} values (E_{CORR}(72 h)) are also above the E_{eq} values of the oxidation of Fe^0 to $Fe(OH)_2$, $Fe(OH)_2$ to Fe_3O_4 and $Fe(OH)_2$ to γ-FeOOH, indicating that all three iron oxides ($Fe(OH)_2$, Fe_3O_4 and γ-FeOOH) can form during corrosion of Alloy 800 at all three pHs in Ar-purged solutions. The E_{CORR}(72 h) values at pH 8.4 and 10.6 at 80 °C as well as pH 10.6 at 21 °C lie above the E_{eq} of Fe_3O_4 oxidation to γ-Fe_2O_3.

The final E_{CORR} values are above the E_{eq} ($Fe(OH)_2 \leftrightarrows$ γ-FeOOH) but below the E_{eq} ($Fe_3O_4 \leftrightarrows$ γ-FeOOH). That is, the oxidation of $Fe(OH)_2$ to γ-FeOOH (reaction 4-3) can couple with the reduction of γ-FeOOH to Fe_3O_4 (reaction 4-4), and the redox coupling (reaction 4-5) accelerates the growth of Fe_3O_4:

$$Fe(OH)_2 + OH^- \rightarrow \text{γ-FeOOH} + H_2O + e^- \tag{4-3}$$

$$3 \text{ γ-FeOOH} + e^- \rightarrow Fe_3O_4 + OH^- + H_2O \tag{4-4}$$

Overall: $Fe(OH)_2 + 2 \text{ γ-FeOOH} \rightarrow Fe_3O_4 + 2 H_2O$ (4-5)
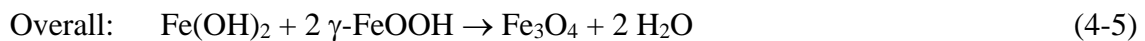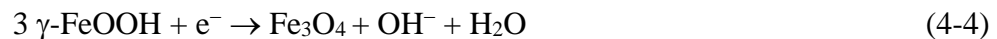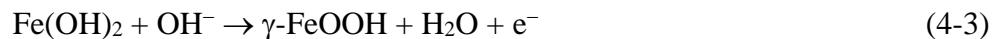
Note that because $Fe(OH)_2$ is in hydrolysis equilibrium with $Fe^{2+}_{(aq)}$ and γ-FeOOH is in equilibrium with $Fe^{3+}_{(aq)}$ the conversion from one oxide to another is likely to occur through dissolution and precipitation.

This catalytic redox coupling will be established earlier at a higher pH and at a higher temperature due to faster saturation of the solution with $Fe^{2+}_{(aq)}$ and $Fe^{3+}_{(aq)}$ and hence faster formation of $Fe(OH)_2$, γ-FeOOH and Fe_3O_4 on the alloy surface.

The catalytic redox coupling can then explain the high $E_{i=0}$(72 h) values observed at pH 8.4 and pH 10.6 at 80 °C. These $E_{i=0}$(72 h) values are higher than the E_{eq} of water reduction in Ar-purged solution, and hence water reduction cannot couple with metal oxidation at these potentials. However, the observed $E_{i=0}$(72 h) values lie between E_{eq}($Fe(OH)_2 \leftrightarrows \gamma$-FeOOH) and E_{eq}(γ-FeOOH $\leftrightarrows Fe_3O_4$) and the overall current during the PD scan corresponds to the sum of the currents generated from these two redox reactions. In addition, the increase in E_{CORR} with time appears to continue after 72 h, which can be attributed to the continuous growth of Fe_3O_4 as the coupled redox reactions continues. The E_{CORR}(72 h) values for some conditions also lie above E_{eq}($Fe_3O_4 \leftrightarrows \gamma$-$Fe_2O_3$) as mentioned before. The overpotential for this oxidation is small and hence, the conversion of Fe_3O_4 to γ-Fe_2O_3 is slow. Nevertheless, γ-Fe_2O_3 is insulating and insoluble and its build-up can suppress the subsequent metal oxidation reactions.

At pH 6.0 at 80 °C the E_{CORR}(72 h) is below E_{eq} ($Fe_3O_4 \leftrightarrows \gamma$-$Fe_2O_3$), whereas the $E_{i=0}$(72 h) is close to E_{eq} ($Fe(OH)_2 \leftrightarrows \gamma$-FeOOH). The E_{CORR}(72 h) and $E_{i=0}$(72 h) values indicate that the net oxidation of $Fe(OH)_2$ to γ-FeOOH is negligible and the catalytic redox coupling of $Fe(OH)_2$ oxidation to γ-FeOOH with γ-FeOOH to Fe_3O_4 cannot be established. Hence, the formation of Fe_3O_4 is mainly via direct oxidation of $Fe(OH)_2$ (in equilibrium with $Fe^{2+}_{(aq)}$ at a saturation level) and is much slower at pH 6.0 than at the other two pHs. Without a thicker layer of Fe_3O_4 (which also oxidizes to γ-Fe_2O_3) the oxidation of Ni^0 to Ni^{II} oxide/hydroxide from which $Ni^{2+}_{(aq)}$ can dissolve will not be suppressed. Thus, the E_{CORR}(72 h) at 80 °C is mainly controlled by the oxidation of Ni^0 to Ni^{II} species coupled with water reduction.

4.3.2.3   **Evolution of Linear Polarization Resistance over 72-h Corrosion**

The linear polarization resistance (LPR) analysis was performed periodically during the 72-h E_{CORR} measurement to determine the evolution of the corrosion rate as corrosion progresses. In this study the potential was scanned from E_{CORR} (t) to (E_{CORR} (t) − 10 mV), and to (E_{CORR} (t) + 10 mV) and back to E_{CORR} (t). A few examples of the LP curves (obtained at 2, 10, 20, 40, 60 and 72 h) are presented in Figure 4-8. Each LP cycle shows a hysteresis loop; the current during negative potential scan is not the same as the current observed during positive scan. Nevertheless, the slope of current versus potential during the negative potential scan is nearly the same as that observed during the positive scan. The inverse of LPR ($1/R_P$) presented in Figure 4-8 are the average value of the slopes obtained from the LP with negative and positive scans.

It is generally considered that in a given corrosion environment the inverse of LPR ($1/R_P$) is proportional to corrosion rate. However, the current obtained during linear polarization consists of a large contribution from charging and discharging current. The magnitude of charging (or discharging) current can be obtained from (half of) the difference in the current values at potentials at which the potential scan direction was switched. The magnitude of the charging current is nearly proportional to the inverse of the polarization resistance ($1/R_P$).
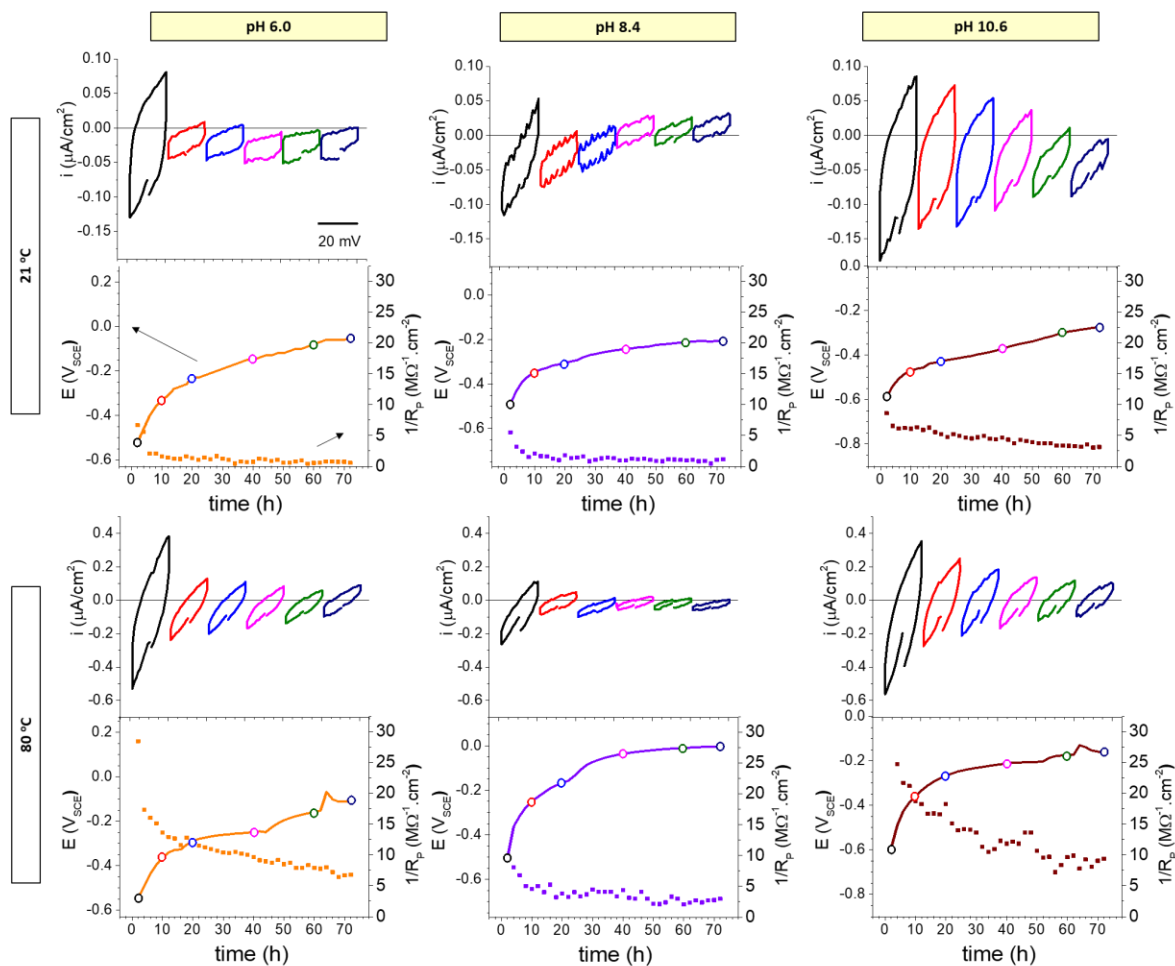
Figure 4-8: **Linear polarization resistant (LPR) measurment on Alloy 800 at 21 °C and 80 °C at pH 6.0, 8.4 and 10.6. for each temperature and pH, the top graph shows the LPR data after 2, 10, 20, 40, 60 and 72 h and the bottom graph shows the $1/R_p$ as well as corrosion potential. Note that the potential scale is corrected to account for the 59 mV/pH difference.**

The average of the currents obtained during negative and positive potential scans corresponds to the current due to interfacial charge transfer. That is, the line for the polarization current due to only interfacial charge transfer (or electrochemical redox reactions) lies in the middle of the two polarization lines during negative and positive scans. The LP results presented in Figure 4-8 show that the current due to interfacial charge transfer at E_{CORR} (t) is not zero, but negative, in all cases except for that of pH 10.6 at 80 °C.

The interfacial charge transfer current (overall current – charging current or overall current + discharging current) consists of two components, anodic and cathodic current. The

anodic current arises from the interfacial transfer of metal cations (produced by metal oxidation) from the metal to the solution phase through the metal oxide phase, if present. The cathodic current arises from the interfacial transfer of electrons (produced by solution reduction) from the solution phase to the metal phase through the metal oxide phase. The observations of the negative current at E_{CORR} (t), while the slopes of current versus potential during negative and positive potential scans are nearly the same, and the large contribution of charging current to the overall current, indicate that the potential dependence of the interfacial charge transfer current arises primarily from that of electron transfer. That is, the electron transfer rate (or solution reduction current) increases exponentially (or linearly over the small potential range of ±10 mV), while the metal cation transfer rate (or metal oxidation rate) is nearly constant, with an increase in externally applied potential.

When the interfacial charge transfer current at E_{CORR}(t) is negative, the $1/R_P$ value is a measure of the potential dependence of the overall electron transfer rate from the solution to the metal phase through the metal oxide phase. Thus, the R_P represents the resistance of the oxide phase to electron transfer from the solution to the metal phase, and not necessarily the resistance to metal oxidation (or corrosion). In particular, direct comparison of the $1/R_P$ values when different oxides are present does not provide any information about their relative corrosion rates. This can explain the observations that higher $1/R_P$ values are observed at pH 10.6 than at pH 6.0 (Figure 4-8), while the dissolved metal concentrations are lower at pH 10.6 than at pH 6.0 (Figure 4-2).

The oxides present on the alloy surface are in hydration and hydrolysis equilibrium with the oxide constituent ions, metal cations and oxygen anions. The observation that the magnitude of the charging current is proportional to $1/R_P$ can then be attributed to the change in the rate of migration of these ions in the double layer due to the changing electric potential gradient in the layer as the potential is scanned.

4.3.3 Effect of γ-Radiation on E_{CORR}

Exposed to γ-radiation, both the alloy and solution phases absorb the γ-photon energy. In the alloy phase, the absorbed energy dissipates predominantly as heat (increasing the alloy's temperature slightly - by 2-3 °C). But in the solution phase it induces ionization and decomposition of water molecules to produce a number of redox active species [15]:

$$H_2O \xrightarrow{\quad\quad} \bullet OH, \bullet e_{aq}^-, \bullet H, HO_2\bullet, H_2, H_2O_2, H^+ \qquad\qquad (4\text{-}6)$$
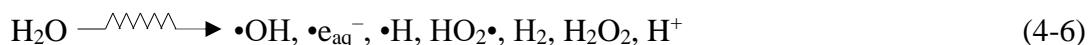
The reducing species are mostly radicals (e.g., $\bullet e_{aq}^-$ and $\bullet H$) and very reactive in the solution phase where they are produced. The probability of the radicals reaching the surface and engaging in electrochemical reactions is much lower than that of the longer-lived oxidizing species (e.g., H_2O_2). Thus, the solution environment quickly becomes highly oxidizing under continuous γ-irradiation [10, 16-21]. Of the radiolytically produced oxidants, H_2O_2 is most effective for metal oxidation [10]. The E_{eq} of H_2O_2 reduction to OH^- is higher than that of O_2 to OH^- and significantly higher than that of H_2O to H_2. The production of H_2O_2 increases the driving force for interfacial electron transfer processes, and hence γ-radiolysis can increase the rate of metal oxidation that is coupled with the reduction of solution species.

Unfortunately, we were not able to measure E_{CORR} during corrosion at 80 °C with radiation present due to concerns over the stability of the reference electrode. Thus, the E_{CORR} measurement with radiation present was performed only at 21 °C and for a shorter period. The E_{CORR} observed during corrosion at 21 °C with and without radiation present are compared in Figure 4-9. The effect of γ-radiation on E_{CORR} depends on the pH of the solution. At all three pHs, the E_{CORR} changes more slowly during corrosion with than without radiation present. The duration of this initial stage depends on pH and is longer at a lower pH. However, the E_{CORR} at later times increases at a faster rate with radiation than without radiation present, and the E_{CORR} values reached after 15-h corrosion with radiation present are the same as those reached after 72-h corrosion without radiation present (Figure 4-6).
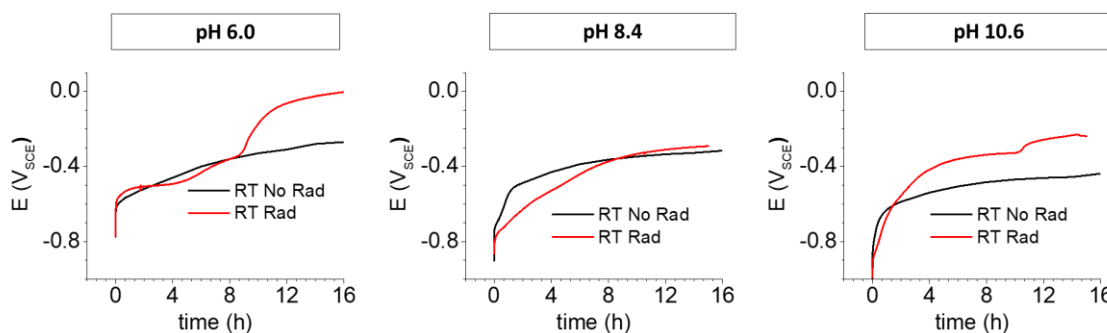
Figure 4-9: E_{CORR} **measurements in the presence and absence of radiation and RT for 15 h at all three pH. The black line is RT No Rad and the red line is with radiation results.**

The faster approach to the final steady-state E_{CORR} during corrosion with radiation than without it is consistent with the expectation that γ-radiolysis produces stronger oxidants and hence, increases metal oxidation rates causing metal oxidation to progress to the formation of metal cations with higher oxidation states. However, the overall rate of corrosion is determined by not only electron transfer but also metal cation transfer. The interfacial metal cation transfer is affected by the rates of dissolution and oxide formation of the metal cation.

4.4   Proposed Corrosion Mechanism

The experimental study indicates that the specific metal oxidation reactions that occur during corrosion of Alloy 800, and their rates, change with time. Based on this analysis a corrosion mechanism consisting of elementary metal oxidation steps is proposed and schematically illustrated in Figure 4-10.
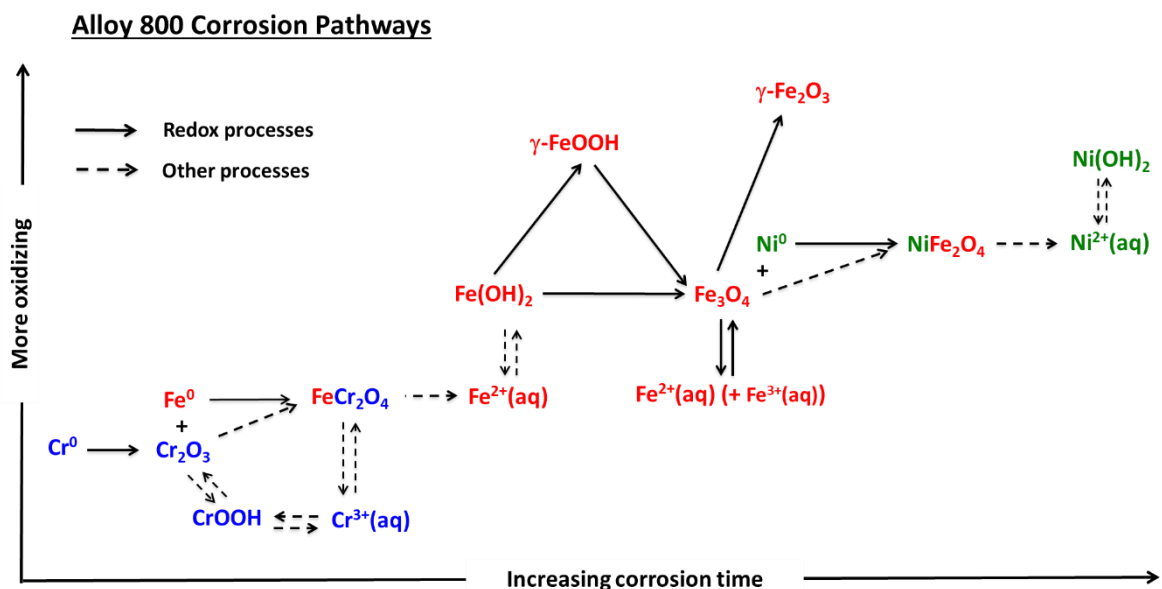
Figure 4-10:   Proposed mechanism for Alloy 800 corrosion

The proposed mechanism considers that Alloy 800 corrosion mechanism involves a series of metal oxidation reactions coupled with solution reduction reactions, and each metal

cation produced either dissolves into solution or precipitates as solid hydroxide/oxide. The metal-solution redox reactions are interfacial charge transfer processes. Thus, the driving force for a specific metal oxidation is the difference between the potential energy of the corroding system (E_{CORR}) and the E_{eq} of the metal oxidation half-reaction. However, because corrosion (loss of metal from the metal phase) involves not only electron but also metal cation transfer, the overall rate of metal oxidation is determined by not only interfacial electron transfer but also other processes that affect the interfacial transfer of metal cation from the alloy phase to the solution phase and, if present, the oxide phase.

Mass and charge conservation during corrosion dictates that the rate of each oxidation reaction producing a metal cation must be equal to the sum of the rates of dissolution and oxide formation of the metal cation. As metal oxidation to produce a specific metal cation continues and the solution near the surface becomes saturated with the metal cation, the dissolution of the metal cation becomes suppressed while the hydrolysis followed by precipitation of the metal cation as solid hydroxide/oxide increases. The oxide present on the metal surface is a potential energy barrier for metal oxidation leading to the formation of the oxide. As long as metal oxidation continues the hydroxide/oxide of the metal cation continues to grow. Once the solution is saturated with the metal cation the overall rate of the metal oxidation is determined by the precipitation and growth of the oxide of the metal cation. However, as the oxide grows it slows down the metal oxidation. Consequently, the rates of metal oxidation, dissolution and oxide formation evolve as corrosion progresses, before the system (consisting of the alloy and solution phases) reaches steady state.

The proposed mechanism shows that different corrosion pathways are available because many metal oxidation reactions occur, some in sequence and some in parallel, and each oxidation leads to dissolution and oxide formation of the metal cation produced. Competition kinetics between different elementary processes determine the corrosion pathway. The pH and γ-radiation affect the rates of individual elementary processes and thereby influence not only the overall rate of corrosion but also the corrosion pathway.

The pH of the solution does not affect the driving force for an electrochemical redox reaction (i.e., metal oxidation coupled with solution reduction), but it affects the hydration and hydrolysis rates and the solubilities of metal cations. The rates of hydration (or solvation)

and hydrolysis of transition metal cation are known to increase with an increase in pH [14]. The solubility of a metal cation in water also depends strongly on pH, but it does not increase continuously with pH but rather has a minimum at a mildly basic pH. Each metal cation has a characteristic pH dependence and a specific pH of minimum solubility, as can be seen in Figure 4-5.

On the other hand, γ-radiolysis produces highly redox active species and increases the driving force for metal oxidation. However, it has a negligible effect of the solvation properties of water such as the hydration rate and the solubility of metal cations.

4.5   Conclusions

This study has found that corrosion of Alloy 800 involves a series of metal oxidation reactions coupled with solution reduction reactions, and each metal cation produced either dissolves into solution or precipitates as solid hydroxide/oxide. The driving force for a specific metal oxidation is the difference between the potential energy of the corroding system (E_{CORR}) and the E_{eq} of the oxidation half-reaction. However, the overall rate of corrosion (sum of dissolution and oxide formation) is determined by not only the electrochemical oxidation but also other chemical and transport processes. Mass and charge conservation during corrosion dictate that the rate of each oxidation reaction producing a metal cation must be equal to the sum of the rates of dissolution and oxide formation of the metal cation. Consequently, the rates of metal oxidation, dissolution and oxide formation evolve as corrosion progresses before the system (consisting of the alloy and solution phases) reaches steady state.

Based on the experimental study, a corrosion mechanism has been proposed. The mechanism shows that different corrosion pathways are available because many metal oxidation reactions occur, some in sequence and some in parallel, and each oxidation leads to dissolution and oxide formation. Competition kinetics between different elementary processes determine the corrosion pathway. The pH and γ-radiation affect the rates of individual elementary processes and thereby influence not only the overall rate of corrosion but also the corrosion pathway. The pH of the solution does not affect the driving force for

metal oxidation, but it affects the hydration and hydrolysis rate and the solubility of metal cation. Gamma-radiolysis produces highly redox active species and increases the driving force for metal oxidation. However, it has a negligible effect of the solvation properties of water such as hydration rate and solubility of metal cation.

The combined effect of pH and γ-radiation on 3-d corrosion of Alloy 800 in Ar-purged solution at 80 $^{\circ}$C is that γ-radiation increases the overall dissolution of $Ni^{2+}_{(aq)}$ at pH 6.0 whereas it promotes the formation of a passive oxide layer at pH 10.6.

4.6   References

[1] F. Cattant, D. Crusset, D. Féron, Corrosion issues in nuclear industry today, Materials Today, 11 (2008) 32-37.

[2] W. Garland, The Essential CANDU, University Network of Excellence in Nuclear Engineering (UNENE), (2014).

[3] M.C. Biesinger, B.P. Payne, A.P. Grosvenor, L.W. Lau, A.R. Gerson, R.S.C. Smart, Resolving surface chemical states in XPS analysis of first row transition metals, oxides and hydroxides: Cr, Mn, Fe, Co and Ni, Applied Surface Science, 257 (2011) 2717-2730.

[4] B. Beverskog, I. Puigdomenech, Revised Pourbaix diagrams for iron at 25–300 C, Corrosion Science, 38 (1996) 2121-2135.

[5] B. Beverskog, I. Puigdomenech, Revised Pourbaix diagrams for nickel at 25–300 C, Corrosion Science, 39 (1997) 969-980.

[6] B. Beverskog, I. Puigdomenech, Revised Pourbaix diagrams for chromium at 25–300 C, Corrosion Science, 39 (1997) 43-57.

[7] B. Beverskog, I. Puigdomenech, Pourbaix diagrams for the ternary system of iron-chromium-nickel, CORROSION, 55 (1999) 1077-1087.

[8] M. Momeni, J. Wren, A mechanistic model for oxide growth and dissolution during corrosion of Cr-containing alloys, Faraday discussions, 180 (2015) 113-135.

[9] M. Momeni, M. Behazin, J. Wren, Mass and charge balance (MCB) model simulations of current, oxide growth and dissolution during corrosion of Co-Cr alloy Stellite-6, Journal of The Electrochemical Society, 163 (2016) C94-C105.

[10] R.P. Morco, A.Y. Musa, M. Momeni, J.C. Wren, Corrosion of carbon steel in the [P14666][Br] ionic liquid: The effects of γ-radiation and cover gas, Corrosion Science, 102 (2016) 1-15.

[11] M. Pourbaix, Atlas of Electrochemical Equilibria in Aqueous Solutions, National Association of Corrosion Engineers, 1966.

[12] P.A. Yakabuskie, J.M. Joseph, J.C. Wren, The effect of interfacial mass transfer on steady-state water radiolysis, Radiation Physics and Chemistry, 79 (2010) 777-785.

[13] J.M. Joseph, B.S. Choi, P. Yakabuskie, J.C. Wren, A combined experimental and model analysis on the effect of pH and $O_{2(aq)}$ on γ-radiolytically produced H_2 and H_2O_2, Radiation Physics and Chemistry, 77 (2008) 1009-1020.

[14] C.F. Baes, R.E. Mesmer, The Hydrolysis of Cations, Robert E. Krieger, 1986.

[15] A. Mozumder, Fundamentals of Radiation Chemistry, Elsevier Science, 1999.

[16] M. Behazin, "Radiation Induced Corrosion of Stellite-6" (2014). Electronic Thesis and Dissertation Repository. 2434.

[17] M. Behazin, J.J. Noël, J.C. Wren, Combined Effects of pH and γ-Irradiation on the Corrosion of Co-Cr Alloy Stellite-6, Electrochimica Acta, 134 (2014) 399-410.

[18] K. Daub, "A Study of Gamma Radiation Induced Carbon Steel Corrosion" (2013). Electronic Thesis and Dissertation Repository. 1074.

[19] K. Daub, X. Zhang, J.J. Noël, J.C. Wren, Gamma-radiation-induced corrosion of carbon steel in neutral and mildly basic water at 150 °C, Corrosion Science, 53 (2011) 11-16.

[20] Q.W. Knapp, J.C. Wren, Film formation on type-316L stainless steel as a function of potential: Probing the role of gamma-radiation, Electrochimica Acta, 80 (2012) 90-99.

[21] A.Y. Musa, J.C. Wren, Combined effect of gamma-radiation and pH on corrosion of Ni–Cr–Fe alloy inconel 600, Corrosion Science, 109 (2016) 1-12.

Chapter 5

Combined Effects of Gamma-Radiation and pH on Corrosion of Alloy 800 at 150 ºC

5.1   Introduction

Alloy 800, a member of the Fe-Cr-Ni alloy-family, is widely used in heat exchangers in power generation plants, and especially nuclear power plants, due to its good mechanical properties and acceptable corrosion behaviour [1-3]. It is typically used for applications that involve long-term exposure to high temperature. Normally, in nuclear power plants, the primary water coolant passes through tubes made of Alloy 800 where they exchange their heat with the secondary system which has a different temperature and water chemistry [2, 4]. In pressurized light water reactors (PLWR) the primary coolant has a $pH_T \sim 7$ and the temperature ranges from ~ 270 to 325 °C [4] whereas in the pressurized heavy water reactors (PHWR) also known as Canadian deuterium uranium (CANDU) it has a pH range of 10.2 – 10.4 and operates at temperature range of 265-325 °C [2, 4].

In this chapter, electrochemical experiments were performed to investigate the general corrosion behaviour of Alloy 800 at a higher temperature in borate buffer solutions at $pH_{25 °C}$ 6.0 and 10.6. The corrosion tests were performed at 150 °C for different time periods to study the effect of pH and γ-radiation on the corrosion behaviour of Alloy 800.

5.2   Experimental

5.2.1   Material and Solutions

The electrochemical experiments and coupon exposure tests were performed as shown in Figure 5-1. The details of the composition of Alloy 800 and sample preparation are described in detail in Chapter 3. For the electrochemical measurement, only one side of the

samples with surface area 0.785 cm^2 was exposed to the solution. All experiments were conducted in argon-purged 0.01 M sodium borate (Na$_2$B$_4$O$_7$.10H$_2$O) solution at pH$_{25\ °C}$ 6.0 and 10.6. The pH of the solutions was adjusted to 10.6 by adding the required amount of sodium hydroxide (NaOH) and to 6.0 by adding boric acid (H$_3$BO$_3$). All solutions were prepared with water purified using a Nano pure Diamond UV ultra-pure water system from Barnstead International to give a resistivity of 18.2 MΩ·cm.
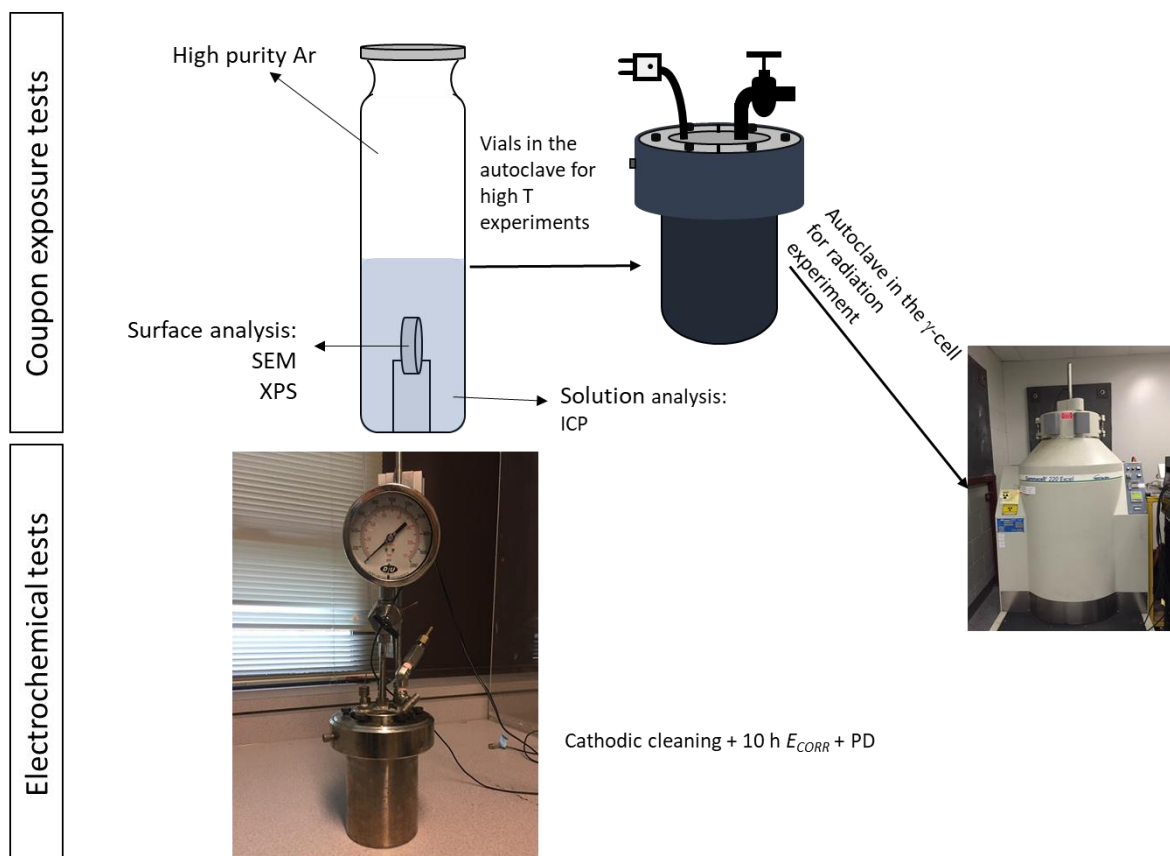
Figure 5-1: **Experimental setup for coupon exposure tests and electrochemical experiments**

5.2.2 Electrochemical Tests

Open-circuit potential (E_{CORR}) and potentiodynamic polarization (PD) experiments were performed at 150 °C with borate buffer solution at pH$_{25\ °C}$ 6.0 and 10.6. The tests were carried out using an autoclave with a built-in 3-electrode electrochemical cell. The working

electrode was the Alloy 800 sample under study, the counter electrode used was a high surface area platinum mesh, and the reference electrode used was a high-temperature high-pressure external saturated Ag/AgCl electrode. All measured potentials are converted to SCE values at room temperature using the procedure reported in Chapter 3. The borate solution was purged with argon gas for an hour prior to start of experiment to remove dissolved oxygen from the test solution. The working electrode was cathodically cleaned for 5 minutes prior to the start of experiments to remove any organic impurities from the sample's surface. After cathodic cleaning, the corrosion potential was recorded for 10 h. At the end of this 10 h potential measurement, PD was performed from -0.3 V vs. E_{CORR} to anodic potentials with the same scan rate of 1 mV/s.

5.2.3 Corrosion Experiments

For coupon exposure experiments, both sides of the sample were exposed to the test solution with a total surface area of 2.5 cm^2 in a sealed quartz vial. The vials were then placed in an autoclave and irradiated using a MDS Nordion Gammacell 220 Excel Cobalt-60 irradiator as described in detail in Chapter 3. The dose rate during the period of experimentation was 2.7-2.9 kGy·h^{-1}, as calibrated by Fricke dosimetry.

5.2.4 Post-test Analysis

After the coupon exposure test, the test solution was analysed for dissolved metal concentration using inductively coupled plasma – optical emission spectroscopy (ICP-OES). The lower limits of quantitation for Ni, Cr and Fe were 5 µg·L^{-1}, 2 µg·L^{-1} and, 2 µg·L^{-1}, respectively.

The corroded coupons were rinsed with water, dried with argon gas and stored under vacuum prior to surface analysis. The morphology of the oxide formed on the coupon surface was analyzed using a scanning electron microscope (SEM). The composition and thickness of oxide formed was analyzed using Auger electron spectroscopy (AES).

5.3   Results

The E_{CORR} measurement was performed only for the first 10 h of Alloy 800 corrosion and only without radiation present and was followed by a potentiodynamic (PD) scan. The E_{CORR} and PD scan results are shown with the calculated equilibrium potentials of metal redox half-reactions at 150 °C in Figure 5-2. The pH-dependent E_{eq} values were calculated from thermodynamic data available in literature [5-10]. Only the E_{eq} values that are within the observed E_{CORR} ranges are shown in Figure 5-2.

The E_{CORR} value increased rapidly upon removal of the externally applied potential for cathodic cleaning. The increase was faster at $pH_{25°C}$ 10.6 (~ 30 min) than that at 6.0 (~ 2 h). This was followed by a slow change in E_{CORR} before it reached a steady-state value. At $pH_{25°C}$ 6.0 the E_{CORR} stabilized at –0.2 V_{SCE} for almost 90 min before it dropped to –0.25 V_{SCE} for the rest of the measurement. The steady-state E_{CORR} value at $pH_{25°C}$ 10.6 is about 100 mV higher than that observed at $pH_{25°C}$ 6.0. Not only the E_{CORR} value, but also the difference between E_{CORR} and E_{eq} for any given reaction is larger at $pH_{25°C}$ 10.6 than that at $pH_{25°C}$ 6.0.

The steady-state E_{CORR} values all lie above the E_{eq} of the oxidation half-reactions of Fe^0 to $FeCr_2O_4$, Fe^0 to $Fe(OH)_2$, $Fe(OH)_2$ to Fe_3O_4, Ni^0 to Ni^{II} species ($NiFe_2O_4$ and $Ni(OH)_2$), Fe_3O_4 to $\gamma-Fe_2O_3$ and $Fe(OH)_2$ to $\gamma-FeOOH$, but they are below the E_{eq} of the redox half-reactions of Cr^{III} to Cr^{VI} species (not shown in Figure 5-2) and at $pH_{25°C}$ 6.0 it is below the equilibrium potential of Fe_3O_4 to $\gamma-FeOOH$. Note that the metal oxidation that can lead to these oxides and hydroxides also results in the dissolution of the metal cations.

126
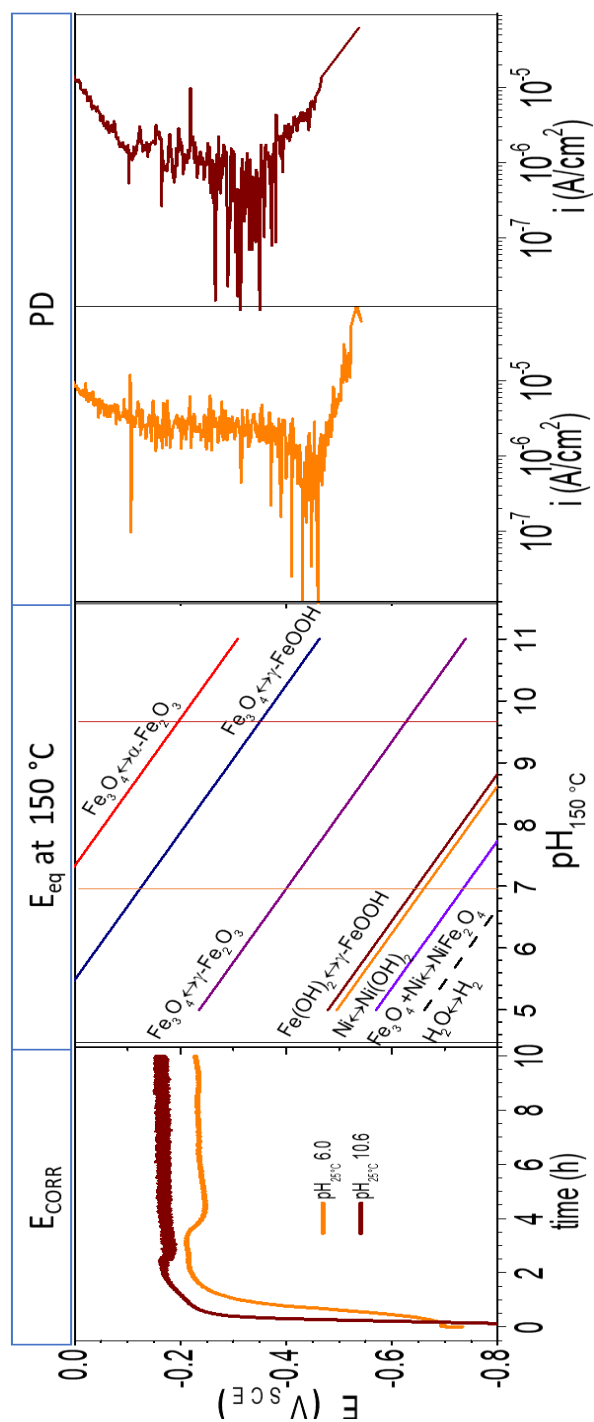
Figure 5-2: E_{CORR} observed as a function of time for Alloy 800 corrosion in Ar-purged solutions at $pH_{25°C}$ 6.0 ($pH_{15 °C}$ ~7) and $pH_{25°C}$ 10.6 ($pH_{150°C}$ ~9.6) (left panel); equilibrium potentials of redox half-reactions of metal species as a function of $pH_{150°C}$ (centre panel); and the potentiodynamic (PD) polarization curves obtained at 10 h (right panel).

At $pH_{25°C}$ 10.6 the E_{CORR}(10 h) value is above the E_{eq} ($Fe_3O_4 \leftrightarrows \gamma$-FeOOH) and close to E_{eq} ($Fe_3O_4 \leftrightarrows \alpha$-$Fe_2O_3$). That is, the oxidation of Fe_3O_4 to γ-FeOOH and the dehydration of γ-FeOOH to α-Fe_2O_3 [11-13] can couple with the reduction of α-Fe_2O_3 to Fe_3O_4. Note that α-Fe_2O_3 is a stable phase and if it has formed, its reduction would be slow. Therefore, the E_{CORR}(10 h) is close to E_{eq} ($Fe_3O_4 \leftrightarrows \alpha$-$Fe_2O_3$), due to the slow kinetics of the reaction. At $pH_{25°C}$ 6.0 the E_{CORR}(10 h) value is below the E_{eq} ($Fe_3O_4 \leftrightarrows \gamma$-FeOOH) and above the E_{eq} ($Fe(OH)_2 \leftrightarrows \gamma$-FeOOH). This is similar to the observed behaviour at lower temperature presented in Chapter 4. Once Fe is oxidized to Fe^{2+}, it hydrates forming $Fe(OH)_2$ and it can be further oxidized to γ-FeOOH. The electrode potential is below E_{eq} ($Fe_3O_4 \leftrightarrows \gamma$-FeOOH) and causes reduction of γ-FeOOH to Fe_3O_4. In addition to Fe_3O_4 formation by this cycle, reduction of γ-FeOOH can also oxidize Ni to Ni^{II} species ($Ni(OH)_2$ and $NiFe_2O_4$ in the presence of magnetite). Note that because Fe_3O_4 is in hydrolysis equilibrium with $Fe^{2+}_{(aq)}$ and $Fe^{3+}_{(aq)}$ and γ-FeOOH is in equilibrium with $Fe^{3+}_{(aq)}$ the conversion from one oxide to another is likely to occur through dissolution and precipitation. This catalytic redox coupling will be established earlier at the pH with lowest solubility of a certain cation, due to the faster saturation of the solution with $Fe^{2+}_{(aq)}$ and $Fe^{3+}_{(aq)}$ and hence the faster formation of $Fe(OH)_2$, γ-FeOOH and Fe_3O_4 on the alloy surface.

The potential at which the current switches from negative to positive during PD scan will be referred to as the potential of zero current ($E_{i=0}$). The potentials of zero current ($E_{i=0}$(10 h)) are below the E_{CORR}(10 h) values at both pHs. At $pH_{25°C}$ 6.0 (= $pH_{150°C}$ ~7) the $E_{i=0}$(10 h) value is closer to the E_{eq} of the redox reaction between Fe_3O_4 and γ-Fe_2O_3, while at $pH_{25°C}$ 10.6 (= $pH_{150°C}$ 9.6) the $E_{i=0}$(10 h) the value is closer to the E_{eq} of the redox reaction between Fe_3O_4 and γ-FeOOH. These $E_{i=0}$(10 h) values are too high for the water reduction half-reaction to effectively couple with the metal oxidation half-reactions (Figure 5-2). Because at $E_{i=0}$ the overall oxidation rate is the same as the overall reduction reaction, the PD scan results indicate that at $pH_{25°C}$ 6.0, the current as a function of potential near $E_{i=0}$(10 h) is primarily determined by the oxidation and reduction cycle of Fe_3O_4 and γ-Fe_2O_3 and that of γ-FeOOH and Fe_3O_4 at $pH_{25°C}$ 10.6. The comparison of E_{CORR}(10 h) with E_{eq} indicates that adequate amounts of Fe_3O_4 and γ-Fe_2O_3 are present on the surface corroded

for 10 h at pH_{25^oC} 6.0 while sufficient amounts of γ-FeOOH and Fe_3O_4 are present on the surface corroded for 10 h at pH_{25^oC} 10.6, to allow these redox cycles to occur.

The electrochemical analysis results are consistent with the results obtained in the studies at room temperature and 80 ^oC presented in Chapter 4. The corrosion kinetic pathways proposed from the low temperature studies are still applicable to the corrosion of Alloy 800 in Ar-purged solution at 150 ^oC. The proposed corrosion pathways are presented again here in Figure 5-3. The different observed behaviours at different temperatures can be attributed to the fact that the rates of different elementary processes have different temperature dependences.
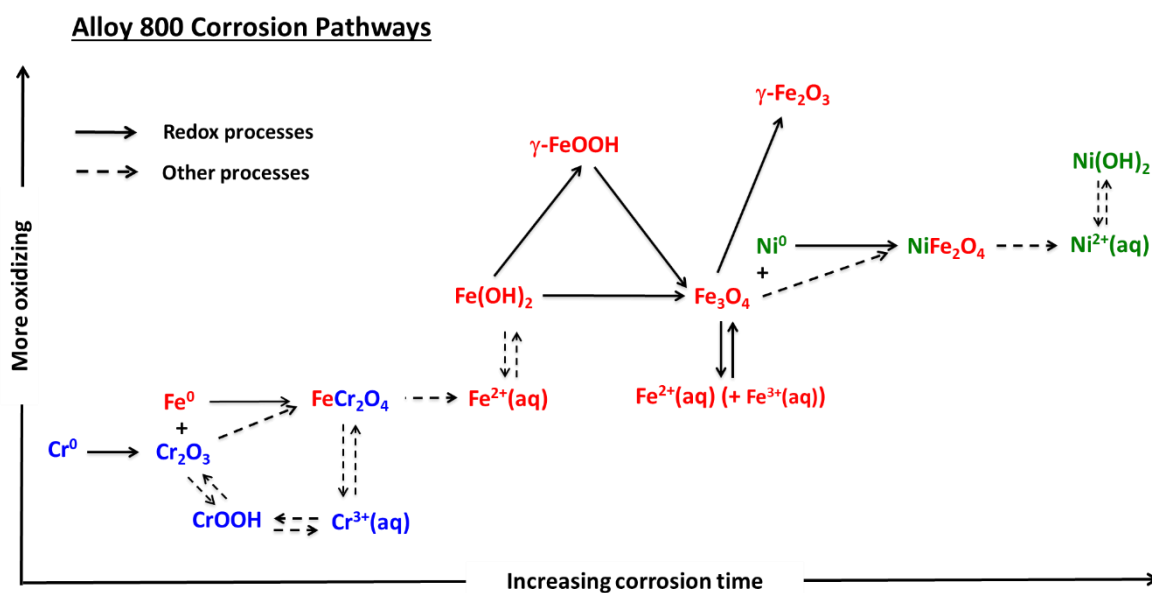
Figure 5-3:   Proposed Alloy 800 corrosion pathways

Alloy 800 corrosion kinetics at 150 ^oC over longer times (up to 5 d) were studied by analyzing dissolved metal concentrations and the surfaces of coupons corroded for different durations at $pH_{25\ ^oC}$ 6.0 and $pH_{25\ ^oC}$ 10.6 with or without γ-radiation present. The SEM images of the surfaces and the dissolved concentrations of three different metal ions from the same tests are presented in Figure 5-4.
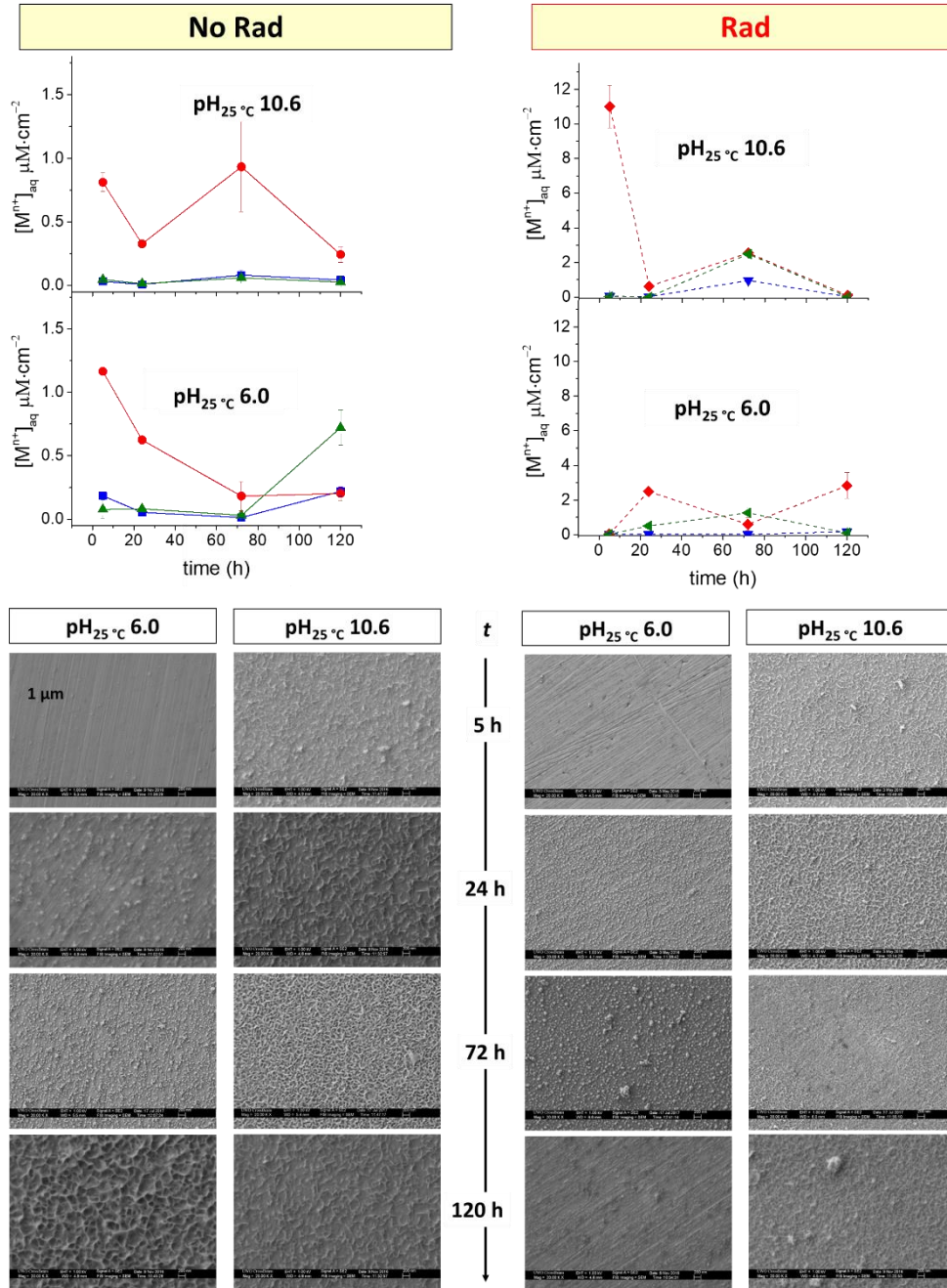
Figure 5-4: Dissolved metal concentrations (Cr in blue, Fe in red and Ni in green) and SEM micrographs of the surfaces of the coupons corroded for different durations in Ar-purged solutions at $pH_{25\,°C}$ 6.0 and 10.6 with γ-radiation (Rad) or without γ-radiation present (No Rad). The experimental uncertainties in the dissolved concentrations are indicated with bars.

The dissolved metal concentrations are also listed in Table 5-1. Note that the dissolved concentrations determined by ICP-OES include colloid particles dispersed in the solutions as well as completely soluble species.

Table 5-1: Concentrations of metal cations dissolved over different durations of Alloy 800 corrosion in Ar-purged solutions at pH$_{25^oC}$ 6.0 and 10.6 at 150 ^{o}C with radiation (Rad) and without radiation present (No Rad).

	Duration (h)	Concentration (μM/cm^2)					
		pH$_{25\,^{\circ}C}$ 6.0			pH$_{25\,^{\circ}C}$ 10.6		
		Cr	Fe	Ni	Cr	Fe	Ni
No Rad	5	0.18	1.16	0.08	0.03	0.81	0.05
	24	0.05	0.63	0.08	0.01	0.33	0.01
	72	0.01	0.18	0.03	0.08	0.93	0.06
	120	0.22	0.20	0.72	0.04	0.24	0.03
Rad	5	0.05	0.04	0.03	0.06	11.00	0.04
	24	0.02	2.49	0.51	0.02	0.63	0.00
	72	0.03	0.60	1.26	0.97	2.55	2.48
	120	0.17	2.83	0.10	0.02	0.11	0.02

Although the E_{CORR} reaches a steady state within 5 h (the first data collection time) at a given pH without radiation present (Figure 5-2), the dissolved metal concentrations fluctuate with time, showing wave patterns, under all conditions studied. The SEM images of the surfaces also show changes in morphological characteristics with time. The dissolved concentrations of metal cations are sometimes above their solubility limits except for the solubility of ferrous ion. The solubilities for iron, chromium and nickel cations as a function of pH at 150 °C were calculated from the Gibbs free energy of formation reported in literature [5-8] and are presented in Figure 5-5.
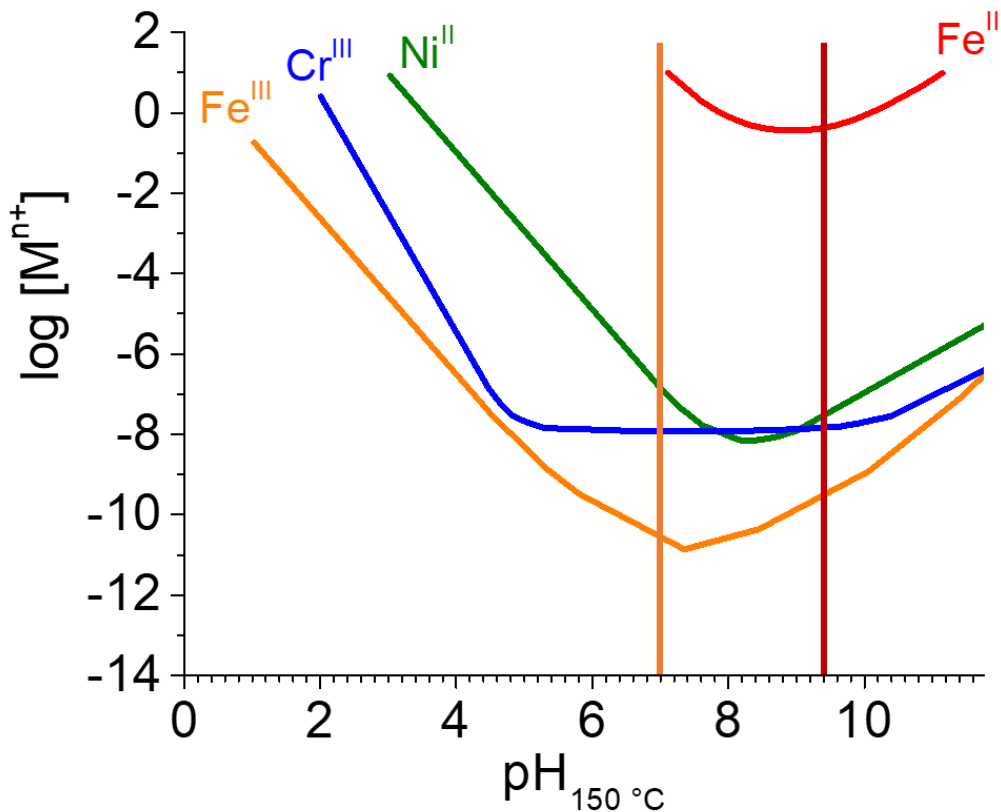
Figure 5-5: Solubilities of Fe^{II}, Fe^{III}, Ni^{II} and Cr^{III} ions in water at 150 °C calculated using the Gibbs free energies of formation reported in refs [5-8].

The decrease in the concentration of dissolved metal cations accumulated over the duration of corrosion with time indicates that the fluctuation in dissolved metal concentration is not due to fluctuation in the metal oxidation rate. While metal oxidation is occurring, the overall amount of metal cation accumulated should increase, irrespective of the rate of oxidation. Rather, the fluctuation in dissolved concentration indicates that the metal cations dissolved at earlier times precipitate as solid oxide/hydroxide adhering to the surface at later times. The period when dissolved metal concentration is observed to decrease is when the rate of metal dissolution is lower than the precipitation of metal cation on solid metal hydroxide and/or oxide.

The dissolved concentrations of individual metal ions as a function of time presented in Figure 5-4 show wave patterns. For example, the dissolved Fe concentration is highest at

5 h (the first data collection time) under all conditions except for $pH_{25\,°C}$ 6.0 with radiation. This is followed by a decrease before the dissolved Fe concentration increases again. The cycle of increase-decrease of dissolved concentration repeats within the studied duration. Different metals have different rates of increase and decrease in dissolved concentration, and the rates for individual metal cations depend on pH and whether radiation is present or not.

The cycling of dissolved metal concentration with time is a form of chemical wave, a typical pattern produced by oscillating reactions. Chemical waves can be observed in the time domain such as observed in the iodine clock reaction [14, 15], or in the space domain such as observed in the Belousov–Zhabotinsky (B-Z) reaction [16-20]. Observation of a chemical wave indicates that the reaction system is far from equilibrium and remains so for a significant length of time. A feature of B-Z reactions is that they oscillate between two or more metastable states. This does not contradict the laws of thermodynamics, as over longer times these oscillations move towards equilibrium of the overall reaction system.

During corrosion, the concentration of dissolved metal cations in solution is initially controlled by the rate of metal oxidation coupled with solution reduction. However, as corrosion progresses and the solution becomes saturated with metal cations, the metal cations precipitate and grow hydroxides/oxides. As the metal hydroxides/oxides grow they can suppress further oxidation of metals. For Alloy 800 corrosion at 150 $°C$, the time to approach the overall slow metal oxidation rate appears to be short (in 5 h). After 5 h the oxidation of metallic species would have slowed down considerably.

The metal cations from oxide/hydroxide particles can be hydrated and hydrolyzed. The dissolved metal cations that are in dynamic equilibrium with solid metal hydroxides can diffuse into solution and then reprecipitate onto other oxide/hydroxide particles some distance away. This coarsening (or Ostwald ripening) is considered mainly responsible for the changes in the surface morphology and dissolved concentration at longer times. The wave of dissolved metal concentration at times longer than 5 h may be attributed to the oscillation between net dissolution (hydration and diffusion) of metal cations from oxide particles and net precipitation of dissolved metal ions on oxide particles, while the overall amounts of individual metal cations (as dissolved and oxide species) increase slowly as corrosion

133

progresses; see further discussion below. The metal oxides/hydroxides can further oxidize and convert to different oxides.

The depth profiles of the atomic percentages (at.%) of the three main metal elements, carbon and oxygen were determined by AES with Ar^+ ion sputtering. The depth profiles for the surface layers of the coupons corroded for 5 h and 120 h are shown in Figure 5-6.

The depth profiles presented in Figure 5-6 show that the C at.% near the surface is significantly higher than its at.% in the bulk alloy and the front of the high C at.% moves to a deeper depth with time. In addition, in the depth range over which the C at.% is high the atomic percentages of Fe, Ni and Cr are very low while the O at.% is high. As discussed in more detail later, these depth profiles suggest that the metal species have been dissolved from this layer, enriching the fraction of carbon in the alloy bonded to titanium (which is very low) in this layer. Note that a distinct solid phase of metal carbide is not likely to be present in this alloy. However, carbon forms a strong covalent bond with titanium and chromium at the alloying temperature in the interstitial sites of the FCC crystal structure of austenite and is likely to be distributed uniformly in the alloy phase. These phases are hard to dissolve, and as Fe and Ni (and to some extent Cr) dissolves into the solution, they remain on the surface. Therefore, as the surface is sputtered by Ar^+ in the AES analysis, because of depletion of Fe, Cr and Ni, it shows a high C concentration. It should be noted that the first monolayers of C on the surface might be because of contamination, but those deep into the metal are an indication of carbon bonded to metals.

Dissolution of metal cations from the alloy phase results in high C at.% while very low metal at.%. At later times, as the solution becomes saturated with the dissolved metal cations, the metal cations can precipitate easily as metal hydroxide/oxide particles and films. Accumulation of metal oxide/hydroxide increases the atomic percentages of metal elements and O, and accordingly C at.% decreases. The depth profile of C at.% will depend on the relative progression of dissolution and metal oxide growth.
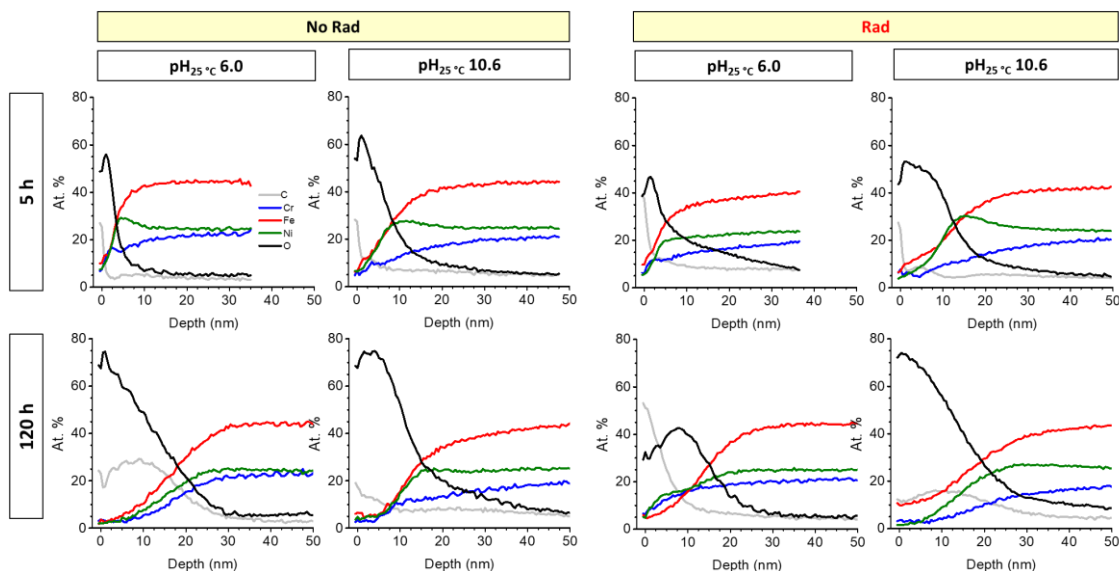
Figure 5-6: AES depth analysis for coupons exposed to pH$_{25°C}$ 6.0 and 10.6 for 5 h and 120 h in the presence and absence of radiation at 150 °C. The black line represents oxygen, **red Fe**, **blue Cr**, **green Ni** and **gray is C**.

Due to the large contribution of C to the atomic percentages of other elements the ratio of the atomic percentages of O to total metal (1.5Cr + Fe + Ni), not their absolute atomic percentages, provides the type and thickness of the oxide/hydroxide deposited on the surface. The depth profiles of O/(1.5Cr + Fe + Ni) obtained for the coupons corroded for 5 h and 120 h are compared in Figure 5-7. Also shown in the figure are the depth profiles of C at.% on the same coupons. The depth at which the ratio of O/(1.5Cr + Fe + Ni) is one is the depth where all of the metal species are present in oxide forms of metals in their lowest stable oxidation states (e.g., FeCr$_2$O$_4$ and NiO). The depth at which the ratio is 0.5 thus represents the average depth of the metal oxide/metal interface. The depth at which the ratio is 2.0 is that at which the metal cations are in hydroxide forms, Cr(OH)$_3$, FeOOH (or Fe(OH)$_2$) and Ni(OH)$_2$. A ratio greater than 2.0 indicates the presence of highly hydrated metal cations (e.g., Fe(OH)$_3$·3(H$_2$O)) and adsorbed water molecules (or electrolyte ions). The ratio does not stay constant with depth for all of the surfaces studied. The steep change in the ratio with depth indicates that the oxides/hydroxides do not grow as pure or distinct oxide phases, although with time they may slowly convert to stable distinct oxide phases. Note that the lines representing different oxide compositions such as the line of O/(2Cr + 2Fe + 2Ni)

135

representing CrOOH, FeOOH and Ni(OH)$_2$ can be constructed. However, the variation in the ratio of O to metal is within a factor of 1.5.

Because of the continuous nature of the metal oxide/hydroxide transition, we define the range between the depth at which the ratio is 0.5 and the depth at which the ratio is 3.0 (both arbitrary values based on the oxygen analysis) as the layer of metal oxide. The oxide that grows on the surface can be considered as a spinel with a composition of Ni$_x$Fe$_{1+x}$Cr$_{2-2x}$O$_4$ (0<x<1) where x=0 at the region close to the interface of metal and oxide and x=1 close to the interface of solution and oxide. The range of depths shallower than this range is depleted of metals and has not yet filled with metal oxides, consisting of mostly molecular metal carbides and highly hydrated surfaces.

The average depth of the oxide/metal interface (i.e., the depth at which the ratio of O/(1.5Cr + Fe + Ni) is 0.5) coincides with the depth at which the Ni at.% (Figure 5-6) is at its maximum under all studied conditions. This is consistent with the general observation that Ni is enriched at the interface of metal and oxide [21, 22]. This also indicates that Ni dissolution is initially slower than Fe and Cr dissolution.

Under all studied conditions, the depth at which the interface lies increases steadily with corrosion time. At 5 h the interface front is at a deeper depth at pH$_{25\,°C}$ 10.6 than at pH$_{25\,°C}$ 6.0 without or with radiation present. However, the interface front moves more slowly at pH$_{25\,°C}$ 10.6 than at pH$_{25\,°C}$ 6.0, and the difference in the interface depths at the two pH$_{25\,°C}$ values is much smaller at 120 h. These observations indicate that the rate of metal dissolution is initially higher at higher pH, but metal dissolution continues longer at a lower pH. As discussed in detail later, rates of surface hydration and hydrolysis of metal cations are higher at a higher pH. This can explain the observation that the oxide/metal interface is at a greater depth for the coupons corroded for 5 h at pH$_{25\,°C}$ 10.6 than at pH$_{25\,°C}$ 6.0. However, the faster the dissolution of metal cation, the faster the solution near the surface becomes saturated by the metal cation, and the hydroxide/oxide of the metal cation is formed earlier and grows faster. The solubilities of metal cations are in general lower at pH$_{25\,°C}$ 10.6 than at pH$_{25\,°C}$ 6.0 (Figure 5-5). The combination of faster hydrolysis and lower solubility at pH$_{25\,°C}$ 10.6 thus promotes earlier and faster growth of metal oxide particles and films on the surface, passivating the surface earlier.
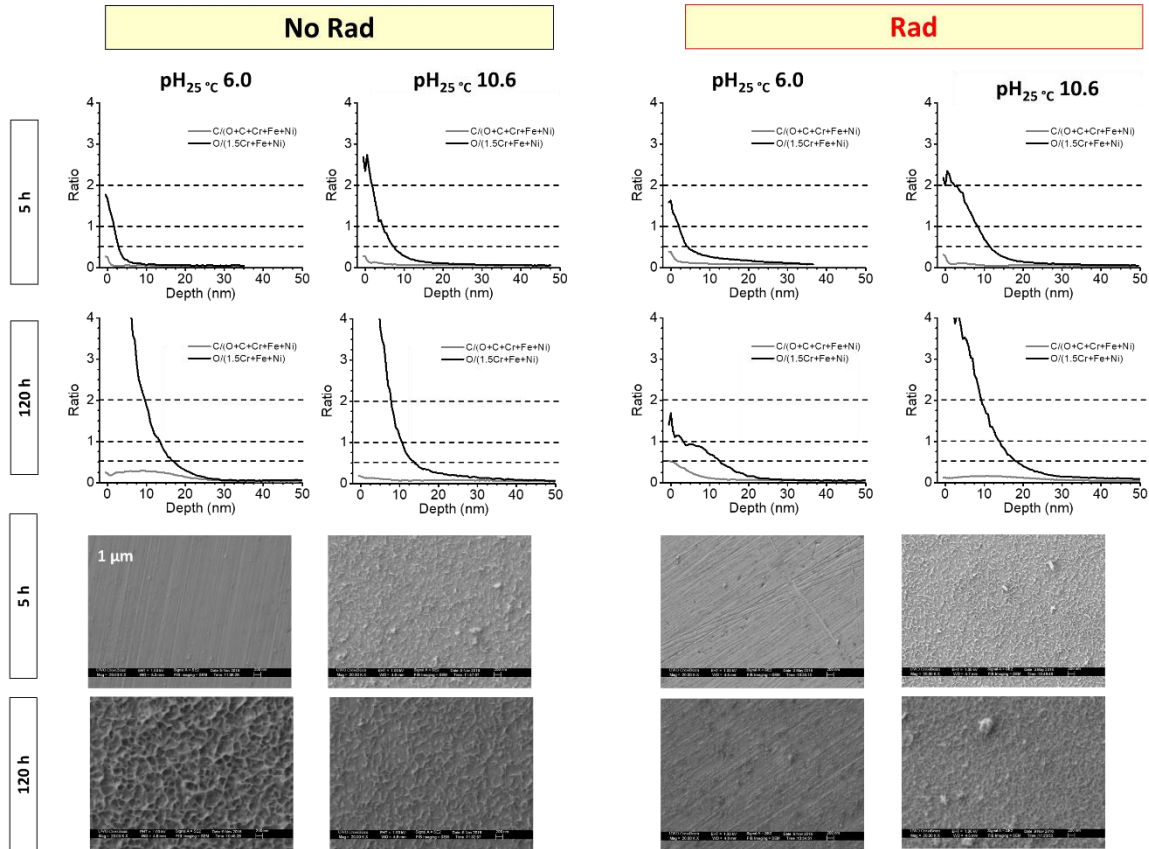
Figure 5-7: Oxygen and carbon analysis of AES results on Alloy 800 after 5 h and 120 h immersion at pH$_{25°C}$ 6.0 and 10.6 at 150 °C in the presence and absence of γ-radiation. The dashed vertical lines shows where the ratio is 0.5, 1.0 and 2.0. The ratio of 0.5 for the oxygen line is considered to be the interface of metal and oxide, 1.0 is the oxide region and 2.0 is the hydroxide layer.

The depleted region changes with pH and the presence of radiation. Without radiation, the depth range increases with time at both pHs. With radiation, the change is not significant for pH$_{25\,°C}$ 6.0 while it increases with time at pH$_{25\,°C}$ 10.6. The reason for the different behaviour at pH$_{25\,°C}$ 6.0 in the presence of radiation could be the homogeneous oxidation of metal cations (mostly Fe) in the solution, as reported previously [23].

5.3.1   Corrosion at first 5 h

The rate of metal dissolution will be highest at the beginning of corrosion when the solution is free of metal cations. The electrochemical results presented in Figure 5-2 indicate that the E_{CORR} already reaches a high steady-state value by 5 h, and the overall metal oxidation rate should slow down considerably by the time the E_{CORR} reaches the steady-state value. Thus, most of metal dissolution occurs in the first 5 h, and perhaps even earlier.

The evolution of Alloy 800 corrosion at 150 °C in the first 5 h is difficult to observe experimentally. However, the E_{CORR} and the PD polarization results indicate that while the E_{CORR} approaches steady state faster, Alloy 800 corrosion at 150 °C involves the same metal oxidation reactions and transport processes as those observed at lower temperatures, as schematically shown in Figure 5-3.

The proposed mechanism suggests that corrosion of Alloy 800 proceeds first by oxidizing Fe^0 to Fe^{II} which quickly dissolves into solution as $Fe^{2+}_{(aq)}$. Because its solubility is high at all pHs the dissolution can continue for some time. The concentration near the surface is determined by the rate of its production (i.e., Fe^0 oxidation to Fe^{II}) and the rate of Fe^{II} removal from the surface. The removal of metal cation from the surface of solid metal or solid metal oxide requires hydration of the metal cation followed by diffusion from the surface to the bulk solution phase. The surface hydration of metal cation increases with an increase in pH (assisted by base catalyzed hydrolysis) and with temperature.

As the metal oxidation continues the concentration of $Fe^{2+}_{(aq)}$ in the solution near the surface increases. When the concentration of $Fe^{2+}_{(aq)}$ in the solution near the surface approaches its saturation limit, the diffusion of $Fe^{2+}_{(aq)}$ from the surface into the solution phase is significantly hindered. This slows down the net dissolution of the Fe^{II} species to the solution phase and the concentration of Fe^{II} on the surface increases and the formation of $FeCr_2O_4$ and hydrolysis of $Fe^{2+}_{(aq)}$ to $Fe(OH)_2$ increase accordingly. The Fe^{II} species on the surfaces of metal or growing oxide/hydroxide particles are also more easily oxidized to the less soluble Fe^{II}/Fe^{III} oxide (Fe_3O_4) and/or γ-FeOOH, compared to homogeneous solution oxidation. Thus, once the solution near the metal surface becomes saturated with $Fe^{2+}_{(aq)}$ the growth of iron hydroxides/oxides is accelerated.

As the layer of solid oxide/hydroxide particles grow, the oxidation of Fe^0 to Fe^{II} slows down because an oxide layer present on metal surface is an energy barrier for metal oxidation. The conversion of the Fe^{II} species to the less soluble Fe^{III} species will deplete the surface of adsorbed ferrous ions, and $Fe^{2+}_{(aq)}$ will continue to adsorb on the surface.

The E_{CORR} values observed at 5 h are also above the E_{eq} of Ni^0 oxidation to Ni^{II} and hence dissolution of Ni^{2+} also occurs. Similarly, once the solution near the surface reaches the Ni^{II} saturation limit, the formation and growth of $Ni(OH)_2$ and/or $NiFe_2O_4$ starts to accelerate. The rate of nickel oxidation is affected by the type of iron hydroxide/oxide as well as the nickel hydroxide/oxide that forms and grows. The overall nickel oxidation slows down while the growth of $Ni(OH)_2$ and/or $NiFe_2O_4$ by precipitation of $Ni^{2+}_{(aq)}$ continues, decreasing the concentration of $Ni^{2+}_{(aq)}$. The surface of Alloy 800 would be covered with air-formed Cr_2O_3. Dissolution of Cr is limited by the hydration and hydrolysis of Cr^{III} ions from the chromium oxide which is replenished by oxidation of Cr^0 to Cr_2O_3. As the $FeCr_2O_4$ starts to form by precipitation of $Fe^{2+}_{(aq)}$ and $Cr^{3+}_{(aq)}$ the dissolved Cr concentration can decrease.

The observed effects of pH on Alloy 800 corrosion in Ar-purged solutions at 150 ^{o}C over 5 h can thus be explained as follows. The pH has a negligible effect on the driving force (or overpotential) of metal oxidation coupled with water reduction (because of the same pH dependences of the metal redox half-reaction and the water reduction half-reaction). However, pH affects the rate of surface hydration and hydrolysis of metal cation and the solubility of metal cation. The net dissolution rates of $Fe^{2+}_{(aq)}$ and $Ni^{2+}_{(aq)}$ are initially higher at $pH_{25\ ^oC}$ 6.0 than at $pH_{25\ ^oC}$ 10.6. Their solubility limits are higher at $pH_{25\ ^oC}$ 6.0 than at $pH_{25\ ^oC}$ 10.6. Thus, the rate of metal dissolution is initially faster at $pH_{25\ ^oC}$ 6.0 than at $pH_{25\ ^oC}$ 10.6 and the maximum dissolved concentration reached is higher at $pH_{25\ ^oC}$ 6.0 than at $pH_{25\ ^oC}$ 10.6 because hydroxide/oxide formation is negligible until the concentration of $Fe^{2+}_{(aq)}$ in the solution near the surface reaches its saturation limit.

The faster metal dissolution at $pH_{25\ ^oC}$ 6.0 than at $pH_{25\ ^oC}$ 10.6 at early stages of corrosion is consistent with the observed depth profiles of the atomic percentages of C and the three metal elements determined by AES (Figure 5-6). On the coupon corroded for 5 h without radiation present the depth at which the Ni at.% is maximum and the C at.% is

approximately that of the bulk alloy phase, and is deeper at $pH_{25\,°C}$ 6.0 than at $pH_{25\,°C}$ 10.6. This layer is severely depleted of Fe, Ni and Cr. However, the dissolved concentrations of all three metal elements observed at 5 h are lower at $pH_{25\,°C}$ 10.6 than at $pH_{25\,°C}$ 6.0, indicating that the concentrations of these ions near the surface may have reached their solubility limits and that hydroxide/oxide formation has occurred more significantly at $pH_{25\,°C}$ 10.6 than at $pH_{25\,°C}$ 6.0. These observations are consistent with the observed effect of pH over 5-h corrosion on the depth profile of O at.% (Figure 5-7) as well as the surface morphology observed by SEM (Figure 5-4).

Corrosion under γ-radiation in the first 5-h seems to be faster than that with no radiation. For $pH_{25°C}$ 10.6, dissolved Cr concentration is almost double of that of no radiation and it is more than an order of magnitude higher for Fe while Ni dissolution is similar to the No Rad condition. Also, for this sample, oxide is thicker than its no radiation counterpart. These observations suggest that the rate of corrosion is higher in the presence of radiation because radiolytic products act as oxidants and increase the overall rate of oxidation.

At pH 6.0, the results are different from that of no radiation. The dissolved metal cation concentrations are lower than those with no radiation and the oxide is thicker. This observed difference could be because of partial radiolytic oxidation of metal cations and formation of nano-particles. In the other words, the highest dissolved metal concentration in the presence of radiation might have been attained at a time shorter than 5 h. Therefore, it is possible that similar behaviour to that of no radiation happens in the presence of radiation, albeit in a shorter time scale than that studied here.

5.3.2 Corrosion at longer times

As exposure time increases the depleted region changes as well as the morphology and the amount of dissolved metal cations in the solution. The E_{CORR} measurement shows that corrosion potential does not change significantly and no other oxidation / reduction reactions except for those already seen in the shorter time are taking place. This suggests a significant role for the solution pH at longer times. The solution pH dictates the solubility of metal cations (Figure 5-5) and the difference between E_{CORR} and E_{eq} (Figure 5-2) and therefore, the corrosion pathway (Figure 5-3). The rate of solution reduction species is

significantly lower and most of metal and oxides oxidation is coupled with the reduction of oxides with higher oxidation state. The adsorbed metal cations on the surface can precipitate on the surface and form an oxide or diffuse into the solution. In the presence of radiation, radiolytic precipitation of metal oxides is possible.

When time increases from 5 h to 24 h, the number of oxide particles on the surface increases. This increase is greater for $pH_{25\,°C}$ 10.6 than that for $pH_{25\,°C}$ 6.0, which is consistent with the more significant drop in the dissolved metal cations determined by ICP for $pH_{25\,°C}$ 10.6. At both pHs, the surface is covered with more oxide for the sample exposed for 72 h than that for 24 h. However, the morphology of oxide is different as it is more dispersed small particles with size less than 100 nm for the $pH_{25\,°C}$ 6.0 sample and filament-like film for $pH_{25\,°C}$ 10.6. It seems that the particles that form after 24 h (at $pH_{25\,°C}$ 6.0) did not grow and there are more particles that nucleated on the surface. The ICP-OES measurements support this interpretation, as the concentration of the dissolved metal cations decreased from 24 h to 72 h at this pH. However, the sample immersed in a $pH_{25\,°C}$ 10.6 solution has oxides with a filament-like morphology. This type of morphology was previously reported for transition metals at alkaline pH [3, 24-28]. The surface morphology after 72 h shows denser and smaller filament-like oxides than those after 24 h at the same pH. However, the only difference between 24 h and 5 h at $pH_{25\,°C}$ 10.6 with no radiation is the increase in the number of the filament-like oxides. The fact that the morphology of the sample after 72 h is different from shorter times suggests that the type of oxide that forms on the surface is different in this case. This new type of oxide is probably formed because of the change in the oxidation pathway. The final morphology of the oxide on the surface after 120 h shows filament-like oxide for both pHs. However, the filaments are larger at $pH_{25\,°C}$ 6.0 than that at $pH_{25\,°C}$ 10.6. Generally, oxides are thicker at longer times; however, the change in the thickness is pH-dependent.

The dissolved metal concentration of Cr at $pH_{25\,°C}$ 6.0 under radiation is similar to that with no radiation except for the continuous increase in the metal cation concentration in the solution from 24 h to 120 h, after the initial drop from 5 h to 24 h. Cr dissolution at $pH_{25\,°C}$ 10.6 and Ni dissolution at both pH under radiation show an initial increase in the dissolved metal concentrations up to 72 h but then decrease as time increases to 120 h. Iron dissolution

at $pH_{25\,°C}$ 10.6 under radiation mirrors that of no radiation except for the faster rate of dissolution or redeposition. This shows that at $pH_{25\,°C}$ 10.6, radiation affects mainly the rate at which iron dissolves or forms an oxide.

The morphology of the oxides on the surface is similar to that in the no radiation experiments except for the size of particles and the density and length of the filament-like oxides. The only significant difference is observed for $pH_{25\,°C}$ 6.0 after 120 h of experiments which shows a surface where the particles that formed earlier are flattening on the surface and forming an oxide layer instead of forming oxide filaments. In addition, at $pH_{25\,°C}$ 6.0, the particles formed under radiation are more spherical rather than the elongated oxides formed in the absence of radiation. This may be due to the fast redeposition of the oxide on the surface. As this rate is very high, the particles prefer to maintain the lowest possible surface area to volume, which produces spheres.

The concentrations of metal cations dissolved during corrosion with radiation present determined by ICP-OES are far above their solubility limits which also suggests that some of these metal cations may be present as hydroxide/oxide colloid particles dispersed uniformly in the solutions. Consequently, the ICP-OES analysis required considerable digestion of the solution samples prior to the analysis.

5.4   Conclusions

The effects of pH and γ-radiation on oxide formation and metal dissolution on Alloy 800 surface in high temperature aqueous solution were investigated by coupon exposure experiments and electrochemical tests. The results show that the rates of oxide formation and metal dissolution vary with pH, but the main effect of γ-radiation is on the oxidation rate. Normally, the oxide formed at $pH_{25°C}$ 10.6 is thicker than that at 6.0. Homogeneous radiolytic oxidation of metal cations happens at $pH_{25°C}$ 6.0 but not at $pH_{25°C}$ 10.6. The oxide that grows on the surface can be considered to be a spinel with the composition of $Ni_xFe_{1+x}Cr_{2-2x}O_4$ (0<x<1) where x=0 at the region close to the interface of metal and oxide and x=1 close to the interface of solution and oxide. The electrochemical experiments show that at higher pHs, the difference in the equilibrium potential of oxidation (E_{eq}) and corrosion potential (E_{CORR})

is higher than that at low pH. This indicates that at higher pH, the oxide film provides a greater potential barrier for the oxidation reaction.

5.5   References

[1] F. Cattant, D. Crusset, D. Féron, Corrosion issues in nuclear industry today, Materials today, 11 (2008) 32-37.

[2] W. Garland, The Essential CANDU, University Network of Excellence in Nuclear Engineering (UNENE), (2014).

[3] A. Musa, J. Wren, Combined effect of gamma-radiation and pH on corrosion of Ni–Cr–Fe alloy inconel 600, Corrosion Science, 109 (2016) 1-12.

[4] J. Killeen, F. Nordmann, J. Schunk, K. Vonkova, Optimisation of water chemistry to ensure reliable water reactor fuel performance at high burnup and in ageing plant (FUWAC): an International Atomic Energy Agency coordinated research project, (2010).

[5] B. Beverskog, I. Puigdomenech, Revised Pourbaix diagrams for iron at 25–300 C, Corrosion Science, 38 (1996) 2121-2135.

[6] B. Beverskog, I. Puigdomenech, Revised Pourbaix diagrams for nickel at 25–300 C, Corrosion Science, 39 (1997) 969-980.

[7] B. Beverskog, I. Puigdomenech, Revised Pourbaix diagrams for chromium at 25–300 C, Corrosion Science, 39 (1997) 43-57.

[8] B. Beverskog, I. Puigdomenech, Pourbaix diagrams for the ternary system of iron-chromium-nickel, Corrosion, 55 (1999) 1077-1087.

[9] O. Kubaschewski, C.B. Alcock, P.J. Spencer, Materials thermochemistry, Pergamon Press, 1993.

[10] J. Majzlan, E. Lang Brian, R. Stevens, A. Navrotsky, F. Woodfield Brian, J. Boerio-Goates, Thermodynamics of Fe oxides: Part I. Entropy at standard temperature and pressure and heat capacity of goethite (α-FeOOH), lepidocrocite (γ-FeOOH), and maghemite (γ-Fe2O3), in: American Mineralogist, 2003, pp. 846.

[11] J.W. Geus, Preparation and properties of iron oxide and metallic iron catalysts, Applied Catalysis, 25 (1986) 313-333.

[12] H. Franz, Process for the preparation of gamma-FeOOH, in, Google Patents, 1968.

[13] R. Jasinski, A. Iob, FTIR measurements of iron oxides on low alloy steel, Journal of the Electrochemical Society, 135 (1988) 551-556.

[14] A.P. Oliveira, R.B. Faria, The chlorate− iodine clock reaction, Journal of the American Chemical Society, 127 (2005) 18022-18023.

[15] R.S. Mitchell, Iodine clock reaction, J. Chem. Educ, 73 (1996) 783.

[16] Y. Pomeau, J. Roux, A. Rossi, S. Bachelart, C. Vidal, Intermittent behaviour in the Belousov-Zhabotinsky reaction, Journal de Physique Lettres, 42 (1981) 271-273.

[17] V.K. Vanag, I.R. Epstein, Pattern formation in a tunable medium: The Belousov-Zhabotinsky reaction in an aerosol OT microemulsion, Physical review letters, 87 (2001) 228301.

[18] V.K. Vanag, A.M. Zhabotinsky, I.R. Epstein, Oscillatory clusters in the periodically illuminated, spatially extended Belousov-Zhabotinsky reaction, Physical review letters, 86 (2001) 552.

[19] V. Petrov, V. Gaspar, J. Masere, K. Showalter, Controlling chaos in the Belousov—Zhabotinsky reaction, Nature, 361 (1993) 240-243.

[20] L. Györgyi, R.J. Field, A three-variable model of deterministic chaos in the Belousov–Zhabotinsky reaction, Nature, 355 (1992) 808-810.

[21] C.-O. Olsson, D. Landolt, Passive films on stainless steels—chemistry, structure and growth, Electrochimica acta, 48 (2003) 1093-1104.

[22] I. Olefjord, B.-O. Elfstrom, The composition of the surface during passivation of stainless steels, Corrosion, 38 (1982) 46-52.

[23] T. Sutherland, C. Sparks, J. Joseph, Z. Wang, G. Whitaker, T. Sham, J. Wren, Effect of ferrous ion concentration on the kinetics of radiation-induced iron-oxide nanoparticle formation and growth, Physical Chemistry Chemical Physics, 19 (2017) 695-708.

[24] K. Daub, X. Zhang, L. Wang, Z. Qin, J.J. Noël, J.C. Wren, Oxide growth and conversion on carbon steel as a function of temperature over 25 and 80°C under ambient pressure, Electrochimica acta, 56 (2011) 6661-6672.

[25] Q.W. Knapp, J.C. Wren, Film formation on type-316L stainless steel as a function of potential: Probing the role of gamma-radiation, Electrochimica acta, 80 (2012) 90-99.

[26] M. Behazin, M.C. Biesinger, J.J. Noël, J.C. Wren, Comparative study of film formation on high-purity Co and Stellite-6: Probing the roles of a chromium oxide layer and gamma-radiation, Corrosion Science, 63 (2012) 40-50.

[27] M. Behazin, J.J. Noël, J.C. Wren, Combined Effects of pH and γ-Irradiation on the Corrosion of Co-Cr Alloy Stellite-6, Electrochimica Acta, 134 (2014) 399-410.

[28] A.Y. Musa, M. Behazin, J.C. Wren, Potentiostatic Oxide Growth Kinetics on Ni-Cr and Co-Cr Alloys: Potential and pH Dependences, Electrochimica Acta, 162 (2015) 185-197.

Chapter 6

The Effect of Oxygen Content and Gas Phase Radiolysis on Corrosion of Alloy 800H in High-Temperature Steam

6.1 Introduction

The importance of safe and optimal operation of nuclear power plants motivates researchers to better understand the factors influencing the corrosion of metal alloys. Uniform corrosion of system components in nuclear reactors introduces dissolved metal impurities in the reactor coolant that can lead to the formation of insoluble metal oxide particulates that deposit in the heat transport system. In addition, the circulation of these dissolved metal species through the reactor core can cause neutron absorption by stable isotopes to form radioactive products (e.g., ^{54}Mn, ^{58}Co, ^{59}Fe, ^{60}Co, or ^{58}Ni) [1]. Deposition of radioactive materials on coolant system components outside of the shielding of the reactor core creates a potential source of radiation exposure for plant workers.

The emphasis in this study is on the effects of radiolysis products on the corrosion of structural materials in high temperature steam. Strongly oxidizing radiolysis products such as H_2O_2 and O_2 can interact with the protective oxide on different materials and influence their subsequent corrosion behaviour. Furthermore, it is important to understand the release of corrosion products from these structural materials, as this influences the radioactivity transport within the coolant circuit.

This study investigates the effect of O_2 and γ-radiation on Alloy 800H corrosion in steam at 285 ^{o}C. Alloy 800H is one of the candidate fuel cladding materials being investigated for potential use in a Canadian design of a Generation IV supercritical water reactor (SCWR). Because the solvent properties [2-10] and the radiolysis kinetics [10] of SCW lie somewhere between those of liquid water and steam, this study on steam corrosion, combined with existing studies [10-17], may provide an insight into SCW corrosion of Alloy

800H and, in particular, the effect of γ-radiolysis on the SCW corrosion. Due to difficulties in performing SCW corrosion tests in the presence of high dose γ-radiation, it has been suggested that SCW corrosion in the highly oxidizing environment induced by radiolysis could be simulated by adding a high concentration of O_2 into SCW. This study tries to partially address this possibility by performing corrosion tests with different O_2 concentrations in steam with or without radiation present.

6.2 Experimental

6.2.1 Materials

The Alloy 800H was purchased in rod form (American Special Metals Corp.). The chemical composition of this alloy is given as (in wt.%) 45 Fe, 31 Ni and 23 Cr. The rod was cut into discs. The total surface area of Alloy 800H exposed in each experiment was 9.12 cm². Prior to each experiment, the discs were ground manually in sequence with 180, 400, 800 and 1200 grit silicon carbide papers, followed by polishing on a Texmet micro cloth (Buehler) with a 1 µm MetaDi Supreme diamond paste suspension (Buehler), and lastly, sonication in a 1:1 acetone/methanol mixture for five minutes to remove polishing residues.

6.2.2 Experimental Conditions

Corrosion experiments were conducted in saturated steam at 285 °C. The corrosion studies were carried out in a 300 mL AISI 316 stainless steel autoclave purchased from Parr Instrument Company. The test specimens were arranged in a pre-oxidized zirconium specimen holder to ensure no exposure of the test specimen to the condensed phase during the experiments. At the time of closure, the autoclave contained 20 mL (only 7% of the autoclave volume) of liquid Type-1 water (Barnstead International NANOpure Diamond UV, 18.2 MΩ·cm). The gaseous headspace of the vessel was filled with either ultra-high purity Ar (99.999%, Praxair), or a 35% O_2 + 65% Ar or a 50% O_2 + 50% Ar mixture (Praxair), which was introduced by sparging the partially closed vessel for 90 min before the autoclave was sealed. The experiments were carried out either during exposure to γ-radiation or without radiation. The duration of each exposure was 5 h.

All experiments involving irradiation were conducted in a MDS Nordion Gammacell 220 Excel Cobalt-60 irradiator. As described in Chapter 3, in irradiation experiments, the autoclave was positioned inside the gammacell sample chamber, and the chamber lowered into the gammacell irradiation zone, centred within a cylinder bounded by 11 tubular pencils containing ^{60}Co. The dose rate during the period of experimentation was 3.1-3.3 kGy·h^{-1}, as calibrated by Fricke dosimetry.

6.2.3 Surface Characterization

Scanning electron microscopy (SEM) images were obtained using a LEO (Zeiss) 1540XB focussed ion beam (FIB)/SEM/EDX. X-ray photoelectron spectroscopic (XPS) analyses were performed using a Kratos Axis Ultra XPS with a monochromatic Al K(α) source. Raman scattering measurements were performed using a Renishaw model 2000 instrument. Auger electron spectroscopy (AES) combined with argon-ion sputtering provided a depth profile of the chemical composition of surface oxides. The AES analyses were performed using a Physical Electronics Model PHI 660 instrument with an excitation energy of 5 keV.

6.3   Results

The surfaces of Alloy 800H coupons corroded for 5 h in saturated steam containing different concentrations of O_2 with or without radiation present were examined using several surface analysis techniques. The SEM micrographs are shown in Figure 6-1. On the sample exposed to 285 °C saturated steam in an Ar atmosphere in the absence of radiation, scattered crystallites of 100 nm dimensions were observed to be distributed over a surface that appears to have experienced only minor amounts of corrosion, since the scratches from surface preparation are still clearly visible. This picture shows that there is no preferential site for nucleation of particles and they are randomly distributed on the surface. The sample exposed to 285 °C saturated steam with added 35 % oxygen showed numerous particles, mostly in the ~30 nm range, carpeting the Alloy 800H surface. Here also the superficial scratches from the initial surface preparation remain visible, indicating that the total amount of corrosive attack was minimal, but in this case the fine particulate corrosion products are found

everywhere on the surface including the ridges and valleys of surface scratches, however they are too small to obscure the surface topography. The surface of the sample exposed to the 50 % O_2 shows an underlying oxide layer which is covered by secondary oxide particles. These particles (generally less than few nm size) are agglomerated locally to form a network of particles linked to each other. The effect of change in the oxygen content of environment can be clearly seen in the number of particles nucleated on the surface and their size after growth.

In the presence of gamma radiation, in the Ar environment, Alloy 800H appears similar to the one in the absence of radiation except for the size and distribution of the particles on the surface. In this case, number of density of particles is less and they are bigger in the size than the one in the absence of radiation. In oxygen-bearing steam at 285 °C, with the autoclave exposed to gamma radiation, only a few, widely dispersed filaments of deposited material could be seen, along with the scratches from surface preparation. However, in the presence of 50% O_2, these particles seem to form on top of a thick oxide layer underneath.

The oxide morphology analysis shows that the effect of change in the oxygen content is not as significant as the presence of radiation. In the presence of radiation, increase in the oxygen content significantly affect the surface morphology and oxide thickness. However, in the absence of radiation, when oxygen content increases, change in the corrosion rate is not as fast as in presence of radiation. In fact, it seems that presence of radiation completely changes the corrosion pathway however, oxygen only changes the rate at which the reactions happen under saturated steam corrosion.
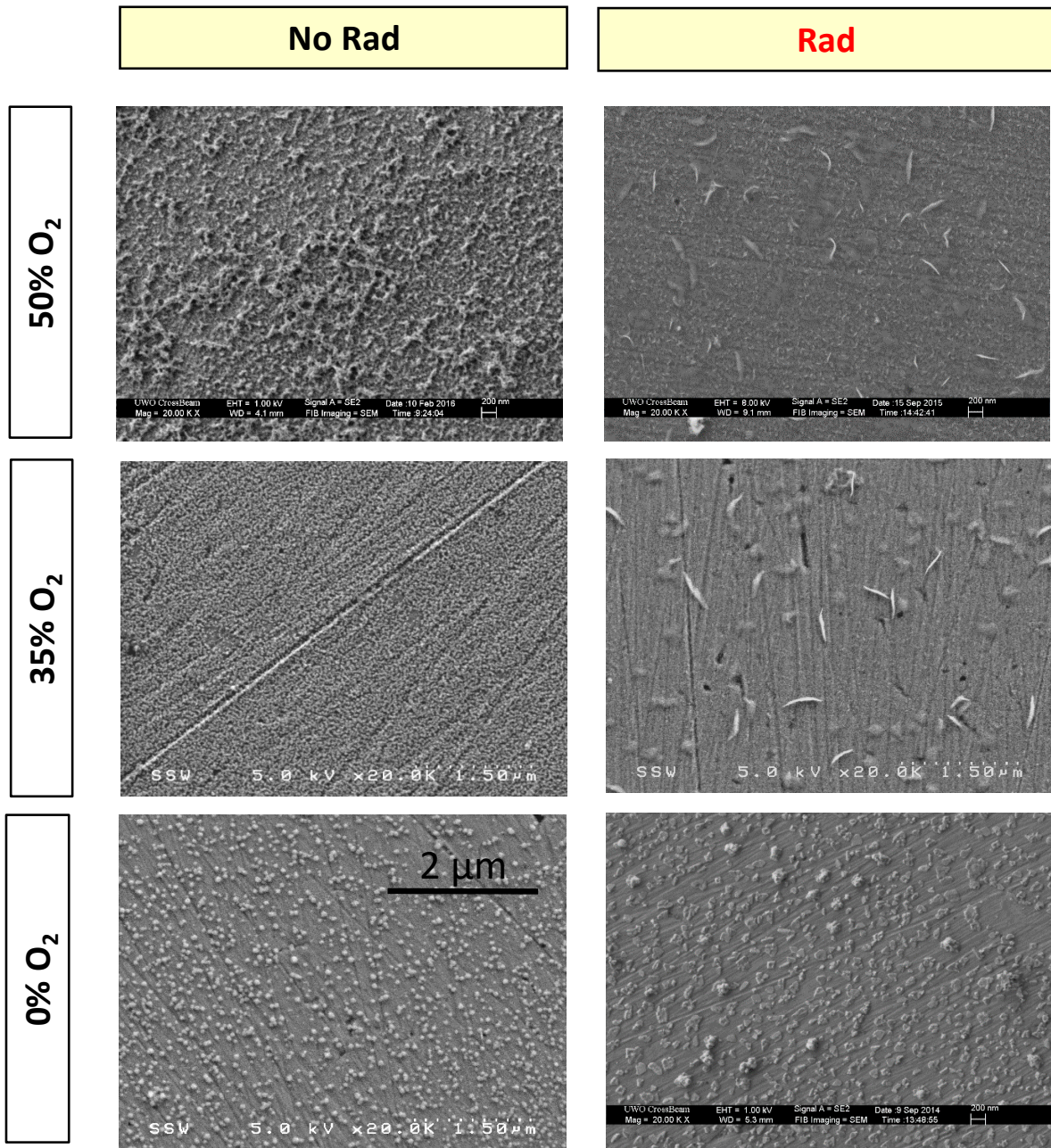
Figure 6-1: SEM micrographs of the surfaces of Alloy 800H coupons exposed for 5 h to saturated steam in Ar gas containing different O_2 concentrations, without (No Rad) or with (Rad) γ-radiation present.

The Raman spectra are compared with the spectra of standard powder samples of various Cr, Fe and Ni oxides in Figure 6-2 [18]. Although more granular particles are present on the coupons corroded without radiation, the intensities of the Raman spectra are much

lower than those observed for the coupons corroded with radiation. For the coupons corroded without radiation present, the spectrum of the coupon corroded in 0% O_2 in Ar shows the peaks that correspond to the two main peaks of $FeCr_2O_4$ and the main peak of Fe_3O_4 while that spectrum of the coupon corroded in 50% O_2 in Ar matches more closely that of magnetite (Fe_3O_4). For the coupons corroded with radiation present, the spectrum of the coupon corroded in 35% O_2 in Ar consists of the main peak associated with Fe_3O_4 and minor peaks that are associated with $CrOOH$ and $Ni(OH)_2$. The Raman spectrum of the coupon corroded in 50% O_2 in Ar is similar to that observed for the coupon corroded in a lower O_2 concentration environment, but the intensities of the peaks associated with Fe_3O_4 and $Ni(OH)_2$ are higher while those of $CrOOH$ are lower.

The Raman analysis suggests that the main oxide present on these surfaces is Fe_3O_4 (except for the coupon corroded in 0% O_2 in Ar without radiation present). However, the morphologies of the granular oxide particles are very different. These observations suggest that the oxide particles may grow into different shapes and that the oxide morphology evolution depends on the exposure environment. The oxide thickness and the depth variation of the oxide composition can provide some information on oxide growth.
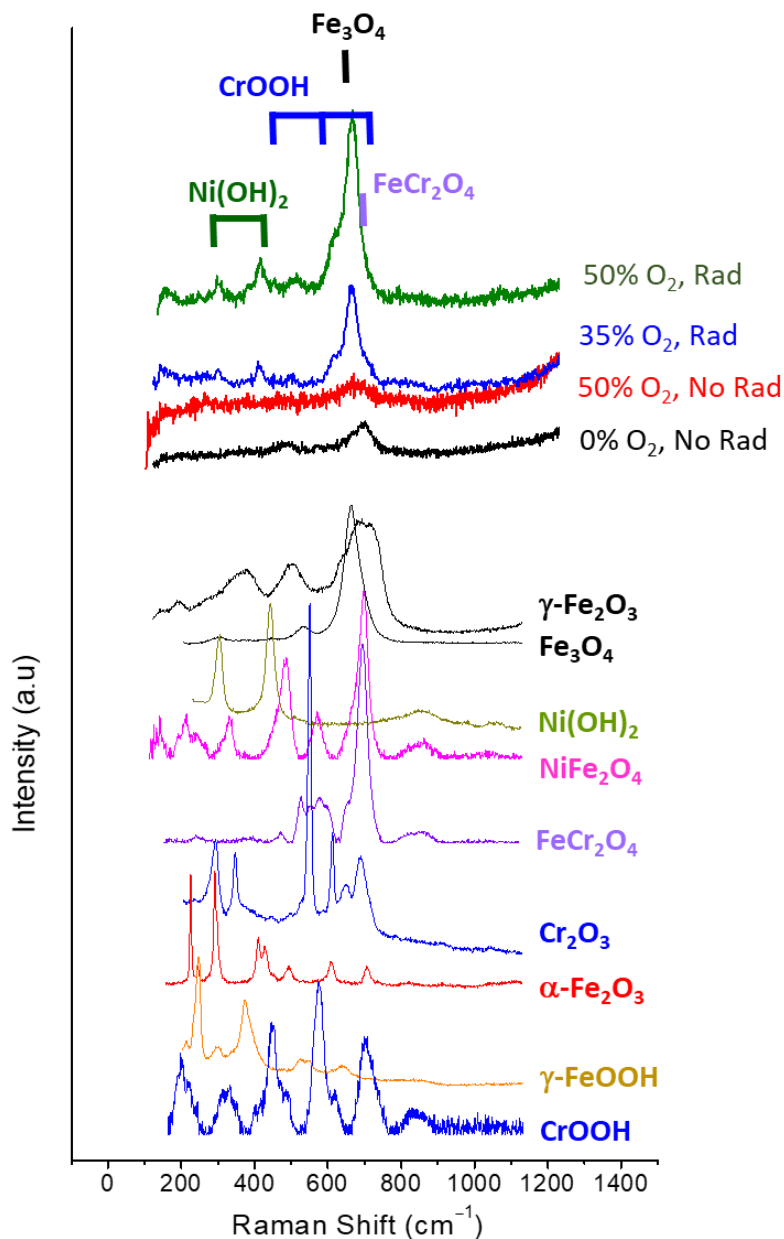
Figure 6-2: Raman spectra of the surfaces of Alloy 800H coupons exposed for 5 h to saturated steam in Ar gas containing 0% or 50% O_2, without γ-radiation present and spectra for surfaces exposed in Ar gas containing 35% or 50% O_2 with γ-radiation present. Shown below the coupon spectra are the spectra of standard powder samples of various Cr, Fe and Ni oxides. The Raman shifts of the main peaks of these oxides are also noted on the top of the coupon spectra [18].

The XPS analysis was performed to determine the oxidation-state composition of the metal elements in the top ~ 8 nm surface layer. A low-resolution survey spectrum over a wide binding energy range of 0 to 1200 eV and high-resolution spectra over the binding energy ranges of Cr-2$p_{3/2}$, Fe-2$p_{3/2}$ and Ni-2$p_{3/2}$ along with those of O-1s and C-1s were taken. Examples of the raw XPS spectra are shown in Figure 6-3. The high-resolution XPS spectra were deconvoluted using reference spectra taken from well-characterized oxide powder samples to obtain the composition of the oxidation states present of individual metal elements. For chromium, contributions of Cr^0, Cr_2O_3, $Cr(OH)_3$ and Cr^{VI} to the Cr-2$p_{3/2}$ spectra were considered. For iron, those from Fe^0, FeO, Fe_3O_4 (mixed Fe^{II}/Fe^{III} oxide), Fe_2O_3 and FeOOH to the Fe-2$p_{3/2}$ spectra, and for nickel those of Ni^0, NiO and $Ni(OH)_2$ to the Ni-2$p_{3/2}$ spectra were considered. The separation of metal oxide from metal hydroxide was further aided by deconvolution of the O-1s and C-1s spectra (results not shown). Detailed descriptions of binding energies and the spectral deconvolution method can be found elsewhere [19-22]. The results of the deconvolution of the high-resolution XPS data into metallic and oxidized components for the three main metal elements are presented in Figure 6-4.
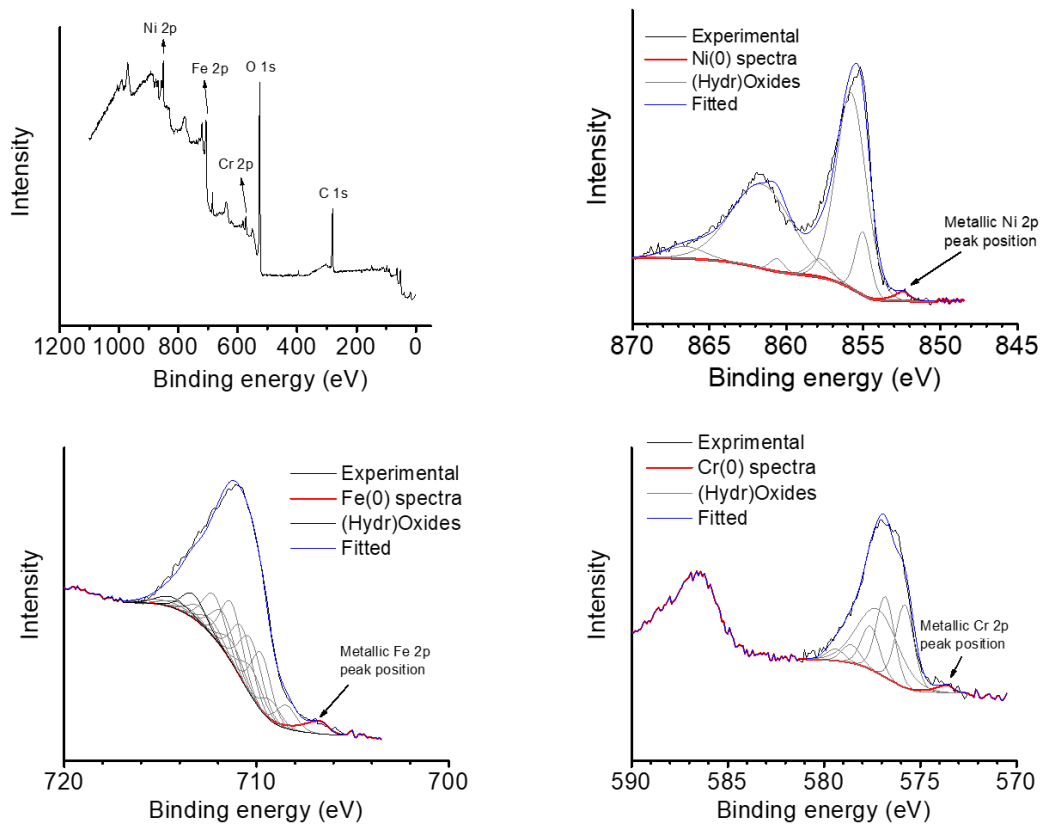
Figure 6-3: **XPS spectra taken from an Alloy 800H surface corroded for 5 h in saturated steam in 50% O₂ in Ar at 285 ºC without γ-radiation: (a) the survey spectrum and the high-resolution spectra of (b) Ni 2p₃/₂, (c) Fe 2p₃/₂ and (d) Cr 2p₃/₂. Also shown are the deconvoluted spectra of individual components, each consisting of multiple peaks, and the fitted spectra from the deconvoluted spectra.**
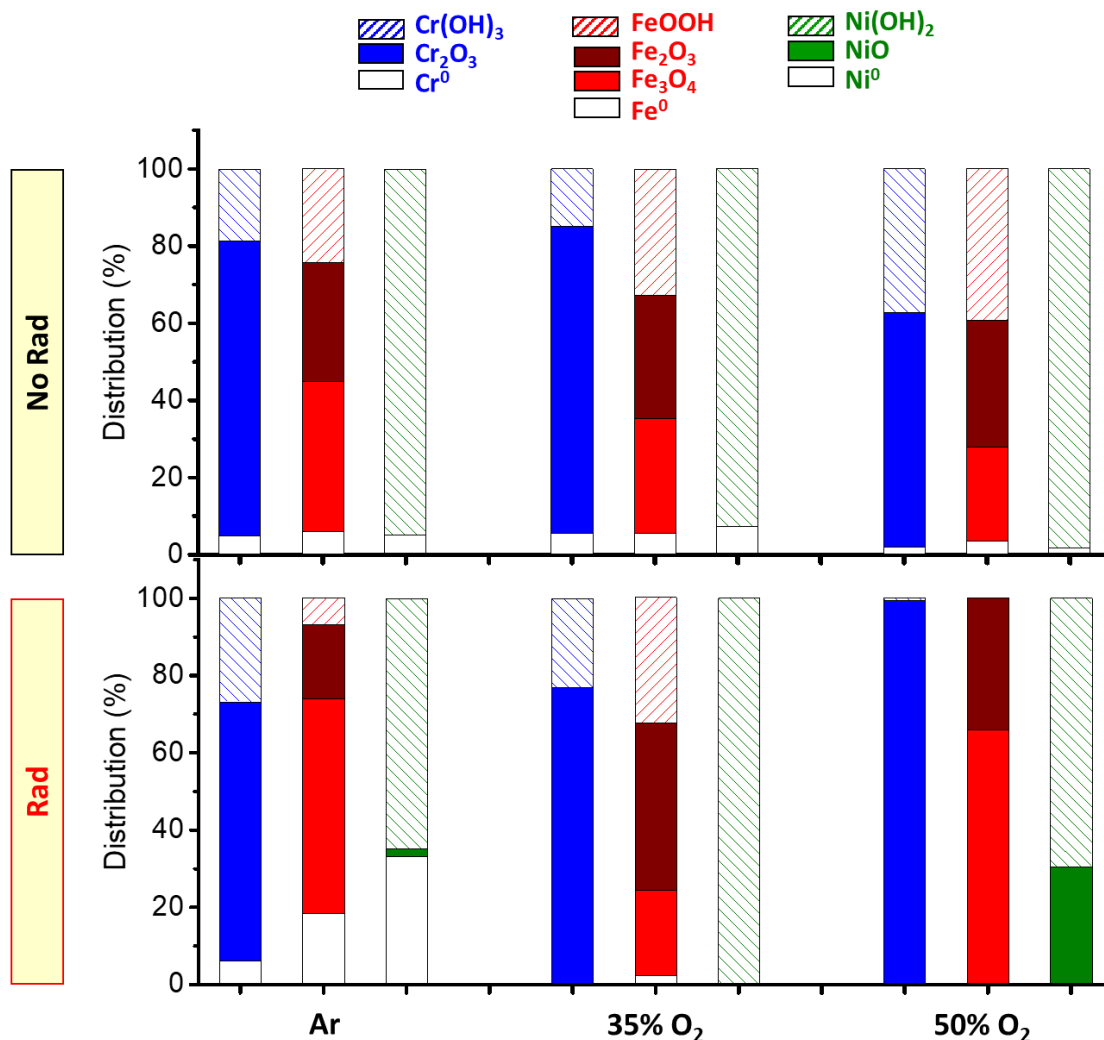
Figure 6-4: Oxidation-state compositions of chromium (blue), iron (red) and nickel (green) determined by XPS analysis of Alloy 800H coupons exposed for 5 h to saturated steam in Ar gas containing different O_2 concentrations without (No Rad) or with (**Rad**) γ-radiation present. The atomic percentages of metallic components are shown with white bars, those of oxide components with solid bars, and those of hydroxides or oxyhydroxides with patterned bars.

Except for the surface layer of the coupon corroded in 0% O_2 in Ar with radiation present, the metallic fractions are small but not negligible. For a given radiation condition, the metallic fraction is generally lower at a higher O_2 concentration in the exposure environment. The lower the metallic fraction is, the thicker the oxide layer is. Interestingly,

for the coupons corroded in 0% O_2 in Ar, the metallic fraction is higher on the coupon corroded with radiation than on the one corroded without radiation present. However, the metallic fraction decreases more extensively with increased O_2 concentration in the exposure environment with radiation present. Consequently, with radiation present the metal fraction is extremely small or zero in the surface layer of the coupon corroded in 35% O_2 or 50% O_2.

Comparison of the oxidation-state compositions presented in Figure 6-4 with the surface morphologies presented in Figure 6-1 provides interesting observations. The coupon corroded in 50% O_2 without radiation present shows more granular oxide than the one corroded with radiation present, but the XPS analysis results indicate that the average thickness of the oxide present on the coupon corroded without radiation present is thinner (there is a higher metallic component) than that on the coupon corroded with radiation present. Similarly, with radiation present the number density of oxide particles decreases with increasing O_2 concentration while the average thickness of the oxide increases.

The ratio of hydroxide to oxide fraction in the surface layer shows a different dependence on O_2 concentration depending on the metal element. For chromium, the oxidized components in the surface layer are Cr^{III} oxide and Cr^{III} oxyhydroxide. Although they are labeled as Cr_2O_3 and $Cr(OH)_3$ they may not be present as pure Cr_2O_3 and $Cr(OH)_3$ phases. For nickel, the oxidized components in the surface layer are Ni^{II} oxide and Ni^{II} hydroxide. Although the Ni^{II} oxide is labeled as NiO in Figure 6-4 it may be present as $NiFe_2O_4$ and $NiCr_2O_4$. For iron, the oxidized components in the surface layer are Fe^{II}/Fe^{III} oxide (labeled as Fe_3O_4), Fe^{III} oxide (labeled as Fe_2O_3) and Fe^{III} oxyhydroxide (FeOOH).

On the coupons corroded without radiation present, the oxyhydroxide fraction of iron in the surface layer increases, while the metallic Fe^0 fraction decreases, with increasing O_2 concentration in Ar. For chromium, the hydroxide fraction is lowest while the metallic fraction is highest on the coupon corroded in 35% O_2 in Ar. For nickel, the Ni^{II} is all in the form of hydroxide and the dependence of the Ni^{II} hydroxide fraction on the O_2 concentration follows that of Cr. These observations suggest that $Ni(OH)_2$ and $Cr(OH)_3$ are present in the outer-most surface layer and underneath this hydrated and hydroxide layer is a layer of iron oxides/hydroxides that grows thicker in a higher O_2 environment.

On the coupons corroded with radiation present, the metallic fractions of all three metal elements decrease with increasing O_2 concentration. However, the $Cr(OH)_3$ fraction

decreases with increasing O_2 concentration, the opposite trend to that observed without radiation present. In addition, the FeOOH and $Ni(OH)_2$ fractions are highest when the O_2 concentration is 35%. In 50% O_2 in Ar, the average thickness of oxide is thicker than 8 nm and within this surface layer, most of the chromium is present as Cr^{III} oxide and most of the iron is present as mixed Fe^{II}/Fe^{III} oxide and Fe^{III} oxide, while a significant fraction of the oxidized nickel is in the form of Ni^{II} oxide as well as Ni^{II} hydroxide.

The XPS analysis results are consistent with the Raman analysis results. The combined results indicate that during 5 h steam corrosion without radiation present the metal oxidation progresses up to the oxidation of Fe^0 to Fe^{II} forming $FeCr_2O_4$ (in the presence of Cr_2O_3) but not to the oxidation to Fe^{II}/Fe^{III} and Fe^{III} oxides/hydroxides. The rate of formation of Fe_3O_4 (and its conversion to $\gamma\text{-}Fe_2O_3$) increases with increasing O_2 concentration. Without radiation present the oxidation of Ni^0 to Ni^{II} is limited to the formation of a few monolayers of $Ni(OH)_2$. The rates of the oxidation reactions are slow without radiation present even under high O_2 concentration conditions. The higher fractions of $Cr(OH)_3$ and $Ni(OH)_2$ with an increase in O_2 concentration are consistent with the claim that the formation of Fe^{II}/Fe^{III} and Fe^{III} oxides is not fast enough to cover the metal surface quickly enough to suppress the hydration and hydrolysis of Cr^{III} ions from Cr_2O_3 and $FeCr_2O_4$, and the oxidation of Ni^0 to Ni^{II}, see further discussion later.

Gamma-radiolysis of water produce stronger oxidants than O_2, such as $\bullet OH$ and H_2O_2 [23]. Hence, the rates of the oxidation of Fe^0 to Fe_3O_4 ($\gamma\text{-}Fe_2O_3$) and Ni^0 to Ni^{II} oxide and hydroxide will all increase with radiation present. Of the radiolytically produced oxidants, H_2O_2 is the more effective oxidant for surface reactions, and the steady-state concentration of H_2O_2 produced by a continuous radiation flux increases with an increase in O_2 concentration in steam. This is consistent with the observed increases in the Raman peaks associated with Fe_3O_4 ($\gamma\text{-}Fe_2O_3$) and $Ni(OH)_2$ and the reduction in the peaks associated with $Cr(OH)_3$ with increasing O_2 concentration with radiation present.

The SEM, Raman and XPS analysis results all indicate that different oxides are formed at different rates and different stages of corrosion. The rates of individual oxide formation and growth vary depending on O_2 concentration and whether radiation is present or not. To understand how the oxidation may have progressed over 5-h corrosion the depth profiles of different metal elements and O atom were examined by AES with Ar^+ sputtering.

The depth profiles of atomic percentages of three main metal elements (Cr, Fe and Ni) and oxygen (O) are presented in Figure 6-5.

The depth profiles of elemental atomic percentages show four depth ranges with different characteristic depth dependences. The four depth zones are most noticeable on the coupon corroded in 50% O_2 in Ar with radiation present, and the different zones on the depth profiles of this coupon are illustrated in Figure 6-6. Also shown in the figure are the depth profiles of atomic percentage ratios of O/(Fe + Ni + 1.5Cr) and O/(1.5Fe + 2Ni + 1.5Cr). On this coupon, in the depth range of 0 - 8 nm (zone 1) the Cr at.% and Ni at.% remains nearly constant with depth at ~ 5 at.%, while the Fe at.% increases very slowly with increasing depth and the O at.% decreases at a similar rate. In zone 1, the ratio of O/(1.5Fe + 2Ni + 1.5Cr) is greater than 1.0. In depth range of 8 – 18 nm (zone 2), the Cr at.% and the Ni at.% increase with increasing depth while the Fe at.% and the O at.% decrease with increasing depth. In zone 2, the rate of decrease in the Fe at.% is faster than that of the O at.%. In this zone, the ratio of O/(1.5Fe + 2Ni + 1.5Cr) is less than 1.0 while the ratio of O/(Fe + Ni + 1.5Cr) is greater than 1.0. At greater depths (> 18 nm) the O at.% decreases sharply while the atomic percentages of all three metal elements increase. The Fe at.% and the Cr at.% increase steadily until they reach constant values as the O at.% decreases to a background level (~ 5 at.%), but the Ni at.% shows a maximum at ~ 25 nm before it decreases to a constant value (Figure 6-5). The depth where the Ni at.% is maximum is typically the depth where the ratio of O/(Fe + Ni + 1.5Cr) is 0.5. The ratio of 0.5 is the average depth of oxide/metal interface. Thus, zone 3 is defined as the depth range over which the ratio of O/(Fe + Ni + 1.5Cr) lies between 1.0 and 0.5. Zone 4 (22 – 30 nm) is the oxide-metal phase transition range. The pure (unoxidized) alloy phase begins below zone 4.
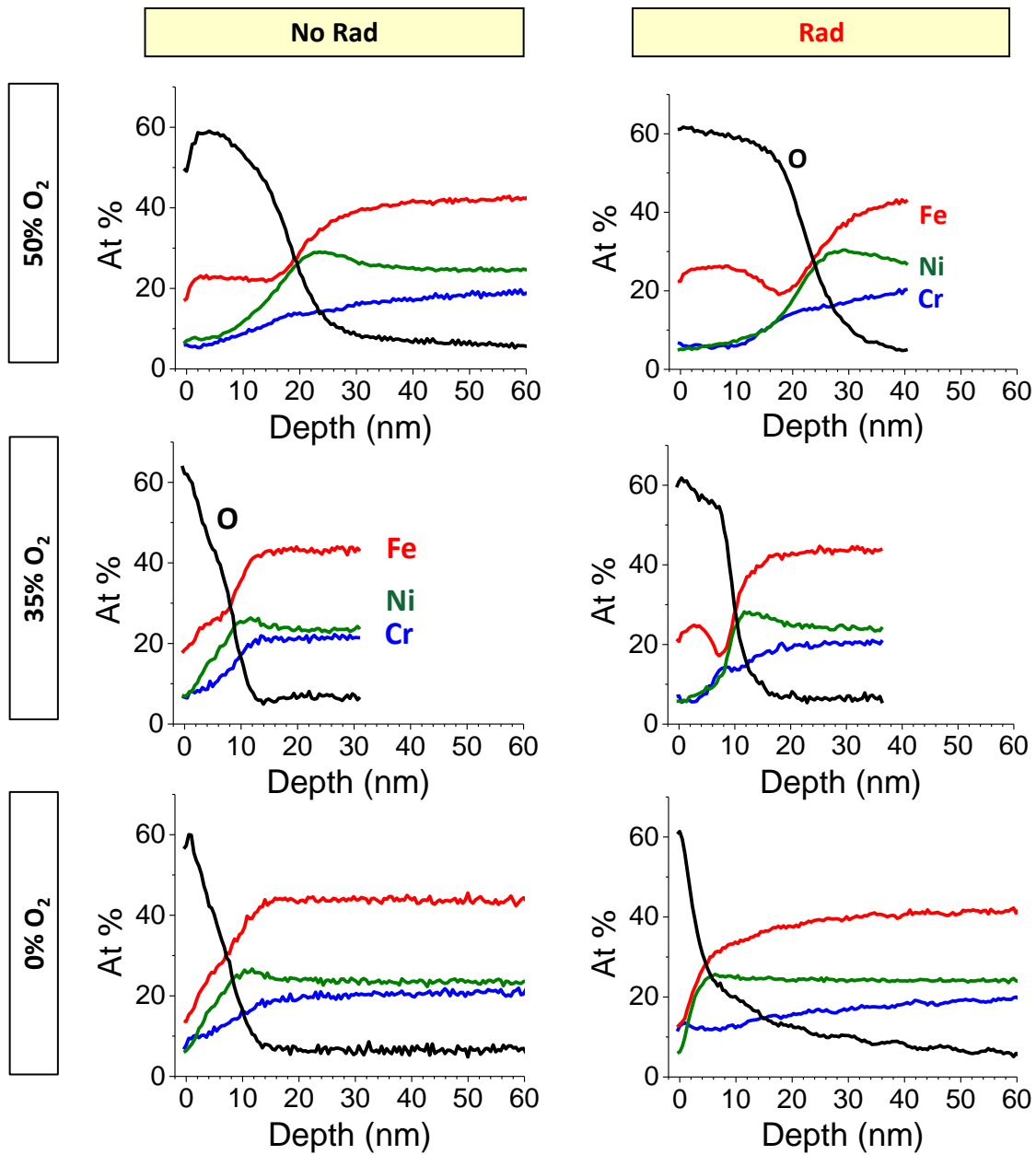
Figure 6-5: AES depth profiles of the atomic percentages of metal elements (Fe, Cr and Ni) and oxygen (O) obtained for Alloy 800H after 5-h exposure to saturated steam containing different O_2 concentrations without (No Rad) or with (Rad) γ-radiation present.
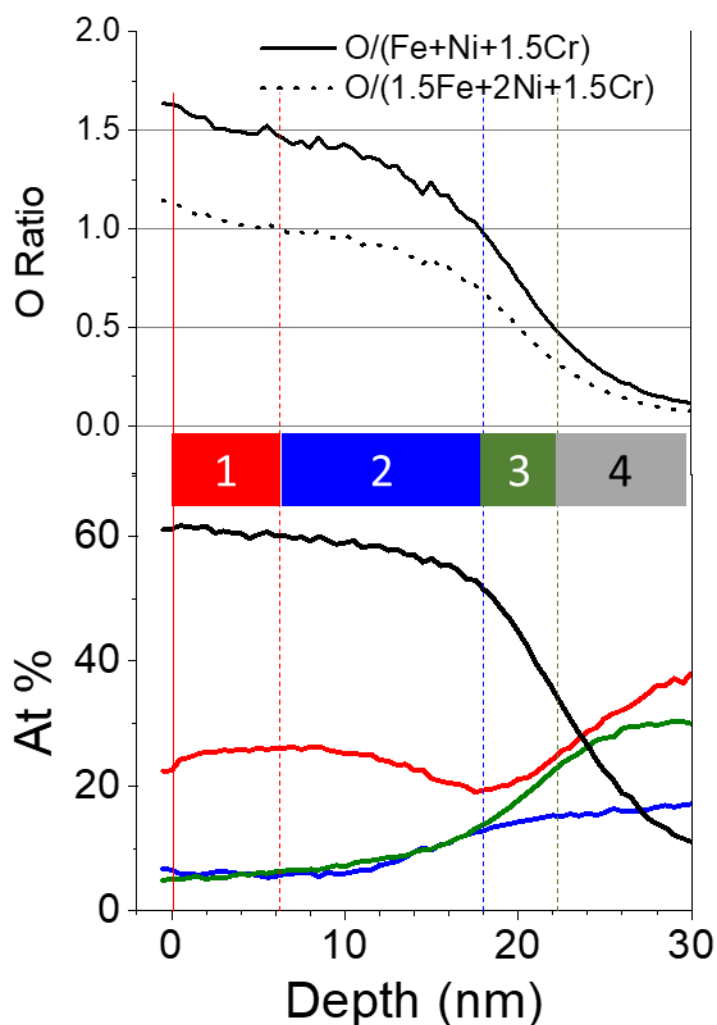
Figure 6-6: Schematic of the four depth zones of different characterisitic depth profiles of the atomic percentateges of metal elements (**Fe**, **Cr** and **Ni**) and O (black line) and the ratios of O/(Fe + Ni + 1.5Cr) and O/(1.5Fe + 2Ni + 1.5Cr) on a coupon corroded for 5 h in saturated steam and 50% O_2 in Ar with γ-radiation present.

In summary, there are four characteristic oxide zones and their depth ranges correlate well with the atomic percentage ratios of O/(1.5Fe + 2Ni + 1.5Cr) and O/(Fe + Ni + 1.5Cr). Zone 1 is the depth range where the ratio of O/(1.5Fe + 2Ni + 1.5Cr) is greater than 1.0, and the high ratio indicates that this outermost layer is a hydrated or hydroxide layer. Zone 2 is the range where the ratio of O/(1.5Fe + 2Ni + 1.5Cr) is less than 1.0 but the ratio of O/(Fe + Ni + 1.5Cr) is greater than 1.0. This is the layer where all of the metals are in oxidized states.

In this oxide layer the chemical and phase composition may change with depth from that consisting of Fe^{III} and Cr^{III} oxides and Ni^{II} hydroxide to that consisting of the oxides of Fe^{II}, Cr^{III} and Ni^{II}. Zone 3 is the range where the ratio of $O/(Fe + Ni + 1.5Cr)$ is between 1.0 and 0.5. In this layer, not all metals are in oxidized states.

Because the different ratios of $O/(1.5Fe + 2Ni + 1.5Cr)$ and $O/(Fe + Ni + 1.5Cr)$ are good indicators of the depths where the transitions from one zone to the next occur, the depth profile data presented in Figure 6-5 are replotted as the depth profiles of the ratios in Figure 6-7. The depth range of each zone varies with O_2 concentration and whether radiation is present or not. Without radiation present, the range of zone 1 is very thin and it increases with increasing O_2 concentration. The ranges of zone 2 and zone 3 increase with increasing O_2 concentration. The increases in zone 2 and zone 3 are not significant when the O_2 concentration is increased from 0% to 35%, but are more significant when the O_2 concentration is increased from 35% to 50%. With radiation present, the depth ranges of all three zones increase with increasing O_2 concentration. The depth range of zone 3 is narrower while the depth range of zone 2 is wider with radiation present compared to without radiation present.
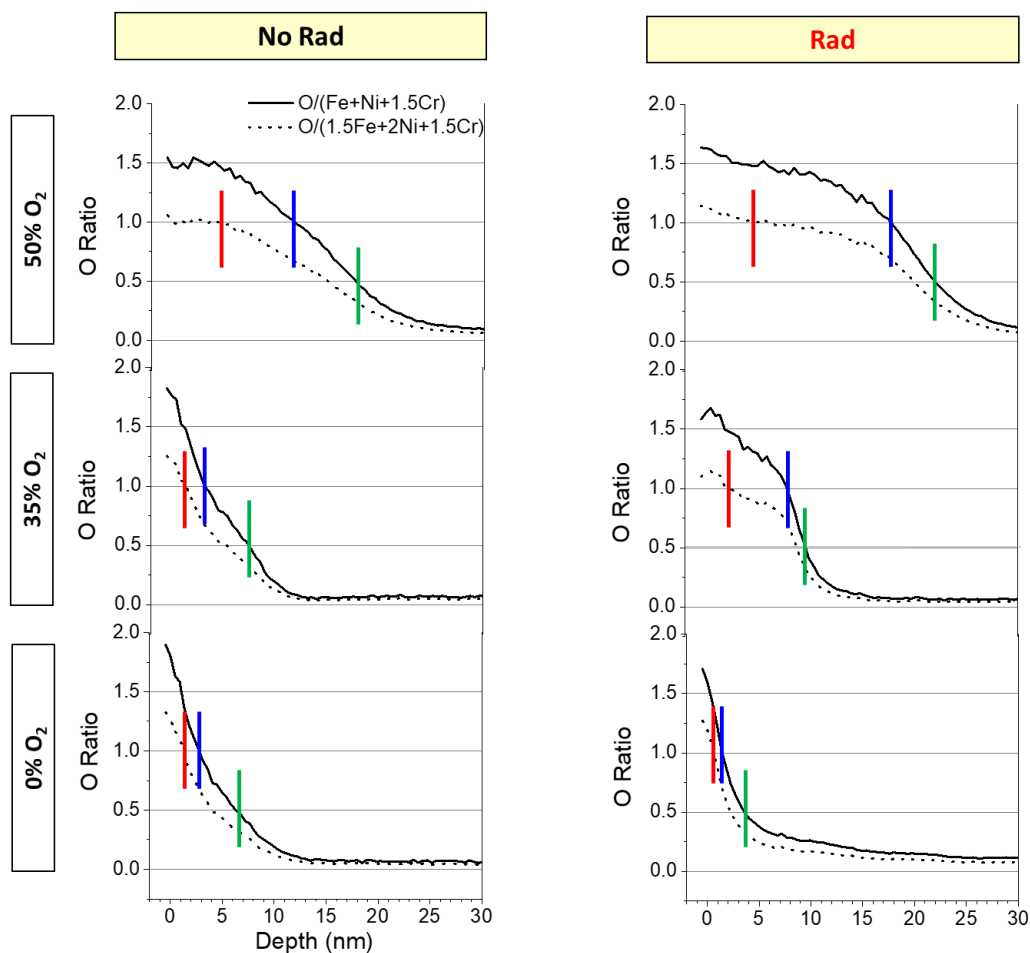
Figure 6-7: **Atomic percentage ratios of O/(Fe + Ni + 1.5Cr) and O/(1.5Fe + 2Ni + 1.5Cr) calculated from the AES depth profiles taken for Alloy 800H after 5-h exposure to saturated steam containing different O_2 concentrations without (No Rad) or with (Rad) γ-radiation present. The vertical bars indicate the depths where the ratios of O/(Fe + Ni + 1.5Cr) and O/(1.5Fe + 2Ni + 1.5Cr) are 1.0 and the ratio of O/(Fe + Ni + 1.5Cr) is 0.5 as shown in Figure 6-6.**

The AES depth profiles are consistent with the XPS results. The dependences of the average oxide thickness (or the depth of the oxide/metal interface) on O_2 concentration and radiation determined by AES depth profile analysis are inversely related to the dependences of the metallic fractions in the top ~ 8 nm layer determined by the XPS analysis. The dependences of the thickness of zone 1 which contains a high fraction of hydrated and hydrolyzed metal cations on O_2 concentration and radiation correlate well with the

162

hydroxide/oxyhydroxide fractions in the top 8 nm layer, except for the coupon corroded in 50% O_2 with radiation present which has an average oxide thickness far greater than the XPS analysis depth.

6.4 Discussion

The depth profiles, the oxidation-state compositions determined by XPS, the chemical and phase compositions of oxides characterized by Raman analysis and the surface morphologies seen by SEM suggest that the oxide formation and growth over 5-h corrosion in saturated steam may progress as schematically shown in Figure 6-8.
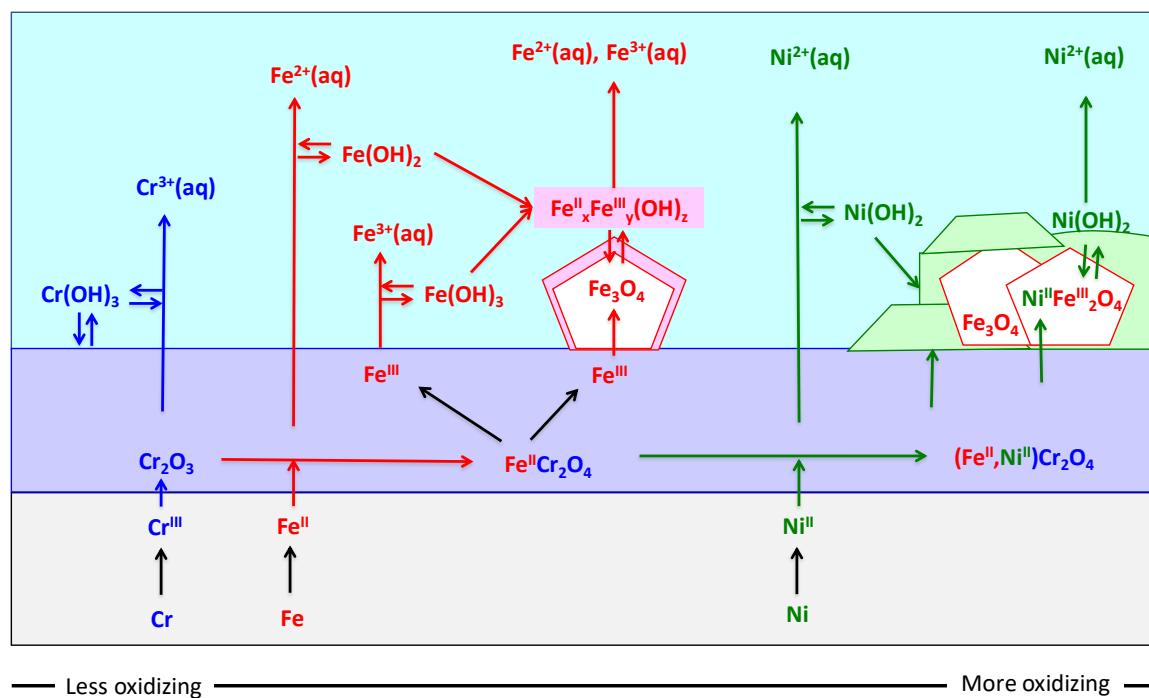
Figure 6-8: **Schematic of oxide formation and growth pathways during corrosion of Alloy 800H in saturated steam.**

According to the proposed mechanism metal oxidation progresses to form metal cations (Figure 6-8) having different oxidation states at different rates, depending on how

oxidizing the exposure environment is. Steam with no added O_2 (0% O_2) without radiation present provides the least oxidizing environment, and in this exposure environment the dominant process is the oxidation of Fe^0 to Fe^{II} which either dissolves into any condensed steam droplets present as $Fe^{2+}_{(aq)}$, grows as $FeCr_2O_4$, or further oxidizes to Fe^{III} which dissolves as $Fe^{3+}_{(aq)}$ followed by precipitation as mixed Fe^{II}/Fe^{III} hydroxides and their conversion to Fe_3O_4. The rate of oxidation to form Fe^{II} is slow in 0% O_2 without radiation and hence the oxides that could be formed over 5 h are primarily $FeCr_2O_4$ and some Fe_3O_4. The oxidation of Ni^0 to Ni^{II} which either dissolves into condensed steam or precipitates as $Ni(OH)_2$ upon saturation of the condensed water with $Ni^{2+}_{(aq)}$ may occur, but the 0% O_2 environment is not oxidizing enough for the nickel oxidation to occur at any substantial rate. Steam with 35% O_2 in Ar without radiation present is more oxidizing and this increases the rate of Fe^0 oxidation to Fe^{II} and Fe^{III} and the rate of formation and growth of Fe_3O_4. However, the rates of metal oxidation and particle growth are still too slow to form an extensive layer of Fe_3O_4 over 5 h. When the O_2 concentration is increased to 50 % in Ar the formation and growth of Fe_3O_4 over 5 h is more extensive. Without radiation present the oxidation of Ni^0 to Ni^{II} is still too slow to compete with the formation of Fe_3O_4. The proposed mechanism is consistent with the observed dependences of the thickness and composition of oxide on O_2 concentration during 5-h corrosion of Alloy 800H in saturated steam without radiation present.

As described earlier, γ-radiolysis of water produces stronger oxidants than O_2. With radiation present, the iron oxidation can progress beyond the formation of Fe_3O_4 as the radiolytically produced oxidants can oxidize Fe_3O_4 to $γ-Fe_2O_3$. This oxidative conversion is very fast because the two oxides share the same oxide phase structure [24]. The rates of oxidation of Fe^0 to Fe_3O_4 ($γ-Fe_2O_3$) and Ni^0 to Ni^{II} oxide and hydroxide will also all increase with radiation present. Of the radiolytically produced oxidants H_2O_2 is the more effective oxidant for surface reactions, and the steady-state concentration of H_2O_2 increases with an increase in O_2 concentration in steam under a continuous radiation flux [25, 26]. Thus, the thickness of Fe_3O_4 ($γ-Fe_2O_3$) and $Ni(OH)_2$ increase with increasing O_2 concentration with radiation present, consistent with the surface analysis results presented above.

In 0% O_2 a thinner oxide is formed with radiation present than with no radiation despite the presence of oxidizing radiolysis products. This can be explained by the effect of

oxide growth on subsequent metal oxidation. As the layer of solid oxide/hydroxide particles grows, metal oxidation slows down because an oxide layer present on metal surface is an energy barrier for further metal oxidation. Thus, depending on how fast oxide can form and grow, metal oxidation can be suppressed earlier in a more oxidizing environment.

Because γ-radiolysis produces more powerful oxidants, the relative rates of different metal oxidation reactions occurring during corrosion with radiation present will be very different from those occurring during corrosion without radiation present. It is often suggested that the effect of radiolysis on steam or supercritical water corrosion can be simulated by using a high O_2 concentration. Comparison of the results observed for the corrosion in 50% O_2 without radiation with those observed for corrosion in 0% O_2 with radiation present indicates that using a high O_2 concentration may not be able to simulate the oxidizing environments induced by radiation.

The mechanism proposed for oxide formation and growth during steam corrosion of Alloy 800H is the same as the mechanism proposed for aqueous corrosion based on studies under wide ranges of temperature and pH with or without radiation present (Chapters 4 and 5). The aqueous corrosion mechanism consists of the same reaction steps involving metal oxidation and dissolution, and oxide formation. The corrosion of Alloy 800 in saturated steam at 285 °C occurs primarily through electrochemical oxidation of metals coupled with reduction of oxidants dissolved in condensed steam or a thin water film. The main difference between steam corrosion and aqueous corrosion would be the thickness or volume of the water layer which affects the total amounts of metal cations that can dissolve. This, in turn, can affect how early the metal cations can precipitate as solid hydroxide/oxide particles.

6.5   Conclusions

This study indicates that the corrosion of Alloy 800H in saturated steam at 285 °C occurs primarily through electrochemical oxidation of metals coupled with reduction of oxidants dissolved in condensed steam or a thin water film. The thin water film is quickly saturated with the metal cations and the metal cations quickly precipitate as solid hydroxide/oxide particles. Without γ-radiation present the oxides formed over 5-h corrosion consist of mainly $FeCr_2O_4$ (without O_2 present in steam) or Fe_3O_4 (with O_2 present in steam).

An increase in O_2 concentration in steam increases the amount of Fe_3O_4 formed and changes the shape of the oxide particles. With radiation present, the oxides formed consist of Fe_3O_4/γ-Fe_2O_3 and $Ni(OH)_2$.

These short-term exposure studies showed that corrosion of Alloy 800H in steam progresses differently with γ-radiation present and that the effect of γ-radiolysis on corrosion in steam cannot be simulated by simply adding high concentrations of O_2 to steam.

6.6   References

[1] W. Garland, The Essential CANDU, University Network of Excellence in Nuclear Engineering (UNENE), (2014).

[2] D. Guzonas, F. Brosseau, P. Tremaine, J. Meesungnoen, J.-P. Jay-Gerin, Water chemistry in a supercritical water-cooled pressure tube reactor, Nuclear Technology, 179 (2012) 205-219.

[3] J. Cline, K. Takahashi, T.W. Marin, C.D. Jonah, D.M. Bartels, Pulse radiolysis of supercritical water. 1. Reactions between hydrophobic and anionic species, The Journal of Physical Chemistry A, 106 (2002) 12260-12269.

[4] D. Bartels, M. Anderson, P. Wilson, T. Allen, K. Sridharan, Supercritical water radiolysis chemistry. Supercritical water corrosion, INL Generation IV Nuclear Energy Systems, Technical Document, http://nuclear.inel.gov/deliverables/docs/uwnd_scw_level_ii_sep_2006_v3. pdf, (2006).

[5] D.M. Bartels, K. Takahashi, J.A. Cline, T.W. Marin, C.D. Jonah, Pulse radiolysis of supercritical water. 3. Spectrum and thermodynamics of the hydrated electron, The Journal of Physical Chemistry A, 109 (2005) 1299-1307.

[6] G. Wu, Y. Katsumura, Y. Muroya, X. Li, Y. Terada, Hydrated electron in subcritical and supercritical water: a pulse radiolysis study, Chemical Physics Letters, 325 (2000) 531-536.

[7] W.G. Cook, R.P. Olive, Pourbaix diagrams for the nickel-water system extended to high-subcritical and low-supercritical conditions, Corrosion Science, 58 (2012) 284-290.

[8] W.G. Cook, R.P. Olive, Pourbaix diagrams for the iron–water system extended to high-subcritical and low-supercritical conditions, Corrosion Science, 55 (2012) 326-331.

[9] W.G. Cook, R.P. Olive, Pourbaix diagrams for chromium, aluminum and titanium extended to high-subcritical and low-supercritical conditions, Corrosion Science, 58 (2012) 291-298.

[10] V. Subramanian, J.M. Joseph, H. Subramanian, J.J. Noël, D.A. Guzonas, J.C. Wren, Steady-State Radiolysis of Supercritical Water: Model Predictions and Validation, Journal of Nuclear Engineering and Radiation Science, 2 (2016) 021021-021021-021026.

[11] L. Marchetti, S. Perrin, F. Jambon, M. Pijolat, Corrosion of nickel-base alloys in primary medium of pressurized water reactors: New insights on the oxide growth mechanisms and kinetic modelling, Corrosion Science, 102 (2016) 24-35.

[12] S. Hariharan, M. Momeni, V. Subramanian, J.J. Noel, J. Joseph, J.C. Wren, The Influence of Water Radiolysis on Corrosion By Supercritical Water, in: Meeting Abstracts, The Electrochemical Society, 2015, pp. 682-682.

[13] Y. Behnamian, A. Mostafaei, A. Kohandehghan, B. Zahiri, W. Zheng, D. Guzonas, M. Chmielus, W. Chen, J.L. Luo, Corrosion behavior of alloy 316L stainless steel after exposure to supercritical water at 500° C for 20,000 h, The Journal of Supercritical Fluids, 127 (2017) 191-199.

[14] K.I. Choudhry, D.A. Guzonas, D.T. Kallikragas, I.M. Svishchev, On-line monitoring of oxide formation and dissolution on alloy 800H in supercritical water, Corrosion Science, 111 (2016) 574-582.

[15] L. Tan, T.R. Allen, Y. Yang, Corrosion behavior of alloy 800H (Fe–21Cr–32Ni) in supercritical water, Corrosion Science, 53 (2011) 703-711.

[16] D. Guzonas, R. Novotny, Supercritical water-cooled reactor materials–Summary of research and open issues, Progress in Nuclear Energy, 77 (2014) 361-372.

[17] D. Guzonas, W. Cook, Cycle chemistry and its effect on materials in a supercritical water-cooled reactor: a synthesis of current understanding, Corrosion Science, 65 (2012) 48-66.

[18] RRUFF, RRUFF Project website containing an integrated database of Raman spectra, X-ray diffraction and chemistry data for minerals., in, The University of Arizona, 2017.

[19] M.C. Biesinger, B.P. Payne, L.W. Lau, A. Gerson, R.S.C. Smart, X-ray photoelectron spectroscopic chemical state quantification of mixed nickel metal, oxide and hydroxide systems, Surface and Interface Analysis, 41 (2009) 324-332.

[20] A.P. Grosvenor, M.C. Biesinger, R.S.C. Smart, N.S. McIntyre, New interpretations of XPS spectra of nickel metal and oxides, Surface Science, 600 (2006) 1771-1779.

[21] A. Grosvenor, B. Kobe, M. Biesinger, N. McIntyre, Investigation of multiplet splitting of Fe 2p XPS spectra and bonding in iron compounds, Surface and Interface Analysis, 36 (2004) 1564-1574.

[22] M.C. Biesinger, B.P. Payne, A.P. Grosvenor, L.W. Lau, A.R. Gerson, R.S.C. Smart, Resolving surface chemical states in XPS analysis of first row transition metals, oxides and hydroxides: Cr, Mn, Fe, Co and Ni, Applied Surface Science, 257 (2011) 2717-2730.

[23] A. Mozumder, Fundamentals of Radiation Chemistry, Elsevier Science, 1999.

[24] A.J. Davenport, L.J. Oblonsky, M.P. Ryan, M.F. Toney, The structure of the passive film that forms on iron in aqueous environments, Journal of The Electrochemical Society, 147 (2000) 2162-2173.

[25] P.A. Yakabuskie, J.M. Joseph, J. Clara Wren, The effect of interfacial mass transfer on steady-state water radiolysis, Radiation Physics and Chemistry, 79 (2010) 777-785.

[26] J.M. Joseph, B. Seon Choi, P. Yakabuskie, J. Clara Wren, A combined experimental and model analysis on the effect of pH and $O_{2(aq)}$ on γ-radiolytically produced H_2 and H_2O_2, Radiation Physics and Chemistry, 77 (2008) 1009-1020.

Chapter 7

A Mechanistic Model for Oxide Growth and Dissolution during Corrosion of Cr-Containing Alloys[1]

Abstract

We have developed a corrosion model that can predict metal oxide growth and dissolution rates as a function of time for a range of solution conditions. Our model considers electrochemical reactions at the metal/oxide and oxide/solution interfaces, and the metal cation flux from the metal to the solution phase through a growing oxide layer, and formulates the key processes using classical chemical reaction rate or flux equations. The model imposes mass and charge balance and hence, has been named the "Mass Charge Balance (MCB)" model. Mass and charge balance dictate that at any given time the oxidation (or metal cation) flux must be equal to the sum of the oxide growth flux and the dissolution flux. For each redox reaction leading to the formation of a specific oxide, the metal oxidation flux is formulated using a modified Butler-Volmer equation with an oxide-thickness-dependent effective overpotential. The oxide growth and dissolution fluxes have a first-order dependence on the metal cation flux. The rate constant for oxide formation also follows an Arrhenius dependence on the potential drop across the oxide layer and hence decreases exponentially with oxide thickness. This model is able to predict the time-dependent potentiostatic corrosion behaviour of both pure iron, and Co-Cr and Fe-Ni-Cr alloys.

7.1 Introduction

Several corrosion models have been developed for predicting the rate of metal dissolution in the presence of an oxide film [1-13]. To obtain the rate of corrosion under a given driving force (V), many of these models focus on solving the transport rate equations for individual charge carriers (interstitial cations and anions, cation and anion vacancies, and electrons and holes) across the oxide film, in addition to the rates of their creation at their respective interfaces (i.e. electrochemical redox reaction rates). Since the rate of charge transport (charge flux) depends on the electric field gradient (electric potential), the electrochemical potentials of the metal, oxide and solution phases are important parameters in determining the corrosion rate. These potentials may change with time as corrosion progresses. However, these models do not specifically define the driving force for corrosion as a function of quantifiable potentials such as the equilibrium potential of a redox pair involved in corrosion (E_{rdx}^{eq}), or the electrode potential (corrosion potential (E_{CORR})) on open circuit, or the applied potential (E_{app}) during polarization.

In these models, the distribution of the driving force for corrosion on a corroding surface is often presented schematically as shown in Figure 7-1. The implicit assumptions in this schematic are that the driving force for corrosion (V) is the potential difference between the Fermi levels in the metal and the solution phases, that the driving force is distributed between the metal/oxide (m|ox) and oxide/solution (ox|sol) interfaces and the oxide film present, and that the potential may not be constant across the oxide film. The models differ in their assumptions on how the driving force is distributed and on how the potential distribution changes as the oxide film grows. For example, the potential drop across an oxide film is assumed to be independent of oxide thickness in the Cabrera-Mott model [4], while it increases with oxide thickness in other models [9-13]. Alternatively the potential difference at the ox|sol interface may be assumed to be constant as the oxide grows (the Point Defect Model (PDM)) [9] while the potential difference at the m|ox interface is assumed to be constant in the Generalized Model for Oxide Film Growth [12, 13].
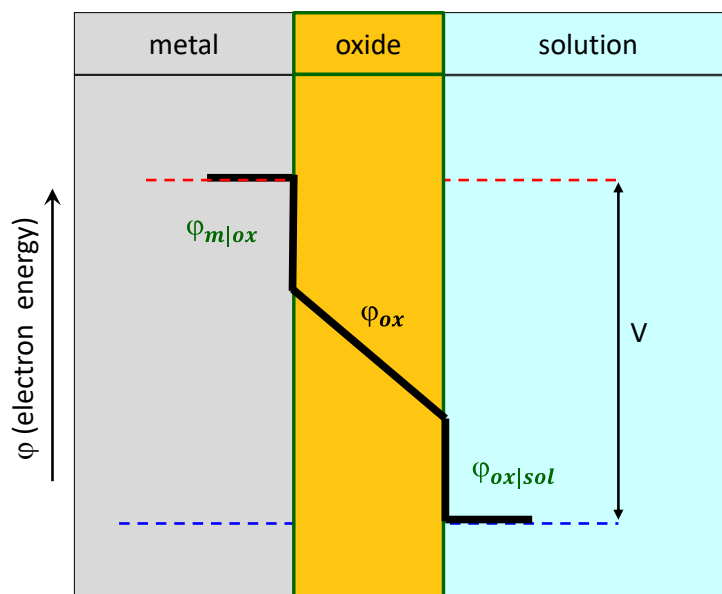
Figure 7-1: **Commonly accepted scheme for the distribution of the potential difference between the metal and solution phases, V, in a metal/oxide/solution system.**

In addition, these models do not explicitly express the potentials that control the charge transport rates as a function of quantifiable potentials such as E_{corr} or E_{rdx}^{eq}. The models assign different rates for the transport of different charge carriers across the solid oxide phase (ions, ion vacancies, electrons and holes). The individual transport rate parameters are difficult to verify, and this limits the predictive capabilities and the application ranges of these models. Oddly, mass and charge balance for the overall corrosion process, clear physical requirements, are not generally invoked in these models.

We have developed a corrosion kinetic model that can simulate both oxide film growth and metal dissolution as a function of time for a range of potentials, pHs and temperatures. Our model considers many of the elementary processes that are included in other models: electrochemical redox reactions at the m|ox and ox|sol interfaces, the transport of charged species across the oxide film, metal oxide formation and growth, and metal ion dissolution. The rates of the individual elementary reactions/processes are formulated using classical chemical reaction rate, and mass and charge flux equations. However, our model imposes mass and charge balance requirements on these rates, and reaction thermodynamic

and kinetic constraints on electrochemical redox reactions. Hence, we have named our model the "Mass Charge Balance (MCB)" model.

In this paper, we describe the fundamental physical and chemical processes that underlie the MCB model and show how it can predict both oxide growth and dissolution during corrosion of an alloy. The rationales for the MCB model assumptions and the rate or charge flux equations used in the model are presented. In particular, we establish the driving force for corrosion as a function of equilibrium potential and how the driving force is distributed among the m|ox and ox|sol interfaces and across the oxide layer. The model includes relationships between the potential drop across the oxide film and the film thickness, and between the potential drop and the activation energy for oxide formation, and the rate of oxide growth as a function of the oxide thickness. We present a few comparisons of model simulations of the time-dependent corrosion current and oxide growth during potentiostatic polarization with data obtained for pure iron (using data from Sato et al. [14]) and for Cr-containing alloys: a Co-Cr alloy, Stellite 6 [15], and an Fe-Ni-Cr alloy, Alloy 800.

7.2   The MCB model

7.2.1   Overview of the MCB Model

The MCB model considers corrosion to consist of four elements: electrochemical redox reactions at the m|ox and ox|sol interfaces, the transport of charged species across the oxide film, metal oxide formation and growth, and metal ion dissolution. The rates of the individual elementary reactions/processes in the model are formulated using classical chemical reaction rate, and mass and charge flux equations. The MCB model imposes mass and charge balance requirements on these rates, and reaction thermodynamic and kinetic constraints on electrochemical redox reactions. The mass and charge balance requirements invoked in the MCB model dictate that the rate of metal oxidation must equal the rate of its coupled solution species reduction, and the rate of metal oxidation must equal the sum of the rates of oxide formation and metal dissolution. This allows us to avoid the need for detailed modeling of charge transport across the oxide film. Instead, the MCB model takes into

account the dependence of the potential drop across the oxide film on the type and thickness of the oxide(s) that grow with time.

Metal alloys may contain more than one active element that may form an oxide or hydroxide. This oxide may contain only a single metal element, or it can be a mixed oxide/ hydroxide with more than one metal element. In addition, transition metals have many stable oxidation states and this, combined with the possibility of forming several different stable oxides and hydroxides, leads to the possible formation of many different layers of oxides/hydroxides on a metal surface. The MCB model recognizes that different metal oxides can form and that the oxide composition and structure may change as corrosion progresses [15, 16]. The result can be a complex and shifting set of oxides that form and grow as a function of time, even at a fixed potential [15]. The different types of metal oxides can have different oxide layer resistances and this will affect the potential drop across the oxide, and evolution in the nature of the oxide layer with time will change the potential drop as a function of time.

Irrespective of the type of oxide that forms and the rate of its formation, oxide formation is an electrochemical reaction and constrained by reaction thermodynamics. The thermodynamic constraints invoked in the MCB model dictate that metal oxidation (coupled with solution reduction) leads to formation of a certain type of oxide with a driving force given by the difference in the equilibrium potentials of the two coupled redox half-reactions for that process. Energy pathway minimization prevents an oxide that requires a higher free energy of reaction from forming in competition. The MCB model assumes that the thermodynamic driving force is distributed between the m|ox and ox|sol interfaces and the oxide layer, in a manner somewhat similar to that shown in Figure 7-1. Due to the potential distribution, the effective driving force for metal oxidation decreases as the oxide grows. In the MCB model the distribution of the driving force at the m|ox and ox|sol interfaces and across the oxide layer is dictated by the mass and charge balance requirements. That is, the potential is distributed such that the rate of metal oxidation that produces metal cations must be the same as the rate of the metal cations moving across the oxide film, and these rates must be the same as the sum of the rates of metal oxide formation and metal ion dissolution.

The MCB model assumes that for a given type of oxide there is a charge distribution across the oxide layer (there is a higher metal cation concentration near the m|ox interface and a higher oxygen anion concentration near the ox|sol interface). In this case the oxide film on a corroding surface resembles a p-n junction in a solid-state diode device and is not a uniform semiconductor. Consequently, the potential drop across an oxide layer ($\Delta V_{oxide} = -\Delta \varphi_{oxide}$) increases linearly with oxide thickness. An increase in ΔV_{oxide} decreases the effective overpotentials for the redox half-reactions at the two interfaces. The result is that the metal oxidation rate can be formulated using a modified Butler-Volmer equation with an effective overpotential, provided that one can define the linear rate of oxide growth with time.

The MCB model assumes that the rate of oxide growth has a first order dependence on the flux of metal cations and that the oxide growth rate constant has an Arrhenius dependence on the activation energy for the metal oxide formation. The activation energy increases with an increase in ΔV_{oxide}, and hence, the rate constant for metal oxide formation decreases exponentially with an increase in oxide thickness.

The last key component of the MCB model takes into account the competition between oxide formation and dissolution for the metal cations produced by metal oxidation. Due to the mass and charge balance requirements the rate of metal oxidation must be the same as the sum of the rates of metal oxide formation and dissolution. In contrast to the changing oxide growth rate with oxide thickness, the rate constant for metal dissolution at the ox|sol interface is generally assumed to be independent of oxide thickness, but dependent on the type of dissolving oxide and the metal cation dissolution properties of the contacting solution (pH, temperature, etc.).

The principles behind the MCB model assumptions and the formulation of the rate equations are described next.

7.2.2 **Elementary Electrochemical and Transport Processes**

The elementary physical processes considered in the MCB model are schematically presented in Figure 7-2 [15]. Metal oxidation occurs at the m|ox interface (Process 1a) and

174

the reduction of aqueous species occurs on a counter electrode (Process 1b). On a naturally corroding surface (an open circuit) both the metal oxidation and the aqueous species reduction occur on the same (on a macroscopic scale) surface. When an alloy electrode is polarized in an electrochemical cell the two redox reactions occur on separated surfaces. The redox half-reactions are coupled via a flux of metal cations from the m|ox interface to the ox|sol interface (Process 2). The metal cations at the ox|sol interface can be hydrated and dissolve into the solution (Process 3), or combine with oxygen anions in the solution (O^{2-} or OH^-) to form a solid metal oxide that attaches to the ox|sol interface (Process 4). In this schematic, the metal cations are depicted as moving from the m|ox interface to the ox|sol interface. This does not mean that the individual metal cations physically move through the oxide layer, but rather that there is relative movement of the interfaces with respect to each other. Oxygen anions moving from the ox|sol to the m|ox interface results in the same transport rate equation. The net result is the transfer of metal species from the metal phase to the solution phase.

The oxyhydroxides of transition metals typically exhibit semiconducting properties [17]. For a chemically inert semiconductor, charge transport through the semiconductor is normally accomplished by movement of electrons (for an n-type) and holes (for a p-type). On a corroding metal surface, transfer of more massive charged species (metal cations and/or oxygen anions) also occurs. Movement of relatively massive ions through a solid oxide phase is not easy. To account for the charge flux through a solid oxide lattice, many mechanisms, such as transport of metal cations (or oxygen anions) via interstitials, or cation and anion vacancies, and electron hopping (or ion exchanges), have been proposed [4, 5, 9, 11-13]. Irrespective of the ion transport mechanism, the charge flux through a corroding surface can be modeled as the net flux of metal cations from the m|ox interface to the ox|sol interface.

For simplicity, only one active metal element, M, and its oxidation to one oxidation state M^{2+} are shown in Figure 7-2. Similarly, only water is reduced. However, for an alloy the set of elementary reactions will be much larger, taking into account all of the metal components of the alloy and their possible stable oxidation states, and the solution redox conditions. For example, in a highly oxidizing solution (e.g., containing H_2O_2) the oxide growth process (Process 4) on a Ni-Fe-Cr alloy may consist of (1) oxidative conversion of

an pre-existing layer of defective Cr_2O_3 to $FeCr_2O_4$, followed by (2) formation and growth of Fe_3O_4 and $NiFe_2O_4$ and then (3) formation and growth of $NiO/Ni(OH)_2$ [16]. On a Co-Cr alloy Process 4 may consist of (1) conversion of pre-existing Cr_2O_3 to $CoCr_2O_4$, followed by (2) formation and growth of $CoO/Co(OH)_2$ and then (3) formation and growth of $CoOOH$ and Co_3O_4 [15].
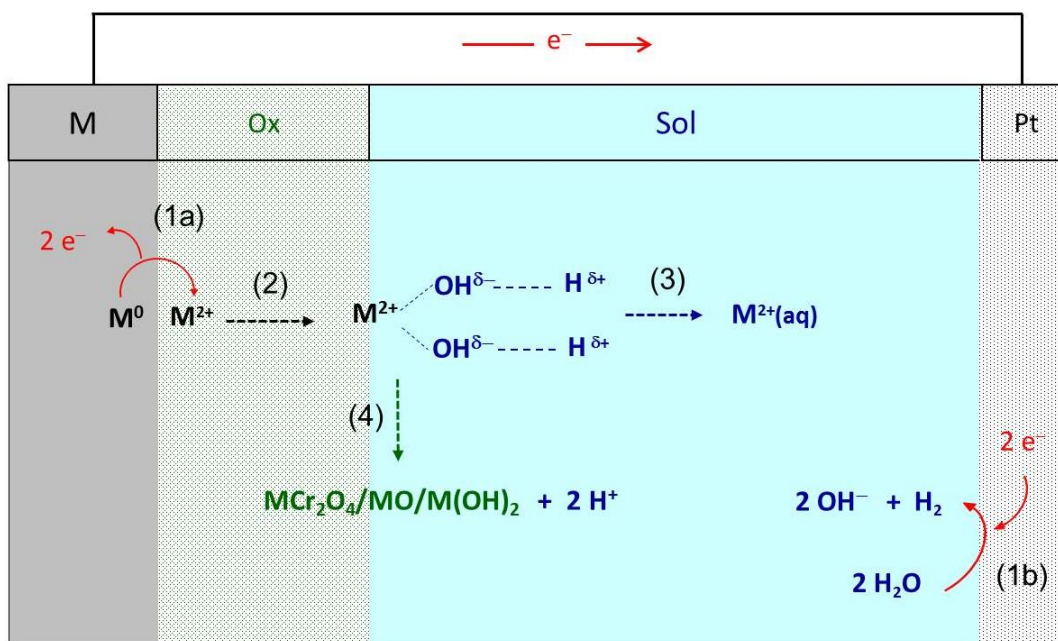
Figure 7-2: **Schematic of the elementary processes considered in the MCB model**

7.2.3 Mass and Charge Balance

In the MCB model, the rates of individual reactions/processes are formulated using classical chemical reaction rate and mass and charge flux equations. The rates of the individual processes shown in Figure 7-2 cannot vary independently. The mass and charge balance requirements dictate that at any given time, the rate of metal oxidation must satisfy

$$\text{Oxidation rate} = \text{rate (1a)} = \text{rate (1b)} = \text{rate (2)} = \text{rate (3)} + \text{rate (4)} \qquad (7\text{-}1)$$

Mass balance dictates that the rates of the reactions that occur in series must be the same. Also, the total rate of reactions in parallel is the sum of the individual reaction rates. Hence, the slowest in a series of reactions dictates the oxidation rate while dissolution (3) and oxide formation (4) in parallel compete for the metal cations.

For processes occurring at an interface the rates are better expressed in terms of fluxes than in terms of the change in concentration of a species (although the flux may depend on concentration gradient of a species at the interface). Furthermore, in electrochemical studies of corrosion, the current (charge flux) is the measured quantity. The mass and charge balance requirements in terms of charge flux are:

The flux of positive charges from the metal to the oxide phase at the m|ox interface (Process 1a) must be equal to the flux of negative charges from the solution to oxide phase at the ox|sol interface (Process 1b). Hereafter, these fluxes are referred to as the metal oxidation flux, $J_{M\#^{n+}}(t)|_{m|ox}$ and the oxidant reduction flux, $-J_{red\#}(t)|_{ox|sol}$, respectively.

$$J_{M\#^{n+}}(t)|_{m|ox} = -J_{red\#}(t)|_{ox|sol} \tag{7-2}$$

where the fluxes are in units of mol·s^{-1}·cm^{-2}.

The metal oxidation flux at the m|ox interface must be equal to the average flux of the metal cations across the oxide phase, $\langle J_{M^{n+}}(z,t)\rangle_{oxide}$, (Process 2) and hence the total flux of metal cations arriving at the ox|sol interface:

$$J_{M\#^{n+}}(t)|_{m|ox} = \langle J_{M\#^{n+}}(z,t)\rangle_{oxide} = J_{M\#^{n+}}(t)|_{ox|sol} \tag{7-3}$$

The flux of the metal cations may vary along the oxide layer but the MCB model does not formulate this in detail. The average flux is assumed to be inversely proportional to the thickness of the oxide layer, $L_{oxide}(t)$, that may be initially present or growing

$$\langle J_{M\#^{n+}}(z,t)\rangle_{oxide} = \frac{1}{L_{MO}(t)} \cdot \left(\int_0^{L_{MO}(t)} J_{M\#^{n+}}(z,t) \cdot dz \right) \tag{7-4}$$

Again, it should be emphasized that a flux of the metal cations from the m|ox to ox|sol interface does not mean the physical movement of individual cations through the solid oxide

phase but rather the relative movement of the interfaces with respect to each other. A flux of oxygen anions from the ox|sol to m|ox interface in the opposite direction yields the same flux equation for positive charges.

The charge flux must be equal to the sum of the fluxes of metal cations that dissolve into the solution phase (Process 3) and those that are used for growing an oxide film (Process 4)

$$J_{M\#^{n+}}(t)|_{ox|sol} = J_{diss\#}(t)|_{sol} + J_{MO\#}(t)|_{oxide} \qquad (7-5)$$

and these are referred to as the dissolution flux, $J_{diss\#}(t)|_{sol}$, and the oxide growth flux, $J_{MO\#}(t)|_{oxide}$, respectively.

The condition of equal fluxes for metal oxidation and solution reduction dictates the potential on a naturally corroding surface (E_{CORR}) with the net current at E_{CORR} being zero. Under polarization, the rate of oxidation (or reduction) occurring on the working electrode must equal the rate of reduction (or oxidation) occurring on the counter electrode, and this rate depends on the polarization potential (E_{app}).

In the MCB model we formulate the metal oxidation flux, $J_{M\#^{n+}}(t)|_{m|ox}$ and the oxide growth flux, $J_{MO\#}(t)|_{oxide}$ as functions of corrosion parameters (potentials, pH, T, etc.) and the other fluxes are determined using the mass and charge balance equations (equations 7-1 to 7-5).

In formulating $J_{M\#^{n+}}(t)|_{m|ox}$ and $J_{MO\#}(t)|_{oxide}$, the MCB model takes the free energy of reaction for the redox reaction forming a specific oxide MO as the driving force (or reaction potential) for the reaction. The driving force is then distributed between the m|ox and ox|sol interfaces and the oxide film present on the surface. How the potential is distributed between the three components is discussed in Section 7.2.5.

Equal rates for metal oxidation and the sum of the metal oxide formation and metal ion dissolution rates then dictate the rate of oxide growth and its dependence on pH and temperature. Since metal oxidation results in both metal cation dissolution and oxide

formation, the competing kinetics of these two pathways affects the rate of oxide growth [15, 16]. These fluxes are discussed in Section 7.2.6.

7.2.4 Formulation of the Metal Oxidation Flux, $J_{M\#^{n+}}(t)|_{m|ox}$

The overall redox reaction of M during corrosion can be expressed as,

$$M + Ox \leftrightarrows M^{n+} + Red \tag{7-6}$$
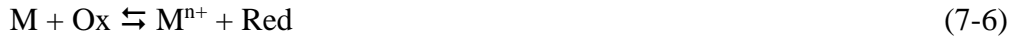
where Ox represents the solution oxidant and Red represents its reduced species. Knowing the nature of the metal and the solution redox species we can calculate the Gibbs free energy of this reaction. The driving force for the overall reaction (the free energy of reaction, $-\Delta_r G(t)$) is the difference in electrochemical potential of the reacting system at time t ($E_{rdx}(t)$) and at equilibrium (E_{rdx}^{eq}):

$$-\Delta_r G(t) = -n \cdot F \cdot \Delta_r E(t) \tag{7-7a}$$

$$-\Delta_r G(t) = n \cdot F \cdot \left(E_{rdx}(t) - E_{rdx}^{eq} \right) \tag{7-7b}$$

By convention the electrochemical potential scale uses the reduction potential with respect to the standard hydrogen electrode potential (SHE), but the scale zero point is not important. A chemical reaction depends on the difference in potential and not the absolute values of the potentials. The overall redox reaction is often expressed using two half-reactions:

$$Ox: M \leftrightarrows M^{n+} + n\,e^- \tag{7-8a}$$

$$Red: Ox + n\,e^- \leftrightarrows Red \tag{7-8b}$$

This division is used for convenience in evaluating reaction thermodynamics. The electrochemical equilibrium potential for the overall redox reaction (7-6) can then be expressed using the equilibrium potentials of the two half-reactions,

$$\Delta E_{rdx}^{eq} = E_{red}^{eq} - E_{ox}^{eq} \tag{7-9a}$$

On the potential scale with respect to V_{SHE} this becomes

$$\Delta E_{rdx}^{eq} = E_{rdx}^{eq}(V_{SHE}) \tag{7-9b}$$

For an electrochemical reaction of a specific redox pair, *rdx#*, the net rate of the reaction (or the net flux of charges) can be defined by the Butler-Volmer equation. In terms of current:

$$i_{rdx\#}(t) = i_{rdx\#}^{eq} \cdot \left(exp\left(\frac{n \cdot F}{RT} \cdot \alpha_{rdx\#} \cdot \eta_{rdx\#}(t) \right) - exp\left(-\frac{n \cdot F}{RT} \cdot (1 - \alpha_{rdx\#}) \cdot \right.$$

$$\left. \eta_{rdx\#}(t) \right) \right) \tag{7-10a}$$

$$\eta_{rdx\#}(t) = E_{elec}(t) - E_{rdx\#}^{eq} \tag{7-10b}$$

where $i_{rdx\#}^{eq}$ is the exchange current, or the anodic or cathodic current at equilibrium, n is the number of electrons involved in the reaction, $\alpha_{rdx\#}$ is the transfer coefficient (typically with a value of 0.5), F is Faraday's constant, R is the universal gas constant (8.314 J·mol^{-1}·K^{-1}), T is absolute temperature (K), $\eta_{rdx\#}(t)$ is the overpotential at the reaction interface, and $E_{elec}(t)$ is the electrode potential or the potential at the reaction interface at time t. The electrode potential is the potential that we measure as the corrosion potential, E_{CORR}, on an open circuit or the applied potential, E_{app}, on polarization. When $E_{elec}(t)$ is sufficiently more positive or more negative than the equilibrium potential $E_{rdx\#}^{eq}$, the Butler-Volmer equation can be approximated to:

$$i_{rdx\#}(t) \approx i_{ox\#}(t) = i_{ox\#}^{eq} \cdot \left(exp\left(\frac{0.5 \cdot n \cdot F}{RT} \cdot \eta_{ox\#}(t) \right) \right) \text{ for } \eta_{rdx\#}(t) > 0$$

$$\tag{7-11a}$$

$$i_{rdx\#}(t) \approx i_{red\#}(t) = i_{red\#}^{eq} \cdot \left(-exp\left(-\frac{0.5 \cdot n \cdot F}{RT} \cdot \eta_{red\#}(t) \right) \right) \text{ for } \eta_{rdx\#}(t) < 0$$

$$\tag{7-11b}$$

where

$$i_{rdx\#}^{eq} = i_{ox\#}^{eq} = -i_{red\#}^{eq} \tag{7-11c}$$

$$\eta_{rdx\#}(t) = \eta_{ox\#}(t) = -\eta_{red\#}(t) \tag{7-11d}$$

The transfer coefficient is often empirically determined for a particular corrosion process [18]. In the MCB model the transfer coefficient for each elementary redox reaction, *rdx#*, is fixed at 0.5 and is not an adjustable parameter.

On a bare metal surface, there is only one reaction interface, the metal/solution interface, and the overpotential at the interface is defined as in Eq. 7-10b. In the presence of an oxide film the corrosion process involves reactions between three phases and at two different interfaces. The metal oxidation half-reaction (7-8a) occurs at the m|ox interface and the aqueous reduction half-reaction (7-8b) occurs at the ox|sol interface and/or on a counter electrode. The rate of each redox half-reaction can still be expressed using the Butler-Volmer equation (Eq. 7-11). However, not all of the free energy of reaction is available due to the potential barrier of the oxide film, $\Delta V_{oxide}(t)$:

$$\eta_{rdx\#}(t) = \eta_{ox\#}(t) = -\eta_{red\#}(t) = \left(E_{elec}(t) - E_{rdx\#}^{eq}\right) - \Delta V_{oxide}(t) \tag{7-12}$$

Thus, the rate of metal oxidation depends strongly on how the thermodynamic driving force is distributed between the two interfaces and across the oxide film.

For each possible metal/metal cation oxidation reaction, *rdx#*, in a specific solution environment the metal oxidation flux is formulated by a modified Butler-Volmer equation with the overpotential for the metal oxidation as defined in equation (7-12):

$$J_{M\#^{n+}}(t)|_{m|ox} = J_{rdx\#}^{eq} \cdot \left(exp\left(\frac{0.5 \cdot n \cdot F}{RT} \cdot \eta_{rdx\#}(t)\right)\right) \tag{7-13}$$

7.2.5 **Potential Distribution**

The potential energy for an interfacial charge transfer process is often described using the Fermi-levels (the total chemical potential of electrons (φ)) in the reacting phases. For a given interfacial redox reaction, the change in the chemical potential of electrons and the change in the chemical potential of the redox species must be the same. Although the electron potential energy scale uses a different reference point and is opposite in sign to that of the hydrogen reduction potential scale, the relative values are the same in both scales, $\Delta\varphi = -\Delta E$.

At phase equilibrium, the Fermi-levels of the two reacting phases at the interface must be the same. On a bare metal surface the Fermi-levels of the metal and solution phases at the m|sol interface must be the same, $\varphi_f^{eq} = \varphi_m^{eq} = \varphi_{sol}^{eq}$. Thus,

$$\eta_{ox\#}(t) = \varphi_m(t) - \varphi_m^{eq} \tag{7-14a}$$

$$-\eta_{red\#}(t) = \varphi_{sol}^{eq} - \varphi_{sol}(t) \tag{7-14b}$$

$$\varphi_m(t) - \varphi_{sol}(t) = E_{red}^{eq} - E_{ox}^{eq} = \Delta E_{rdx}^{eq} = E_{rdx}^{eq} \text{ (V}_{SHE}) \tag{7-14c}$$

These relationships are schematically presented in Figure 7-3. The driving force for corrosion on a bare metal surface is equivalent to the difference between the Fermi-levels of the metal and solution phases at time t, and this is the same as the difference in the equilibrium potentials of the two half-reactions. If there is no change in the electrochemical potential of the solution as corrosion progresses, the corrosion rate on a bare metal surface does not change.
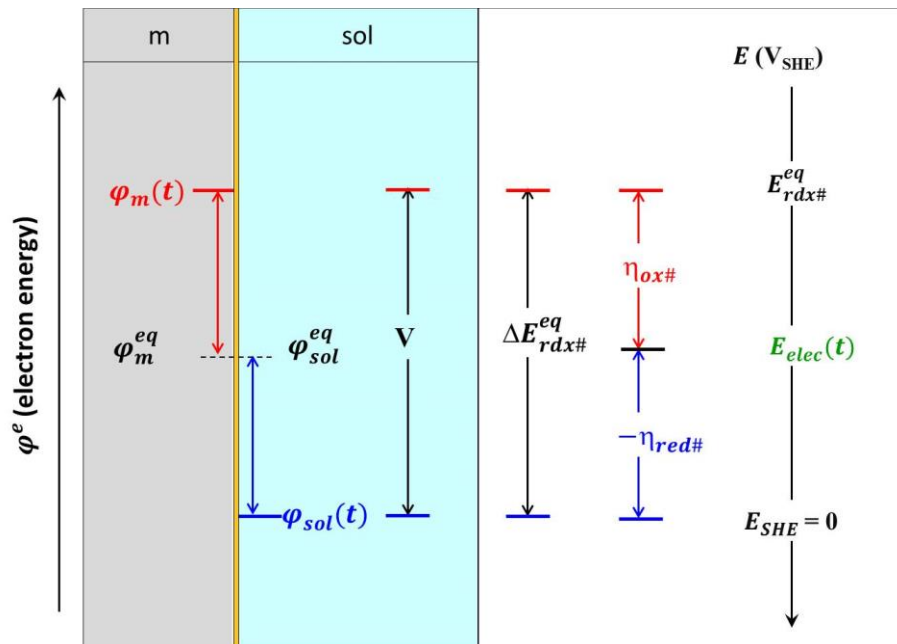
Figure 7-3: Relative positions of the redox reaction potentials at time t during corrosion on a bare metal surface. The potential drops across the double layer and diffusion layer are not considered for simplicity.

The Fermi level in the solution at equilibrium is the electron energy level where the density of unoccupied electron energy states ($\varphi_{E(Ox)}$) and the density of occupied electron energy states ($\varphi_{E(Red)}$) are the same. In the presence of an oxide, the Fermi-levels of the solution and the oxide at the ox|sol interface must be the same. The Fermi level in the metal phase at equilibrium is the electron energy level where the density of unoccupied electron energy states ($\varphi_{E(M^{n+})}$) and the density of occupied electron energy states ($\varphi_{E(M)}$) are the same. In the presence of an oxide film the Fermi-levels of the metal and the oxide at the m|ox interface must be the same. The questions are then, "What is the Fermi gap across the oxide layer?" and "Is this gap constant across the oxide layer during corrosion?"

Most of the transition metal oxides present on corroding surfaces exhibit semiconducting properties [17]. The Fermi level of a pure n-type semiconductor lies closer to the lowest energy of the conduction band, φ_{CB}, whereas the Fermi level of a pure p-type semiconductor lies closer to the highest energy of the valence band, φ_{VB}. In order for corrosion to progress at any appreciable rate, the Fermi-level of the metal at the interface must lie above the φ_{CB} of the semiconducting oxide while the Fermi-level of the solution phase must lie below the φ_{VB} of the oxide:

$$\varphi_m(t) > \varphi_{CB} \text{ and } \varphi_{sol}(t) < \varphi_{VB} \tag{7-15}$$

These conditions reduce the overpotential that is available for metal oxidation or solution reduction:

$$\eta_{ox}(t) = \varphi_m(t) - \varphi_m^{eq} - \Delta\varphi_{oxide}(t) \text{ for a p-type semiconductor} \tag{7-16a}$$

$$\eta_{red}(t) = \varphi_{sol}(t) - \varphi_{sol}^{eq} + \Delta\varphi_{oxide}(t) \text{ for an n-type semiconductor}$$

$$\tag{7-16b}$$

The mass and charge balance conditions further dictate that the effective overpotentials for the metal oxidation and its coupled solution reduction are related as given in Eq. (7-13). Thus, for both n-type and p-type semiconductors,

$$\eta_{rdx}(t) = \eta_{ox}(t) + \left(-\eta_{red}(t)\right) = \varphi_m(t) - \varphi_{sol}(t) - \Delta\varphi_{oxide}(t)$$

$$= E_{rdx}^{eq} - \Delta V_{oxide}(t) \tag{7-17}$$

These relationships are schematically presented in Figure 7-4. (Here the potential drops across the space charge layers such as Mott-Schottky and double layers are not considered for simplicity. On a corroding surface, these barriers should be negligible compared to the potential barrier of the oxide film.)

On a pure semiconductor, the potential drop, $\Delta\varphi_{oxide}(t)$, is the band gap (V_{bg}). If the oxide film is a pure phase, the band gap does not change with an increase in oxide thickness and the growth of that oxide should not affect the interfacial charge transfer rate. This can explain some of the observations where the potential drop across an oxide film is independent of oxide thickness and justifies this assumption in the Cabrera-Mott model [4]. However, typically the oxide film composition on a corroding surface will not be uniform. Instead, there will be a charge distribution within the oxide lattice; the M^{n+} concentration will be higher nearer the m|ox interface and the O^{2-} concentration will be higher nearer the ox|sol interface. Therefore, the oxide near the m|ox interface will behave more like a p-type semiconductor (due to doping of the positive charges) while near the ox|sol interface the oxide will behave more like an n-type semiconductor (due to doping of the negative charges). The oxide film present on a corroding surface will then behave like a p-n junction in a solid-state diode device.
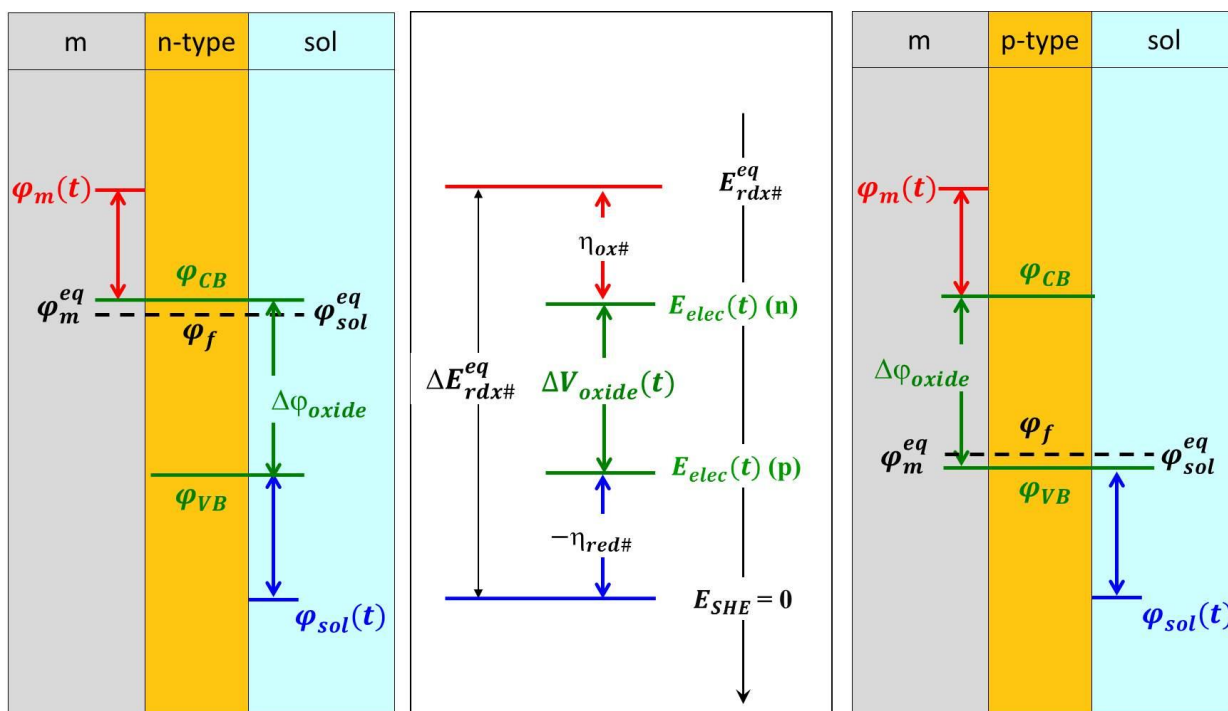
Figure 7-4: **Relative positions of the reaction potentials at a time t during corrosion: (middle panel) on the reduction potential scale (E(V$_{SHE}$)), (left panel) for an n-type film on the electron energy scale (φ^e), and (right panel) for a p-type film on the electron**

In the absence of any external potential the Fermi levels of two reacting phases at the reaction interface must be the same. At equilibrium (no external force) the φ_{CB} of the p-type semiconductor is higher than the φ_{CB} of the n-type semiconductor. This results in a potential barrier to the flow of electrons (the majority of charge carriers). Similarly, holes cannot flow forward (from p-type to n-type regions) unless a positive external potential (V_{ext}) is applied to overcome the potential barrier across the junction, and this potential barrier (V_j, the junction potential) is not the band gap (V_{bg}). Only when V_{ext} is larger than V_j and the Fermi-level in the n-type semiconductor region is raised above the φ_{CB} of the p-type semiconductor region can electrons flow from the n-type to p-type regions.

We can envision the potential distribution across an oxide film on a corroding surface as being similar to that in a p-n junction. In the presence of an oxide layer, the corrosion redox reaction can occur only when the potential is sufficient to overcome the oxide potential

185

barrier, $\Delta\varphi_{oxide}$ (equivalent to V_j) so that electrons can migrate from the ox|sol interface to the m|ox interface. If the potential at the m|ox interface is the same as the aqueous redox potential, there will not be any current – i.e., no metal oxidation. The potential distribution on such a corroding system is schematically shown in Figure 7-5.

Figure 7-5: Relative positions of the reaction potentials at a time t during corrosion in the presence of a n-p type oxide film: (left panel) on the electron energy scale (φ^e) and (right panel) on the reduction potential scale ($E(V_{SHE})$).

Figure 7-6 presents the potential energy distribution on a corroding surface at a specific time under a specific solution redox condition. If the oxide grows as corrosion progresses the potential barrier across the oxide film increases. For a system where a specific metal oxidation coupled with a specific aqueous reduction reaction that leads to growth of a specific oxide film, MO#, it is reasonable to assume that $\Delta V_{oxide}(t)\big(=-\Delta\varphi_{oxide}(t)\big)$ is proportional to the changing oxide thickness:

$$\Delta V_{oxide}(t) = \Delta V_{oxide}(0) + \Delta V_{MO\#}(t) \tag{7-18a}$$

$$\Delta V_{MO\#}(t) = \varepsilon_{MO\#} \cdot L_{MO\#}(t) \tag{7-18b}$$

where $\Delta V_{oxide}(0)$ is the potential drop over, if present, the pre-existing oxide layer, $\varepsilon_{MO\#}$ is the proportionality constant or the specific potential gradient (potential drop per unit length) of oxide MO# and $L_{MO\#}(t)$ is the thickness of oxide MO# grown over time t.

Since the reaction potential energy is distributed such that it will satisfy the mass and charge balance requirements, the effective overpotential for metal oxidation will change according to Eq. (7-17). For a given solution redox condition where $E_{rdx\#}^{eq}$ is constant, the potential gaps at the two interfaces and across the oxide film at two different times are schematically shown in Figure 7-6. For simplicity $\Delta V_{oxide}(0)$ is assumed to be zero. This schematic also illustrates that even with a constant solution redox environment, as the oxide layer thickens the corrosion potential, E_{CORR}, which is the Fermi-level at pseudo equilibrium (or steady state), increases. This occurs even though the effective overpotential and, hence, the rate of the metal oxidation decreases. If the electrode potential, E_{app}, instead of E_{rdx}^{eq}, is maintained constant, as is the case for potentiostatic polarization, the effective overpotential for metal oxidation decreases as the oxide grows, as schematically shown in Figure 7-7.
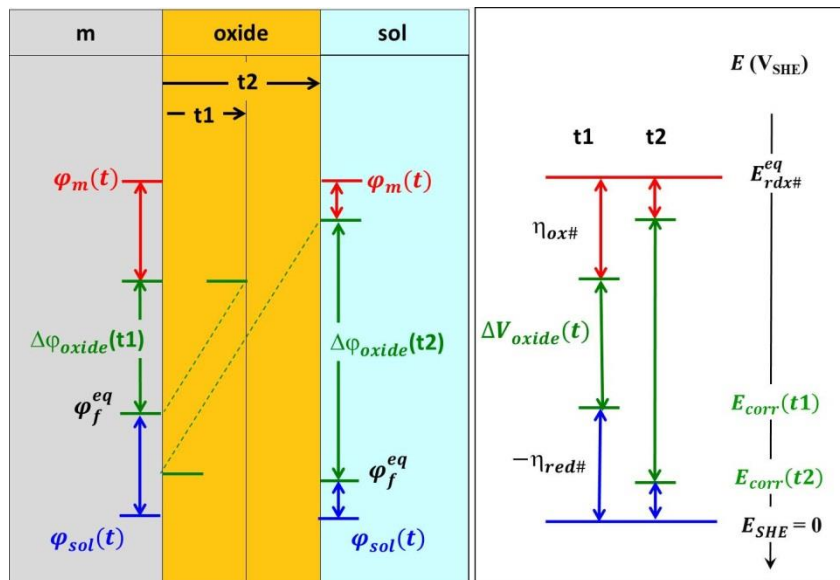
Figure 7-6: **Effect of linear oxide growth on the potential distribution in a corroding system: (left panel) on the electron energy scale (φ^e) and (right panel) on the reduction potential scale (E(V_{SHE})).**
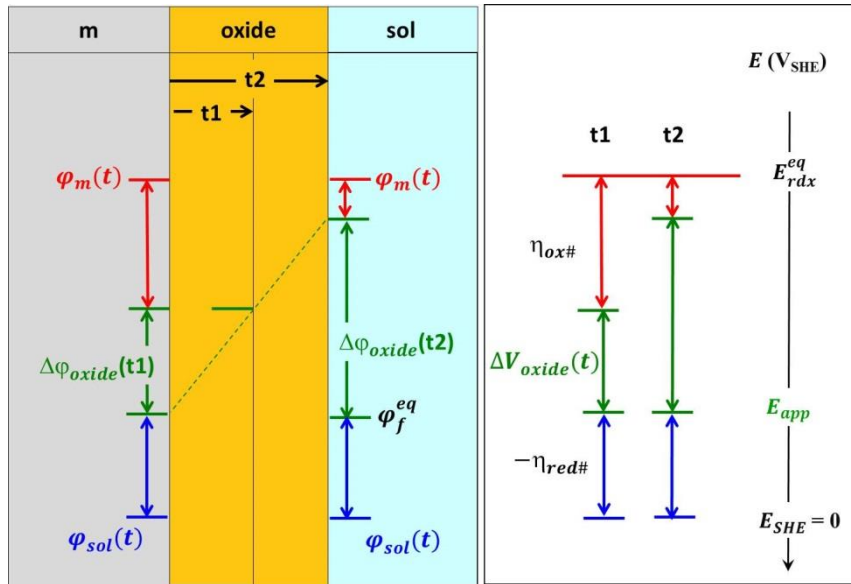
Figure 7-7: Effect of linear oxide growth on the potential distribution during potentiostatic polarization: (left panel) on the electron energy scale (φ^e) and (right panel) on the reduction potential scale (E(V$_{SHE}$)).

The potential energy diagrams presented in Figure 7-5, Figure 7-6 and Figure 7-7 describe a system where there is only one redox reaction occurring. In a real system for an alloy with multiple elements, there may be multiple redox reactions that occur in parallel or in series. Nevertheless, the same principles apply to each individual redox reaction (rdx#) with its own electrochemical equilibrium potential, $E_{rdx\#}^{eq}$. The existence of multiple redox reactions is also the reason that E_{CORR} depends on the aqueous redox environment and the type(s) of oxide that can be formed.

7.2.6 Formulation of the Oxide Growth and the Dissolution Fluxes

The electric potential barrier across the oxide film is an important rate controlling parameter. As discussed above, for a specific redox reaction that leads to a specific oxide film, it is reasonable to assume that $\Delta V_{MO\#}(t)$ is proportional to the oxide thickness, $L_{MO\#}(t)$ (Eq. 7-18). The oxide growth flux and the time dependence of $L_{MO\#}(t)$ can be established as follows. Oxide formation will compete with dissolution for the metal cations. Assuming that both processes have a first order dependence on [M#$^{n+}$] with rate constants, k$_{MO\#}$ and k$_{diss\#}$, respectively, the mass balance requirement results in:

$$J_{MO\#}(t)|_{oxide} = f_{k-MO\#}(t) \cdot J_{M\#^{n+}}(t)|_{m|ox} \qquad (7\text{-}19)$$

$$J_{diss\#}(t)|_{sol} = \left(1 - f_{k-MO\#}(t)\right) \cdot J_{M\#^{n+}}(t)|_{m|ox} \qquad (7\text{-}20)$$

$$f_{k-MO\#}(t) = \left(\frac{k_{MO\#}(t)}{k_{MO\#}(t) + k_{diss\#}}\right) \qquad (7\text{-}21)$$

The ratio of the rate constants, $f_{k-MO\#}(t)$, depends strongly on pH and temperature. An increase in temperature will increase both the oxide formation and dissolution rates whereas a change in pH will primarily affect the dissolution rate.

Oxide formation is a chemical reaction and its rate constant can be assumed to have a normal Arrhenius dependence on the activation energy for the reaction. The electric potential energy gap across the oxide layer ($\Delta V_{MO\#}(t)$) contributes to the activation energy for the formation of an oxide (MO#) ($\Delta Ea_{MO\#}(t)$):

$$\Delta Ea_{MO\#}(t) = \Delta Ea_{MO\#}(0) + c' \cdot \Delta V_{MO\#}(t) = \Delta Ea_{MO\#}(0) + c_{MO\#} \cdot L_{MO\#}(t)$$

$$(7\text{-}22)$$

where c' is the dependency of activation energy of oxide growth of the potential drop across a layer of MO# and $c_{MO\#}$ is the specific activation energy gradient of oxide. The activation energy for the oxide formation increases as the oxide grows and the rate constant for the oxide formation decreases accordingly:

$$k_{MO\#}(t) = k_{MO\#}(0) \cdot exp\left(-\frac{c_{MO\#} \cdot L_{MO\#}(t)}{RT}\right) \qquad (7\text{-}23a)$$

where

$$k_{MO\#}(0) = k_{0-MO\#} \cdot exp\left(-\frac{(\Delta Ea_{MO\#}(0))}{RT}\right) \qquad (7\text{-}23b)$$

Note that the other contributors to the reaction activation energy are included in $\Delta Ea_{MO\#}(0)$ and the value of $k_{0-MO\#}$ which is the pre-exponential factor for the oxide formation, and they are assumed to be constant with time.

The fluxes calculated in the model are related to physical parameters that can be measured. For example, the metal oxidation flux, $J_{M\#^{n+}}(t)|_{m|ox}$, can be measured as anodic current if metal oxidation current can be effectively separated from the water reduction current in an electrochemical cell:

$$i_{ox\#}(t) = n \cdot F \cdot J_{M\#^{n+}}(t)|_{m|ox} \tag{7-24}$$

The dissolution flux, $J_{diss\#}(t)|_{sol}$, is related to the amount of dissolved metal:

$$A_{sol} \cdot (J_{diss\#}(t)|_{sol}) \cdot dt = dm_{diss\#}(t) \tag{7-25}$$

where $dm_{diss\#}(t)$ represents the amount of dissolved metal over time dt (mol) and A_{sol} is the surface area exposed to solution (cm^2). The oxide growth flux, $J_{MO\#}(t)|_{oxide}$, is related to the thickness of the oxide:

$$\upsilon_{MO\#} \cdot (J_{MO\#}(t)|_{oxide}) \cdot dt = dL_{MO\#}(t) \tag{7-26}$$

where $\upsilon_{MO\#}$ is the molar volume of MO# (cm$^3 \cdot$mol^{-1}).

Equation (7-23) shows that the rate constant for oxide formation decreases exponentially with increase in oxide thickness. If the metal oxidation flux does not depend on oxide thickness, the oxide grows at a progressively slower rate (exponentially slower with time). However, since the metal oxidation flux also decreases exponentially with oxide thickness (Eqs. (7-11c), (7-13a) and (7-18)), the slower rate of oxide growth with time also slows down the rate of decrease in metal oxidation flux with time (Eq. (7-22)). As derived in more detail in Appendix A, the net effect is that the oxide thickness can be approximated to increase logarithmically with time under a constant electrode potential ($E_{elec}(t)$) condition (i.e., constant E_{CORR} or E_{app}):

$$L_{MO\#}(t) \approx \frac{1}{\lambda_{MO\#}} (ln(\lambda_{MO\#} \cdot J_{MO\#}{}'') + \ln t) \tag{7-27a}$$

$$\lambda_{MO\#} = \frac{0.5 \cdot n \cdot F}{RT} \cdot \varepsilon_{MO\#} \tag{7-27b}$$

$$J_{MO\#}'' = \upsilon_{MO\#} \cdot f_{k-MO\#}(0) \cdot J_{rdx\#}^{eq} \cdot \left(exp \left(\frac{0.5 \cdot n \cdot F}{RT} \cdot \left(E_{elec}(t) - E_{ox\#}^{eq} - \right. \right. \right.$$

$$\Delta V_{oxide}(0) \Big)\Big)\Big) \tag{7-27c}$$

$$f_{k-MO\#}(0) = \left(\frac{k_{MO\#}(0)}{k_{MO\#}(0) + k_{diss\#}} \right) \tag{7-27d}$$

where $\lambda_{MO\#}$ represents a constant related to the potential drop across a unit length of the layer of oxide in inverse-length equivalent units, and $J_{MO\#}''$ represents the constant component of the metal cation flux.

The approximated analytical solution of the flux equations in the MCB model (equation 7-27a) has the form that we recognize for logarithmic film growth as previously reported by McDonald in his PDM model [6]. They expressed the rate law for film growth (for $L_{MO\#}(t) > 5 \; \mathring{A}$) as

$$L_{MO}(t) \approx \frac{1}{2K} \left(ln\big(2K \cdot A \cdot (B-1)\big) + \ln t \right) \tag{7-28}$$

where *K, A* and *B* are constants. That their derivation for the oxide growth rate is based on very different physical and chemical descriptions, but results in the same rate expression, suggests that the simpler approach used in the MCB model is sound.

7.2.7 **Summary of the Mathematical Formulation of Model and Model Parameters**

The MCB model is summarized in Table 7-1. It consists of three key flux equations: metal oxidation flux, $J_{M\#^{n+}}(t)|_{m|ox}$, and metal oxide growth flux, $J_{MO\#}(t)|_{oxide}$ and metal cation dissolution flux, $J_{diss\#}(t)|_{sol}$. Due to mass and charge balance requirements the oxide growth and dissolution fluxes cannot vary independently, and their sum must be the same as the metal oxidation flux. Thus, the MCB model consists of really only two independent flux equations. These flux equations are applied to each redox pair (designated with # in the flux equation) of metal oxidation and solution reduction.

In the MCB model these flux equations are formulated based on well-established classical rate equations. The metal oxidation flux is formulated using a modified Butler-

Volmer equation with an effective overpotential, where the effective overpotential takes into account the decrease in the driving force due to the potential drop across the oxide layer that is present or growing during corrosion. The oxide growth flux is formulated based on a first-order dependence of the oxide formation on the metal cation flux, and on an Arrhenius dependence of the rate constant on activation energy, which increases with an increase in the potential drop across the oxide layer. The metal ion dissolution flux is simply the difference between the metal oxidation flux and the metal oxide growth flux. The ratio of the oxide growth flux to the dissolution flux is determined by their rate constants. The rate constant of the oxide growth changes with time as the oxide grows while the rate constant for dissolution from a given oxide surface is constant with time.

In the MCB model, the model parameters are: (1) the equilibrium potentials of the two coupled half-redox reactions ($E_{red\#}^{eq}$ and $E_{ox\#}^{eq}$), (2) the potential drop over the initially present oxide layer ($\Delta V_{oxide}(0)$) and the specific potential drop over the MO# oxide that is growing ($\varepsilon_{MO\#}$), and (3) the rate constant for MO# oxide formation without an oxide barrier ($k_{MO\#}(0)$). The last term can be further divided into two more fundamental parameters, a pre-exponential factor and an activation energy ($k_{0-MO\#}$ and $\Delta Ea_{MO\#}(0)$). These model parameters for a given alloy depend on the corrosion environment (which includes the type and concentration of aqueous redox species present, pH and temperature). The effects of the environmental parameters on the overall corrosion kinetics are thus modeled through their effects on the model parameters. The flux equations can be numerically solved using any standard computer software differential equation solver. The results presented below were obtained using MATLAB.

Table 7-1: Mathematical Formulation of the Model.

Flux Equations used in the Model		Model Output
1	$J_{M\#^{n+}}(t)\|_{m\|ox} = J_{rdx\#}^{eq} \cdot \left(exp\left(\frac{0.5 \cdot n \cdot F}{RT} \cdot \eta_{ox\#}(t) \right) \right)$	Current (t) $i_{ox\#}(t) = n \cdot F$ $\cdot J_{M\#^{n+}}(t)\|_{m\|ox}$
2	$J_{MO\#}(t)\|_{oxide} = \left(\frac{k_{MO\#}(t)}{k_{MO\#}(t) + k_{diss\#}} \right) \cdot J_{M\#^{n+}}(t)\|_{m\|ox}$	Oxide thickness (t) $L_{MO\#}(t)$ $= \upsilon_{MO\#}$ $\cdot \int_{t=0}^{t} (J_{MO\#}(t)\|_{oxide}) \cdot dt$
3	$J_{diss\#}(t)\|_{sol} = J_{M\#^{n+}}(t)\|_{m\|ox} - J_{MO\#}(t)\|_{oxide}$	Dissolved amount (t) $m_{diss\#}(t)$ $= A_{sol} \cdot \int_{t=0}^{t} (J_{diss\#}(t)\|_{sol}) \cdot dt$

Time Dependent Terms in the Flux Equations		Model Parameters
1	$\eta_{rdx\#}(t) = E_{red\#}^{eq} - E_{ox\#}^{eq} - \Delta V_{oxide}(t)$ $\eta_{ox\#}(t) = E_{elec}(t) - E_{ox\#}^{eq} - \Delta V_{oxide}(t)$	$J_{rdx\#}^{eq}, E_{red\#}^{eq}, E_{ox\#}^{eq}$
2	$\Delta V_{oxide}(t) = \Delta V_{oxide}(0) + \varepsilon_{MO\#} \cdot L_{MO\#}(t)$	$\Delta V_{oxide}(0), \varepsilon_{MO\#}, \upsilon_{MO\#}$
3	$\Delta Ea_{MO\#}(t) = \Delta Ea_{MO\#}(0) + c_{MO\#} \cdot L_{MO\#}(t)$	$\Delta Ea_{MO\#}(0), c_{MO\#}$
4	$k_{MO\#}(t) = k_{MO\#}(0) \cdot exp\left(-\frac{c_{MO\#} \cdot L_{MO\#}(t)}{RT} \right)$	$k_{MO\#}(0), k_{diss\#}$

7.3 Examples of model simulation results

The fluxes that the MCB model calculates correspond to measurable quantities, the current, the oxide thickness and the amount of dissolved metal as a function of corrosion time. These are all independently measurable quantities and so the model's capability to predict corrosion kinetics over a wide range of environmental conditions can be verified experimentally. We have applied the MCB model to simulate the potentiostatic polarization

of a number of alloys including carbon steel, stainless steel, Co-Cr alloy Stellite 6, and Fe-Ni-Cr alloys Inconel 600 and Alloy 800. The preliminary results are very promising in all cases modelled to date and a few examples are presented here.

7.3.1 Oxide Thickness on Pure Iron

We have applied the MCB model to predict the thickness of iron oxide grown as a function of E_{app} and compared the results to experimental data obtained from potentiostatic polarization of pure iron in mildly basic solutions by Sato *et al.*[14]. The model simulation results and the experimental data are compared in Figure 7-8, showing an excellent agreement. For this simulation, following parameters were used: $i^{eq}_{Fe3O4} = 6 \times 10^{-6}$, $f_{k-MO\#}(0) = 0.9$, $\varepsilon_{Fe3O4} = 3 \times 10^6$ $v_{MO\#} = 30$ and $E^{eq}_{ox\#}$ was calculated based on the Eq. 5 of Sato's work [19].
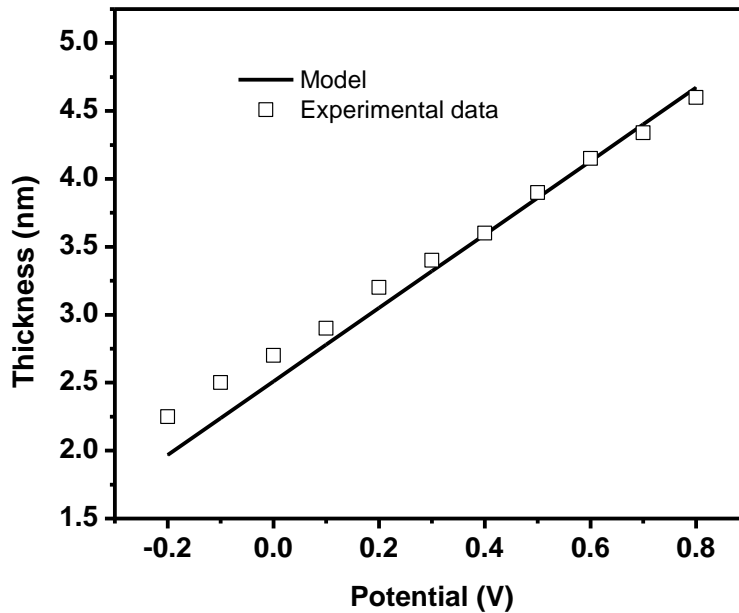
Figure 7-8: Measured average oxide thickness on pure iron after 1 h potentiostatic polarization at 25 °C in a range of pHs from 7.45 to 10.45 in 0.15 N boric-borate solution (symbols are data from Table 7-2 of Ref. [14]). The straight line is the prediction of the MCB model at pH=10.45. (Note that Sato's work showed no dependence of oxide thickness on pH over the range studied.)

7.3.2 Corrosion of Cr-containing Alloys

Model simulations and the results of polarization tests (at -0.6 V$_{SCE}$) of two alloys, Co-Cr (Stellite 6) and Fe-Ni-Cr (Alloy 800), are shown in Figure 7-9. The tests were performed at two different pHs, 10.6 and 8.4, in 0.01 M borate buffer solutions at 25 °C. The polarization potentials modelled are near the corrosion potentials measured on these alloys in deaerated solutions. The model predictions of the current behaviour are in very good agreement with the data.

In these simulations, the surface was assumed to be initially covered with a 2 nm thick layer of chromium oxide (Cr_2O_3) [20]. With this Cr_2O_3 layer present the only oxidation pathway that is thermodynamically possible at -0.6 V$_{SCE}$ is the conversion of the chromium oxide to chromite ($CoCr_2O_4$ or $FeCr_2O_4$) [15]. (When this conversion is complete Fe_3O_4 may grow over the chromite layer for the Fe-Ni-Cr alloy. For simplicity, this process is not considered in the following discussion as it did not occur under the test conditions.) Since the solubility of chromium is much lower than that of cobalt (for the Co-Cr alloy) and iron and nickel (for the Fe-Ni-Cr alloy) under the test conditions [21], we assumed that only cobalt dissolution occurred (from the Co-Cr alloy), or that only iron dissolution occurred (from the Fe-Ni-Cr alloy). The solubility of nickel is also lower than that of iron and hence nickel dissolution from the Fe-Ni-Cr alloy at this low potential was not modeled. Nevertheless, the oxidative conversion of Cr_2O_3 to chromite requires additional modeling considerations.
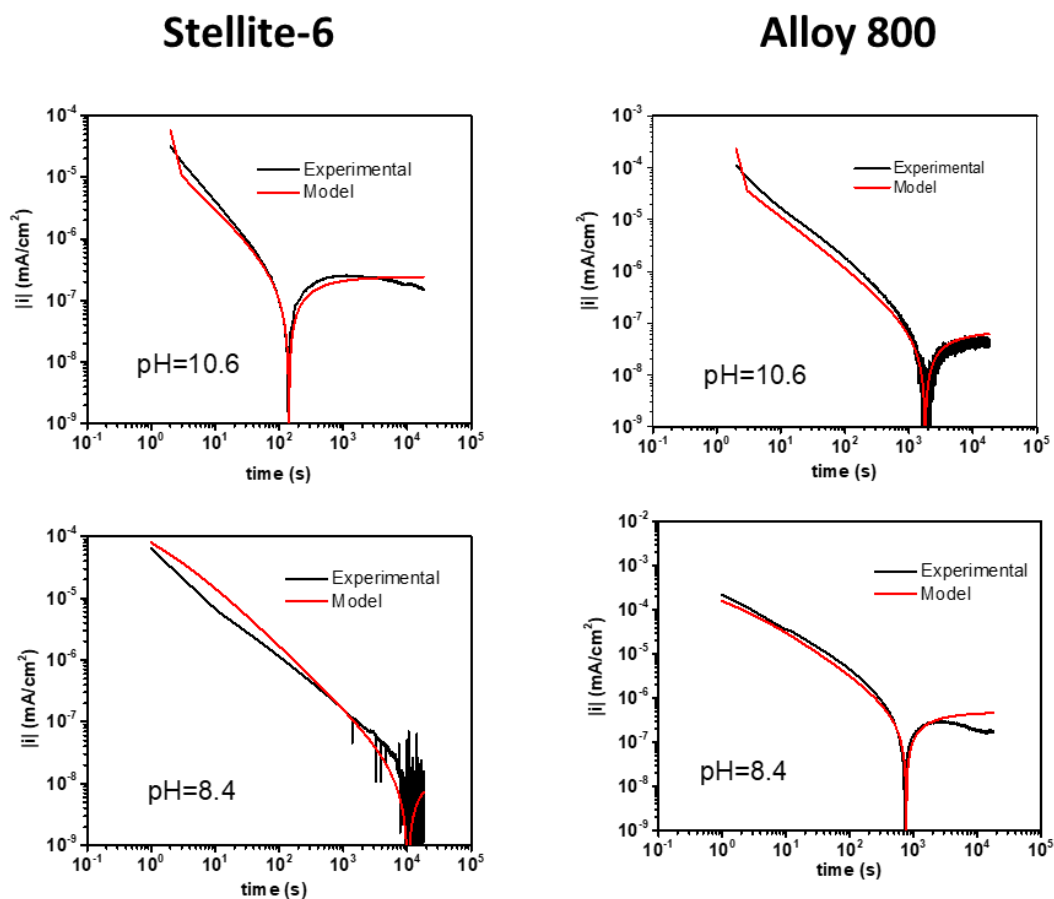
Figure 7-9: **Current observed during polarization at −0.6 VSCE of (left panel) Co-Cr alloy Stellite 6 and (right panel) Fe-Ni-Cr alloy 800 at (top row) pH 10.6 and (bottom row) pH 8.4. Experimental results are in black and modelling results are in red.**

Alloys which contain more than about 10% Cr typically display corrosion resistance because of the presence of a thin protective layer of air-formed Cr_2O_3 on the surface. This is the case for the Fe-Cr-Ni and Co-Cr alloys that we have studied. Mott [3] has shown that there can be a 5 nm maximum thickness of chromium oxide formed after long time of exposure to room temperature air. Even in deaerated solutions ($E_{CORR} \approx -0.48$ V_{SCE} and -0.59 V_{SCE} on Stellite 6 in deaerated solutions at pH 10.6 and 8.4, respectively [21]), this chromium oxide is converted to a mixed element chromate layer ($CoCr_2O_4$ for cobalt alloys and $FeCr_2O_4$ for Fe-Cr-Ni alloys):

$$M + Cr_2O_3 + 2\,OH^- \rightarrow MCr_2O_4 + H_2O + 2\,e^- \text{ on WE} \qquad (7\text{-}29a)$$

$$Ox + n\,e^- \rightarrow Red \text{ on CE} \qquad (7\text{-}29b)$$
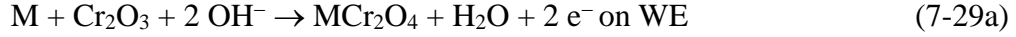
While this occurs, there are two types of oxide in the oxide film: a more chromite-like layer and a more chromium oxide-like layer. During conversion of chromium oxide to chromite, the thickness of the chromium oxide layer decreases while that of the chromite layer increases correspondingly [20]:

$$L_{Cr2O3}(t) = L_0 - f_l \cdot L_{MCr2O4}(t) \qquad (7\text{-}30)$$

where $L_{Cr2O3}(t)$ and $L_{MCr2O4}(t)$ are the thicknesses of the chromium oxide and chromite layers, L_0 is the initial air-formed chromium oxide thickness. The factor f_l is used to adjust for differences in the unit cell lengths of Cr_2O_3 and chromite oxide. In actuality, there may not be a sharp division of the oxide into two distinct layers but a gradation between the two oxide types. In the model, the oxide thicknesses in equation (32) are for pure-oxide-phase equivalent thicknesses. The potential drop across the film can then be expressed as:

$$\Delta V_{oxide}(t) = \varepsilon_{Cr2O3} \cdot L_{Cr2O3}(t) + \varepsilon_{MCr2O4} \cdot L_{MCr2O4}(t) \qquad (7\text{-}31)$$

$$\Delta V_{oxide}(t) = \varepsilon_{Cr2O3} \cdot L_0 + (\varepsilon_{MCr2O4} - f_l \cdot \varepsilon_{Cr2O3}) \cdot L_{MCr2O4}(t) \qquad (7\text{-}32)$$

where and ε_{Cr2O3} and ε_{MCr2O4} are the specific potential drops across the different oxide layers, respectively. The specific potential drop, $\varepsilon_{MO\#}$, is characteristic of the oxide [9] (with a value in the range of 10^5 to 10^7 V·cm^{-1}). The values for ε_{Cr2O3} and ε_{MCr2O4} are not known and the values used in the simulations were those that yielded best fits of data on a given alloy. The values used in the simulations shown in Figure 7-8 are listed in Table 7-2. Ideally, at a given temperature these values are fixed, independent of pH and E_{app}. The best-fit values of these parameters in the MCB model are indeed nearly the same at two different pHs. The values of the other model parameters are also listed in Table 7-2 and discussed below.

Under potentiostatic polarization, the aqueous reduction reaction that is not coupled with metal oxidation, but coupled with aqueous oxidation on the counter electrode, can also occur on the working electrode. This aqueous reduction reaction on the working electrode is

treated as a separate independent redox reaction with its own equilibrium potential (or the difference of the equilibrium potentials of the two half-reactions of aqueous reduction and aqueous oxidation). For example, reduction of H_2O or dissolved O_2 (at an impurity level) can occur on the working electrode coupled with oxidation of H_2 or H_2O on the counter electrode:

$$2\ H_2O + 2\ e^- \rightarrow H_2 + 2\ OH^-\ \text{on WE} \tag{7-33a}$$

$$H_2 + 2\ OH^- \rightarrow 2\ H_2O + 2\ e^-\ \text{on CE} \tag{7-33b}$$

and/or

$$O_2 + 4\ H^+ + 4\ e^- \rightarrow 2\ H_2O + 2\ e^-\ \text{on WE} \tag{7-34a}$$

$$2\ H_2O \rightarrow O_2 + 4\ H^+ + 4\ e^-\ \text{on CE} \tag{7-34b}$$

The aqueous redox reactions do not contribute to the metal oxidation flux or oxide growth flux, but only to the net current. Nevertheless, the aqueous reduction flux on the working electrode is expressed in a manner similar to that used for the metal oxidation flux, using an effective cathodic overpotential as a function of potential drop across the oxide layer.

Table 7-2: Fitting parameters for Cr-alloy potentiostatic simulations.

Alloy system	pH	i^{eq}_{MCr2O4} (mA·cm^{-2})	ε_{Cr2O3} (V·cm^{-1})	ε_{MCr2O4} (V·cm^{-1})	c_{MCr2O4}	$f_{k-MCr2O4}(0)$
Co-Cr	10.6	1.0×10^{-7}	1.7×10^6	5.5×10^6	1×10^7	0.91
	8.4	5.0×10^{-7}	1.2×10^6	5.5×10^6	1×10^7	0.15
Fe-Ni-Cr	10.6	1.0×10^{-6}	1.9×10^6	3.2×10^6	1×10^7	0.88
	8.4	1.0×10^{-6}	1.2×10^6	3.2×10^6	1×10^7	0.26

The values of the model parameters, the exchange current density (i^{eq}_{MCr2O4}) for the metal oxidation (30) and the exchange current ($i^{eq}_{aq-rdx\#}$) for the solution redox reaction (31, 32) and the initial rate constants ratio $f_{k-MO\#}(0)$ are also listed in Table 7-2. Although these

values were obtained from best fits to the data, these values are nearly the same for a given alloy and all within acceptable ranges. The exchange current densities depend on the solution conditions and factors related to the surface characteristics. The larger variation in the exchange currents on Stellite 6 due to pH change can be attributed to the presence of two alloy phases, Cr-rich and Co-rich phases, on Stellite 6.

The ratio $f_{k-MO\#}(0)$ depends on the solution environment, the type of growing oxide, and other factors, but this ratio is always less than one, and the ratio should be higher at a pH where the oxide solubility is lower. The solubilities of Fe^{2+} and Co^{2+} species are lower at pH 10.6 than at pH 8.4, and the best-fit values for the ratio $f_{k-MO\#}(0)$ do indeed reflect this pH dependence.

At a higher potential, more oxidation pathways are available. In the MCB model the individual oxidation reactions are modelled separately and their contributions are added to obtain the overall corrosion kinetics.

7.4   Summary

In this study, a new classical model for oxide growth and metal dissolution is presented. This Mass Charge Balance (MCB) model is based on mass and charge balance and consists of three key flux equations: metal oxidation, oxide growth, and dissolution flux. The mass and charge balance requirements dictate that the oxide growth and dissolution fluxes cannot vary independently, but their sum must be the same as the metal oxidation flux. The metal oxidation flux is formulated using a modified Butler-Volmer equation with an oxide-thickness-dependent effective overpotential. The oxide growth and dissolution fluxes have a first-order dependence on the metal oxidation flux. Mass balance dictates that the ratio of the oxide growth and the dissolution fluxes is determined by their respective first-order rate constants. The rate constant for oxide growth is assumed to have a normal Arrhenius dependence on the activation energy for the reaction where the potential drop across the growing oxide layer contributes to the activation energy. Thus, the rate constant for oxide growth decreases exponentially with oxide thickness while the rate constant for dissolution

remains constant. The analytical solution of this model results in a logarithmic dependence of the thickness of oxide on time.

7.5   References

[1] N.F. Mott, A theory of the formation of protective oxide films on metals, Transactions of the Faraday Society, 35 (1939) 1175-1177.

[2] N.F. Mott, The theory of the formation of protective oxide films on metals, II, Transactions of the Faraday Society, 35 (1940) 472-483.

[3] N.F. Mott, The theory of the formation of protective oxide films on metals.-III, Transactions of the Faraday Society, 43 (1947) 429-434.

[4] N. Cabrera, N.F. Mott, Theory of the oxidation of metals, Reports on Progress in Physics, 12 (1949) 163.

[5] F.P. Fehlner, N.F. Mott, Low-temperature oxidation, Oxidation of Metals, 2 (1970) 59-99.

[6] C.Y. Chao, L.F. Lin, D.D. Macdonald, A Point Defect Model for Anodic Passive Films: I . Film Growth Kinetics, Journal of The Electrochemical Society, 128 (1981) 1187-1194.

[7] L.F. Lin, C.Y. Chao, D.D. Macdonald, A Point Defect Model for Anodic Passive Films: II . Chemical Breakdown and Pit Initiation, Journal of The Electrochemical Society, 128 (1981) 1194-1198.

[8] G.T. Burstein, A.J. Davenport, The Current-Time Relationship during Anodic Oxide Film Growth under High Electric Field, Journal of The Electrochemical Society, 136 (1989) 936-941.

[9] D.D. Macdonald, The Point Defect Model for the Passive State, Journal of The Electrochemical Society, 139 (1992) 3434-3449.

[10] V. Battaglia, J. Newman, Modeling of a Growing Oxide Film: The Iron/Iron Oxide System, Journal of The Electrochemical Society, 142 (1995) 1423-1430.

[11] M. Bojinov, G. Fabricius, T. Laitinen, K. Mäkelä, T. Saario, G. Sundholm, Coupling between ionic defect structure and electronic conduction in passive films on iron, chromium and iron–chromium alloys, Electrochimica Acta, 45 (2000) 2029-2048.

[12] K. Leistner, C. Toulemonde, B. Diawara, A. Seyeux, P. Marcus, Oxide Film Growth Kinetics on Metals and Alloys: II. Numerical Simulation of Transient Behavior, Journal of The Electrochemical Society, 160 (2013) C197-C205.

[13] A. Seyeux, V. Maurice, P. Marcus, Oxide Film Growth Kinetics on Metals and Alloys: I. Physical Model, Journal of The Electrochemical Society, 160 (2013) C189-C196.

[14] N. Sato, K. Kudo, T. Noda, The anodic oxide film on iron in neutral solution, Electrochimica Acta, 16 (1971) 1909-1921.

[15] M. Behazin, J.J. Noël, J.C. Wren, Combined Effects of pH and γ-Irradiation on the Corrosion of Co-Cr Alloy Stellite-6, Electrochimica Acta, 134 (2014) 399-410.

[16] Q.W. Knapp, J.C. Wren, Film formation on type-316L stainless steel as a function of potential: Probing the role of gamma-radiation, Electrochimica Acta, 80 (2012) 90-99.

[17] S. Fujimoto, Photoelectrochemical Response and Corrosion Property of Passive Films on Fe-18Cr Alloy, in: P. Marcus, V. Maurice (Eds.) Passivation of Metals and Semiconductors, and Properties of Thin Oxide Layers, Elsevier Science, Amsterdam, 2006, 285-290.

[18] W.A. Mueller, Theory of the polarization curve technique for studying corrosion and electrochemical protection, Canadian Journal of Chemistry, 38 (1960) 576-587.

[19] N. Sato, T. Noda, K. Kudo, Thickness and structure of passive films on iron in acidic and basic solution, Electrochimica Acta, 19 (1974) 471-475.

[20] K.J. Vetter, General kinetics of passive layers on metals, Electrochimica Acta, 16 (1971) 1923-1937.

[21] A.Y. Musa, M. Behazin, J.C. Wren, Potentiostatic Film Growth Kinetics on Ni-Cr and Co-Cr Alloys: Potential and pH Dependences, Electrochimica Acta, 162 (2015) 185-197.

Chapter 8

Mass and Charge Balance (MCB) Model Simulations of Current, Oxide Growth and Dissolution in Corrosion of Co-Cr Alloy Stellite-6[1]

Abstract

A mass and charge balance (MCB) model that can simulate oxide growth and dissolution kinetics simultaneously during corrosion of an alloy has been recently developed. In this study, the MCB model was applied to the corrosion of the Co-Cr alloy Stellite-6. The construction of the model and the assignment of values to the rate parameters for the model are presented. The model simulation results are then compared with experimental corrosion data collected as a function of pH, temperature and polarization potential. The data include the current during potentiostatic polarization, the corrosion potential under open-circuit conditions, and post-test analyses of the oxide formed and the amount of metal dissolved. Excellent agreement between the model results and experimental data are found. This is evidence that the MCB model is a useful tool for predicting time-dependent corrosion while an oxide film is evolving.

Keywords: Modeling; Corrosion; Oxide Growth; Dissolution

8.1 Introduction

Alloys owe their corrosion resistance to protective oxide films formed on their surfaces [1-17]. Corrosion involves surface redox reactions (metal oxidation coupled with solution reduction) and interfacial transfer of the charged species involved in the redox reactions. The presence of an oxide film hinders the interfacial charge transfer, slowing the rate of corrosion. Modeling oxide formation and growth as a function of solution environments is an important component in predicting the corrosion behaviour of an alloy.

Several corrosion models have been developed for predicting the rate of oxide growth [11, 18-31] and/or the rate of metal dissolution in the presence of an oxide film. To obtain the overall rate of corrosion, many of these models focus on solving the transport rate equations for individual charge carriers (interstitial cations and anions, cation and anion vacancies, and electrons and holes) across the oxide film, in addition to the rates of their creation at respective interfaces (i.e. electrochemical redox reaction rates). These models assign rates to the transport of different charge carriers that are difficult to verify. Since the rate of interfacial charge transfer depends on the electric field present at the interface, the electrochemical potentials of the alloy, the oxide and the solution phases are important parameters in determining the corrosion rate.

Many of the existing models acknowledge that the driving force for corrosion depends on the potential of the corroding system (the corrosion potential (E_{CORR}) in an open circuit or the applied potential (E_{app}) during polarization). However, these models do not specifically quantify the driving force as a function of electrode potential and/or other quantifiable potentials such as the equilibrium potential of a redox pair involved in corrosion (E_{rdx}^{eq}). The electrode potential and the redox pair may change with time as corrosion progresses. The nature of oxide and the oxide layer structure can also change with time as corrosion progresses even under potentiostatic polarization or constant solution conditions [8-10, 12-17]. The type of oxide that can form and its rate of formation depend on solution environmental parameters such as pH, temperature and the concentrations of redox active species. Few existing models specifically incorporate the solution environment in their model parameters and, even in those models that do so, the effects are formulated primarily based

on empirical relationships. No existing models consider changes in oxide composition and layer structure as corrosion progresses. These shortcomings limit the predictive capabilities and the application ranges of these models.

Recently, we have developed a corrosion kinetics model that can simulate the metal oxidation rate (as a current), oxide film growth and metal dissolution as a function of electrode potential, pH and temperature [11]. This Mass and Charge Balance (MCB) model considers the elementary processes that are included in other models: electrochemical redox reactions at the m|ox and ox|sol interfaces, the transport of charged species across the oxide film, metal oxide formation and growth, and metal ion dissolution. The rates of the individual elementary reactions/processes in the model are formulated using classical (electro-)chemical reaction rate equations and mass and charge flux equations. However, the MCB model imposes mass and charge balance requirements on these rates, and chemical reaction thermodynamic and kinetic constraints on the electrochemical redox reactions involved in corrosion. The mass and charge balance requirements invoked in the MCB model dictate that the rate of metal oxidation must equal the rate of its coupled solution species reduction, and the rate of metal oxidation must equal the sum of the rates of oxide formation and metal dissolution. This allows us to avoid the need for detailed modeling of transport of different charged species across the oxide film. Instead, the MCB model takes into account the dependence of the potential drop across the oxide film on the type and thickness of the oxide(s) that grow with time.

We have previously presented detailed descriptions of the fundamental physical and chemical properties and processes that underlie the MCB model, and a few model calculation results that show its capability of simulating corrosion. In this chapter, we expand on the capabilities of the MCB model and its construction for an application to the corrosion of the Co-Cr alloy, Stellite-6. Model simulation results are compared with experimental measurements of current, potential, oxide composition and layer structure, and dissolved metal concentrations at various pHs, temperatures and polarization potentials.

8.2 Overview of The MCB Model

Detail descriptions of the fundamental physical and chemical processes that underlie the MCB model and the general formulation of the flux equations included in the model can be found elsewhere [11]. Only brief description of the MCB model is provided here. The MCB model takes into account the dependence of the potential drop across an oxide film on the type and thickness of the oxide(s) that grow with time. Thus, the MCB model contains only three flux equations, for metal oxidation ($J_{M\#^{n+}}(t)|_{m|ox}$), oxide growth ($J_{MO\#}(t)|_{oxide}$) and metal dissolution ($J_{diss\#}(t)|_{sol}$), and of these only two fluxes are independent of each other, see schematic in Figure 8-1. The mathematical formulae of these fluxes are given in Table 8-1.
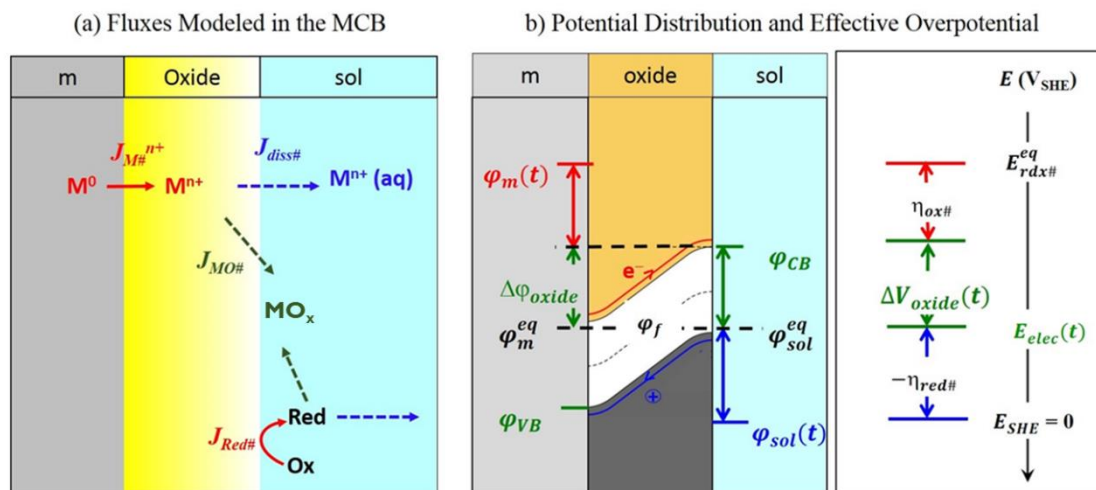
Figure 8-1: **Schematics illustrating (a) the fluxes considered in the MCB model, and (b) the distribution of the driving force for a corrosion reaction and the relationship between the driving force and the effective overpotential.**

The MCB model formulates the oxidation flux arising from each electrochemical redox reaction using a modified Butler-Volmer equation with an effective overpotential, $\eta_{ox\#}(t)$ (Formula 1 in Table 8-1). The oxidized metal either participates in oxide formation or dissolves into solution. The MCB model formulates the fluxes of both oxide growth and

dissolution to have first-order dependences on the oxidation flux (Formula 2 and Formula 3, respectively, in Table 8-1). However, due to mass balance the sum of the oxide growth and dissolution fluxes must equal the oxidation flux, and their relative fluxes are determined by competition kinetics, controlled by their first-order rate constants, $k_{MO\#}(t)$ and $k_{diss\#}$, respectively.

The flux equations in the MCB model contain time-dependent terms, the effective overpotential ($\eta_{ox\#}(t)$) in the oxidation flux and the first-order rate constant for oxide MO# formation ($k_{MO\#}(t)$) in the oxide growth flux. These kinetic parameters are further defined as listed in Table 8-1. Irrespective of the type of oxide that forms and the rate of its formation, oxide formation is an electrochemical reaction and is constrained by reaction thermodynamics. The thermodynamic constraints invoked in the MCB model include a requirement that the driving force for metal oxidation (coupled with solution reduction) leading to formation of a specific oxide is the difference in the equilibrium potentials of the two coupled redox half-reactions for that redox reaction $\left(E_{red\#}^{eq} - E_{ox\#}^{eq}\right)$. The MCB model distributes this thermodynamic driving force between the m|ox and ox|sol interfaces and the oxide layer. The potential drop in the oxide ($\Delta V_{oxide}(t)$) is assumed to be linearly dependent on the oxide thickness ($L_{MO\#}(t)$), see the schematic in Figure 8-1. This increase in $\Delta V_{oxide}(t)$ with $L_{MO\#}(t)$ decreases the effective overpotentials for the redox half-reactions at the two interfaces. This allows the flux of metal oxidation to be formulated using a modified Butler-Volmer equation with an effective overpotential. The effective overpotential for a specific metal oxidation reaction can then be defined as a function of the thickness of the oxide that is growing, as presented in Formula 4 and Formula 5 in Table 8-1, respectively. Table 8-1 also provides formula for the model output of experimentally measured parameters, current, oxide thickness and dissolved amount of metal ions.

The potential drop across a growing oxide layer depends on oxide thickness, and the oxide thickness depends on the linear (1-D) rate for oxide growth with time. The MCB model assumes that the rate of oxide growth has a first-order dependence on the oxidation flux, the oxide growth rate constant ($k_{MO\#}(t)$) has an Arrhenius dependence on the activation energy, and the oxide layer is an activation energy barrier. Because the activation energy increases with an increase in $\Delta V_{oxide}(t)$ (Formula 6 in Table 8-1), the rate constant for oxide formation

decreases exponentially with an increase in oxide thickness (Formula 7 in Table 8-1). In contrast to the changing oxide growth rate with oxide thickness, the rate constant for metal dissolution at the ox|sol interface is generally assumed to be independent of oxide thickness. It is recognized as being dependent on the type of dissolving oxide and the metal cation dissolution properties of the contacting solution (pH, temperature, flow).

Alloys may contain more than one redox-active element that can form an oxide or hydroxide of a single metal element. As well, an alloy can support the formation of a mixed oxide/hydroxide that contains more than one metal element. In addition, transition metals can exist in more than one oxidation state and this, combined with the possibility of forming several different stable oxides and hydroxides, leads to the possible formation of many different layers of oxides/hydroxides on a metal surface. The MCB model recognizes that different metal oxides can form and that the oxide composition and structure may change as corrosion progresses. The result can be a complex and shifting set of oxides that form and grow as a function of time [10, 13-17]. The MCB model applies the three flux equations to each metal oxidation reaction leading to the formation of a specific oxide and the dissolution of the different metal ions. For each oxidation reaction, the MCB model imposes the mass and charge balance requirements and the reaction thermodynamic and kinetic constraints on each metal oxidation process. The MCB model formulates the specific (per unit thickness) potential drop across an oxide layer to depend on the type of oxide and temperature but not on the solution pH or electrode potential. The model allows the type and the thickness of the oxide layer to evolve with time according to the flux equations. This in turn allows for changes in the overall potential drop across the oxide layer as corrosion progresses.

Table 8-1: Mathematical Formulae of the Fluxes in the MCB Model.

Flux Equations used in the Model	Model Output	
$J_{M\#^{n+}}(t)\|_{m\|ox} = J_{rdx\#}^{eq} \cdot \left(exp\left(\frac{0.5 \cdot n \cdot F}{RT} \cdot \eta_{ox\#}(t) \right) \right)$ when $\eta_{ox\#}^{eff}(t) > 0$ $J_{M\#^{n+}}(t)\|_{m\|ox} = 0$ when $\eta_{ox\#}^{eff}(t) \leq 0$	Current (t) $i_{ox\#}(t) = n \cdot F \cdot J_{M\#^{n+}}(t)\|_{m\|ox}$	1
$J_{MO\#}(t)\|_{oxide} = \left(\frac{k_{MO\#}(t)}{k_{MO\#}(t) + k_{diss\#}} \right) \cdot J_{M\#^{n+}}(t)\|_{m\|ox}$	Oxide thickness (t) $L_{MO\#}(t) = \upsilon_{MO\#} \cdot \int_{t=0}^{t} (J_{MO\#}(t)\|_{oxide}) \cdot dt$	2
$J_{diss\#}(t)\|_{sol} = J_{M\#^{n+}}(t)\|_{m\|ox} - J_{MO\#}(t)\|_{oxide}$	Dissolved amount (t) $m_{diss\#}(t) = A_{sol} \cdot \int_{t=0}^{t} (J_{diss\#}(t)\|_{sol}) \cdot dt$	3
Time Dependent Terms in the Flux Equations	**Model Parameters**	
$\eta_{rdx\#}(t) = E_{red\#}^{eq} - E_{ox\#}^{eq} - \Delta V_{oxide}(t)$ $\eta_{ox\#}(t) = E^{elec}(t) - E_{ox\#}^{eq} - \Delta V_{oxide}(t)$	$J_{rdx\#}^{eq}, E_{red\#}^{eq}, E_{ox\#}^{eq}$	4
$\Delta V_{oxide}(t) = \Delta V_{oxide}(0) + \varepsilon_{MO\#} \cdot L_{MO\#}(t)$	$\Delta V_{oxide}(0), \varepsilon_{MO\#}, \upsilon_{MO\#}$	5
$\Delta Ea_{MO\#}(t) = \Delta Ea_{MO\#}(0) + c_{MO\#} \cdot L_{MO\#}(t)$	$\Delta Ea_{MO\#}(0), c_{MO\#}$	6
$k_{MO\#}(t) = k_{MO\#}(0) \cdot exp\left(-\frac{c_{MO\#} \cdot L_{MO\#}(t)}{RT} \right)$	$k_{MO\#}(0), k_{diss\#}$	7

8.3   The MCB Model for Stellite-6 Corrosion

In this section, we show how the MCB model (i.e., elementary corrosion reactions and the corresponding flux equations) is constructed for Stellite-6 at different temperatures (room temperature and 80 °C, pHs (8.4 and 10.6) and range of potential from –0.4 to 0.1 V$_{SCE}$, and the rate parameters and boundary conditions that are formulated in the model. The model simulations results are presented in Section 8.4.

8.3.1   Alloy composition

The alloy composition of Stellite-6 is provided in Table 8-2. The morphology of the alloy surface shows two distinct phases, a Cr-carbide network (darker areas in the SEM images) distributed in a Cr-Co solidus solution, Figure 8-2. For the model simulations

presented here, we assumed that the surface activity of Cr or Co is proportional to its atomic fraction in the alloy. Hence, the oxidation flux of each metal element is the oxidation flux determined by the modified Butler-Volmer equation multiplied by its atomic fraction. The implicit assumption is that the surface electrochemical reactions of the individual elements do not interact synergistically. Oxidation reactions of all other minor elements were ignored for simplicity (not due to a model limitation). The model included all of the possible oxidation reactions of the two main alloy elements that can occur within the reaction thermodynamic constraints. Different rates of oxide growth on different alloy phases may be possible, but the model simulation presented in this paper did not separate the rate equations occurring over different phases. This again made the model simpler and it also reflects our lack of verifiable experimental data for separate corrosion rates on the two phases.
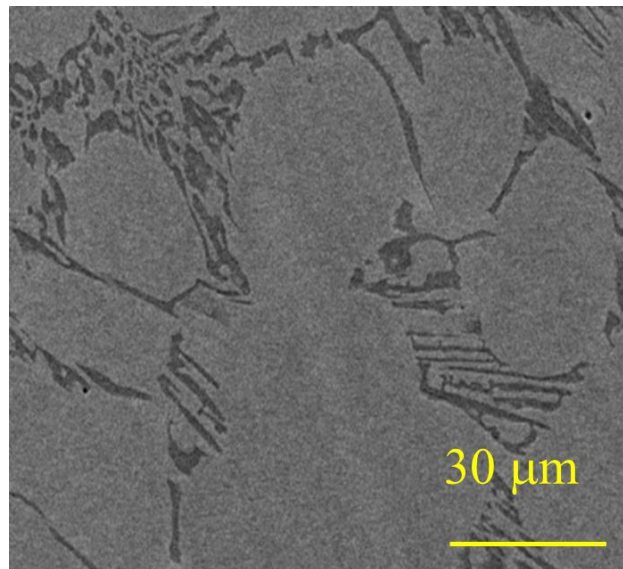
Figure 8-2: **SEM of a freshly polished surface of Stellite-6 showing two alloy phases. The dark regions are the chromium-carbide phase and the grey regions are the Co-Cr solidus solution phase.**

Table 8-2: Elemental composition of Stellite-6 in both weight percentage (wt.%) and atomic percentage (at.%).

	Co	Cr	C	W	Ni	Fe	Si	Mo
wt.%	57	27	1.4	4.1	2.6	2.9	1.1	0.4
at.%	54.7	29.4	6.6	1.3	2.5	2.9	2.2	0.2

8.3.2 **Redox reactions and their equilibrium potentials**

The oxidation flux $(J_{M\#^{n+}}(t)|_{m|ox})$ for a specific metal oxidation reaction ($ox\#$) is determined by a modified Butler-Volmer equation with an effective overpotential ($\eta_{ox\#}^{eff}(t)$), Formula 1 in Table 8-1:

$$J_{M\#^{n+}}(t)|_{m|ox} = J_{rdx\#}^{eq}\cdot\exp\left(\frac{0.5nF}{RT}\cdot\eta_{ox\#}^{eff}(t)\right) \text{ when } \eta_{ox\#}^{eff}(t) > 0 \qquad (8\text{-}1a)$$

$$J_{M\#^{n+}}(t)|_{m|ox} = 0 \text{ when } \eta_{ox\#}^{eff}(t) \leq 0 \qquad (8\text{-}1b)$$

where $J_{rdx\#}^{eq}$ is the forward and reverse rates of the redox reaction at equilibrium and is equivalent to the exchange current, $i_{rdx\#}^{0}$.

The oxidation flux equation contains two rate parameters, $\eta_{ox\#}^{eff}(t)$ and $J_{rdx\#}^{eq}$. The MCB model defines $\eta_{ox\#}^{eff}(t)$ as a function of the system potential (created by corrosion or external polarization) ($E^{elec}(t)$), the equilibrium potential ($E_{ox\#}^{eq}$) for reaction $ox\#$ and the potential drop across a growing oxide layer(s) ($\Delta V_{oxide}(t)$) (Formula 4 in Table 8-1):

$$\eta_{ox\#}^{eff}(t) = E^{elec}(t) - E_{ox\#}^{eq} - \Delta V_{oxide}(t) \qquad (8\text{-}2)$$

where $E^{elec}(t)$ and $\Delta V_{oxide}(t)$ may change with time. Even for constant $E^{elec}(t)$, the effective overpotential can change due to a change in $\Delta V_{oxide}(t)$ as corrosion progresses and the oxide layer changes.

The exchange-current equivalent parameter, $J_{rdx\#}^{eq}$, is the forward or reverse rate of a redox reaction at equilibrium (e.g., $Co^0 \leftrightarrows Co^{II}$). The exchange current is a fundamental parameter that is specific to a specific metal oxidation in a given corrosion environment. The MCB model recognizes this. For example, the exchange current for the cobalt oxidation of ($Co^0 \leftrightarrows Co^{II} + 2\ e^-$) involving the alloy and a Co^{II} oxide (e.g., $CoCr_2O_4$) phase will be different from the chromium oxidation reaction of ($Cr^0 \leftrightarrows Cr^{III} + 3\ e^-$) between the alloy and that oxide. The values for these exchange currents are not generally available. To obtain a consistent set of exchange current values we extracted them from our data for the total current

measured during potentiostatic polarization experiments. These experiments were performed for sufficiently large number of different parameters to give us enough data for the fitting process. We estimated an initial set of exchange current values and used them in the model to calculate the total current (as a function of time) for a given experiment. We then modified our initial estimates, repeated the calculation and compared the calculation result with the data. This process was repeated until the difference between experiment and model calculation was judged to be acceptably small. The final values of the exchange currents obtained from this fitting process were then used in the model for the calculation of the results of other experiments.

The MCB model consists of a set of oxidation flux equations (Eq. 8-1) for individual redox reactions that can occur during corrosion of an alloy. The metal oxidation reactions considered for the simulation of Stellite-6 corrosion are listed in Table 8-3. The equilibrium potentials of these reactions are well established and their values at pH 10.6 and 25 °C are presented also in Table 8-3 and Figure 8-3 [10, 16, 17]. Direct oxidation of metal to an aqueous metal ion is not explicitly included in the oxidation flux calculations since metal cation dissolution is formulated using the dissolution flux ($J_{diss\#}(t)|_{sol}$). For metal oxidation that can lead to formation of both oxide and hydroxide phases, the lower potential of the two options was used in calculating the effective overpotential for that oxidation. For example, reaction (1) of Table 8-3 occurs in the presence of Cr_2O_3 on a Stellite-6 surface and hence the equilibrium potential for the oxidation of Cr to Cr^{III} is that of Cr forming Cr_2O_3. The Cr_2O_3 that is in contact with water can be hydrated and hydrolyzed ($Cr_2O_3 + x\ H_2O \leftrightarrows 2\ Cr(OH)_{3-x}^{x+} + 2x\ OH^-$, $x = 0,1,2,3$) [32], leading to either formation of solid $Cr(OH)_3$ or dissolution of the hydrated Cr^{III} ions into the solution. In contrast, the equilibrium potential used for the oxidation of Co to Co^{II} is the value that leads to the formation of $CoCr_2O_4$ with Cr_2O_3 on the surface (reaction 2 of Table 8-3), or the formation of $Co(OH)_2$ when Cr_2O_3 is not available (reaction 3 of Table 8-3). Similarly, any $CoCr_2O_4$ or $Co(OH)_2$ in contact with water can then be hydrated and hydrolyzed, leading to either formation and growth of solid $Co(OH)_2$ or dissolution of the hydrated Co^{II} ions into the solution. Any solid $Co(OH)_2$ that forms can build up and be slowly dehydrated to form solid CoO. The surface hydration and

hydrolysis of metal cations and the solid-state conversion of the oxide/hydroxide phases do not generate a net current, but influences oxide growth and dissolution of metal.
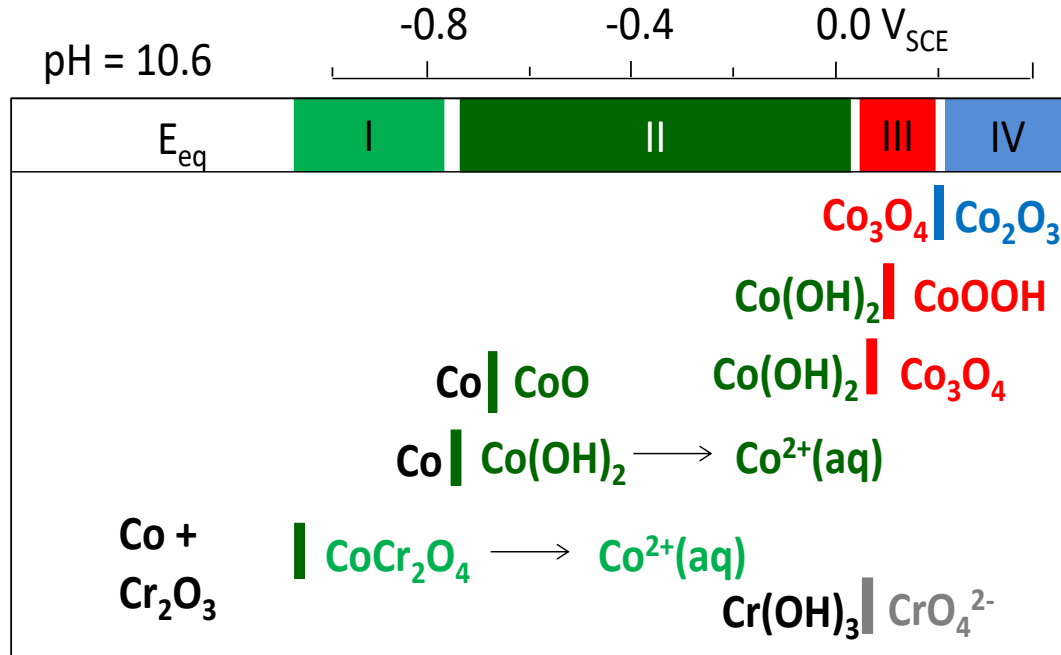
Figure 8-3: **Equilibrium potentials for the redox reactions that can occur on Stellite-6. The potential regions of stability of different oxides are indicated on top as bars with roman numerals. The arrows indicate dissolution pathways of Co^{II}.**

Table 8-3: The metal oxidation reactions considered in the simulation of Stellite-6 corrosion and the corresponding equilibrium reactions and equilibrium potentials.

$M\#^{n+}$	Metal Oxidation Reaction	Corresponding Equilibrium Reaction	E_{eq} at pH 10.6 (SCE)
1	$Cr \rightarrow Cr_2O_3/Cr(OH)_3$	$2\,Cr + 3\,H_2O = Cr_2O_3 + 3\,H_2$ $(Cr_2O_3 + 3\,H_2O = 2\,Cr(OH)_3)^*$	-1.4
2	$Co + Cr_2O_3 \rightarrow CoCr_2O_4$	$Co + Cr_2O_3 + H_2O = CoCr_2O_4 + H_2$	-1.1
3	$Co \rightarrow CoO/Co(OH)_2$	$Co + 2\,H_2O = Co(OH)_2 + H_2$ $(Co(OH)_2 = CoO + H_2O)^*$	-0.7

The oxide layer formed on an alloy may be passive for ion or ion vacancy transport but not for electron and hole transport [33, 34]. Thus, while the presence of an oxide layer

may supress further metal oxidation, under potentiostatic polarization the reduction reaction of a solution species that is not coupled with metal oxidation but is coupled with the oxidation of another solution species on the counter electrode, can continue to occur. For example, reduction of H_2O or dissolved O_2 (at an impurity level) can occur on a 'non-corroding' working electrode coupled with oxidation of H_2 or H_2O on the counter electrode:

$$2\ H_2O + 2\ e^- \rightarrow H_2 + 2\ OH^- \text{ on WE} \tag{8-3a}$$

$$H_2 + 2\ OH^- \rightarrow 2\ H_2O + 2\ e^- \text{ on CE} \tag{8-3b}$$

and/or

$$O_2 + 2\ H_2O + 4\ e^- \rightarrow 4\ OH^- \text{ on WE} \tag{8-4a}$$

$$4\ OH^- \rightarrow O_2 + 2\ H_2O + 4\ e^- \text{ on CE} \tag{8-4b}$$
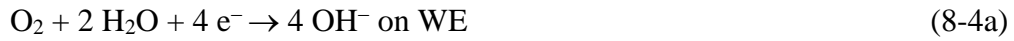
These solution redox reactions do not contribute to either a metal oxidation flux or an oxide growth flux (on a passive alloy), but they do contribute to the net current that is being monitored during polarization. To compare the results of model calculations with the experimentally measured net current, the contribution of any such solution reactions on the WE must be taken into account. To do this we considered a solution reduction reaction on the working electrode as a separate independent redox reaction with its own equilibrium potential (or the difference of the equilibrium potentials of the two half-reactions of aqueous reduction and aqueous oxidation).

The solution reduction flux was modelled the same way as the metal oxidation flux, i.e., using a modified Butler-Volmer equation with an effective overpotential:

$$J_{sol-red}(t)|_{ox|sol} = -J_{sol-rdx}^{eq} \cdot \exp\left(\frac{0.5nF}{RT}\left(-\eta_{sol-red}^{eff}\right)\right) \quad \text{when } \eta_{ox\#}^{eff}(t) < 0$$

$$\tag{8-5}$$

$$\eta_{ox\#}^{eff}(t) = E_{sol-red}^{eq} - E^{elec}(t) - f_{sol} \cdot \Delta V_{oxide}(t) \tag{8-6}$$

where $E_{sol-red}^{eq}$ is the equilibrium potential for the solution redox reaction, and the factor f_{sol} is used to adjust for the difference in the potential barrier for electron transfer for solution redox reactions and that for ion and ion vacancy transfer for metal/metal oxide redox reactions. Since the resistance to ion and ion vacancy transport across a solid oxide layer is several orders of magnitude higher than that of electrons and holes, f_{sol} was assumed to be zero. Due to difficulties in accurately measuring the dissolved concentrations of H_2, O_2 and other potential redox active impurities, $E_{sol-red}^{eq}$ was obtained by measuring the open circuit potential on a Pt working electrode in the same solution environment.

8.3.3 Potential drop across a growing oxide layer

Solving the oxidation flux equation requires formulation of $\Delta V_{oxide}(t)$ as corrosion progresses and the oxide layer changes. In the MCB model the potential drop is formulated as:

$$\Delta V_{oxide}(t) = \sum \varepsilon_{MO\#} \cdot L_{MO\#}(t) \tag{8-7}$$

where $L_{MO\#}(t)$ is the thickness of the layer of oxide, MO#, at time t, $\varepsilon_{MO\#}$ is the specific potential drop per unit thickness, or field strength of the MO# layer, and the summation is over all of the different types of oxides that comprise the oxide layer. The specific potential drop is characteristic of the oxide and should be independent of solution pH and the polarization potential but dependent upon temperature. The metal oxides that can form on Stellite-6 within the studied potential range (–0.4 V_{SCE} to 0.1 V_{SCE}) are Cr_2O_3, $CoCr_2O_4$ and $CoO/Co(OH)_2$. The values for the specific potential drops across these oxides are not available. As for the exchange currents, we determined values for the specific potential drops by comparing the results of model calculations with trail values against the oxide data obtained as a function of potential at a given temperature. Recursion was used to obtain 'best' fit values. The values that were determined are within ranges of the values found for transition metal oxides (10^5 to 10^7 V·cm^{-1}) [11, 18-29].

In the simulations of Stellite-6 corrosion, the surface was assumed to be initially covered with a 2-nm thick layer of chromium oxide (Cr_2O_3) [35]. It has been well established that alloys containing more than 12% Cr display corrosion resistance and this resistance is

attributed to the presence of a thin protective layer of air-formed Cr_2O_3 on the surface. Mott has shown that the thickness of the oxide on the surface of self-passivating metals like chromium after long exposure to air at room temperature can be 5 nm thick at maximum [27]. The oxide thickness used in the simulations is within this limit.

Our studies on oxide formation and growth on a range of Cr-containing alloys have shown that the pre-formed chromium oxide can be converted to chromite under conditions where oxide growth is favoured over dissolution, e.g., at a high pH [10, 16, 17]. On Stellite-6 the redox reaction for this conversion is:

$$Co^0 + Cr_2O_3 + H_2O = CoCr_2O_4 + H_2 \qquad (8\text{-}8)$$
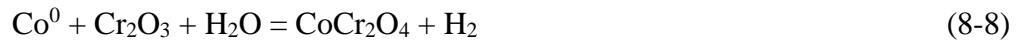
As corrosion progresses the oxide film changes from a chromium oxide layer to a more chromite-like layer [16, 17]. While this occurs there is a slow change in the electric field across the oxide layer. As the oxide changes two layers will become present, chromium oxide and chromite. The boundary between the layers will not be sharp, but we can treat them as distinct layers for mathematical formulation of the potential drop across the mixed oxide film. The oxidation of chromium (albeit very slowly) will increase, while its conversion into chromite will decrease the thickness of the chromium oxide layer with time:

$$L_{Cr2O3}(t) = L_0 - f_l \cdot L_{CoCr2O4}(t) + \frac{dL_{Cr2O3}(t)}{dt} \Delta t \qquad (8\text{-}9)$$

where $L_{Cr2O3}(t)$ and $L_{CoCr2O4}(t)$ are the thicknesses of the chromium oxide and chromite layers, and L_0 is the initial air-formed chromium oxide thickness. The factor f_l accounts for the thickness change associated with the different sizes of the Cr_2O_3 and chromite oxide crystal lattices. For the purpose of our initial simulations we have set $f_l = 1$.

The oxidative conversion of Co^0 to Co^{II} to form $CoCr_2O_4$ is assumed to occur only in the presence of Cr_2O_3. Thus, when all of the air-formed Cr_2O_3 has been converted to chromite or dissolved into solution, the rate of formation of $CoCr_2O_4$ is limited by the rate of oxidation of Cr^0 to form Cr_2O_3. For an alloy in de-oxygenated water this rate is very slow. This is because the activation energy for the Cr^0 oxidation increases very rapidly with increasing oxide thickness due to a very high lattice energy for Cr_2O_3 (15.186 kJ/mol) [27, 36].

In addition to the formation of $CoCr_2O_4$ the oxidation of Co^0 to Co^{II} can also lead to formation of the $CoO/Co(OH)_2$. In our simulations, we consider CoO to be a dehydrated form of $Co(OH)_2$ and treat them as a same oxide for the purpose of calculating oxidation fluxes. The potential drop across the entire oxide layer on Stellite-6 at a given time can be expressed as:

$$\Delta V_{oxide}(t) = \varepsilon_{Cr2O3} \cdot L_{Cr2O3}(t) + \varepsilon_{CoCr2O4} \cdot L_{CoCr2O4}(t) + \varepsilon_{Co(OH)2} \cdot L_{Co(OH)2}(t)$$

(8-10)

where and ε_{Cr2O3}, $\varepsilon_{CoCr2O4}$ and $\varepsilon_{Co(OH)2}$ are the specific potential drops across Cr_2O_3, $CoCr_2O_4$ and $Co(OH)_2$ layers, respectively.

8.3.4 Formulation of oxide growth and dissolution fluxes

Oxide formation will compete with dissolution for the metal cations produced by the electrochemical oxidation reactions. Due to mass balance the oxide growth flux $(J_{MO\#}(t)|_{oxide})$ and the dissolution flux $(J_{diss\#}(t)|_{sol})$ are not independent and are related to the oxidation flux as:

$$J_{MO\#}(t)|_{oxide} = f_{k-MO\#}(t) \cdot J_{M\#^{n+}}(t)|_{m|ox}$$

(8-11)

$$J_{diss\#}(t)|_{sol} = \left(1 - f_{k-MO\#}(t)\right) \cdot J_{M\#^{n+}}(t)|_{m|ox}$$

(8-12)

$$f_{k-MO\#}(t) = \left(\frac{k_{MO\#}(t)}{k_{MO\#}(t) + k_{diss\#}}\right)$$

(8-13)

where $k_{MO\#}(t)$ is the first-order rate constant for the formation of oxide, MO# at time t and $k_{diss\#}$ is the first-order rate constant for the dissolution of $M\#^{n+}$ from the oxide into solution.

The dissolution of the metal cations formed during corrosion occur via surface hydration of the metal cation and the rate constant for this process will then depend only on the surface hydration energy of the oxide. The MCB model recognizes this and the rate constant for the dissolution of $M\#^{n+}$ depends on the type of oxide and the solution environment (pH, temperature, flow rate). Hence it does not change with time as corrosion progresses and the oxide layer thickens. However, the rate of dissolution changes with time

because of the changes in $J_{M\#^{n+}}(t)|_{m|ox}$ and $k_{MO\#}(t)$ as corrosion progresses. The flow rate included in the solution environmental parameters is intended to encompass all of the processes affecting mass transfer to and from the alloy surface in the solution (diffusion, turbulence, buoyancy flow, etc.). In our experiments, all of the parameters affecting mass transfer rates were held constant (except for temperature) and the mass transfer process were not included in the model.

The rate constant for oxide growth depends on the oxide layer thickness. Oxide formation is a chemical reaction, and it is reasonable to assume that its rate constant has an Arrhenius dependence on the activation energy for the reaction. The MO# layer constitutes an activation energy barrier for the chemical bond formation between metal cation formed on one side of the oxide and an oxygen anion present on the other side. One approximation for this activation energy is the Coulombic potential energy gap across the oxide layer $(\Delta V_{MO\#}(t))$, $(\Delta Ea_{MO\#}(t))$:

$$\Delta Ea_{MO\#}(t) = \Delta Ea_{MO\#}(0) + c' \cdot \Delta V_{MO\#}(t) = \Delta Ea_{MO\#}(0) + c_{MO\#} \cdot L_{MO\#}(t)$$

$$(8\text{-}14)$$

where c' is the proportionality constant of the activation energy for the formation of MO# (in J·mol^{-1}) to the potential drop across the MO# layer (in V·cm^{-1}) and $c_{MO\#}$ is the specific activation energy gradient of the oxide MO# (J·mol^{-1}·cm^{-1}). The activation energy for the oxide formation increases as the oxide grows and the rate constant for the oxide formation decreases accordingly:

$$k_{MO\#}(t) = k_{MO\#}(0) \cdot exp\left(-\frac{c_{MO\#} \cdot L_{MO\#}(t)}{RT}\right) \qquad (8\text{-}15a)$$

where

$$k_{MO\#}(0) = k_{0-MO\#} \cdot exp\left(-\frac{(\Delta Ea_{MO\#}(0))}{RT}\right) \qquad (8\text{-}15b)$$

(Note that any other contributors to the reaction activation energy are included in $\Delta Ea_{MO\#}(0)$ and the value of $k_{0-MO\#}$ which is the pre-exponential factor for the oxide formation; they are assumed to be constant with time.)

The rate constants at time 0, $k_{MO\#}(0)$ and $k_{diss\#}$, and the activation energy, $\Delta Ea_{MO\#}(0)$, can be independently measured. However, these values as a function of solution pH and temperature are not available for the cobalt and chromium oxides. In the model simulations, the individual values of $k_{MO\#}(0)$ and $k_{diss\#}$ are not needed but only their fractional contributions because mass balance requires the metal oxidation flux to be the same as the sum of the oxide flux and dissolution flux. The initial oxide-flux fraction of the metal oxidation flux at time 0, $f_{k-MO\#}(0)$, is defined as:

$$f_{k-MO\#}(0) = \left(\frac{k_{MO\#}(0)}{k_{MO\#}(0) + k_{diss\#}} \right) \tag{8-16}$$

The fractions are independent of the polarization potential and dependent upon pH and temperature because of their impact on $k_{diss\#}$. As for the exchange currents and specific potential drops across oxides, we determined values for the initial oxide-flux fractions in the same manner using the potentiostatic data obtained as a function of potential and pH at a given temperature. Recursion was used to obtain 'best' fit values.

The oxide-flux fraction, $f_{k-MO\#}(t)$, changes with time because $k_{MO\#}(t)$ changes with oxide thickness according to Eq. 8-9. The value for the proportionality constant, $c_{MO\#}$, was also the best fit of potentiostatic polarization data and was independent of potential, pH and temperature but dependent only upon oxide type. The values used in the simulations are listed in Section 8.4.

8.3.5 Model output of experimental quantities

In order to compare the model simulation results with experimental data, the different fluxes calculated in the model were converted to the experimentally measured quantities (e.g., oxide thickness, dissolved metal quantities).

Current: The current monitored as a function of time is the sum of the anodic current arising from the oxidation fluxes, $J_{M\#^{n+}}(t)|_{m|ox}$, of all the cobalt and chromium reactions listed in

Table 8-3, and the cathodic current arising from the reduction flux of solution species at the working electrode (reactions 8-3a and 8-4a):

$$i_{net}(t) = i_a(t) + i_c(t) \tag{8-17a}$$

$$i_a(t) = n F \cdot \Sigma f_M \cdot J_{M\#^{n+}}(t)|_{m|ox} \tag{8-17b}$$

$$i_c(t) = -nF \cdot J_{sol-red}(t)|_{ox|sol} \tag{8-17c}$$

Oxide composition and thickness: The oxide growth flux, $J_{MO\#}(t)|_{oxide}$, is related to the thickness of the oxide, MO#:

$$\upsilon_{MO\#} \cdot (J_{MO\#}(t)|_{oxide}) \cdot dt = dL_{MO\#}(t) \tag{8-18}$$

where $\upsilon_{MO\#}$ is the molar volume of MO# ($cm^3 \cdot mol^{-1}$). The molar volumes of Cr_2O_3, $CoCr_2O_4$ and CoO, $Co(OH)_2$ reported in the literature are 24, 45 and 12 $cm^3 \cdot mol^{-1}$, respectively, and these values are used in the simulations.

Amount of dissolved metal: The dissolution flux, $J_{diss\#}(t)|_{sol}$, is the rate of dissolution of metal cation $M\#^{n+}$ per unit surface area exposed to solution:

$$J_{diss\#}(t)|_{sol} = \frac{dm_{diss\#}(t)}{dt} \tag{8-19a}$$

$$m_{diss\#}(t) = \frac{MW_{M\#} \cdot A_{int}}{V_{sol}} \cdot \int_0^t (J_{diss\#}(t)|_{sol} \cdot dt) \tag{8-19b}$$

where $m_{diss\#}(t)$ represents the amount of dissolved $M\#^{n+}$ over time t in units of $g \cdot L^{-1}$, $MW_{M\#}$ is the molar mass of metal M# ($g \cdot mol^{-1}$), $J_{diss\#}(t)|_{sol}$ is in units of $mol \cdot cm^{-2} \cdot s^{-1}$, A_{int} is the interfacial surface area (cm^2) and V_{sol} is the volume of solution (L). The molar masses of Co and Cr are 59 and 52 $g \cdot mol^{-1}$, respectively.

8.4 Model Simulation Results

We have performed a combination of electrochemical and coupon-exposure experiments to investigate the corrosion kinetics of Stellite-6 as a function of potential, pH,

temperature and γ-radiation exposure [16, 17]. The electrochemical experiments include potentiostatic polarization as a function of potential, E^{elec}(t). The electrochemical experiments were augmented by post-test surface morphology and depth analyses using scanning electron microscopy (SEM), X-ray photoelectron spectroscopy (XPS) and Auger electron spectroscopy (AES) with Ar^+ sputtering. The coupon exposure experiments were performed in sealed quartz vials and the dissolved cobalt and chromium concentrations in the solutions were determined using inductively coupled plasma – mass spectrometry (ICP-MS). Some of these studies have been published and the details of the experiments can be found elsewhere [16, 17]. The AES depth-profile data from those studies were reanalyzed to enable comparison of the experimental results with model calculations. This AES data reanalysis is summarized in Appendix B.

The MCB model calculations were performed for the experiments on Stellite-6 at two different pHs (10.6 and 8.4) and two different temperatures (25 and 80 °C). The model calculation results of potentiostatic polarization experiments as a function of potential are presented in Section 8.4.1 and corrosion potential measurements and coupon exposure tests in Section 8.4.2. The values of the rate parameters used in the model calculations are listed in Table 8-4. It should be emphasized that at a given pH and temperature all of the model parameters are independent of the electrode potential (corrosion potential or polarization potential), and that at a given temperature, the only model parameter that depends on pH is the initial oxide-flux fraction ($f_{k-MO\#}(0)$). The temperature affects $f_{k-MO\#}(0)$ and the specific potential drop ($\varepsilon_{MO\#}$).

Table 8-4: The parameters derived for use in the MCB model for corrosion of Stellite-6.

T (°C)	pH	Initial Oxide-Flux Fraction $\left(\dfrac{k_{MO\#}(0)}{k_{MO\#}(0)+k_{diss\#}}\right)$			Specific Potential Drop $\varepsilon_{MO\#}$ (10^6 V·cm^{-1})			Specific ΔE_a Gradient, $c_{MO\#}$ (10^6 J·mol^{-1}·cm^{-1})			Exchange Current, $i^0_{rdx\#}$ (µA·cm^{-2})			
		Cr_2O_3	$CoCr_2O_4$	$Co(OH)_2$	Cr_2O_3	$CoCr_2O_4$	$Co(OH)_2$	Cr_2O_3	$CoCr_2O_4$	$Co(OH)_2$	$Cr^{III}\leftrightarrows Cr$	$Co\leftrightarrows Co^{II}$	$(O_2\leftrightarrows OH^-)$	$(H_2O\leftrightarrows H_2)$
25	8.4	0.97	0.53	0.40	3.2	5.2	1.0	50	10	0.1	2×10^{-6}	0.1	-10^{-4}	-0.1
	10.6	0.99	0.70	0.28										
80	10.6	0.96	0.53	0.42	3.0	4.4	0.1							

8.4.1 Model calculations of potentiostatic polarization experiments

The model calculation results are compared with the data from potentiostatic polarization experiments, the time-dependent behaviour of current in Figure 8-4, the layer structure and thickness of the oxide formed at the end of each polarization test in Figure 8-5 and the composition of the oxide in the top 3 nm layer in Figure 8-6 (oxidized Co[II & III] and metallic Co[0]). The oxide-layer structure presented in Figure 8-5 was determined by analyzing the elemental depth profiles obtained by AES with Ar^{+} sputtering, as described in reference [10] and summarized in the Appendix.
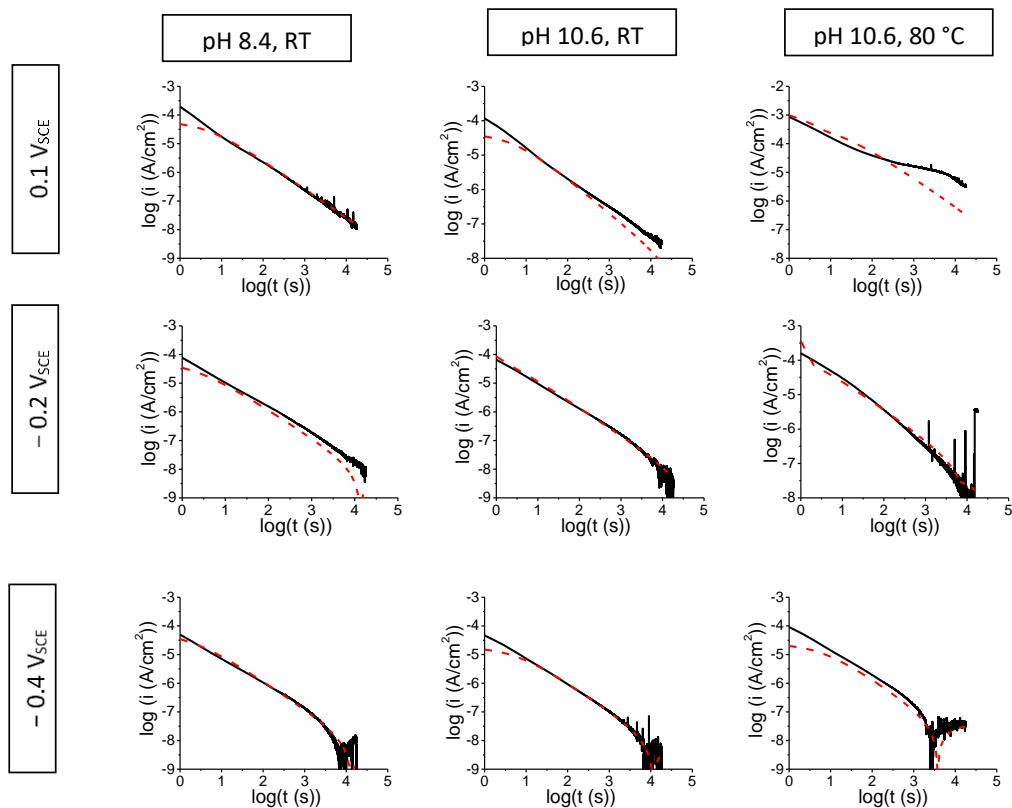
Figure 8-4: **Experimental (solid lines) and model calculations (broken lines) of current density as a function of time during potentiostatic polarization. Data obtained at three different potentials, +0.1, − 0.1 and − 0.4 V_{SCE}, at pH 8.4 and 10.6, and at 25 °C and 80 °C.**

In the Figure 8-5, at high potentials, model does not show any chromium oxide while experimental results show that the oxide chemistry at the interface of metal and oxide is close to Cr_2O_3. The reason for this behaviour, is not that the model cannot predict chromium oxide formation but it is because of its slow formation and rapid conversion to the cobalt chromite. In fact, based on the analytical method presented in the Appendix, we can consider interface of oxide and metal at the deepest point that all chromium elements are bounded to oxygen and form chromium oxide. Below this depth, there are chromium atoms that are not bonded to oxygen due to the insufficient amount of oxygen and above that, part of this chromium oxide is converted to cobalt chromite. This is well matched with our model results, however it shows it as cobalt chromite layer on the surface.

222
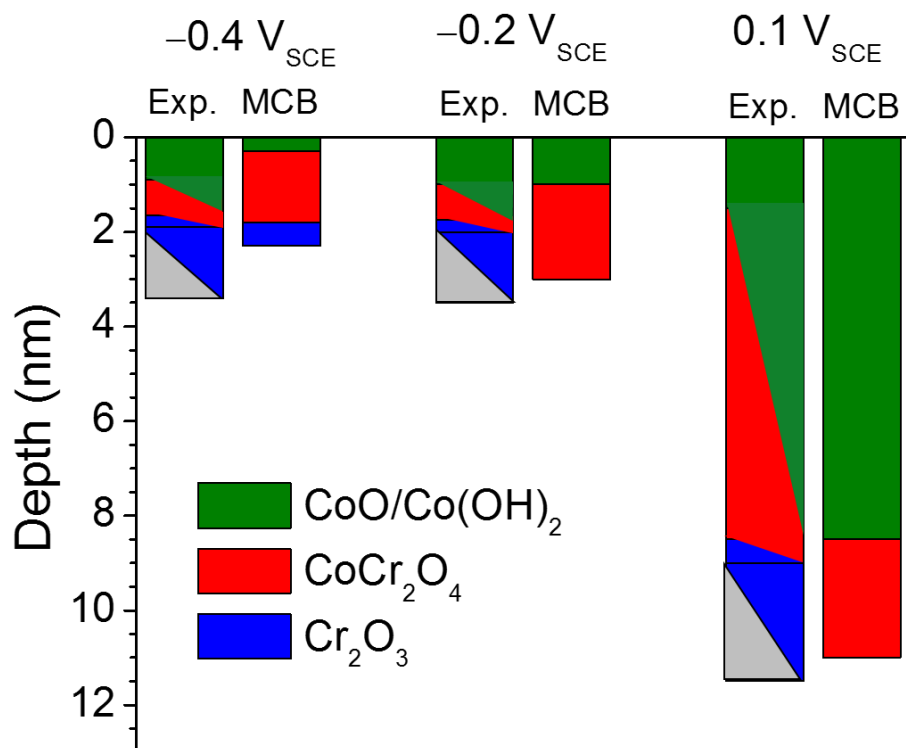
Figure 8-5: Comparison of the MCB model calculations with experimentally determined oxide-layer structures on Stellite-6 electrodes polarized for 5 h at different potentials at pH 10.6 and 80 °C. The numbers on the top of the graph indicate the polarization potentials

The experimental data for the fraction of oxidized cobalt were obtained from deconvolution of high resolution XPS O-1s, Co-2p and Cr-2p bands [16, 17]. Note that the analysis depth of the XPS instrument for a chromium oxide and cobalt oxide covered surface is not well defined and hence the XPS results are compared with the calculated fraction of oxidized cobalt in only the outer 3 nm of the oxide layer. The results obtained at only three potentials are shown for brevity in Figure 8-4, Figure 8-5 and Figure 8-6. The model also simulates the results obtained at other potentials (ranging from −0.8 V_{SCE} to 0.1 V_{SCE}) very well.
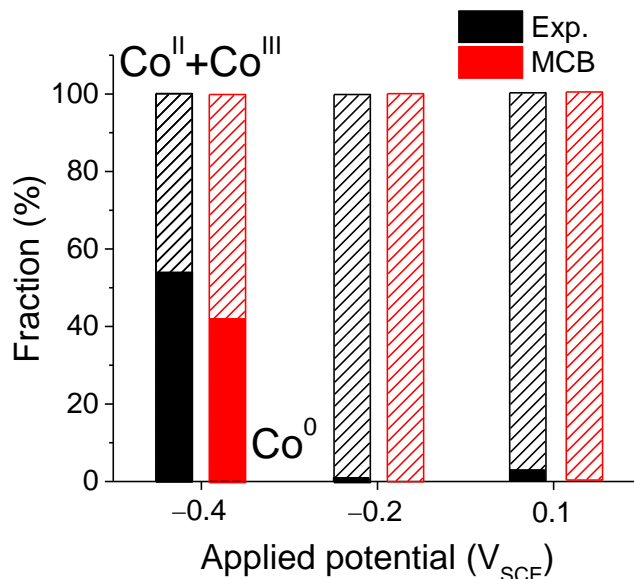
Figure 8-6: **Comparison of the MCB model calculations with experimental measurements of the fraction of oxidized cobalt in the top 3-nm layer on electrodes polarized for 5 h at different potentials at pH 10.6 and 80 °C. The solid columns show the metallic fraction (Co^0) and the dashed columns show the oxide fraction (Co^{II} & Co^{III})).**

8.4.2 **Corrosion under open-circuit conditions**

Under potentiostatic polarization the potential on the working electrode is controlled and any oxidation or reduction occurring on the working electrode is coupled with a redox reaction on the counter electrode. Under naturally corroding or open-circuit conditions, both half-reactions occur on the same (macroscopic) surface. In this case, the sum of all of the oxidation fluxes (the anodic current) must be the same as the sum of all of the reduction fluxes (the cathodic current) due to the charge and mass balance requirements, and these requirements dictate the corrosion potential:

$$\sum i_a = |\sum i_c| \text{ at corrosion potential} \qquad (8\text{-}20)$$

This is a necessary condition for the time evolution of the corrosion potential.

The MCB model determination of E_{CORR} on Stellite-6 in deaerated water was carried out as follows. The flux equations and the values of the rate parameters used for the E_{CORR} simulations were those determined by fits to the potentiostatic polarization data. For the solution reduction flux, Eqs. 8-5 and 8-6 were used. There is no data available for the exchange current density on Co-Cr alloys, so we set the exchange current density for water reduction (reaction 8-3a) on the surface of Stellite-6 at 10^{-7} A/cm^2 (Table 8-4). This value is in the range reported for the water reduction exchange current densities on the transitional metals [37]. Hydrogen (H$_2$) is produced by corrosion and quickly reaches a saturation level at room temperature of 5×10^{-5} atm. This value is used to calculate the equilibrium potential for water reduction, $E^{eq}_{H2O/H2} = -0.74$ V$_{SCE}$ at pH 10.6. Since the test solutions were Ar-purged the partial pressure of oxygen is very low, on the order of 10^{-6} atm. This value was used to calculate the equilibrium potential for the oxygen reduction reaction, $E^{eq}_{OH-/O2} = 0.2$ V$_{SCE}$ at pH 10.6. The equilibrium potential for oxygen reduction is greater than the corrosion potential measured on Stellite-6 under all conditions studied. Hence we assume that the rate of oxygen reduction is limited by the rate of aqueous diffusion of O$_2$ to the surface and not by the rate of the reduction at the surface. It is possible to calculate a diffusion-controlled current density for the O$_2$ reduction if the value for the dissolved O$_2$ concentration in the Ar-purged solution is known. We could not measure this O$_2$ concentration with our instruments. For a dissolved O$_2$ concentration of 10 ppb the diffusion-controlled current density is about -10^{-10} A/cm^2. This value was used as the limiting current density of oxygen reduction on the Stellite-6 surface.

The model calculation starts at -1.1 V$_{SCE}$ (the potential used for cathodic cleaning for 5-min prior to the E_{CORR} measurement). At the end of cathodic cleaning the surface is covered with a thin layer of chromium oxide formed by air oxidation that cannot be removed by this cathodic cleaning. The anodic current density from the sum of cobalt and chromium oxidation fluxes and the total cathodic current density from the sum of solution reduction fluxes were calculated according to Eqs. 8-1 and 8-5. Current density calculations were carried out at a potential over a potential range from -1.1 V$_{SCE}$ to the solution oxidation potential of 0.2 V$_{SCE}$. The upper limit was established by measuring open-circuit potential using a platinum working electrode. The potential for the calculations was stepped by 0.1

mV and the potential at which the difference between the anodic and cathodic current densities was less than 1% is taken as the corrosion potential.

Figure 8-7 compares the calculated and experimental corrosion potentials as a function of time for a few selected conditions. The MCB model calculation results are in excellent agreement with the data.
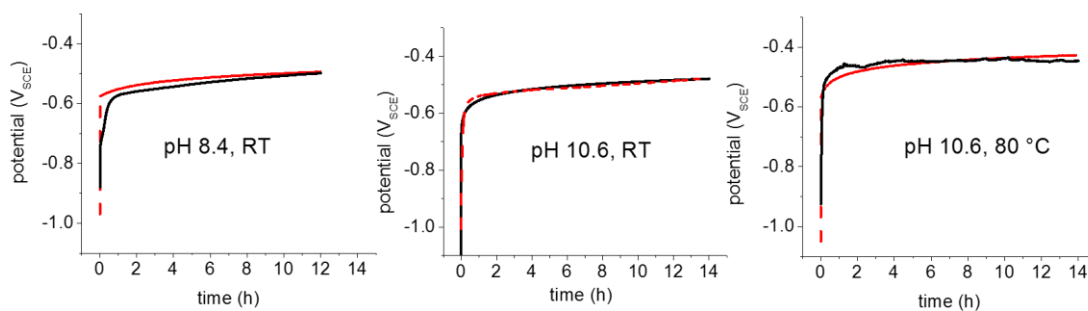
Figure 8-7: **Comparison of the MCB model calculations with experimentally determined corrosion potentials as a function of time for pH 8.4 and 25 °C, pH 10.6 and 25 °C, and pH 10.6 and 80 °C. The solid black lines are experimental data and the broken red lines are experimental data and the broken red lines are model simulation results.**

8.4.3   Oxide formation and dissolution

We have also performed MCB model simulations of the 3-d corrosion tests for Stellite-6 coupons. The same set of kinetic parameters derived from the potentiostatic polarization data were used for these calculations. The model results are compared with the experimental data for oxide formation and metal ion dissolution in Figure 8-8 and Figure 8-9. The MCB model simulates the corrosion tests very well. The model predicts correctly the effect of pH and temperature on not only the layer structure and thickness of the oxide formed but also the amounts of Co and Cr dissolved. The rate parameters used in the modeling of the corrosion tests were the same as those used for the other model calculations.
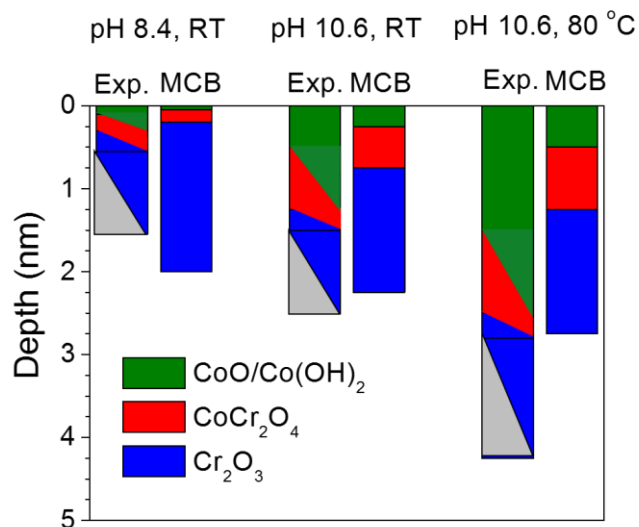
Figure 8-8: Comparison of the MCB model calculations with experimentally determined oxide-layer structures on Stellite-6 coupons corroded for 3 d in deaerated solutions at pH 8.4 and pH 10.6 at 25 °C, and at pH 10.6 at 80 °C.
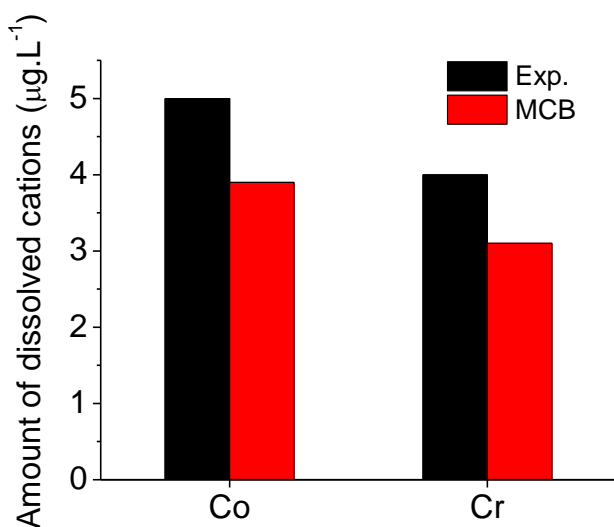
Figure 8-9: Comparison of the MCB model calculations with experimental measurements of the amounts of dissolved Co and Cr ions at pH 10.6 and 80 °C.

8.5   Conclusions

We have applied the mass and charge balance (MCB) model to simulate corrosion tests and electrochemical experiments performed on the Co-Cr alloy, Stellite-6. We have shown how the rate or flux equations for metal oxidation, oxide growth and dissolution are constructed and the values of the rate parameters in the model can be derived. Most of the model parameters are fundamental thermodynamic and reaction properties of the chemical elements involved in the corrosion reactions. Of these parameters, the rate constants for metal oxide growth and metal ion dissolution are the only ones that are sensitive to temperature and solution pH.

The model simulation results are in excellent agreement with the data obtained from different sets of experiments (electrochemical and corrosion tests) at two different pHs and at two different temperatures. The data compared include the time-evolution of current during polarization as a function of potential, the layer structure and thickness of oxide formed, and the amounts of Co and Cr ions dissolved in the solutions.

This study demonstrates that the MCB model can simulate the oxide growth and metal ion dissolution simultaneously during corrosion, even for an alloy with multiple oxidizing elements, and predict the effects of different solution environmental conditions on the overall corrosion rate.

8.6   References

[1] B.E. Wilde, The Role of Passivity in the Mechanism of Stress-Corrosion Cracking and Metal Dissolution of 18Cr - 8Ni Stainless Steels in Boiling Magnesium and Lithium Chlorides, Journal of The Electrochemical Society, 118 (1971) 1717-1725.

[2] S. Virtanen, H. Wojtas, P. Schmuki, H. Böhni, Passivity of High Corrosion Resistant Cu-Al-Sn Alloys, Journal of The Electrochemical Society, 140 (1993) 2786-2790.

[3] H.H. Uhlig, P. Bond, H. Feller, Corrosion and Passivity of Molybdenum-Nickel Alloys in Hydrochloric Acid, Journal of The Electrochemical Society, 110 (1963) 650-653.

[4] N.D. Tomashov, R.M. Altovsky, G.P. Chernova, Passivity and Corrosion Resistance of Titanium and Its Alloys, Journal of The Electrochemical Society, 108 (1961) 113-119.

[5] E. McCafferty, Graph Theory and the Passivity of Binary Alloys: More Examples, Journal of The Electrochemical Society, 151 (2004) B82-B89.

[6] D.B. Hibbert, S.V. Murphy, Kinetic Model of Iron Corrosion and Passivity, Journal of The Electrochemical Society, 138 (1991) L30-L32.

[7] A.P. Bond, H.H. Uhlig, Corrosion Behavior and Passivity of Nickel-Chromium and Cobalt-Chromium Alloys, Journal of The Electrochemical Society, 107 (1960) 488-493.

[8] L. Wang, K. Daub, Q. Knapp, Z. Qin, J.J. Noël, J.C. Wren, Effect of Ferrous Ions on Oxide Film Formation and Conversion on Stainless Steel, Journal of The Electrochemical Society, 159 (2012) C503-C512.

[9] Q.W. Knapp, J.C. Wren, Film formation on type-316L stainless steel as a function of potential: Probing the role of gamma-radiation, Electrochimica Acta, 80 (2012) 90-99.

[10] A.Y. Musa, M. Behazin, J.C. Wren, Potentiostatic Oxide Growth Kinetics on Ni-Cr and Co-Cr Alloys: Potential and pH Dependences, Electrochimica Acta, 162 (2015) 185-197.

[11] M. Momeni, J.C. Wren, A mechanistic model for oxide growth and dissolution during corrosion of Cr-containing alloys, Faraday Discussions, 180 (2015) 113-135.

[12] L. Wang, K. Daub, Z. Qin, J.C. Wren, Effect of dissolved ferrous iron on oxide film formation on carbon steel, Electrochimica Acta, 76 (2012) 208-217.

[13] K. Daub, X. Zhang, L. Wang, Z. Qin, J.J. Noël, J.C. Wren, Oxide growth and conversion on carbon steel as a function of temperature over 25 and 80 °C under ambient pressure, Electrochimica Acta, 56 (2011) 6661-6672.

[14] K. Daub, X. Zhang, J.J. Noël, J.C. Wren, Gamma-radiation-induced corrosion of carbon steel in neutral and mildly basic water at 150 °C, Corrosion Science, 53 (2011) 11-16.

[15] K. Daub, X. Zhang, J.J. Noël, J.C. Wren, Effects of γ-radiation versus H2O2 on carbon steel corrosion, Electrochimica Acta, 55 (2010) 2767-2776.

[16] M. Behazin, J.J. Noël, J.C. Wren, Combined Effects of pH and γ-Irradiation on the Corrosion of Co-Cr Alloy Stellite-6, Electrochimica Acta, 134 (2014) 399-410.

[17] M. Behazin, M.C. Biesinger, J.J. Noël, J.C. Wren, Comparative study of film formation on high-purity Co and Stellite-6: Probing the roles of a chromium oxide layer and gamma-radiation, Corrosion Science, 63 (2012) 40-50.

[18] W.A. Mueller, Theory of the polarization curve technique for studying corrosion and electrochemical protection, Canadian Journal of Chemistry, 38 (1960) 576-587.

[19] F.P. Fehlner, N.F. Mott, Low-temperature oxidation, Oxididation of Metals, 2 (1970) 59-99.

[20] G.T. Burstein, A.J. Davenport, The Current-Time Relationship during Anodic Oxide Film Growth under High Electric Field, Journal of The Electrochemical Society, 136 (1989) 936-941.

[21] V. Battaglia, J. Newman, Modeling of a Growing Oxide Film: The Iron/Iron Oxide System, Journal of The Electrochemical Society, 142 (1995) 1423-1430.

[22] K. Leistner, C. Toulemonde, B. Diawara, A. Seyeux, P. Marcus, Oxide Film Growth Kinetics on Metals and Alloys: II. Numerical Simulation of Transient Behavior, Journal of The Electrochemical Society, 160 (2013) C197-C205.

[23] A. Seyeux, V. Maurice, P. Marcus, Oxide Film Growth Kinetics on Metals and Alloys: I. Physical Model, Journal of The Electrochemical Society, 160 (2013) C189-C196.

[24] N. Cabrera, N.F. Mott, Theory of the oxidation of metals, Reports on Progress in Physics, 12 (1949) 163-184.

[25] N.F. Mott, The theory of the formation of protective oxide films on metals.-III, Transactions of the Faraday Society, 43 (1947) 429-434.

[26] N.F. Mott, The theory of the formation of protective oxide films on metals, II, Transactions of the Faraday Society, 35 (1940) 472-483.

[27] N.F. Mott, A theory of the formation of protective oxide films on metals, Transactions of the Faraday Society, 35 (1939) 1175-1177.

[28] M. Bojinov, G. Fabricius, T. Laitinen, K. Mäkelä, T. Saario, G. Sundholm, Coupling between ionic defect structure and electronic conduction in passive films on iron, chromium and iron–chromium alloys, Electrochimica Acta, 45 (2000) 2029-2048.

[29] D.D. Macdonald, The Point Defect Model for the Passive State, Journal of The Electrochemical Society, 139 (1992) 3434-3449.

[30] L.F. Lin, C.Y. Chao, D.D. Macdonald, A Point Defect Model for Anodic Passive Films: II . Chemical Breakdown and Pit Initiation, Journal of The Electrochemical Society, 128 (1981) 1194-1198.

[31] C.Y. Chao, L.F. Lin, D.D. Macdonald, A Point Defect Model for Anodic Passive Films: I . Film Growth Kinetics, Journal of The Electrochemical Society, 128 (1981) 1187-1194.

[32] C.F. Baes, R.E. Mesmer, The hydrolysis of cations, Wiley, 1976.

[33] N. Sato, Chapter 8 - Electrode reactions in electron transfer, in: N. Sato (Ed.) Electrochemistry at Metal and Semiconductor Electrodes, Elsevier Science, Amsterdam, 1998, pp. 235-288.

[34] N. Sato, Chapter 9 - Electrode reactions in ion transfer, in: N. Sato (Ed.) Electrochemistry at Metal and Semiconductor Electrodes, Elsevier Science, Amsterdam, 1998, pp. 289-323.

[35] K.J. Vetter, General kinetics of passive layers on metals, Electrochimica Acta, 16 (1971) 1923-1937.

[36] L.T. Mančić, Z.V. Marinković, P. Vulić, O.B. Milošević, The synthesis: Structure relationship in the ZnO-Cr2O3 system, Science of Sintering, 36 (2004) 189-196.

[37] L.L. Shreir, R.A. Jarman, G.T. Burstein, Corrosion. - 2: Corrosion control, Butterworth-Heinemann, 1994.

Chapter 9

Mass and Charge Balance (MCB) Model Simulations of Potential, Oxide Growth and Dissolution During Corrosion of Alloy 800

9.1 Introduction

In the previous chapters, it was shown how environmental factors affect the corrosion behaviour of Alloy 800. A mechanism for corrosion of Alloy 800 is presented and a model is developed based on the mechanism to account for both oxide formation and metal dissolution during corrosion of Cr-containing alloys [1]. This model was applied to the Co-Cr system [2] and it was shown that it can simulate the observed electrochemical results and oxide thickness on the surface as well as the dissolved metal cations in the solution. The preliminary results on the corrosion modeling in the Alloy 800 system have been presented previously [1, 3]. Here, the results for the Alloy 800 modeling in the presence and absence of radiation are presented.

9.2 The MCB Model for Alloy 800 Corrosion

The method used for alloy 800 corrosion modeling and simulation is similar to that used for the Co-Cr alloy Stellite-6 [2] and is not repeated here. The MCB model is applied for Alloy 800 at different pHs (6.0, 8.4 and 10.6) based on the experimental and thermodynamic data presented in Chapter 4, and the rate parameters and boundary conditions that are formulated in the model. The model simulation results are presented in Section 9-3.

9.3 Model Simulation Results

We have performed a combination of electrochemical and coupon-exposure experiments to investigate the corrosion kinetics of Alloy 800 as a function of pH, temperature and γ-radiation exposure. The electrochemical experiments include corrosion potential measurements, E_{CORR}. The coupon exposure experiments were performed in sealed quartz vials and the dissolved iron, chromium and nickel concentrations in the solutions were determined using inductively coupled plasma – mass spectrometry (ICP-MS). These data are presented in Chapter 4. The AES depth-profile data from those studies were reanalyzed to enable comparison of the experimental results with model calculations. This AES data analysis is summarized in Appendix B.

The MCB model calculations were performed for the experiments on Alloy 800 at three different pHs (6.0, 8.4 and 10.6) in the presence and absence of radiation. Note that under radiation, it is not possible to measure the corrosion potential at 80 °C. Therefore, only the coupon test results under radiation are modeled. The model calculation results of corrosion potential measurements and coupon exposure tests are described in Section 9-3-2. The values used to obtain these results are listed in Table 9-1.

Table 9-1: The parameters derived for use in the MCB model for corrosion of Alloy 800.

pH	Initial Oxide-Flux Fraction $\left(\dfrac{k_{MO\#}(0)}{k_{MO\#}(0)+k_{diss\#}}\right)$			Specific Potential Drop $\varepsilon_{MO\#}$ (10^6 V·cm^{-1})			Specific ΔE_a Gradient, $c_{MO\#}$ (10^6 J·mol^{-1}·cm^{-1})			Exchange Current, $i^0_{rdx\#}$ (μA·cm^{-2})				
	Cr_2O_3	$FeCr_2O_4$	Fe_3O_4	Cr_2O_3	$FeCr_2O_4$	Fe_3O_4	Cr_2O_3	$FeCr_2O_4$	Fe_3O_4	$Cr \leftrightarrows Cr^{III}$	$Fe \leftrightarrows Fe^{II}$	$Ni \leftrightarrows Ni^{II}$	$(O_2 \leftrightarrows OH^-)$	$(H_2O \leftrightarrows H_2)$
10.6	0.99	0.498	0.498	3.2 ± 0.3	4.0 ± 1.0	1.0	50	1	1	10^{-5}	15	3000	-10^{-4}	-1
8.4	0.99	0.498	0.498											
6.0	0.99	0.07	0.154											

9.3.1 Corrosion under open-circuit conditions in the absence of radiation

Under naturally corroding conditions or during corrosion potential measurements, the anodic and cathodic reactions happen on the same macroscopic surface. Under these conditions, the rate at which electrons are produced is the same as their rate of consumption.

$$\sum i_a = \left| \sum i_c \right| \text{ at corrosion potential} \tag{9-1}$$

This is a necessary condition for the time evolution of the corrosion potential.

To determine E_{CORR} on the Alloy 800 surface under deaerated conditions in the absence of radiation, the steps used are similar to those for the Co-Cr alloy Stellite-6 presented in Chapter 8 [2]. The flux equations and the values of the rate parameters used for the E_{CORR} simulations were those determined by the best fit to the corrosion potential data. There are no data available for the exchange current density on the Alloy 800 surface, so we set the exchange current density for water reduction on the surface of Alloy 800 at 10^{-6} A/cm^2 (Table 9-1). This value is in the range reported for the water reduction exchange current densities on the transition metals [4]. The cathodic current calculations are the same as those presented in Chapter 8 [2].

The model calculation starts at the cathodic cleaning potential for 5-min prior to the E_{CORR} measurement at each pH. At the end of cathodic cleaning the surface is covered with a thin layer of chromium oxide formed by air oxidation that cannot be removed by this cathodic cleaning [5]. The anodic current density from the sum of iron, nickel and chromium oxidation fluxes and the total cathodic current density from the sum of solution reduction fluxes were calculated. Current density calculations were carried out over a potential range from the cathodic cleaning potential for each pH (Chapter 4) to the solution oxidation potential determined from the equilibrium potential of the most oxidizing species in the environment. The potential for the calculations was stepped by 0.1 mV and the potential at which the difference between the anodic and cathodic current densities was less than 1% of the cathodic current at that potential is taken as the corrosion potential.

Figure 9-1 compares the calculated and experimental corrosion potentials as a function of time. The MCB model calculation results are in excellent agreement with the data.
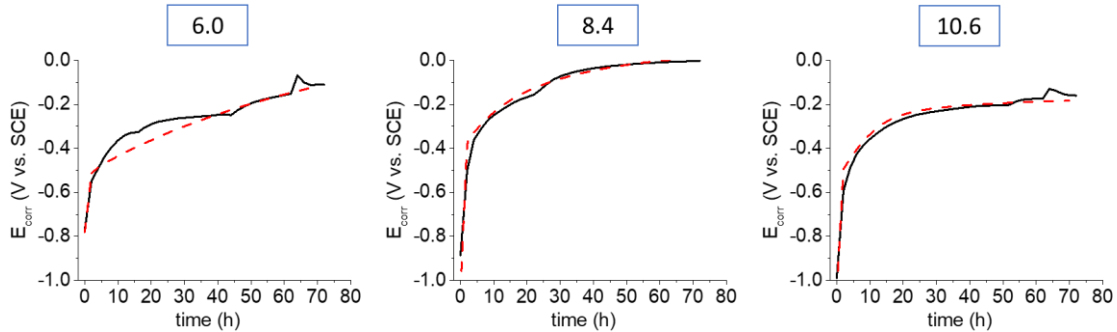
Figure 9-1: The measured E_{CORR} (black solid line) and E_{CORR} calculated using the MCB model (dashed red line) on the surface of Alloy 800 at pH 6.0, 8.4 and 10.6 at 80 °C No Rad. The experimental data are those presented in Chapter 4.

9.3.2 Oxide formation and dissolution

MCB model simulations were also performed for the 3-d corrosion tests for Alloy 800 coupons in the absence and presence of γ-radiation. In the presence of radiation, it is assumed that hydrogen peroxide is produced as the main radiolytic product and its concentration is ~ 100 μM [6, 7]. The standard equilibrium potential for hydrogen peroxide reduction has been determined previously [8] and can be used in the Nernst equation for the equilibrium potential calculations. Our experimental result in the presence of radiation at 25 °C shows that the rate of reduction of H_2O_2 on the surface of Alloy 800 is ~ 10^{-8} A/cm^2. These values are used in the model to add one more cathodic reaction with the same parameters that are used in the absence of radiation. The model results are compared with the experimental data for metal ion dissolution (data presented in Chapter 4) and oxide film thickness on the surface in Figure 9-2 and Figure 9-3, respectively.
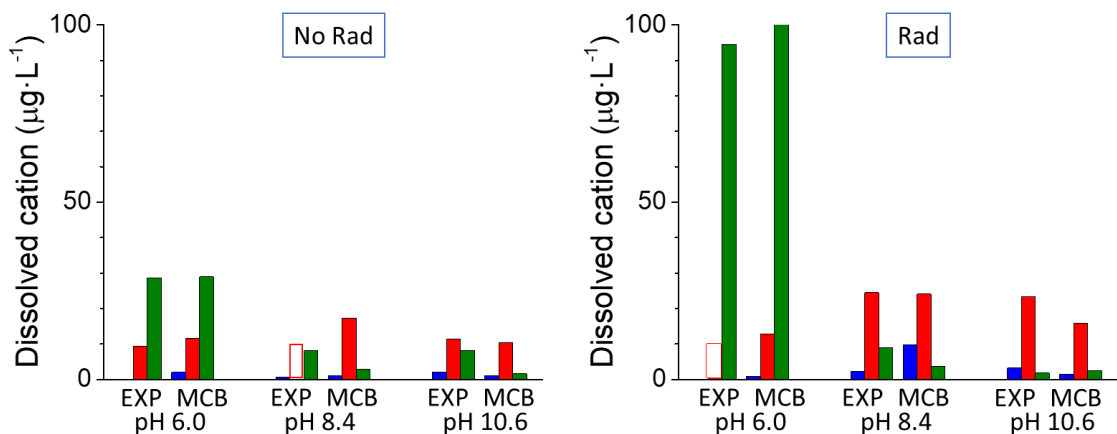
Figure 9-2: Experimentally measured and MCB model calculations for the dissolved Fe, Cr and Ni cations in solutions with pH 6.0, 8.4 and 10.6 at 80 °C in the presence and absence of γ-radiation. The model data in the presence of γ-radiation are calculated by considering the rate of hydrogen peroxide reduction to be 10^{-8} A/cm². **Red is Fe**, **Blue is Cr** and **Green is Ni**.
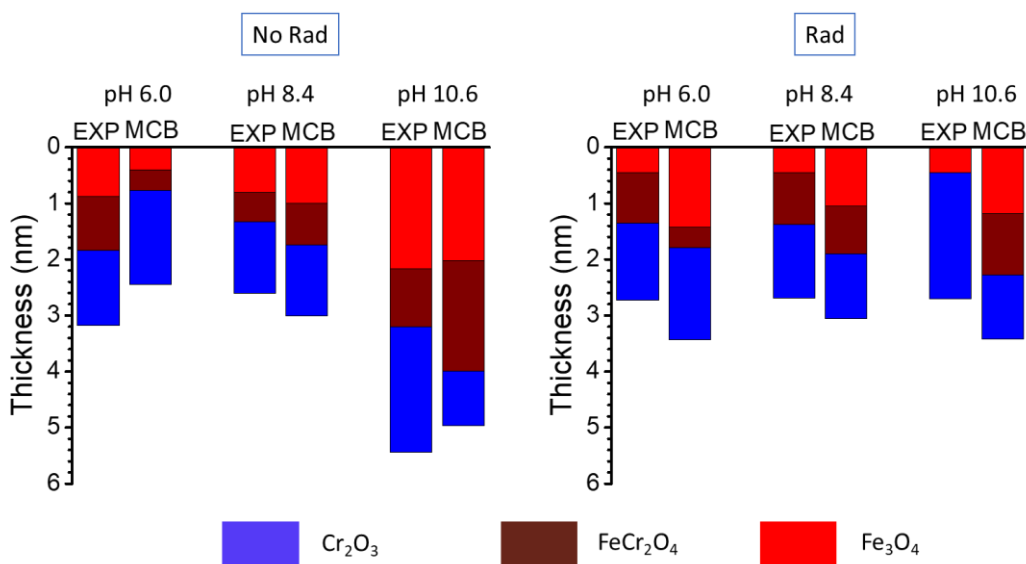
Figure 9-3: Oxide thickness measured by AES and oxide thickness calculated using the MCB model for pH 6.0, 8.4 and 10.6 at 80 °C in the presence and absence of γ-radiation. The colours representing each oxide are shown on the figure.

236

The results presented show that the MCB model can correctly predict the effect of pH and radiation on not only the layer structure and thickness of the oxide formed but also the amounts of cations dissolved in the solution

The predicted corrosion potential in the presence of radiation after 72 h of corrosion is higher than in its absence, as shown in Figure 9-4. Although it was not possible to measure the actual corrosion potential in the presence of radiation at temperatures above 25 °C, the higher E_{CORR} is not surprising. The results presented in Chapter 4 for Alloy 800 corrosion and several other corrosion systems show that in the presence of radiation, the corrosion potential on the surface of transition metals and alloys is higher than in its absence [9-13].
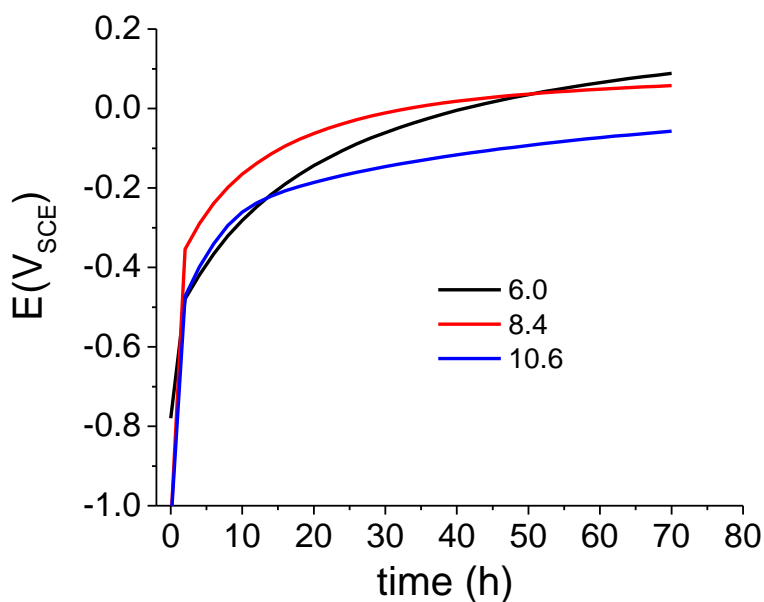
Figure 9-4: **Predicted E_{CORR} on Alloy 800 at pH 6.0, 8.4 and 10.6 at 80 °C in the presence of γ-radiation.**

The predicted corrosion potentials show that the rate of E_{CORR} evolution on the surface of Alloy 800 at 80 °C and in the presence of radiation, as well as the steady state E_{CORR}, is pH-dependent. At pH 10.6, E_{CORR} is generally lower and its steady state value is reached faster than at the other two pHs. It is predicted that the behaviour at pH 8.4 would

be similar to that at pH 10.6, which seems reasonable based on the measured oxide thickness that forms on the surface and the amount of dissolved metal cations in the solution. As was observed in the experimental results in the absence of radiation for pH 6.0 (Chapter 4 and Figure 9-1), the corrosion potential on the surface of a sample exposed to a solution at pH 6.0 is not likely to reach its steady state value even after 72 h.

These types of analyses are important because in nuclear reactor environments, the radiation dose rate, temperature and corrosion environment are different from the experimental conditions in this work. However, in each set of conditions, it is possible to calculate the concentration of oxidizing species and their rate of reduction at the surface [6, 7]. Combining these data and employing the MCB model can help to predict the corrosion potential in reactor environments. This electrode potential value could be helpful in predicting whether the alloy is operating within safe parameters [14] and whether it can last for the desired lifetime.

9.4   Conclusions

The mass and charge balance (MCB) model was used to simulate corrosion tests and electrochemical experiments performed on Alloy 800. The rate equations for metal oxidation, oxide growth and dissolution were determined using the previously presented methods [1-3]. Most of the model parameters are fundamental thermodynamic and reaction properties of the chemical elements involved in the corrosion reactions. Of these parameters, the rate constants for metal oxide growth and metal ion dissolution are the only ones that are sensitive to solution pH.

The model simulation results are in excellent agreement with the data obtained from different sets of experiments in the presence and absence of γ-radiation. The simulation results show that the effect of radiation on the corrosion of Alloy 800 can be simulated by adding just one reaction, the hydrogen peroxide reduction reaction, to the system. This study demonstrates that the MCB model can simulate oxide growth and metal ion dissolution simultaneously during corrosion, even for an alloy with multiple oxidizing elements, and predict the effects of different solution environment conditions on the overall corrosion rate.

238

9.5   References:

[1] M. Momeni, J.C. Wren, A mechanistic model for oxide growth and dissolution during corrosion of Cr-containing alloys, Faraday Discussions, 180 (2015) 113-135.

[2] M. Momeni, M. Behazin, J. Wren, Mass and charge balance (MCB) model simulations of current, oxide growth and dissolution during corrosion of Co-Cr alloy Stellite-6, Journal of The Electrochemical Society, 163 (2016) C94-C105.

[3] M. Momeni, J.C. Wren, Mass and Charge Balance (MCB) Model Simulations of Corrosion of Cr Containing Alloys, in: F. Bocher, J. Lee, N. Birbilis (Eds.) CORROSION, NACE International, Vancouver, BC, 2016, pp. 129-133.

[4] S. Trasatti, Work function, electronegativity, and electrochemical behaviour of metals: III. Electrolytic hydrogen evolution in acid solutions, Journal of Electroanalytical Chemistry and Interfacial Electrochemistry, 39 (1972) 163-184.

[5] V. Maurice, H. Peng, L.H. Klein, A. Seyeux, S. Zanna, P. Marcus, Effects of molybdenum on the composition and nanoscale morphology of passivated austenitic stainless steel surfaces, Faraday discussions, 180 (2015) 151-170.

[6] P.A. Yakabuskie, J.M. Joseph, J.C. Wren, The effect of interfacial mass transfer on steady-state water radiolysis, Radiation Physics and Chemistry, 79 (2010) 777-785.

[7] J.M. Joseph, B.S. Choi, P. Yakabuskie, J.C. Wren, A combined experimental and model analysis on the effect of pH and O_2 (aq) on γ-radiolytically produced H_2 and H_2O_2, Radiation Physics and Chemistry, 77 (2008) 1009-1020.

[8] R.P. Morco, A.Y. Musa, M. Momeni, J. Wren, Corrosion of carbon steel in the [P 14666][Br] ionic liquid: The effects of γ-radiation and cover gas, Corrosion Science, 102 (2016) 1-15.

[9] M. Behazin, J.J. Noël, J.C. Wren, Combined Effects of pH and γ-Irradiation on the Corrosion of Co-Cr Alloy Stellite-6, Electrochimica Acta, 134 (2014) 399-410.

[10] K. Daub, X. Zhang, J.J. Noël, J.C. Wren, Effects of γ-radiation versus H_2O_2 on carbon steel corrosion, Electrochimica Acta, 55 (2010) 2767-2776.

[11] K. Daub, X. Zhang, L. Wang, Z. Qin, J.J. Noël, J.C. Wren, Oxide growth and conversion on carbon steel as a function of temperature over 25 and 80 °C under ambient pressure, Electrochimica Acta, 56 (2011) 6661-6672.

[12] Q.W. Knapp, J.C. Wren, Film formation on type-316L stainless steel as a function of potential: Probing the role of gamma-radiation, Electrochimica Acta, 80 (2012) 90-99.

[13] A. Musa, J. Wren, Combined effect of gamma-radiation and pH on corrosion of Ni–Cr–Fe alloy inconel 600, Corrosion Science, 109 (2016) 1-12.

[14] W. Garland, The Essential CANDU, A Textbook on the CANDU Nuclear Power Plant Technology, Chap, 7 (2016) 18-20.

Chapter 10
Summary and Future Works

10.1 Summary

In this thesis, a systematic study was carried out to investigate the effect of gamma radiation and different solution environments on the corrosion of Alloy 800. The new Mass and Charge Balance (MCB) model is presented, which is capable of predicting the oxide thickness and metal dissolution the different environments.

The investigation on the effect of pH, temperature, oxygen content and γ-radiation on the corrosion of Alloy 800 showed that changes in the corrosion environment significantly affects the oxide film composition and the corrosion behaviour. The corrosion of Alloy 800 can be expressed in some elementary reactions including the oxidation reaction, the oxide formation and the metal cation dissolution reactions. The rate of each elementary step differs as the corrosion environment changes; however, the main effect of pH change on the corrosion can be seen on the fraction of metal cations that participate in the oxide formation process. At a pH where the solubility of a metal cation is high, the metal cation prefers dissolution over oxide formation. This, in turn, lowers the rate of formation of any oxide that contains that metal cation. The change in the oxide formation affects the oxide thickness on the surface which in turn changes the rate of oxidation.

The main effect of γ-radiation is on the oxidation process. Water when exposed to γ-radiation produces highly oxidizing species that increase the driving force for the corrosion process. The effect of γ-radiation on the oxidation process is similar to that of added oxygen, but differs in terms of the pathways that the Alloy 800 corrosion follows and the final oxide thickness, oxide composition and dissolved metal concentrations. The increase in the oxidation rate is followed by changes in the rates of metal oxide formation and metal cation dissolution. The ratio of these two rates is dictated by the pH of the solution. In more oxidizing environments, the fraction of oxides with high oxidation states is higher. However,

the attempt to use added O_2 as a proxy for gamma irradiation was not successful under steam corrosion conditions.

A change in temperature affects the rate of every process involved in the corrosion of Alloy 800. The dependence of the rate of a chemical or an electrochemical reaction on the temperature is represented by the Arrhenius equation. As temperature changes, depending on the activation energy of each reaction (and if it is rate-controlling), the pathway of Alloy 800 corrosion might change. In addition to the kinetics of reactions, temperature also influences the thermodynamics of formation of certain oxides and the dissolution of metal cations. The thermodynamic calculations show that the range of stability of an oxide or an ion is significantly affected by temperature.

The parameters determined in this study allowed a mechanism for the corrosion of Alloy 800 to be developed. The MCB model was developed based on mass and charge conservation and consists of three key flux equations: metal oxidation, oxide growth, and dissolution flux. A key (and common sense) assumption of the model is that oxide growth and dissolution fluxes cannot vary independently, but their sum must be equal the metal oxidation flux. The metal oxidation flux is formulated using a modified Butler-Volmer equation with an oxide-thickness-dependent effective overpotential. The oxide growth and dissolution fluxes have a first-order dependence on the metal oxidation flux. Mass balance dictates that the ratio of the oxide growth and the dissolution fluxes is determined by their respective first-order rate constants. The rate constant for oxide growth is assumed to have a normal Arrhenius dependence on the activation energy for the reaction where the potential drop across the growing oxide layer contributes to the activation energy. Thus, the rate constant for oxide growth decreases exponentially with oxide thickness while the rate constant for dissolution remains constant. The analytical solution of this model results in a logarithmic dependence of the thickness of oxide on time.

The MCB model was used to simulate corrosion tests and electrochemical experiments performed on the Co-Cr alloy Stellite-6 and Alloy 800. Most of the model parameters are fundamental thermodynamic and reaction properties of the chemical elements

involved in the corrosion reactions. Of these parameters, the rate constants for metal oxide growth and metal ion dissolution are the only ones that are sensitive to solution pH.

The model simulation results show excellent agreement with the data obtained from different sets of experiments in the presence and absence of γ-radiation. The simulation results show that the effect of radiation on the corrosion of Alloy 800 can be simulated by adding only the hydrogen peroxide reduction reaction to the system. This study demonstrates that the MCB model can simulate oxide growth and metal ion dissolution simultaneously during corrosion, even for an alloy with multiple oxidizable elements, and predict the effects of different solution environmental conditions on the overall corrosion rate.

10.2   Future work

The results presented in this thesis showed that there are several unresolved issues providing for future work on the corrosion of Fe-Cr-Ni alloys and their corrosion modelling.

The results presented in this thesis show that the ratio of Fe, Cr and Ni in the alloy can affect the corrosion pathway and could result in completely different behaviours for different alloys. This could explain the different corrosion behaviours of Fe-Cr-Ni alloys like stainless steels and Inconel alloys. There have been attempts to study the effect of alloying elements on the passivation and localized corrosion of these alloys [1-8]. However, none of these works presents a mechanistic understanding of the effect of alloying elements and differing ratios of Ni/Fe, Ni/Cr and Cr/Fe on the corrosion behaviour. The other alloying elements added to the alloys are molybdenum, titanium, etc. to enhance corrosion properties in acidic solutions and/or improve mechanical properties. A mechanistic study on the effect of these alloying elements on the corrosion with a particular focus on the effect of water radiolysis is necessary.

The presented mechanism also shows that the dissolution rate and consequently the oxidation and oxide formation rates can be influenced by the diffusion path of the metal cations in the solution. In the electrochemical studies and most of the corrosion experiments, the solution volume is large enough to not affect the dissolution kinetics. However, in the

243

case of steam corrosion and/or SCW corrosion, the solution volume or the hydration rate changes. This can affect the overall corrosion process and pathway. It would therefore be desirable to study the effect of different solution volume to surface area ratios on the different Fe-Cr-Ni alloys in order to gain a mechanistic understanding of corrosion under water vapour or SCW.

A change in the solution volume can also affect the evolution of the solution pH as corrosion progress. This is more pronounced when the solution is not buffered. This can also be influenced by the ionic strength of the solution. Therefore, an in-depth study on the effect of solution chemistry evolution during corrosion of these alloys seems inevitable. This study will significantly enhance our understanding of the corrosion under pure water steam and the localized corrosion behaviour of these alloys.

These data can then be used to modify or refine the MCB model to account for the evolution of the dissolved metal cations in the solution, as observed in Chapter 5. This behaviour can be incorporated into the detailed process considered in the model which may improve the ability to model corrosion behaviour under gamma radiation at high temperature aqueous and vapour environment. These modifications may also improve the model's localized corrosion prediction capabilities.

10.3   References

[1] R.M. Carranza, M.G. Alvarez, The effect of temperature on the passive film properties and pitting behaviour of a Fe-Cr-Ni alloy, Corrosion Science, 38 (1996) 909-925.

[2] K.N. Goswami, R.W. Staehle, Growth kinetics of passive films on Fe, Fe-Ni, Fe-Cr, Fe-Cr-Ni alloys, Electrochimica Acta, 16 (1971) 1895-1907.

[3] J. Horvath, H.H. Uhlig, Critical Potentials for Pitting Corrosion of Ni, Cr-Ni, Cr-Fe, and Related Stainless Steels, Journal of The Electrochemical Society, 115 (1968) 791-795.

[4] A. Machet, A. Galtayries, S. Zanna, L. Klein, V. Maurice, P. Jolivet, M. Foucault, P. Combrade, P. Scott, P. Marcus, XPS and STM study of the growth and structure of passive films in high temperature water on a nickel-base alloy, Electrochimica Acta, 49 (2004) 3957-3964.

[5] M. Montemor, M. Ferreira, N. Hakiki, M.D.C. Belo, Chemical composition and electronic structure of the oxide films formed on 316L stainless steel and nickel based alloys in high temperature aqueous environments, Corrosion Science, 42 (2000) 1635-1650.

[6] R.C. Newman, The dissolution and passivation kinetics of stainless alloys containing molybdenum—1. Coulometric studies of Fe-Cr and Fe-Cr-Mo alloys, Corrosion Science, 25 (1985) 331-339.

[7] L. Oblonsky, T. Devine, A surface enhanced Raman spectroscopic study of the passive films formed in borate buffer on iron, nickel, chromium and stainless steel, Corrosion Science, 37 (1995) 17-41.

[8] M. Ryan, R. Newman, G. Thompson, An STM study of the passive film formed on iron in borate buffer solution, Journal of The Electrochemical Society, 142 (1995) L177-L179.

Mathematical Derivation of Analytical Solution for Oxide Growth

A1:Growth of a Single Phase Oxide

The metal oxidation flux can be expressed using a modified Butler-Volmer equation:

$$J_{M\#^{n+}}(t)|_{m|ox} = J_{rdx\#}^{eq} \cdot \left(exp\left(a \cdot \eta_{ox\#}(t)\right)\right) \tag{A1}$$

where $a = \frac{0.5 \cdot n \cdot F}{RT}$.

In the presence of an oxide layer, the effective overpotential is

$$\eta_{rdx\#}(t) = E_{elec}(t) - E_{ox\#}^{eq} - \Delta V_{oxide}(t) \tag{A2}$$

The potential drop across the oxide layer is assumed to be proportional to oxide thickness:

$$\Delta V_{oxide}(t) = \Delta V_{oxide}(0) + \varepsilon_{MO\#} \cdot L_{MO\#}(t) \tag{A3}$$

Under potentiostatic conditions, $E_{elec}(t) \approx$ constant with time. Substituting (A3) and (A2) into (A1) and by separating constant terms from time-dependent terms:

$$J_{M\#^{n+}}(t)|_{m|ox} = A_J \cdot \left(exp\left(a \cdot \left(- \varepsilon_{MO\#} \cdot L_{MO\#}(t)\right)\right)\right) \tag{A4}$$

Where

$$A_J = J_{rdx\#}^{eq} \cdot \left(exp\left(a \cdot \left(E_{elec}(t) - E_{ox\#}^{eq} - \Delta V_{oxide}(0)\right)\right)\right) \tag{A5}$$

The oxide growth flux is:

$$J_{MO\#}(t)|_{oxide} = f_{k-MO\#}(t) \cdot J_{M\#^{n+}}(t)|_{m|ox} \tag{A6}$$

where

$$f_{k-MO\#}(t) = \left(\frac{k_{MO\#}(t)}{k_{MO\#}(t) + k_{diss\#}}\right) \tag{A7}$$

$$k_{MO\#}(t) = k_{MO\#}(0) \cdot exp\left(-\frac{c_{MO\#} \cdot L_{MO\#}(t)}{RT}\right) \tag{A8}$$

This is related to the linear rate of oxide growth as:

$$\frac{dL_{MO\#}}{dt} = \upsilon_{MO\#} \cdot J_{MO\#}(t)|_{oxide} \tag{A10}$$

From (A4), (A6) to (A10),

$$\frac{dL_{MO\#}}{dt} = \upsilon_{MO\#} \cdot \left(\frac{k_{MO\#}(0) \cdot exp\left(-\frac{c_{MO\#} \cdot L_{MO\#}(t)}{RT}\right)}{k_{MO\#}(0) \cdot exp\left(-\frac{c_{MO\#} \cdot L_{MO\#}(t)}{RT}\right) + k_{diss\#}} \right) \cdot A_J \cdot \left(exp\left(a \cdot \left(- \varepsilon_{MO\#} \cdot L_{MO\#}(t)\right)\right) \right)$$

$$\tag{A11}$$

$$\frac{dL_{MO\#}}{\upsilon_{MO\#} \cdot \left(\frac{k_{MO\#}(0) \cdot exp\left(-\frac{c_{MO\#} \cdot L_{MO\#}(t)}{RT}\right)}{k_{MO\#}(0) \cdot exp\left(-\frac{c_{MO\#} \cdot L_{MO\#}(t)}{RT}\right) + k_{diss\#}} \right) \cdot A_J \cdot \left(exp\left(a \cdot \left(- \varepsilon_{MO\#} \cdot L_{MO\#}(t)\right)\right) \right)} = dt$$

$$\tag{A12}$$

$$\frac{1}{\upsilon_{MO\#} \cdot A_J} \cdot \left(\frac{k_{MO\#}(0) \cdot exp\left(-\frac{c_{MO\#} \cdot L_{MO\#}(t)}{RT}\right) + k_{diss\#}}{k_{MO\#}(0) \cdot exp\left(-\frac{c_{MO\#} \cdot L_{MO\#}(t)}{RT}\right)} \right) \cdot \frac{dL_{MO\#}}{\left(exp\left(a \cdot \left(- \varepsilon_{MO\#} \cdot L_{MO\#}(t)\right)\right) \right)} = dt \tag{A13}$$

$$\frac{1}{\upsilon_{MO\#} \cdot A_J} \cdot \left(1 + \frac{k_{diss\#}}{k_{MO\#}(0)} \cdot exp\left(\frac{c_{MO\#} \cdot L_{MO\#}(t)}{RT}\right) \right) \cdot \left(exp\left(a \cdot \varepsilon_{MO\#} \cdot L_{MO\#}(t)\right) \right) \cdot dL_{MO\#} = dt$$

$$\tag{A14}$$

$$\frac{1}{\upsilon_{MO\#} \cdot A_J} \cdot \left(exp\left(a \cdot \varepsilon_{MO\#} \cdot L_{MO\#}(t)\right) + \frac{k_{diss\#}}{k_{MO\#}(0)} \cdot exp\left(\left(\frac{c_{MO\#}}{RT} + a \cdot \varepsilon_{MO\#}\right) \cdot L_{MO\#}(t)\right) \right) \cdot$$

$$dL_{MO\#} = dt \tag{A15}$$

The solution for the differential equation is:

$$\frac{1}{\upsilon_{MO\#} \cdot A_J} \cdot \left(\frac{1}{(a \cdot \varepsilon_{MO\#})} \cdot \left(exp\left(a \cdot \varepsilon_{MO\#} \cdot L_{MO\#}(t)\right) - 1\right) + \frac{1}{\left(\frac{c_{MO\#}}{RT} + a \cdot \varepsilon_{MO\#}\right)} \cdot \frac{k_{diss\#}}{k_{MO\#}(0)} \cdot \right.$$

$$\left. \left(exp\left(\left(\frac{c_{MO\#}}{RT} + a \cdot \varepsilon_{MO\#}\right) \cdot L_{MO\#}(t)\right) - 1\right) \right) = t \tag{A16}$$

The typical values of $\varepsilon_{MO\#}$ and $c_{MO\#}$ are such that (see Table 7-2 in the text):

$$\frac{c_{MO\#}}{RT} \ll a \cdot \varepsilon_{MO\#} \tag{A17}$$

For an oxide thicker than a few angstroms:

$$exp(a \cdot \varepsilon_{MO\#} \cdot L_{MO\#}(t)) \gg 1 \tag{A18}$$

Thus,

$$\frac{1}{\upsilon_{MO\#} \cdot A_J} \cdot \frac{1}{(a \cdot \varepsilon_{MO\#})} \cdot \left(1 + \frac{k_{diss\#}}{k_{MO\#}(0)}\right) \cdot \left(exp(a \cdot \varepsilon_{MO\#} \cdot L_{MO\#}(t))\right) \approx t \tag{A19}$$

By defining

$$\lambda_{MO\#} = a \cdot \varepsilon_{MO\#} = \frac{0.5 \cdot n \cdot F}{RT} \cdot \varepsilon_{MO\#} \tag{A20}$$

$$f_{k-MO\#}(0) = \left(\frac{k_{MO\#}(0)}{k_{MO\#}(0) + k_{diss\#}}\right) \tag{A21}$$

$$J_{MO\#}{}'' = \upsilon_{MO\#} \cdot f_{k-MO\#}(0) \cdot A_J$$

$$= \upsilon_{MO\#} \cdot f_{k-MO\#}(0) \cdot J_{rdx\#}^{eq} \cdot \left(exp\left(\frac{0.5 \cdot n \cdot F}{RT} \cdot \left(E_{elec}(t) - E_{ox\#}^{eq} - \Delta V_{oxide}(0)\right)\right)\right) \tag{A22}$$

Taking ln of both sides of Eq. A19 yields:

$$L_{MO\#}(t) \approx \frac{1}{\lambda_{MO\#}}\left(ln(\lambda_{MO\#} \cdot J_{MO\#}{}'') + ln\,t\right) \tag{A23}$$

A2: Conversion of Chromium Oxide to Chromite

For the conversion of chromium oxide to chromite the same derivation can be performed. The only difference is that the overpotential in this case is a function of the potential drop across the two oxide layers:

$$\eta_{rdx\#}(t) = E_{elec}(t) - E_{ox\#}^{eq} - \Delta V_{oxide}(t) \tag{A24}$$

$$\Delta V_{oxide}(t) = \varepsilon_{Cr2O3} \cdot L_{Cr2O3}(0) + (\varepsilon_{MCr2O4} - f_l \cdot \varepsilon_{Cr2O3}) \cdot L_{MCr2O4}(t) \tag{A25}$$

This change also changes the constants in Eq. A23. The thickness of chromite layer is then:

$$L_{MCr2O4}(t) \approx \frac{1}{\lambda_{MCr2O4}}(ln(\lambda_{MCr2O4} \cdot J_{MCr2O4}") + \ln t) \tag{A23}$$

$$J_{MO\#}" = \upsilon_{MO\#} \cdot f_{k-MO\#}(0) \cdot J_{rdx\#}^{eq} \cdot \left(exp\left(\frac{0.5 \cdot n \cdot F}{RT} \cdot \left(E_{elec}(t) - E_{ox\#}^{eq} - \varepsilon_{Cr2O3} \cdot \right.\right.\right.$$
$$\left.\left.\left. L_{Cr2O3}(0) \right)\right)\right) \tag{A22}$$

$$\lambda_{MO\#} = \frac{0.5 \cdot n \cdot F}{RT} \cdot (\varepsilon_{MCr2O4} - f_l \cdot \varepsilon_{Cr2O3}) \tag{A25}$$

APPENDIX B

AES Depth Profile Analysis

B1: Co-Cr system

Auger electron spectroscopy (AES) combined with argon-ion sputtering can provide a depth profile of the chemical composition of a surface oxide. The AES depth profiles on Stellite-6 reported in this study were obtained using a Physical Electronics Model PHI 660 instrument with an excitation energy of 5 keV. The AES scans for Co, Cr, C, Ni and O were performed as a function of sputtering time. The AES intensities were calibrated and converted into mole fractions, and the sputtering time was converted into depth. The sputter depths were calibrated using standard samples under the same sputtering conditions.

An example of the AES depth profiles obtained for Stellite-6 corroded at 80 °C, pH = 10.6, E_{app} = −0.4 V_{SCE} are shown in Fig. B1. Due to the presence of multiple metal elements in the alloy the nature of the oxide as a function of depth is difficult to decipher from the atomic fractions. To identify more clearly the degree of oxidation of the metal elements and their relative abundances in the oxide, the AES data were analyzed as ratios of each metal element (M = Co or Cr) to their sum (M/(Co + Cr)) and the ratio O/(Co + 1.5 Cr) (Fig. B2). An O/(Co + 1.5 Cr) ratio of 1.0 corresponds to an oxide where both Co and Cr have been oxidized to their lowest stable oxidation states, Co^{II} and Cr^{III}. A ratio less than 1.0 corresponds to a layer in which a fraction of the metal atoms has not been oxidized, and a ratio more than 1.0 corresponds to a layer in which some of the metal atoms are present in higher oxidation states or as hydroxides. The abundances of Co and Cr (expressed as M/(Co + Cr)) have different depth profiles in the oxide (Fig. B2) indicating that the oxide layer has a multi-layered structure with different oxides dominating at different depths.

To determine the dominant oxide at a given depth, another analysis methodology has been developed. 'Theoretical' depth profiles are calculated assuming that all of the measured metal present at a particular depth is present solely as a particular metal oxide or mixed metal oxide. Using this theoretical depth profile a corresponding O at.% depth profile (or O profile) can be calculated. For example, a theoretical Cr_2O_3 yields the O profile that one would expect to see if all of the Cr at a given depth was present as Cr_2O_3. Any Co present is assumed to be in metallic state Co^0. Similar profiles can be constructed for the other possible oxides. In the case of a mixed oxide like $CoCr_2O_4$, one assumes that the metal with the lowest concentration

(e.g., Cr) is present as an oxide along with the requisite Co and any excess Co would be present as Co^0. Using this methodology a series of theoretical O depth profiles can be calculated. If the measured O profile is greater than the theoretical O profile determined for all of the possible oxides, it indicates that there is a metal hydroxide present, mostly $Co(OH)_2$ for Stellite-6.

The theoretical O depth profiles calculated for one case are shown in Fig. B2 and compared with the actual measured O depth profile. The theoretical lines do not follow the observed O profile, but intersect with the observed profile at different depths. The order in which the different theoretical oxide lines intersect the observed O profile is for the oxides formed on all of Stellite-6 coupons tested. This order follows the order of the equilibrium potentials of the redox reactions of cobalt and chromium that can occur on a Co-Cr alloy.

The ordered intersection of the theoretical O profiles with the measured O profile indicates that the oxide grows in a multi-layered structure with the order of oxides, from the innermost to outermost layer being:

Cr_2O_3 - $CoCr_2O_4$ - $CoO/Co(OH)_2$
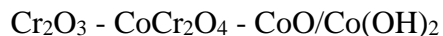
We can use the locations of the intersections of the O profiles to establish the depth span in the oxide layer where a particular oxide species is dominant. The depth where the O profile derived from a theoretical Cr_2O_3 profile intersects the observed O profile corresponds to the point at which the oxide is present predominantly as Cr_2O_3. Similarly, the depth where a theoretical $CoCr_2O_4$ profile intersects the observed O profile corresponds to the point at which the oxide is present predominantly as $CoCr_2O_4$. In the range between these two points the oxide composition changes from predominantly Cr_2O_3 to predominantly $CoCr_2O_4$.

A schematic of the oxide-layer structure determined from this analysis using 'theoretical' O profiles is shown in Fig. B2. The concentration gradient of the oxide between two points where the profiles intersect is not known and is assumed to be linear. This leads to the triangularly shaped oxide zones shown in Fig. B2.
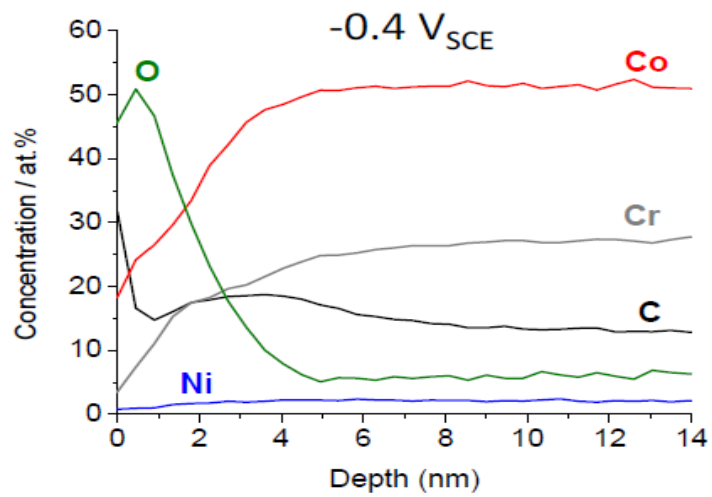
Fig. B1: Elemental depth profiles derived from AES analysis with Ar^+ sputtering for a Stellite-6 electrode polarized at -0.4 V_{SCE} at pH 10.6 and 80 °C.
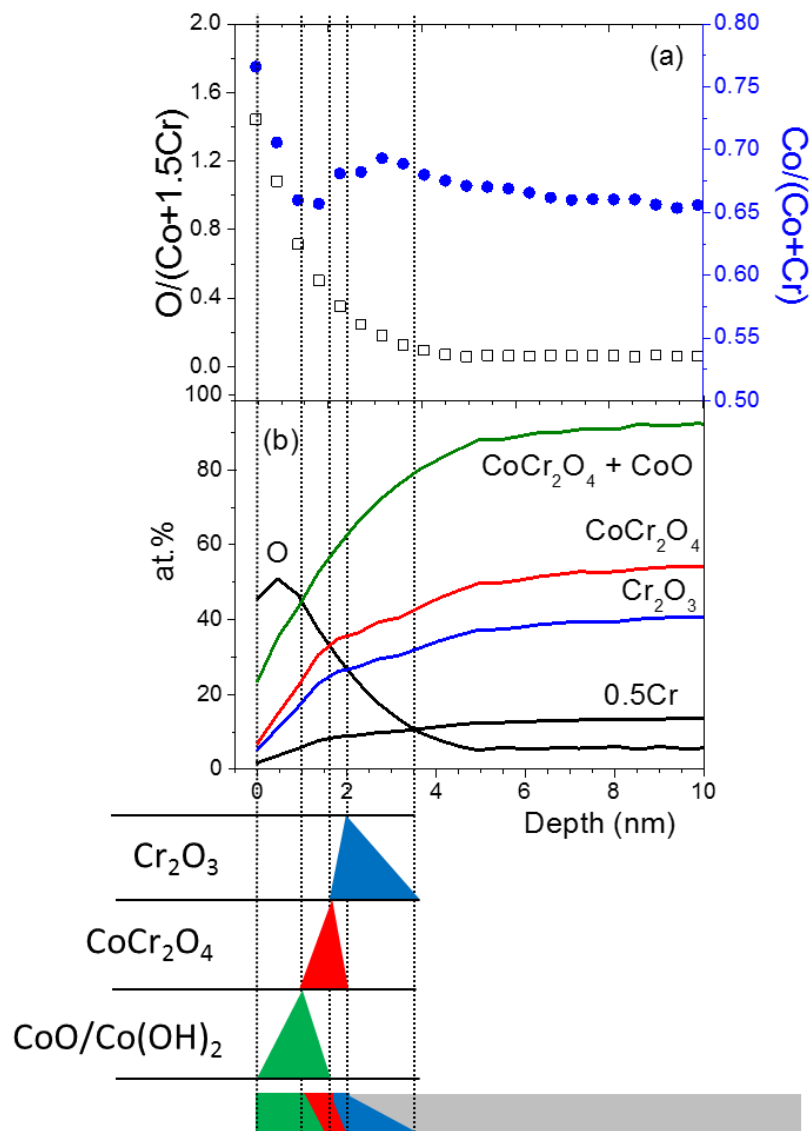
Fig. B2: Oxide layer structure analysis of the AES data shown in Fig. B1: (a) depth profiles of O/(Co + 1.5 Cr) and (b) observed (thick black line) and theoretical (colored lines) O at.% depth profiles. The depths marked by the vertical lines where the O profiles intersect in the middle graph indicate the boundaries of regions where a particular oxide is dominant. These regions are shown in the bar chart below the graphs.

B2: Fe-Cr-Ni System

To identify more clearly the degree of oxidation of the different metal elements and their relative abundances in the oxide with depth, the atomic fraction data were converted to

the ratio of each metal element (M = Ni, Cr or Fe) to the sum of the three main alloy elements (M/(Ni + Cr + Fe)).

The depth profiles of the (M/(Ni + Cr + Fe)), obtained for the coupons corroded for 5 h at pH 10.6 and 150 °C in the presence of radiation is shown in Fig. B3. The plot clearly show that each metal element has a different depth profile of M/(Ni + Cr + Fe) with maximum at a different depth in the oxide layer. These profiles indicate that the O present at a specific depth is bound to a specific metal, and the oxide layer has a multi-layered, albeit graded, structure.

It is known and reported widely that nickel is enriched at the interface of the metal and oxide. Hence, the position of nickel peak is considered as the interface of the metal and oxide. It is important to mention that there is no distinct interface between metal and oxide. The O-line shows gradual decrease to its background noise level for all conditions showing a region as the interface of metal and oxide. This indicates that any line that is considered as the interface of the metal and oxide in an arbitrary line. However, to be consistent throughout this paper and other researches, the nickel peak position is considered as the interface and it is the point the we consider the element with the lowest oxidation potential (in this case chromium) is completely oxidized and forms oxide. In the deeper area, some of Cr are in the metallic state and a region more in the oxide other elements are also in the oxidized form. This is shown with a line in Fig. B3 and the chromium oxide phase (Cr_2O_3) is shown with a blue bar while any Fe and Ni present were in metallic state Fe^0 and Ni^0. Once all chromium present are in the oxidized form, the excess amount of oxygen bonds to the next active element (Fe in this case). In the presence of chromium oxide, the oxidized iron cations form iron chromite ($FeCr_2O_4$) this can be observed based on the Fe line that increases as we probe toward the oxide/ solution interface. In this region, the additional amount of Fe and Ni are in metallic form. The region between nickel peak (metal/oxide interface) to the point that chromium reaches its maximum is the range that we see mostly chromium oxide compounds. It is more likely chromium oxide (Cr_2O_3) at the interface of metal and oxide and converting to $FeCr_2O_4$ as Fe fraction increases and can be considered mostly iron chromite when chromium reaches its maximum. After that iron starts forming its most stable oxide which is magnetite (Fe_3O_4). Up to the point that its line reaches the maximum. After that, it is a region

that we see mostly metallic oxides (mostly Fe and Ni oxides or their spinals). At the top surface, where there is a sudden change in the profile of the metal elements (and is also corresponds to some irregularity in the oxygen profile) is the region that we have hydroxide. The ordered peak position for different elements supports that the oxide grows in a multi-layered structure with the order of oxides, from the innermost to outermost layer being:

$$Cr_2O_3 - FeCr_2O_4 - Fe_3O_4 - NiFe_2O_4 - (Fe, Ni, Cr)(OH)_x$$
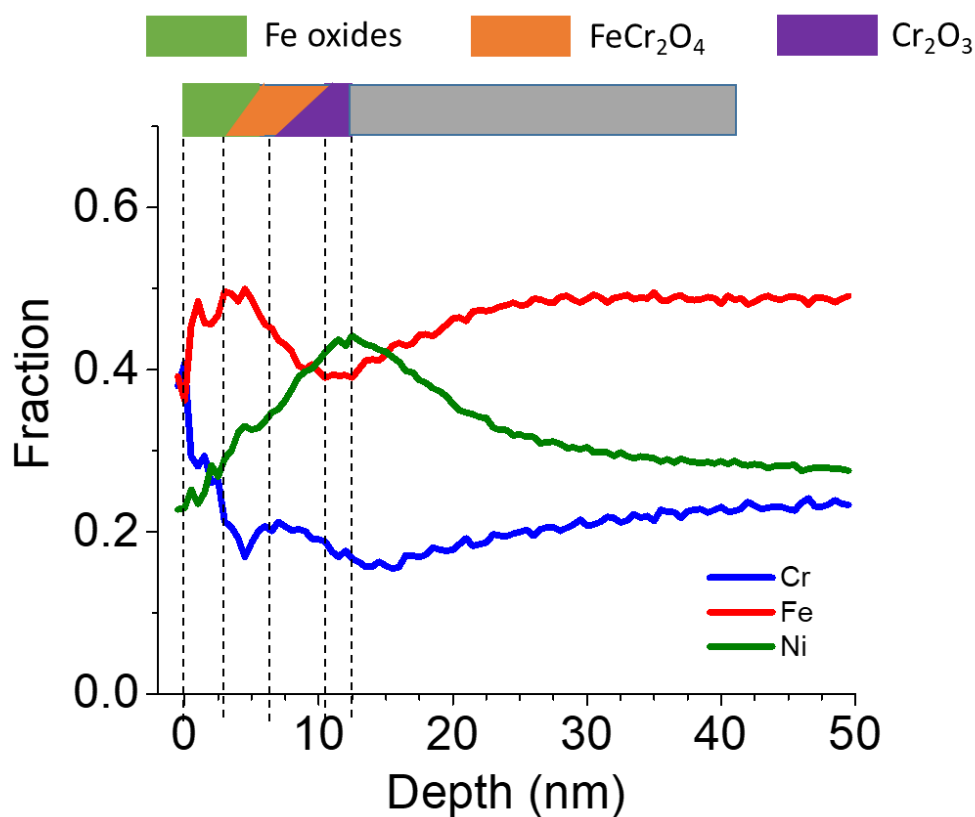
Fig. B3: Oxide layer structure analysis of Fe-Cr-Ni Alloy 800. The depths marked by the vertical lines where is thought is a boundary for different oxide layers. These regions are shown in the bar chart below the graphs.

Copyrights

This article is part of the themed collection: Corrosion Chemistry

About   Cited by   Related

×

A mechanistic model for oxide growth and dissolution during corrosion of Cr-containing alloys

M. Momeni and J. C. Wren, *Faraday Discuss.*, 2015, **180**, 113
DOI: 10.1039/C4FD00244J

If you are not the author of this article and you wish to reproduce material from it in a third party non-RSC publication you must formally request permission using RightsLink. Go to our Instructions for using RightsLink page for details.

Authors contributing to RSC publications (journal articles, books or book chapters) do not need to formally request permission to reproduce material contained in this article provided that the correct acknowledgement is given with the reproduced material.

Reproduced material should be attributed as follows:

- For reproduction of material from NJC:
  Reproduced from Ref. XX with permission from the Centre National de la Recherche Scientifique (CNRS) and The Royal Society of Chemistry.
- For reproduction of material from PCCP:
  Reproduced from Ref. XX with permission from the PCCP Owner Societies.
- For reproduction of material from PPS:
  Reproduced from Ref. XX with permission from the European Society for Photobiology, the European Photochemistry Association, and The Royal Society of Chemistry.
- For reproduction of material from all other RSC journals and books:
  Reproduced from Ref. XX with permission from The Royal Society of Chemistry.

If the material has been adapted instead of reproduced from the original RSC publication "Reproduced from" can be substituted with "Adapted from".

In all cases the Ref. XX is the XXth reference in the list of references.

ECS Copyright and Permissions

NOTICE: Beginning Monday, April 10, 2017, ECS has partnered with the Copyright Clearance Center (CCC) in order to manage permission requests.

- This service will allow authors to immediately receive permission, and will eliminate the need to complete ECS's permission request form.
- As of Monday, April 10, 2017, ECS will no longer accept permission request forms through email. All future requests must be made through CCC.
- Please note that there may be fees involved, depending on the type of material and reuse requested.
- **As has always been ECS's policy, authors are NOT required to request permission to reproduce their own figures or tables.**

Before requesting permission, please confirm the open access status of the article. **ECS does not hold the copyright on the open access articles published in its journals.** Please follow reuse instructions given by Creative Commons for its various licenses.

Guidelines for Use of ECS Material

- **Author Reuse Rights and Self-Archiving Policy**
- **Reusing Open Access Articles**
- **How to Ask for Permission**
- **Permission to Reproduce Full Articles**

Author Reuse Rights and Self-Archiving Policy

Before using ECS material or requesting to reproduce ECS material, please see the ECS Transfer of Copyright Form for the rights retained by authors and employers. **For example, authors may use their own tables and figures** in other scholarly research papers that they write, without writing to ECS for permission. Full credit to the original source should be given, for example:

> Reproduced with permission from *J. Electrochem. Soc.*, 150, H205 (2003). Copyright 2003, The Electrochemical Society.

Permission is not needed if figures and/or tables from one ECS publication will be reused in another forthcoming ECS publication.

Learn more about copyright and fair use.

Authors may deposit the pre-print and/or published versions of their articles in their institutional repository, with no embargo, provided that the files prepared by and/or formatted by ECS (and its vendors) are not used for that purpose. Any posting made or updated after the acceptance of the article for publication should include a link to the online abstract in the ECS publication of origin or to the entry page of that publication.

If authors choose to make their articles open access through Author Choice Open Access, the Version of Record (VoR) will be immediately freely available in our digital library. Authors may also deposit the published PDF of these open access articles in their institutional repositories, if they wish.

Reusing Open Access Articles

ECS does not hold the copyright on the open access articles published in its journals. The copyright is held by the author(s). Please follow reuse instructions given by Creative Commons for its various licenses. ECS articles are published using either CC BY or CC BY-NC-ND licenses.

CC BY

CC BY-NC-ND

Best Practices for Citing CC Licensed Articles

How to Ask for Permission

Beginning Monday, April 10, 2017, the following button may be used to request permission directly from the Copyright Clearance Center:

> **Get Permissions**

- **PERMISSION IS NOT REQUIRED** to reuse your own content (i.e. reusing figures and/or tables from a paper you are an author on). Full credit to the original source should be given.
- **PERMISSION IS NOT REQUIRED** if figures and/or tables from one ECS publication will be reused in another forthcoming ECS publication.

260

APPENDIX D

Curriculum Vitae

Curriculum Vitae

Mojtaba Momeni

PERSONAL INFORMATION:

Positions:

PhD Candidate at the Department of Chemistry

of the University of Western Ontario, London, ON, Canada.

NACE Southern Ontario Student Section (SOSS) Chairman, 2017-Present.

NACE Southern Ontario Student Section (SOSS) Vice-Chairman, 2014-2017.

Student member of Committee of Alumni Relation and Development (CARD) of the Chemistry department of the University of Western Ontario, 2014-Present

EDUCATION BACKGROUND:

2013-Present PhD student in Chemistry Department, Western University (UWO), London, ON, Canada

2007-2010 M.Sc. in Metallurgical Engineering and Material Science Department Ferdowsi University of Mashhad (FUM), Mashhad, Iran

2003-2007 B.Sc in Metallurgical Engineering and Material Science Department, Ferdowsi University of Mashhad (FUM), Mashhad, Iran

POSITIONS AND WORKING EXPERIENCES:

Research Assistant, "Prof. J. Clara Wren, Radiation Assisted Materials Performance Science (RAMPS)", Department of Chemistry, Faculty of Science, The University of Western Ontario, Since Fall 2013.

Corrosion Lecturer, "Institute of Applied Science-Technology, Jahad Daneshgahi Mashhad", September 2011-May 2012.

Research Assistant, "Prof. M.H. Moayed, Corrosion and Oxidation of Metals and Alloys", Metallurgical and Materials Engineering Department, Faculty of Engineering, Ferdowsi University of Mashhad (FUM). October 2010- August 2013.

ACADEMIC AWARDS AND HONORS:

Ontario Trillium Scholarship (OTS) 2013.

Canadian Nuclear Society R. E. Jervis Award, 2017.

First Place, Poster Presentation (Second author), UNENE Annual Meeting, 2016.

Travel Grant Award, CORROSION 2016.

Third Place, Poster Presentation, UNENE Annual Meeting, 2015.

Lightening Poster Presentation in Faraday Discussion – Corrosion Chemistry 2015.

Travel Grant Award, CNS Conference, 2014.

Western International Graduate Student Tuition Scholarship 2013.

Top Student Researcher of Engineering Faculty of Ferdowsi University of Mashhad (FUM) 2010.

PUBLICATIONS:
   1- **Peer-reviewed** (F: Full-Length Journal Paper, P: Conference Proceeding)

[19-P] **M. Momeni** and J.C. Wren, "Mass and Charge Balance (MCB) Model Simulations of Corrosion of Cr Containing Alloys", *CORROSION 2016,* 6-10 Mar. 2016, Vancouver, BC, Canada

[18-F] **M. Momeni**, M. Behazin, J.C. Wren, "Mass and Charge Balance (MCB) Model Simulations of Current, Oxide Growth and Dissolution in Corrosion of Co-Cr Alloy Stellite-6", *Journal of the Electrochemical Society* 163 (2016) C94-C105.

[17-F] R.P. Morco, A.Y. Musa, **M. Momeni** J.C. Wren, "Corrosion of carbon steel in the $[P_{14666}][Br]$ ionic liquid: The effects of γ-radiation and cover gas", *Corrosion Science* 102 (2016), 1-15.

[16-F] **M. Momeni**, J.C. Wren, "A mechanistic model for oxide growth and dissolution during corrosion of Cr-containing alloys", *Faraday Discussions* 180 (2015) 113-135.

[15-P] H. Subramanian, V. Subramanian, **M. Momeni**, J.J. Noël, J.M. Joseph, D.A. Guzonas, J.C. Wren, "The Effect of Water Radiolysis on Corrosion in High-temperature Steam", *17th International Conference on Environmental Degradation of Materials in Nuclear Power Systems - Water Reactors*, August 9-13, 2015, Ottawa, Ontario, Canada

[14-F] M Ebrahimzadeh, M Gholami, **M Momeni**, A Kosari, M.H Moayed, A. Davoodi, "Theoretical and experimental investigations on corrosion control of 65Cu–35Zn brass in nitric acid by two thiophenol derivatives", *Applied Surface Science* 332 (2015) 384-392.

[13-F] M. Hoseinpoor, **M. Momeni**, M.H. Moayed, A. Davoodi, "EIS assessment of critical pitting temperature of 2205 duplex stainless steel in acidified ferric chloride solution", *Corrosion Science* 80 (2014) 197-204.

[12-F] A. Kosari, M.H. Moayed, A. Davoodi, R. Parvizi, **M. Momeni**, H. Eshghi, H. Moradi, "Electrochemical and quantum chemical assessment of two organic compounds from pyridine derivatives as corrosion inhibitors for mild steel in HCl solution under stagnant condition and hydrodynamic flow", *Corrosion Science* 78 (2014) 138-150.

[11-F] B. Hashemi, A. Davoodi, **M. Momeni**, M.H. Moayed, "New high resolution solution for measuring degree of sensitization of duplex stainless steel 2205 by DL-EPR technique", *CORROSION* 69 (2013) 230-242.

[10-F] M. Mirjalili, **M. Momeni**, N. Ebrahimi, M.H Moayed, "Comparative study on corrosion behaviour of Nitinol and stainless steel orthodontic wires in simulated saliva solution in presence of fluoride ions", *Materials Science and Engineering: C* 33 (2013) 2084-2093.

[9-F] Sh. Mohajernia, S. Hejazi, M.H. Moayed, M. Rahimizadeh, A. Eslami, **M. Momeni**, A. Shiri, "Inhibitive assessment of 1-(7-methyl-5-morpholin-4-yl-thiazolo[4,5-d]pyrimidin-2-yl)-hydrazine as a corrosion inhibitor for mild steel in sulphuric acid solution", *Journal of the Iraninan Chemical Society* 10 (2013) 831-839.

[8-F] **M. Momeni**, M. Esfandiari, M.H. Moayed, "Improving Pitting Corrosion of 304 Stainless Steel by Electropolishing Technique", *Iranian Journal of Materials Science & Engineering* 9 (2012) 34-42.

[7-F] M. Noori, **M. Momeni**, M.H. Moayed, "Inhibitive Assesment of Stearamide as a Corrosion Inhibitor for Mild Steel in HCl Solution", *International Journal of Engineering* 25 (2012) 119-125.

[6-F] **M. Momeni**, A. Ale-yassin, M.H. Moayed, "Establishing a New Solution Based on Hydrochloric Acid/Sodium Thiosulfate for Detecting and Measuring Degree of Sensitization of Stainless Steels Using Double-Loop Electrochemical Potentiodynamic Reactivation Method", *CORROSION* 68 (2012) 015007-1-015007-11.

[5-F] N. Ebrahimi, **M. Momeni**, , A.Kosari, M.Zakeri, M.H. Moayed, "A Comparative study of critical pitting temperature (CPT) of stainless steels by Electrochemical Impedance Spectroscopy (EIS), potentiodynamic and potentiostatic techniques", *Corrosion Science* 59 (2012) 96-102.

[4-F] N. Ebrahimi, **M. Momeni**, M.H. Moayed, A. Davoodi, "Correlation between critical pitting temperature and degree of sensitization on alloy 2205 duplex stainless steel" , *Corrosion Science* 53 (2011) 637-644.

[3-F] A. Kosari, **M. Momeni**, R. Parvizi, M. Zakeri, M.H. Moayed, A. Davoodi, H. Eshghi, "Theoretical and electrochemical assessment of inhibitive behavior of some thiophenol derivatives on mild steel in HCl", *Corrosion Science* 53 (2011) 3058-3067.

[2-F] N.S. Ayati, S. Khandandel, **M. Momeni**, M.H. Moayed, A. Davoodi, M. Rahimizadeh, "Inhibitive effect of synthesized 2-(3-pyridyl)-3, 4-dihydro-4-quinazolinone as a corrosion inhibitor for mild steel in hydrochloric acid", *Materials Chemistry and Physics* 126 (2011) 873-879.

[1-F] **M. Momeni**, M.H. Moayed, A. Davoodi, "Tuning DOS measuring parameters based on double-loop EPR in H_2SO_4 containing KSCN by Taguchi method", *Corrosion Science* 52 (2010) 2653-2660.

2- Conferences (O: Oral Presentation, P: Poster Presentation)

[26-O] **M. Momeni**, J.C. Wren, Mass and Charge Balance (MCB) Model Simulations of Corrosion of Cr Containing Alloys, 100th Canadian Chemistry Conference, Toronto ON, May 28th – June 1st 2017.

[25-O] M. Zakeri, **M. Momeni**, J.M. Joseph, O. Yong, J.C. Wren, Investigation of Humid Air Corrosion of Carbon Steel Stainless Steel Welds in the Presence of γ-Radiation, 100th Canadian Chemistry Conference, Toronto ON, May 28th – June 1st 2017.

[24-O] M. Li, **M. Momeni**, J.M. Joseph, O. Yong, J.C. Wren, The Effect of Radiation on the Kinetics of Corrosion of Dissimilar Metal Welds, 100th Canadian Chemistry Conference, Toronto ON, May 28th – June 1st 2017.

[23-P] M. Naghizadeh, A.M. Jean, **M. Momeni**, J.M. Joseph, G. Whitaker, J.C. Wren, The Effect of Different Anions on the Corrosion of Copper, 100th Canadian Chemistry Conference, Toronto ON, May 28th – June 1st 2017.

[22-P] R. Karimihaghighi, **M. Momeni**, J.C. Wren, Effects of pH, Temperature and Radiation on Corrosion and Oxide Formation on Pure Nickel, 100th Canadian Chemistry Conference, Toronto ON, May 28th – June 1st 2017.

[21-P] **M. Momeni**, J.M. Joseph, H. Subramanian, V. Subramanian, J.J. Noël, D.A. Guzonas, J.C. Wren, Effects of Oxygen and Radiation on Steam Corrosion of Fe-Cr-Ni Alloys and Comparison to Supercritical Water Corrosion, NACE Northern Area Eastern Conference, Toronto, ON, Oct 31 – Nov. 2nd 2016.

[20-P] M. Li, **M. Momeni**, J.M. Joseph, O. Yong and J.C. Wren, The Effect of Radiation on the Kinetics of Corrosion of Dissimilar Metal Welds, NACE Northern Area Eastern Conference, Toronto, ON, Oct 31 – Nov. 2nd 2016.

[19-P] M. Naghizadeh, A.M. Jean, **M. Momeni**, J.M. Joseph, G. Whitaker, J.C. Wren, The Effect of Anion on the Evolution of Oxide Formation and Growth During Corrosion of Copper, NACE Northern Area Eastern Conference, Toronto, ON, Oct 31 – Nov. 2nd 2016.

[18-P] <u>M. Zakeri</u>, **M. Momeni**, J.M. Joseph, O. Yong and J.C. Wren, Humid-Air Radiolysis-Induced Corrosion of Carbon Steel – Stainless Steel Welds, NACE Northern Area Eastern Conference, Toronto, ON, Oct 31 – Nov. 2nd 2016.

[17-P] <u>M. Li</u>, R.J. Whyte, **M. Momeni**, J. Joseph, O. Yong and J.C. Wren, Effect of Environment Chemistry on the Corrosion of Dissimilar Metal Welds, 36th Annual CNS Conference, 40th CNS/CNA Student Conference, Toronto, ON, June 20, 2016.

[16-P] <u>R. Karimihaghighi</u>, **M. Momeni**, J.C. Wren, Effect of Temperature and Radiation on Corrosion and Oxide Formation on Pure Nickel, 36th Annual CNS Conference, 40th CNS/CNA Student Conference, Toronto, ON, June 20, 2016.

[15-P] <u>A.M. Jean</u>, **M. Momeni**, J.M. Joseph, J.J. Noel, J.C. Wren, Poster, Polymorphic Cu2O Growth by Oxidation of Copper Metal using Gamma-Radiation, 36th Annual CNS Conference, 40th CNS/CNA Student Conference, Toronto, ON, June 20, 2016.

[14-P] **<u>M. Momeni</u>**, R.J. Whyte, M. Li, J. Joseph, O. Yong and J.C. Wren, "Effect of Radiolysis and Water Chemistry on Galvanic Corrosion of Stainless Steel-Carbon Steel Welds", *CORROSION 2016,* 6-10 Mar. 2016, Vancouver, BC, Canada

[13-P] <u>R.P. Morco</u>, **M. Momeni**, J.C. Wren, "Corrosion of Carbon Steel in Non-aqueous Electrolyte and γ-Radiation Induced Oxide Protection", *CORROSION 2016,* 6-10 Mar. 2016, Vancouver, BC, Canada

[12-P] **<u>M. Momeni</u>**, R.J. Whyte, M. Li, O. Yong and J.C. Wren, "Effects of pH and Radiation on Galvanic Corrosion of Stainless Steel-Carbon Steel Welds", *UNENE Annual Meeting,* 15-16 Dec. 2015, Toronto, On, Canada

[11-P] **<u>M. Momeni</u>**, J.C. Wren, "Effect of pH and temperature on corrosion and oxide film formation on Alloy 800", *NACE Northern Area Eastern Conference*, 18-21 Oct. 2015, Ottawa, ON, Canada.

 [10-O] **M. Momeni**, M. Behazin, <u>J.C. Wren</u>, "MCB (Mass and Charge Balance) Model Simulation of Corrosion of Co-Cr Alloy Stellite-6", *228th ECS Meeting*, 11-15 Oct. 2015, Phoenix, AZ, p. 710.

[9-O] S. Hariharan, **M. Momeni**, V. Subramanian, <u>J.J. Noel</u>, J. Joseph, J.C. Wren, "The Influence of Water Radiolysis on Corrosion by Supercritical Water", *228th ECS Meeting*, 11-15 Oct. 2015, Phoenix, AZ, p. 682.

[8-P] **<u>M. Momeni</u>**, M. Behazin, J.C. Wren, "Modeling of Potentiostatic Polarization and Oxide Film Formation on Stellite-6", *Faraday Discussions*, 13-15 April 2015, London, UK.

[7-P] A.Y. Musa, **<u>M. Momeni</u>**, J.C. Wren, "Comparison of the Observed Effects of pH, Temperature and γ-Radiolysis on Oxide Growth Kinetics during Corrosion of Fe-Ni-Cr Alloys". *Faraday Discussions*, 13-15 April 2015, London, UK.

[6-P] **M. Momeni**, V. Subramanian, H. Subramanian, J.C. Wren, "Effect of Niobium on Zirconium Alloy Oxidation in Borate Buffer Solution at 250 °C", *38th CNS Conference*, 23-28 Aug. 2014, Vancouver, Canada.

[5-O] A. kosari, R. Parvizi, **M. Momeni**, M.H. Moayed, "Anodic dissolution mechanism for iron in presence of pyridine-2-thiol in 0.1 M HCl", *223th ECS Meeting*, 12-16 May 2013, Toronto, Canada.

[4-O] A. Kosari, R. Parvizi, **M. Momeni**, M.H. Moayed, "Inhibitive Behaviour of pyridine 2-thiol on mild steel in HCl acidic media; Effect of hydrodynamic condition", *EuroCorr* 2012, 9-13 Sep. 2012, Istanbul, Turkey.

[3-P] Sh. Mohajernia, S. Hejazi, M.H. Moayed, M. Rahimizadeh, A. Shiri, **M. Momeni**, "Inhibitive assessment of MMTPH as a novel corrosion inhibitor for mild steel in sulphuric acid solution", *EuroCorr* 2012, 9-13 Sep. 2012, Istanbul, Turkey.

[2-P] **M. Momeni**, M.H. Moayed, A. Davoodi, "A New Approach For Detection and Measuring Degree of Sensitization (DOS) By EIS Method", *EuroCorr* 2010, 13-17 Sep. 2010, Moscow, Russia.

[1-O] **M. Momeni**, M.H. Moayed, A. Davoodi, "Introducing a New Solution for Detecting the StSt IGC Susceptibility Based on DL-EPR Method", *216th ECS Meeting*, 4-9 Oct. 2009, Vienna, Austria.

MEMBERSHIPS:
1. Royal Society of Chemistry (RSC) Associate Member, 2015-present.
2. National Association of Corrosion Engineers (NACE) Student Member, 2014-present.
3. Electrochemical Society (ECS) student member, 2016-present.
4. Canadian Nuclear Society (CNS) Student Member, 2013-present.
5. Canadian Society for Chemistry (CSC) student member, 2017-present

NATIONAL PATENTS:
- ❖ New procedure for detection degree of sensitization of stainless steels.
- ❖ New solution for detection degree of sensitization of stainless steels.
- ❖ New procedure for measuring critical pitting temperature (CPT) of stainless steels.